University of Alberta

Pore Pressure Response and Shear Behavior of Shear Zones in Weak Rocks Near Fort McMurray

By

Xueqing Su ©

A thesis submitted to the Faculty of Graduate Studies and Research in partial fulfillment of the requirements for the degree of **Doctor of Philosophy**

in

Geotechnical Engineering

Department of Civil and Environmental Engineering

Edmonton, Alberta

Fall 2005

Library and
Archives Canada

Published Heritage
Branch

395 Wellington Street
Ottawa ON K1A 0N4
Canada

Bibliothèque et
Archives Canada

Direction du
Patrimoine de l'édition

395, rue Wellington
Ottawa ON K1A 0N4
Canada

0-494-08739-0

Your file Votre référence
ISBN:
Our file Notre reterence
ISBN:

NOTICE:
The author has granted a non-exclusive license allowing Library and Archives Canada to reproduce, publish, archive, preserve, conserve, communicate to the public by telecommunication or on the Internet, loan, distribute and sell theses worldwide, for commercial or non-commercial purposes, in microform, paper, electronic and/or any other formats.

The author retains copyright ownership and moral rights in this thesis. Neither the thesis nor substantial extracts from it may be printed or otherwise reproduced without the author's permission.

AVIS:
L'auteur a accordé une licence non exclusive permettant à la Bibliothèque et Archives Canada de reproduire, publier, archiver, sauvegarder, conserver, transmettre au public par télécommunication ou par l'Internet, prêter, distribuer et vendre des thèses partout dans le monde, à des fins commerciales ou autres, sur support microforme, papier, électronique et/ou autres formats.

L'auteur conserve la propriété du droit d'auteur et des droits moraux qui protège cette thèse. Ni la thèse ni des extraits substantiels de celle-ci ne doivent être imprimés ou autrement reproduits sans son autorisation.

In compliance with the Canadian Privacy Act some supporting forms may have been removed from this thesis.

While these forms may be included in the document page count, their removal does not represent any loss of content from the thesis.

Conformément à la loi canadienne sur la protection de la vie privée, quelques formulaires secondaires ont été enlevés de cette thèse.

Bien que ces formulaires aient inclus dans la pagination, il n'y aura aucun contenu manquant.

Canada

In memory of my mother
who supported me with love

and to

my dear wife, Huiqing and son, Hang
for your support, love and understanding all the way

ABSTRACT

Natural deposits in the Athabasca Oil Sands area contain many shear-induced structures such as shear zones or discontinuities. Locations and features of such structures are unknown in advance, and their internal fractures and geometries are complex, so these structures pose a challenge to tailings dam construction. Design or evaluation of a tailings dam demands an understanding of the shear behavior and pore pressure of shear zones. The principal objective of this study is to provide an approach for measuring the pore pressure of a shear zone and its response to different displacement rates.

An innovative large triaxial testing system and related transducers, laboratory techniques, and procedures were developed to measure the pore pressure of a shear zone. The results reveal that pore pressures on the shear plane and on the base of a sample for three materials (compacted Athabasca clay, over-consolidated Highvale mudstone, and Fort McMurray weak rocks) are identical at a shear displacement rate of less than 14.4 mm/day. This implies that at slow movement the pore pressure obtained from *in situ* instrumentation, which may not be set exactly on the shear plane, can be used as the shear zone pore pressure. The results also reveal that the pore-pressure responses differ for different materials with different stress histories (over consolidation ratios).

Detailed geological field mapping by the author has revealed that shear zones in the Athabasca Oil Sands area often develop in clay beds with high clay content such as clay shale, basal clay, Paleosol, pond mud, and highly weathered limestone. The water content

and Atterberg limits of the material in the shear zone are markedly higher than those of the adjacent unsheared material, while the grain size of the material in the shear zone is much smaller than that of the adjacent unsheared material.

The shear behavior of shear zones, especially their post-peak characteristics, was investigated by using a large triaxial cell. The results show that the stress-displacement curve of a shiny planar shear surface in the highly weathered limestone with relatively large prior shear displacement shows no peak, and after a small displacement, reaches the residual strength. Conversely, a rough shear surface in the same material with small prior shear displacement has a significant peak followed by a decrease in the strength with further shear displacement. A large displacement is needed to reach residual strength. When the shearing was imposed in different minor shear combinations in Paleosol, different stress-displacement curves, post-peak characteristics, and shear strength parameters resulted.

ACKNOWLEDGMENTS

I would like to express my sincere and grateful thanks to my supervisors, Drs. C. Derek Martin, Norbert R. Morgenstern, and Dwayne D. Tannant for their guidance and support during these years of research. Their leadership, expertise, experience and advice are invaluable. I am grateful for their exceptional patience and encouragement.

Gratitude is extended to each of the professors within the geotechnical group, who contributed to my personnel and professional development during my study. Thanks to Sally Petaske for always being helpful. I would also like to thank the rest of staff of the Department of Civil and Environmental Engineering at the University of Alberta.

I wish to thank the technical staff of the Geotechnical Group, particularly Gerry Cyre, Steve Gamble, Christine Hereygers, Gilbert Wong, and Ken Leung for their assistance either in the field or in the laboratory. Special thanks are extended to Allan M. Muir, Argyll Innovations Inc., for his prompt help in the development of equipments.

I am indebted to Suncor Energy Inc. and Luscar Ltd., for without their assistance the study would not have been viable. Tim Eaton, Walday Abeda, Andrew MacNabb, Doug Lacey, Douglas Bell, and Jim Chalmers provided valuable assistance.

This research would not have been possible without the financial support provided by several organizations. My sincere gratitude is extended to the Natural Sciences and Engineering Research Council (NSERC), University of Alberta, and the department of Civil and Environmental Engineering at the University of Alberta.

Special acknowledgement is extended to Peter Chavan for his help in English proof-reading and editing.

There are numerous friends and colleagues whom I would like to thank, in particular Janming Pang, Chengmai Guo, Pingke Li, Namkak Cho, Xiaobo Wang, Xiteng Liu, Baoquan An, Junwen Yang, Xuwen Chi, and Linggen Jiang for their help.

The love and support of my family were important to the success of this study. I would like to express my deepest gratitude to my wife for her love, support, and encouragement throughout this study. Despite his young age, my son knew how to be supportive and understanding. The love and support of my parents have always been a source of strength in my work. Unfortunately, my mother passed away during my study and cannot share my success. I miss her very much.

TABLE OF CONTENTS

CHAPTER Page

1. INTRODUCTION 1
    1.1 BACKGROUND 1
    1.2 RESEARCH SCOPE AND OBJECTIVE 4
    1.3 THESIS ORGANIZATION 4
2. LITERATURE REVIEW 11
    2.1 INTRODUCTION 11
    2.2 FIELD OBSERVATIONS AND DESCRIPTIONS OF SHEAR ZONES 11
    2.3 SHEAR-ZONE-FORMING PROCESS IN LABORATORY INVESTIGATION 13
    2.4 SIMILARITY OF SHEAR ZONES 14
    2.5 PHYSICAL PROPERTIES OF SHEAR ZONES 15
    2.6 MECHANICAL PROPERTIES OF SHEAR ZONES 17
    2.7 PORE PRESSURE RESPONSE OF SHEAR ZONES 20
    2.8 HYDRAULIC CONDUCTIVITY OF SHEAR ZONES 20
    2.9 CONCLUSIONS AND COMMENTS 22
3. FIELD INVESTIGATION OF SHEAR ZONES IN WEAK ROCKS 43
    3.1 INTRODUCTION 43
    3.2 INVESTIGATION METHOD 44
        3.2.1 Equipment 44
        3.2.2 Procedures 45
        3.2.3 Presentation of the Mapping 46
    3.3 LOCATION AND GEOLOGY OF THE MAPPING SITES 46
    3.4 DESCRIPTION AND MAPPING OF THE SHEAR ZONE 47
        3.4.1 Shear Zone ("Shear Zone I" hereafter) at Dyke 11A 47
        3.4.2 Shear Zones at Dyke 10 48
            3.4.2.1 Shear zone ("shear zone II" hereafter) in pit 18 48

3.4.2.2 Shear zone ("shear zone III" hereafter) in pit 26 49
3.4.2.3 Shear zone ("shear zone" IV hereafter) in pit 20 49
3.5 PHYSICAL PROPERTIES OF SHEAR ZONES 50
3.5.1 Water Content 50
3.5.2 Grain-size Distribution 51
3.5.3 Atterberg Limits 51
3.6 CONCLUSIONS 52
4. **MECHANICS OF SHEAR RESISTANCE OF SHEAR ZONES AND PARAMETRIC SENSITIVITY ANALYSIS** 75
4.1 INTRODUCTION 75
4.2 SHEAR-RESISTANCE CHARACTERISTICS OF SHEAR ZONES 75
4.3 EFFECT OF RESIDUAL STRENGTH AND PORE PRESSURE ON SLOPE STABILITY AND MOVEMENT 76
4.3.1 Effect of Residual Strength on Slope Stability 76
4.3.2 Effect of Residual Strength on Slope Movement 78
4.3.3 Effect of Pore Pressure on Slope Stability and Movement 78
4.4 CONCLUSIONS 80
5. **DEVELOPMENT OF TEST EQUIPMENT** 96
5.1 INTRODUCTION 96
5.2 TRIAXIAL COMPRESSION CELL AND AXIAL LOADING SYSTEM 97
5.2.1 Triaxial Compression Cell 97
5.2.1.1 Cell body and top 98
5.2.1.2 Cell base 99
5.2.1.3 Loading piston 99
5.2.1.4 Loading caps 100
5.2.2 Axial Loading System 100
5.2.2.1 Loading frame 100
5.2.2.2 Hydraulic jack 101
5.2.2.3 Loading equipment 101

5.3 TRIAXIAL PRESSURE PANEL SYSTEM 102
5.4 PORE-PRESSURE MEASUREMENT SYSTEM 103
5.5 DISPLACEMENT MEASUREMENT SYSTEM 104
    5.5.1 Principle of the Electrolytic Level 105
    5.5.2 Make-up of the Tilt Transducer 105
    5.5.3 Principle of the Tilt Transducer 106
5.6 DATA ACQUISITION SYSTEM 107
5.7 MODIFIED CONVENTIONAL TRIAXIAL EQUIPMENT 109
5.8 SUMMARY 110

6. TESTING PROCEDURES FOR CONSOLIDATED UNDRAINED TRIAXIAL TESTS WITH PORE-PRESSURE MEASUREMENTS ON A SHEAR PLANE 137
6.1 INTRODUCTION 137
6.2 CALIBRATION OF MEASUREMENT INSTRUMENTS 137
6.3 TEST MATERIALS AND SAMPLE PREPARATION 139
    6.3.1 Test Materials 139
    6.3.2 Sample Preparation 139
        6.3.2.1 Reconstituted Athabasca clay samples 139
        6.3.2.2 Highvale mudstone samples 140
        6.3.2.3 Undisturbed weak rock samples from Suncor sites 141
6.4 SAMPLE MOUNTING PROCEDURES 142
    6.4.1 Installation of the Magnet Pieces 142
    6.4.2 Placement of the Internal Pore-pressure Transducer 143
    6.4.3 Sample Mounting 144
6.5 TESTING PROCEDURES 145
    6.5.1 Saturation 145
        6.5.1.1 Rationale for testing under conditions of complete saturation 145
        6.5.1.2 Saturating specimens by back pressure 146
        6.5.1.3 B value 148
        6.5.1.4 Evaluating degree of saturation --- B-test 150

6.5.2 Consolidation 151
6.5.3 Shearing of Samples 152
6.6 ANALYSIS OF DATA 153
6.6.1 Axial Load Correction 154
6.6.2 Area Correction 155
6.6.3 Membrane Correction 156
6.6.4 Side Drain Correction 156
6.7 SUMMARY 157
7. **PORE-PRESSURE RESPONSES AND SHEAR BEHAVIOR OF THE SHEAR ZONES IN THREE MATERIALS** 176
7.1 INTRODUCTION 176
7.2 TEST MATERIALS 176
7.3 TEST CONDITION AND SPECIMEN INFORMATION 178
7.3.1 Test Condition 178
7.3.2 Specimen Information 178
7.4 TEST RESULTS AND OVERVIEW 179
7.4.1 Athabasca Clay 179
7.4.2 Highvale Mudstone 181
7.4.3 Fort McMurray Highly Weathered Limestone 183
7.4.4 Paleosol 185
7.5 ANALYSIS OF TEST RESULTS 187
7.5.1 Consolidation Behavior 187
7.5.2 Pore-Pressure Response 190
7.5.3 Shear Behavior 199
7.6 SUMMARY AND CONCLUSIONS 204
8. **SUMMARY, CONCLUSIONS, AND RECOMMENDATIONS** 241
8.1 SUMMARY AND CONCLUSIONS 241
8.1.1 Field Investigation of Shear Zones and Laboratory Index Tests 242
8.1.2 Testing Equipment and Procedures 243
8.1.3 Laboratory Testing 244

8.2 RECOMMENDATIONS FOR FUTURE RESEARCH 246

REFERENCES 248

APPENDIX A INDEX PROPERTY TEST RESULTS 259

APPENDIX B FLAC PROGRAMS FOR PARAMETER SENSITIVE ANALYSIS 266

APPENDIX C INSTRUMENT CALIBRATION 274

APPENDIX D TRIAXIAL TEST RESULTS 275

LIST OF TABLES

Table 2.1	Typical displacements at various stages of shear in clay having CF> 30% (Skempton, 1985)	25
Table 3.1	Atterberg limits inside and outside the shear zones	53
Table 4.1	Summary of soil properties used in stability analysis (Thomson & Tweedie 1978)	81
Table 7.1	Characteristics of Athabasca clay	208
Table 7.2	Characteristics of mudstone from the Highvale coal mine (after Small 1989)	208
Table 7.3	Characteristics of Paleosol from dyke 10 at pit 20	208
Table 7.4	Characteristics of the highly weathered limestone in pit 18	209
Table 7.5	Characteristics of the highly weathered limestone in pit 26	209
Table 7.6	Displacement rates used for tests	209
Table 7.7	Summary of tests on rate effects and pore-pressure measurements (modified from Sheahan et al., 1996)	210
Table 7.8	Peak pore-pressure-changes at the different shear displacement rates	211
Table 7.9	Water contents in an Athabasca clay sample before and after testing	211
Table A1	Water content of the shear zone II (pit 18) and the shear zone III (pit 26)	259
Table A2	Hydrometer test on MSF in the shear zone I	260
Table A3	Hydrometer test on the material in the shear zone II	261
Table A4	Atterberg Limit test on MSF in the shear zone I	262
Table A5	Atterberg Limit test on material inside the shear zone II	262
Table A6	Atterberg Limit test on material outside the shear zone II	263
Table A7	Hydrometer test on Athabasca clay, Paleosol, and weathered limestone	264
Table A8	Atterberg Limit test on Athabasca clay	265
Table A9	Atterberg Limit test on Paleosol	265
Table A10	Atterberg Limit test on highly weathered limestone	265

Table C1 Summary of the instruments calibration 274
Table D1 Specimen information 275

LIST OF FIGURES

Figure 1.1	Shear zones generated in the laboratory tests	6
Figure 1.2	Shear zones developed by engineering works	6
Figure 1.3	Shear zones developed during geological events	7
Figure 1.4	Photograph of a landslide along Paleosol at Wood Creek at dyke 11A near Fort McMurray	8
Figure 1.5	Shear zone and slope inclinometer displacement at section 53+00E, cell 23 in the Syncrude lease (after Wadage et al., 1998)	9
Figure 1.6	Scenario of shear zone geotechnics	10
Figure 2.1	General features in a shear zone and reference axes (modified from Skempton 1966)	26
Figure 2.2	Details of Geildford shear zone in a thin section. (after Morgenstern and Tchalenko, 1967)	26
Figure 2.3	Successive stages in the development of a shear zone in clay, from laboratory tests (modified from Skempton 1966)	27
Figure 2.4	Stress-displacement curve and shear zone development (modified from Tchalenko 1970)	28
Figure 2.5	Similarity of shear zones in different scales (modified from Tchalenko, 1970)	29
Figure 2.6	Shear zones developed in folded (a) and faulted (b) layers	30
Figure 2.7	Water content profile across basal shear surface of a London clay landslide (modified from Henkel, 1956)	31
Figure 2.8	Water content profiles of a shear zone found at the base of earthflows in the Basento Valley, Italy (modified from Guerrier et al., 1993)	32
Figure 2.9	Water content profiles around shear zones in sensitive clay (a) (modified from Lefebvre, 1981) and in London clay (b) (modified from Chandler et al., 1998)	33
Figure 2.10	Typical stress-displacement curves on a principal slip surface and	

on intact clay (modified from Skempton and Petley, 1967). 34

Figure 2.11 Stress-displacement curves and post-peak features at constant σ_n' (Modified from Skempton, 1985) 35

Figure 2.12 Ring shear tests on sand-bentonite mixtures (modified from Lupini et al., 1981) 36

Figure 2.13 Field residual and ring shear tests on sands, kaolin and bentonite (after Skempton, 1985) 37

Figure 2.14 Mobilized strengths of a clay at different displacements (modified from Skempton, 1985) 38

Figure 2.15 Shear strength of a clay at different rates of displacement (after Skempton, 1985) 39

Figure 2.16 Variation in residual strength of clays at slow rates of displacement (after Skempton, 1985) 40

Figure 2.17 Summary of ring shear tests for Kalabagh Dam, June 1984 (modified from Skempton, 1985) 41

Figure 2.18 Sketch shows the shear-parallel, shear-normal and oedometric hydraulic conductivities in a sheared clay specimen 42

Figure 3.1 Photograph showing the slickensided basal clay (after McRoberts, 2001) 54

Figure 3.2 Photograph of the mapping tools 55

Figure 3.3 A scenario of the shear zone mapping slope; b is a primary horizontal baseline, b′ is a secondary horizontal baseline; c is primary vertical baseline, c′ is a secondary vertical baseline; b, b′, c, and c′ constitute a network. 56

Figure 3.4 Location of Suncor Energy Inc. mine site 57

Figure 3.5 Stratigraphic sequence in the project's area(AGRA 1999, Carrigy 1966, Kosar 1992, and Dewar 1996) 58

Figure 3.6 Location of the shear keys (Scale 1:62500) 59

Figure 3.7 Relationship between shear zone and adjacent rock (not to scale, but vertical about 4m) 60

Figure 3.8 Mapping positions (A and B) at the shear key in dyke 11A of

Pond 8A (scale 1:25000) 61
Figure 3.9 Shear zone in the marine shore face silty clay at dyke 11A (direction of the sections is 175° and 215°, respectively. Position B is about 110 m south of position A) 62
Figure 3.10 Mapping locations (Pits 18, 20, and 26) in dyke 10 west of Pond 7 (scale 1:17000) 63
Figure 3.11 Shear zone in the weathered limestone at pit 18 64
Figure 3.12 Photograph of the shear zone at pit 18 65
Figure 3.13 Photograph of the shear zone at pit 26 66
Figure 3.14 Shear zone in the weathered limestone at pit 26 66
Figure 3.15 Shear zone in Paleosol mapped on south sidewall at pit 20 (lines are discontinuities) 67
Figure 3.16 Shear zone in Paleosol mapped on north sidewall at pit 20 (direction of the section is 067°) 68
Figure 3.17 Photograph showing the shear lenses and minor shear occurrence (length of the eraser is about 3 cm) 69
Figure 3.18 Photograph showing different directions of the striations (diameter of the camera lens cap is about 5cm) 70
Figure 3.19 Two photographs showing rough shear surface (a) and striation (arrow) (b) (diameter of Canadian one-dollar is about 2.6cm) 71
Figure 3.20 Water content profile across shear zone II at pit 18 72
Figure 3.21 Water content profile across shear zone III at pit 26 73
Figure 3.22 Grain size distribution (1 means within shear zone, while 2 out of shear zone at dyke 11A; 3 means within shear zone, while 4 out of shear zone at pit 18) 74
Figure 4.1 Section of the Edgerton landslide with stratigraphic layers and interpreted failure surface 82
Figure 4.2 Factor of safety in the nominal friction angle of 8° 83
Figure 4.3 Relationship between factor of safety and friction angle 84
Figure 4.4 Failure probability in the nominal residual friction angle of 8°

with 1° of standard deviation 85

Figure 4.5 Failure probability in the nominal residual friction angle of 8° with 2° of standard deviation 86

Figure 4.6 Relationship between failure probability and friction angle in SD = 1° (a) and SD = 2° (b) 87

Figure 4.7 Relationship between movement of the landslide and friction angle of potential failure surface 88

Figure 4.8 Relationship between movement and friction angle for a large rockslide (after Corkum and Martin, 2002) (Ks is the shear stiffness of the slip plane and Kn is the normal stiffness of the slip plane) 89

Figure 4.9 Linear relationship between factor of safety, F, and pore pressure ratio, r_u (after Bishop and Morgenstern, 1960) 90

Figure 4.10 Linear relationship between factor of safety and positions of the phreatic surface level (0 meter refers to the *in situ* phreatic level) 91

Figure 4.11 Relationship between the slide's movement and the phreatic surface level (0 meter refers to the *in situ* phreatic level) 92

Figure 4.12 Change in pore water pressure and displacement with time (after Kawabe, 1991) 93

Figure 4.13 Relationship between the strain rate and the pore-water pressure (after Kawabe, 1991) 94

Figure 4.14 Pore pressure and displacements versus time (modified from Faure et al., 1991) 95

Figure 5.1 Sketch of the set-up of the large triaxial cell (not to scale) 111

Figure 5.2 Photograph showing the large triaxial cell and the loading frame 112

Figure 5.3 Structure sketch of the large diameter triaxial cell 113

Figure 5.4 Details of the triaxial cell top (unit: mm) 114

Figure 5.5 Details of the triaxial cell base (unit: mm) 115

Figure 5.6 Details of the large triaxial cell bushing in brass, piston and ram float in stainless steel (unit: mm) 116

Figure 5.7 Top loading cap and its relationship with bearing and loading

piston 117
Figure 5.8 Attachment of the lower loading cap to the cell base 117
Figure 5.9 Basic dimensions and properties of the steel trough C310 x 45 118
Figure 5.10 Details of the C 310 x 45 structural loading frame (unit: mm) 119
Figure 5.11 Details of the C310 x 45 structural loading frame top(unit: mm) 120
Figure 5.12 Details of the hydraulic cylinder ENERPAC RC-1510 121
Figure 5.13 ISCO Series D Model 100DX syringe pump 122
Figure 5.14 Dimensions and properties of 50klb ALD-COMP load cell 123
Figure 5.15 Layout of triaxial panel system 124
Figure 5.16 Design of pore pressure transducer brass container (unit: mm) 125
Figure 5.17 Kyowa Model PS-10KB pressure sensor 126
Figure 5.18 Photo of the pore pressure transducer 127
Figure 5.19 Mount of the pore pressure transducer in a sample 127
Figure 5.20 0725 tilt sensor and its linear output 128
Figure 5.21 0729 signal conditional 128
Figure 5.22 Photograph showing the appearance of the tilt transducer 129
Figure 5.23 Principle of the tilt transducer (assuming a rigid block movement) 129
Figure 5.24 Typical vertical displacements measured by external LVDT and internal "tilt" sensor for an Athabasca clay sample 130
Figure 5.25 Typical vertical displacements measured by external LVDT and internal "tilt" sensor for a Highvale mudstone 131
Figure 5.26 Typical vertical displacements measured by external LVDT and internal LVDT for a Suncor weak rock sample 132
Figure 5.27 Layout of the measurement system 133
Figure 5.28 Schematic representation of data logging and control system 134
Figure 5.29 Agilent 34970A Data Acquisition/Switch Unit 135
Figure 5.30 Data Dolphin data logger 135
Figure 5.31 Sketch of the set-up of the modified triaxial cell (not to scale) 136
Figure 6.1 Effect of a discontinuity on the strength and failure mode of a sample (modified from Hudson and Harrison, 1997) 158
Figure 6.2 Photographs showing a cut plane before (a) and after (b) polishing 159

Figure 6.3 Sketch of sampling of the block samples in the test pits 160
Figure 6.4 Photograph showing a block sample 161
Figure 6.5 Sketch of sampling of the laboratory samples 162
Figure 6.6 Fly-auger type core barrel used for sample coring 163
Figure 6.7 Schematically showing the position of the magnet in a sample 164
Figure 6.8 Schematically showing the relationship between the magnets and the sample, the steel strip, and the LVDT 165
Figure 6.9 Photographs showing the procedures of the internal pore pressure transducer installation 166
Figure 6.10 Photograph showing the seal of the transducer tubing 167
Figure 6.11 Set-up of a mudstone sample 168
Figure 6.12 Installation of the large cell wall with a crane 169
Figure 6.13 Installation of the frame top by using a crane 170
Figure 6.14 Time to reach a degree of saturation using back pressure (modified from Black and Lee, 1973) 171
Figure 6.15 Drainage from end and radial boundary during consolidation 172
Figure 6.16 Mechanism of single-plane slip for area correction 173
Figure 6.17 Membrane corrections for single-plane slip: (a) correction curve, (b) value of factor f_θ for various inclinations of slip plane (modified from Head, 1986) 174
Figure 6.18 Drain correction curve for single-plane slip (modified from Head, 1986) 175
Figure 7.1 Grain-size distribution of Athabasca clay 212
Figure 7.2 Grain-size distribution of Fort McMurray weak rocks 213
Figure 7.3 Consolidation curve: volume change versus square root time for Athabasca clay 214
Figure 7.4 Pore-pressure-dissipation curve for Athabasca clay 214
Figure 7.5 Relationship between normalized deviator stress and shear displacement for Athabasca clay at the axial displacement rate of 2 mm/minute 215
Figure 7.6 Relationship between normalized pore-water pressure and shear

displacement for Athabasca clay at the axial displacement rate of 2 mm/minute 215

Figure 7.7 Normalized effective stress paths for Athabasca clay at the axial displacement rate of 2 mm/minute 216

Figure 7.8 Relationship between the pore-pressure parameter A and the shear displacement for Athabasca clay at the axial displacement rate of 2 mm/minute 216

Figure 7.9 Relationship between mobilized friction angle and shear displacement for Athabasca clay at the axial displacement of 2 mm/minute 217

Figure 7.10 Difference between the pore-pressure-change on the plane and on the base of an Athabasca clay specimen at the axial displacement rate of 2 mm/minute 217

Figure 7.11 Normalized deviator stresses at the different axial displacement rates for Athabasca clay 218

Figure 7.12 Normalized pore-water pressures on the plane at the different axial displacement rates for Athabasca clay 218

Figure 7.13 Normalized pore-water pressures on the base at the different axial displacement rates for Athabasca clay 219

Figure 7.14 Normalized effective stress paths on the shear plane at the different axial displacement rates for Athabasca clay 219

Figure 7.15 Normalized effective stress paths on the base at the different axial displacement rates for Athabasca clay 220

Figure 7.16 Relationship between the pore-pressure parameter A and the shear displacement at the different axial displacement rates for Athabasca clay 220

Figure 7.17 Mobilized friction angles with the shear displacement at the different axial displacement rates for Athabasca clay 221

Figure 7.18 Consolidation curve: volume change versus square root time for Highvale mudstone 221

Figure 7.19 Pore-pressure-dissipation curve for Highvale mudstone 222

Figure 7.20 Relationship between normalized deviator stress and shear displacement for Highvale mudstone at the axial displacement rate of 0.01 mm/minute 222

Figure 7.21 Relationship between normalized pore-water pressure and shear displacement for Highvale mudstone at the axial displacement rate of 0.01 mm/minute 223

Figure 7.22 Normalized stress paths for Highvale mudstone at the axial displacement rate of 0.01 mm/minute 223

Figure 7.23 Relationship between the pore-pressure parameter A and the shear displacement for Highvale mudstone at axial displacement rate of 0.01 mm/minute 224

Figure 7.24 Relationship between mobilized friction angle and shear displacement for Highvale mudstone at the axial displacement of 0.01 mm/minute 224

Figure 7.25 Difference between the pore-pressure-changes on the plane and on the base of a Highvale mudstone specimen at the axial displacement rate of 0.01 mm/minute 225

Figure 7.26 Pore-pressure-dissipation curve for Suncor weathered limestone 225

Figure 7.27 Relationship between normalized deviator stress and shear displacement for Suncor weathered limestone at the axial displacement rate of 0.002 mm/minute 226

Figure 7.28 Relationship between normalized pore-water pressure and shear displacement for Suncor weathered limestone at the axial displacement rate of 0.002 mm/minute 226

Figure 7.29 Normalized effective stress paths for Suncor weathered limestone at the axial displacement rate of 0.002 mm/minute 227

Figure 7.30 Relationship between the pore-pressure parameter A and the shear displacement for Suncor weathered limestone at the axial displacement rate of 0.002 mm/minute 227

Figure 7.31 Relationship between mobilized friction angle and shear displacement for Suncor weathered limestone at the axial

displacement rate of 0.002 mm/minute 228
Figure 7.32 Difference between the pore-pressure-changes on the plane and on the base of a Suncor weathered limestone specimen at the axial displacement rate of 0.002 mm/minute 228
Figure 7.33 Comparison of the normalized pore-pressure-changes for Athabasca clay measured on and off the shear plane at axial displacement rates of 0.001, 0.005, and 0.02 mm/minute 229
Figure 7.34 Sketch of installation of the pore-pressure transducer in a Paleosol specimen 229
Figure 7.35 Pore-pressure-dissipation curve for Paleosol 230
Figure 7.36 Relationship between normalized deviator stress and shear displacement for Paleosol at the axial displacement rate of 0.01 mm/minute 230
Figure 7.37 Relationship between normalized pore-water pressure and shear displacement for Paleosol at the axial displacement rate of 0.01 mm/minute 231
Figure 7.38 Normalized effective stress paths for Paleosol at the axial displacement rate of 0.01 mm/minute 231
Figure 7.39 Relationship between the pore-pressure parameter A and the shear displacement for Paleosol at the axial displacement rate of 0.01 mm/minute 232
Figure 7.40 Relationship between mobilized friction angle and shear displacement for Paleosol under the assumption of no cohesion 232
Figure 7.41 Photograph showing the upper sheared part against the right-angle steel strip 233
Figure 7.42 Lower half sample drainage from the radial boundary 234
Figure 7.43 Relationship between the peak pore-pressure-changes and the shear displacement rates for Athabasca clay in the Cartesian coordinates 234
Figure 7.44 Relationship between the peak pore-pressure-changes and the shear displacement rates for Athabasca clay in the half-

	logarithmic coordinates	235
Figure 7.45	Positions for water content measurements in a Athabasca clay sample after testing	235
Figure 7.46	Relationship between the peak pore-pressure parameter A_p and the shear displacement rates for Athabasca clay	236
Figure 7.47	Relationship between the rate of deviator-stress-increment and the shear displacement for Athabasca clay at the different axial displacement rates	236
Figure 7.48	Sub-planar and moderately rough shear plane in one Paleosol sample (diameter of Canadian one-dollar is 26mm)	237
Figure 7.49	Photo showing a sub-planar and moderately rough shear plane in another Paleosol sample (diameter of Canadian one-dollar is 26mm)	238
Figure 7.50	Photo showing many calcium nodules in Paoleosol (diameter of the specimen is 100mm)	239
Figure 7.51	Photo showing a rough and striated shear plane in the third Paleosol sample (diameter of Canadian one-dollar is 26mm)	240
Figure D1	Consolidation curve: volume change versus square root time for specimen C1	276
Figure D2	Pore-pressure-dissipation curve for specimen C1	277
Figure D3	Relationship between the normalized deviator stress and the shear displacement for specimen C1	277
Figure D4	Relationship between the normalized pore-water pressure and the shear displacement for specimen C1	278
Figure D5	Normalized effective stress paths for specimen C1	278
Figure D6	Relationship between the pore-pressure parameter A and the shear displacement for specimen C1	279
Figure D7	Relationship between the mobilized friction angle and the shear displacement for specimen C1	279
Figure D8	Difference between the pore-pressure-changes on the plane and on the base of specimen C1	280

Figure D9 Consolidation curve: volume change versus square root time for specimen C2 280
Figure D10 Pore-pressure-dissipation curve for specimen C2 281
Figure D11 Relationship between the normalized deviator stress and the shear displacement for specimen C2 281
Figure D12 Relationship between the normalized pore-water pressure and the shear displacement for specimen C2 282
Figure D13 Normalized effective stress paths for specimen C2 282
Figure D14 Relationship between the pore-pressure parameter A and the shear displacement for specimen C2 283
Figure D15 Relationship between the mobilized friction angle and the shear displacement for specimen C2 283
Figure D16 Difference between the pore-pressure-changes on the plane and on the base of specimen C2 284
Figure D17 Consolidation curve: volume change versus square root time for specimen C3 284
Figure D18 Pore-pressure-dissipation curve for specimen C3 285
Figure D19 Relationship between the normalized deviator stress and the shear displacement for specimen C3 285
Figure D20 Relationship between the normalized pore-water pressure and the shear displacement for specimen C3 286
Figure D21 Normalized effective stress paths for specimen C3 286
Figure D22 Relationship between the pore-pressure parameter A and the shear displacement for specimen C3 287
Figure D23 Relationship between the mobilized friction angle and the shear displacement for specimen C3 287
Figure D24 Difference between the pore-pressure-changes on the plane and on the base of specimen C3 288
Figure D25 Consolidation curve: volume change versus square root time for specimen C4 288
Figure D26 Pore-pressure-dissipation curve for specimen C4 289

Figure D27 Relationship between the normalized deviator stress and the shear displacement for specimen C4 289
Figure D28 Relationship between the normalized pore-water pressure and the shear displacement for specimen C4 290
Figure D29 Normalized effective stress paths for specimen C4 290
Figure D30 Relationship between the pore-pressure parameter A and the shear displacement for specimen C4 291
Figure D31 Relationship between the mobilized friction angle and the shear displacement for specimen C4 291
Figure D32 Difference between the pore-pressure-changes on the plane and on the base of specimen C4 292
Figure D33 Consolidation curve: volume change versus square root time for specimen C5 292
Figure D34 Pore-pressure-dissipation curve for specimen C5 293
Figure D35 Relationship between the normalized deviator stress and the shear displacement for specimen C5 293
Figure D36 Relationship between the normalized pore-water pressure and the shear displacement for specimen C5 294
Figure D37 Normalized effective stress paths for specimen C5 294
Figure D38 Relationship between the pore-pressure parameter A and the shear displacement for specimen C5 295
Figure D39 Relationship between the mobilized friction angle and the shear displacement for specimen C5 295
Figure D40 Difference between the pore-pressure-changes on the plane and on the base of specimen C5 296
Figure D41 Consolidation curve: volume change versus square root time for specimen M1 297
Figure D42 Pore-pressure-dissipation curve for specimen M1 298
Figure D43 Relationship between the normalized deviator stress and the shear displacement for specimen M1 298
Figure D44 Relationship between the normalized pore-water pressure and the

shear displacement for specimen M1 299
Figure D45 Normalized effective stress paths for specimen M1 299
Figure D46 Relationship between the pore-pressure parameter A and the shear displacement for specimen M1 300
Figure D47 Relationship between the mobilized friction angle and the shear displacement for specimen M1 300
Figure D48 Difference between the pore-pressure-changes on the plane and on the base of specimen M1 301
Figure D49 Normalized deviator stresses measured by using a ring bearing and not using a ring bearing for Highvale mudstone at the axial displacement rate of 0.001 mm/min. 301
Figure D50 Consolidation curve: volume change versus square root time for specimen M2 302
Figure D51 Pore-pressure-dissipation curve for specimen M2 302
Figure D52 Relationship between the normalized deviator stress and the shear displacement for specimen M2 303
Figure D53 Relationship between the normalized pore-water pressure and the shear displacement for specimen M2 303
Figure D54 Normalized effective stress paths for specimen M2 304
Figure D55 Relationship between the pore-pressure parameter A and the shear displacement for specimen M2 304
Figure D56 Relationship between the mobilized friction angle and the shear displacement for specimen M2 305
Figure D57 Difference between the pore-pressure-changes on the plane and on the base of specimen M2 305
Figure D58 Pore-pressure-dissipation curve for specimen L2 306
Figure D59 Relationship between the normalized deviator stress and the shear displacement for specimen L2 306
Figure D60 Relationship between the normalized pore-water pressure and the shear displacement for specimen L2 307
Figure D61 Normalized effective stress paths for specimen L2 307

Figure D62 Relationship between the pore pressure parameter A and the shear displacement for specimen L2 308
Figure D63 Relationship between the mobilized friction angle and the shear displacement for specimen L2 308
Figure D64 Difference between the pore-pressure-changes on the plane and on the base of specimen L2 309
Figure D65 Pore-pressure-dissipation curve for specimen L3 309
Figure D66 Relationship between the normalized deviator stress and the shear displacement for specimen L3 310
Figure D67 Relationship between the normalized pore-water pressure and the shear displacement for specimen L3 310
Figure D68 Normalized effective stress paths for specimen L3 311
Figure D69 Relationship between the pore-pressure parameter A and the shear displacement for specimen L3 311
Figure D70 Relationship between the mobilized friction angle and the shear displacement for specimen L3 312
Figure D71 Difference between the pore-pressure-changes on the plane and on the base of specimen L3 312
Figure D72 Pore-pressure-dissipation curve for specimen P2 313
Figure D73 Relationship between the normalized deviator stress and the shear displacement for specimen P2 313
Figure D74 Relationship between the normalized pore-water pressure and the shear displacement for specimen P2 314
Figure D75 Normalized effective stress paths for specimen P2 314
Figure D76 Relationship between the pore-pressure parameter A and the shear displacement for specimen P2 315
Figure D77 Relationship between the mobilized friction angle and the shear displacement for specimen P2 under the assumption of no cohesion 315
Figure D78 Difference between the pore-pressure-changes on the plane and on the base of specimen P2 316

Figure D79 Pore-pressure-dissipation curve for specimen P3 316
Figure D80 Relationship between the normalized deviator stress and the shear displacement for specimen P3 317
Figure D81 Relationship between the normalized pore-water pressure and the shear displacement for specimen P3 317
Figure D82 Normalized effective stress paths for specimen P3 318
Figure D83 Relationship between the pore-pressure parameter A and the shear displacement for specimen P3 318
Figure D84 Relationship between the mobilized friction angle and the shear displacement for specimen P3 under the assumption of no cohesion 319
Figure D85 Difference between the pore-pressure-changes on the plane and on the base of specimen P3 319

LIST OF SYMPOLS

CHAPTER 1

τ	shear strength
c_0	cohesion
σ_T	total stress
u	pore pressure
ϕ	friction angle
u_s	pore pressure on the shear surface
u_p	pore pressure near the shear zone

CHAPTER 2

a	a axis of a shear zone
b	b axis of a shear zone
c	c axis of a shear zone
D	displacement shear
R	Riedel shear
R′	conjugate shear of a Riedel shear
P	thrust shear
W_l	liquid limit
W_p	plastic limit
PI	plastic index
σ'	effective normal stress
ϕ_r	residual friction angle
l	striations on the shear surface
D	shear displacement
T	shear force

w	water content
S_p	peak shear strength
S_r	residual shear strength
ΔS	difference between the peak and residual strength
O–C	over-consolidated
N-C	normal-consolidated
σ_n'	effective normal stress
τ	shear strength
ϕ	friction angle
CF	clay fraction
ϕ_{rf}	field residual friction angle
σ	normal stress
LL	liquid limit
PL	plastic limit
ϕ_{max}	maximum friction angle
ϕ_{min}	minimum friction angle

CHAPTER 3

K_m	Cretaceous McMurray Formation
D_w	Devonian Waterways Formation
D	displacement shear
R	Riedel shear
P	thrust shear
W_l	liquid limit
W_p	plastic limit
PI	plastic index
b	primary horizontal baseline or b axis
b'	secondary horizontal baseline
c	primary vertical baseline or c axis
c'	secondary vertical baseline

a	slope surface or a axis
H_o	Muskeg and organic soil
Pfs	Glaciofluvial sand
Pl	Glaciolacustrine sediments
Pg	Glacial till
Kcc	member of the Cretaceous Clearwater Formation
Kcb	member of the Cretaceous Clearwater Formation
Kca	member of the Cretaceous Clearwater Formation
Kcw	Cretaceous Wabiscaw member
MSF	Marine Shore Facies
A'	start point of a shear zone section
B'	end point of a shear zone section
A	start point of a shear zone section
B	middle point of a shear zone section
C	middle point of a shear zone section
D	end point of a shear zone section

CHAPTER 4

SD	standard deviation
c'	cohesion
σ_T	total stress
u	pore pressure
D	displacement shear
FOS	factor of safety
$\dot{\gamma}$	shear strain rate
ϕ'	friction angle
ϕ_r	residual friction angle
P	failure probability
Ks	shear stiffness of a discontinuity
Kn	normal stiffness of a discontinuity

ϕ	friction angle
F	factor of safety
γ_u	pore pressure ratio
γ	bulk density
β	slope angle
D	depth factor
H	height of the slope

CHAPTER 5

D	rate of displacement or outer diameter
Q	syringe pump flow rate
S	hydraulic cylinder effective area
a	valve a or distance
b	valve b or width
c	valve c
d	valve d or depth
e	valve e
Dv	vertical displacement of a shear plane
L	initial distance between the sample wall and the post
θ	initial angle between the two telescoping bars
β	change in angle between the post and the lower telescoping bar
α	change in angle between the post and the upper telescoping bar
S	displacement along the shear plane
ψ	inclination of the shear plane
R	radius
$\varnothing$	diameter
Iy	inertial moment
Sy	section modulus
r_y	inertial distance
E_0	shear center

J	torsional constant or saddle diameter
C_w	warping constant
t	mean thickness
w	web thickness or collar thread
A	collapse height or height
B	extended height or diameter
E	cylinder bore diameter
F	plunge diameter
H	base to average port
K	saddle protrusion from plunger
O	plunger internal thread
P	plunger thread length
U	bolt circle
V	thread
Z	thread depth
X	collar thread length
k	distance
T	distance
OD	outer diameter
ID	inner diameter
BP	back pressure
CP	cell pressure
BPT	base pore pressure transducer
IPT	internal pore pressure transducer

CHAPTER 6

ϕ	friction angle
β_1	minimum inclination of the failure along a discontinuity
β_w	inclination of the discontinuity
β_2	maximum inclination of the failure along a discontinuity

P	change in pressure required to increase saturation from S_i to S
P_i	initial absolute pressure corresponding to S_i
H	Henry's constant
S	final degree of saturation
S_i	initial degree of saturation
P_{100}	back pressure required to provide 100% saturation
B_{100}	pore-pressure parameter for a fully saturated specimen
C_w	compressibility of the pore water
C_s	compressibility of the soil skeleton
n	porosity of the soil
n_i	initial porosity
$\Delta\sigma_3$	change in confining pressure
u_0	initial pore water pressure immediately before consolidation
u_b	back pressure, which is a constant during the consolidation
u	measured pore pressure either on the shear plane or the base
θ	inclination of the slip surface relative to the sample axis
ε_s	axial strain measured from the start slide
D	sample diameter
L	sample length
T	rubber thickness
σ_3	minor principal stress
σ_1	major principal stress
X	horizontal displacement
Y	sample length
ΔY	vertical displacement
f_θ	inclination factor

CHAPTER 7

q	deviator stress
σ_0'	pre-shear consolidation pressure

q'	effective deviator stress
σ_1	compression pressure
σ_3	confining pressure
$\dot{\delta}$	axial displacement rate
Δu	pore water pressure change
p'	mean effective stress
σ_1'	major effective principal stress
σ_3'	minor effective principal stress
A	pore pressure parameter or point A or activity
A_p	peak pore pressure parameter
Uz	degree of consolidation
u	excess pore pressure measured at a certain time
u_i	initial excess pore pressure
$f_1(Z)$	function related to the considered point and geometry
$f_1(T)$	function related to the considered time after starting consolidation
Z	geometry parameter
T	time factor
Tv	time factor
Cv	coefficient of consolidation
H	length of the drainage path
t	time
k	Darcy coefficient of permeability
m_v	soil's coefficient of volume compressibility
U_A	degree of consolidation at the point A
U_B	degree of consolidation at the point B
k_A	coefficient of permeability at the point A
k_B	coefficient of permeability at the point A
m_{vA}	soil's coefficient of volume compressibility at the point A
m_{vB}	soil's coefficient of volume compressibility at the point B
Δu_p	peak pore pressure change or pore pressure change on the shear plane

$\Delta\sigma_3$	change in the confining pressure
$\Delta\sigma_1$	change in the compression pressure
B	point B
$\Delta\dot{q}$	rate of the deviator stress increment
Δq	deviator stress increment
$\Delta\delta$	shear displacement increment
ϕ_p'	mobilized peak friction angle
ϕ_r'	mobilized residual friction angle
ϕ'	friction angle
W_l	liquid limit
W_p	plastic limit
I_p	plastic index
γ_t	total bulk density
γ_d	dry bulk density
CF	clay fraction
Gs	specific gravity
N	natural
$\dot{\varepsilon}_a$	axial strain rate
K_0	coefficient of earth pressure at rest
Δu_b	pore pressure change on the base
Δu_c	pore pressure change at the center of a sample
Δu_m	pore pressure change at the mid-height of a sample
c	cohesion
ψ	inclination of the shear plane

CHAPTER 1 INTRODUCTION

1.1 BACKGROUND

The economics of many geotechnical and mining projects is linked to the stability of their excavated slopes and of the tailings facilities, so that the weak shear zones within such excavated slopes or beneath retaining facilities such as tailings dams must be identified and characterized. These shear zones are often discontinuous, resulting in a wide range of available shear strengths and a possibly different pore-pressure response from their adjacent materials. Engineered structures located in or founded on such weak zones demand a thorough understanding of the material behavior and the detailed geometry of the zone itself.

The term "shear zone," used mainly to refer to a zone with different internal fractures from its adjacent material due to shear strain, is the consequence of strain localization, which is a common phenomenon occurring in a wide variety of solids such as ductile single crystal and polycrystalline structure metals (Asaro and Rice, 1977; Asaro 1978, 1983), concrete (Majorana et al., 1996), geomaterials (rocks and soils) (Bjerrum, 1967; Roscoe, 1970), and even in bone (Nicolella et al., 1997). In terrane, strain localization widely occurs in different scales of geologic units, from the continental lithosphere (Benes and Davy, 1996; Tommasi et al., 1995), to the oceanic lithosphere (Casey, 1987; Jaroslow et al., 1996), structural belts (Gilbert et al, 1994; Ghisetti and Vezzani, 1996), to rock-forming minerals (Scruggs and Tullis, 1998). As well, shear strain localization is a well-known precursor to progressive failure in geotechnical analysis (Bjerrum, 1967; Roscoe, 1970). As Aydan et al. (1993) pointed out "strain localization phenomenon exemplifies itself as a fracturing in actual materials. This fracturing process in most cases after a certain time will end up with the ultimate failure"(p.119). Generally the ultimate form of this fracturing manifests itself as a shear zone or a discontinuity. Observations of many discontinuities (except tension cracks) such as most of the slip surfaces show that an intermediate structure, usually called the "shear zone," surrounds the slip surface (Leroueil, 2001). Observations made by Morgenstern and Tchalenko (1967a) also revealed that a slip surface in a landslide developed within a shear zone. Therefore, strain localization can be referred to as a precursor of the formation of a shear zone. Because strain localization is a common phenomenon in terrane, and the consequence of strain localization in most cases is the formation of a shear zone, shear zones are common in soils and rocks.

Although all shear zones are the result of strain localization, they can be classified into three categories according to their origins: experimental shear zones, engineering shear zones, and tectonic shear zones. An experimental shear zone is generated in samples during laboratory tests such as the direct shear test, uniaxial compressive test, and triaxial compressive test (Figure 1.1) (Morgenstern and Tchalenko, 1967b; Tchalenko, 1968; Picarelli et al., 1998); an engineering shear zone is generated by engineering works such as pit excavations, tunneling, and dam or dyke construction (Figure 1.2); and a tectonic shear zone is formed by geological events such as tectonism, glaciation or ice-thrusting, erosion and landslides (Skempton, 1966; Chandler et al., 1998; Tsui et al., 1988) (Figure 1.3). This study involves only tectonic shear zones.

In geotechnical and mining engineering, a weak shear zone is one of the main causes of large deformation and failure in the slopes or foundations (Small, 1989; Wedage et al., 1998; McRoberts, 2001; Leroueil, 2001). For example, site investigations have found many shear zones and plastic weak zones in Athabasca oil sand mine area near Fort McMurray (AGRA, 1999). These zones have created a major challenge for tailings-dam geotechnics and are one of the key concerns in tailings-dykes design and stability. Figure 1.4 shows one of the slope failures occurring in a shear zone at a Suncor tailings-dyke area. Figure 1.5 shows the large movement along the shear zone in a Syncrude tailings-dyke foundation. Therefore, research on shear zones is very important in order to build tailings facilities founded on such weak shear zones.

Due to the large number of fractures within a shear zone and the displacement that has occurred, a shear zone has different physical and mechanical properties from those of its adjacent materials. When a tailings dam is built on a shear zone, the design and evaluation of such a dam demand a good understanding of the shear behavior and the pore-pressure response of the shear zone. According to the Coulomb-Mohr theory, soils' shear strength can be expressed as: $\tau = c_0 + (\sigma_T - u) \tan\phi$. Generally, cohesion of a well-developed shear zone is zero or very close to zero when a potential slide is along the principal slip surface that is the weakest place in a shear zone. The friction angle of a shear zone can be obtained from laboratory shear-strength testing, while the pore pressure of the shear zone is obtained from *in situ* instrumentation set up before, during, or after the construction of the tailings dam. Not knowing the position of a shear zone in advance makes it difficult placing piezometers in the shear zone, especially right on the shear surface, as does a thin shear zone. Thus, the pore pressure obtained from *in situ* instrumentation is often obtained from an area adjacent to the shear zone. Is this pore pressure a good representative of the pore pressure in the shear zone? What is the difference between the pore pressure generated in a shear zone and that generated in its adjacent material under acceptable displacement rates in practice? Uncertainty about the pore pressure of a shear zone will introduce large risks into the construction of a tailings dam, so research must be undertaken to measure the pore pressure of the shear zone and its pore-pressure response. The scenario of shear-zone geotechnics is shown in Figure 1.6.

This brief overview of shear zones has illustrated three significant aspects:

- Shear zones result from strain localization, and are common in soils and rocks because strain localization is a common phenomenon in terrane.
- In the Athabasca Oil Sands area near Fort McMurray, many shear zones pose a major potential challenge for oil sands geotechnics.
- The pore pressure of a shear zone, an important parameter for the design and evaluation of a tailings facility, cannot be accurately obtained directly from *in situ* instrumentation.

1.2 RESEARCH SCOPE AND OBJECTIVE

Based on the brief overview above, this research provides an approach to measure the pore pressure on the shear plane and to investigate the pore-pressure response of a shear zone and its adjacent material under the normally practical displacement rates. The main objectives were:

- To carry out detailed geological field mapping during the excavation of two shear keys for the construction of tailings dykes at Suncor Energy Ltd.'s oil sand mine near Fort McMurray to establish the shear zone geometry and their *in situ* engineering properties.
- To develop laboratory equipments, a technique, and procedures to measure the pore pressure of such a shear zone and to investigate the pore-pressure response of a shear zone and its adjacent material under an undrained triaxial compression test in the normally practical shear displacement rates (mm/day) by using different materials.
- To investigate the shear behavior of shear zones, especially their post-peak characteristics, by using large dimensional specimens in laboratory triaxial tests using a large triaxial cell. The specimens were directionally drilled from the undisturbed block samples containing shear zones and these block samples were taken from the Suncor Millennium project.

1.3 THESIS ORGANIZATION

A review of previous papers studying the formation and development of shear zones by model tests on clays in the laboratory, naturalistic studies of joints and shear zones in the field, and measurements of the strength and stress-strain characteristics along discontinuities in the shear zone is presented in Chapter 2. This review results in a synopsis of the issues where research advances are pending. The reminder of the thesis focuses on some of these issues.

Chapter 3 presents the results from field studies on shear zones. These results include the detailed field mapping of excavations to establish the shear-zone geometry and the engineering properties of shear zones such as the Atterberg limits, the moisture content across the shear zone, and the particle distribution.

Chapter 4 describes, from a fundamental perspective, the shear-resistance characteristics of shear zones and highlights the key behavioral aspects relevant to a discussion of a shear zone's strength. The influence of minor changes in the residual shear-strength parameter and pore pressure on the slope's stability and the movement is studied in accordance with a case history using G-slope and FLAC, and the results are discussed.

Chapter 5 describes a newly developed large triaxial apparatus and a modified conventional triaxial apparatus for the measurement of the pore pressure on a pre-existing shear plane. The development and principle of a pore-pressure transducer and local-displacement transducer are described, and their performance is discussed.

Chapter 6 describes the laboratory testing method and procedures that were conducted to measure the pore pressure on and the response of a pre-existing shear plane. The sampling techniques both in the field and in the laboratory were described. The required corrections and calculations in the analysis of the resulting data were also described.

Chapter 7 presents the results of the laboratory consolidated undrained triaxial compression tests performed on three materials, Athabasca clay, Highvale mudstone, and Fort McMurray weak rocks, containing a pre-existing shear zone/plane. The results include the pore-pressure responses of the shearing plane and the bottom, and the shear behavior of the shear zones. Analysis of test results was made.

Chapter 8 summarizes the results of this study and its major contributions. Some recommendations are made for future research.

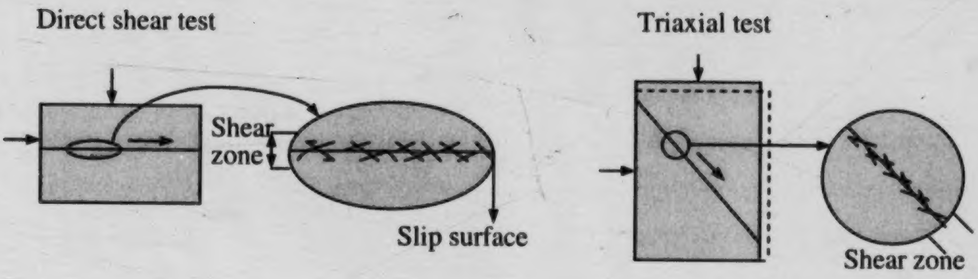
Direct shear test
Shear zone
Slip surface
Triaxial test
Shear zone

Figure 1.1 Shear zones generated in the laboratory tests

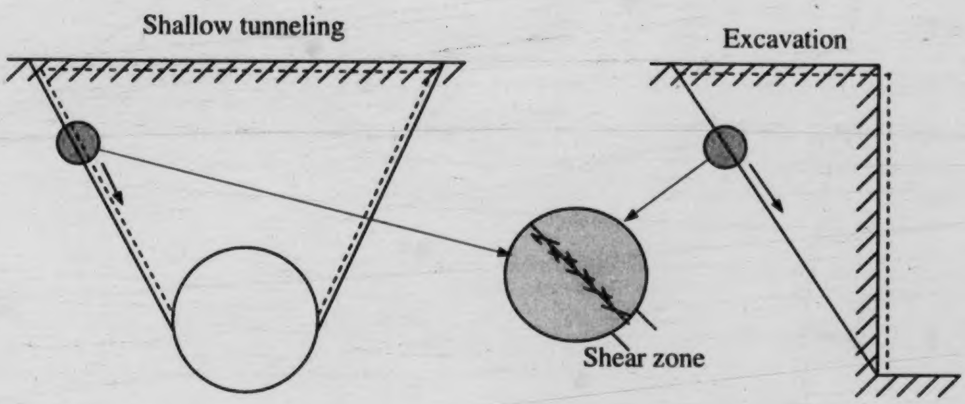
Shallow tunneling
Excavation
Shear zone

Figure 1.2 Shear zones developed by engineering works

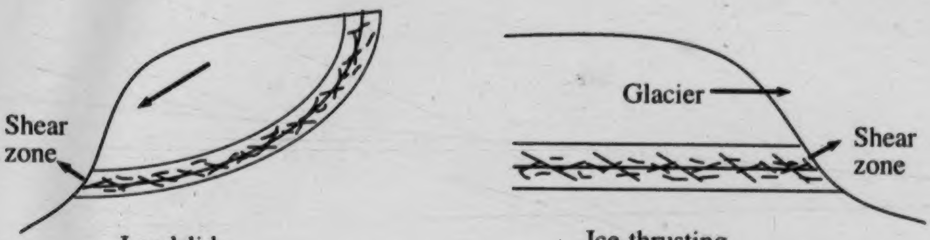
Shear zone
Glacier
Shear zone

Landslide

Ice-thrusting

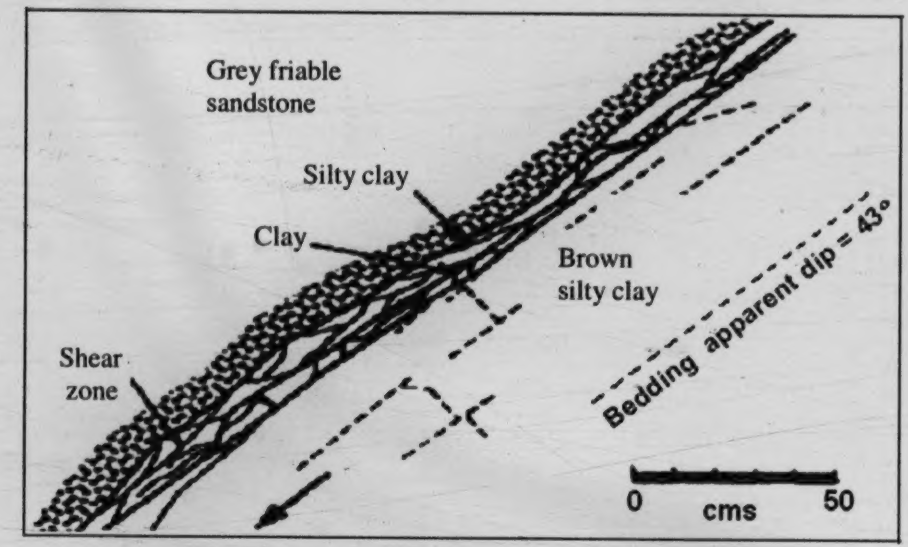
Grey friable sandstone
Silty clay
Clay
Brown silty clay
Shear zone
Bedding apparent dip = 43°
0
cms
50

Jari Pakistan (modified from Skempton and Petley, 1966)

Tectonism

Figure 1.3 Shear zones developed during geological events

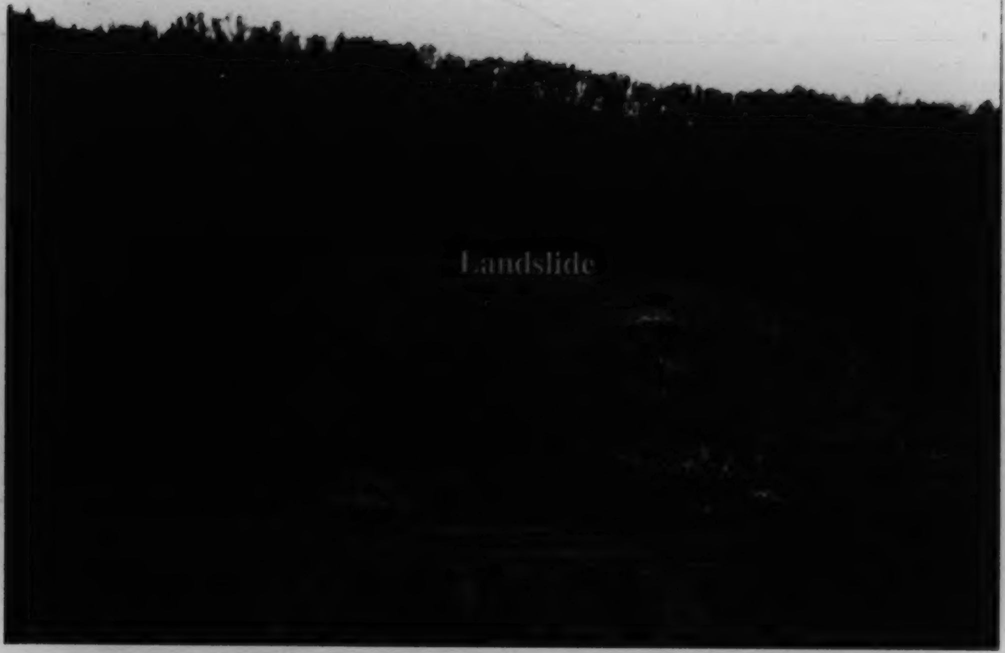

Figure 1.4 Photograph of a landslide along Paleosol at Wood Creek at dyke 11A near Fort McMurray

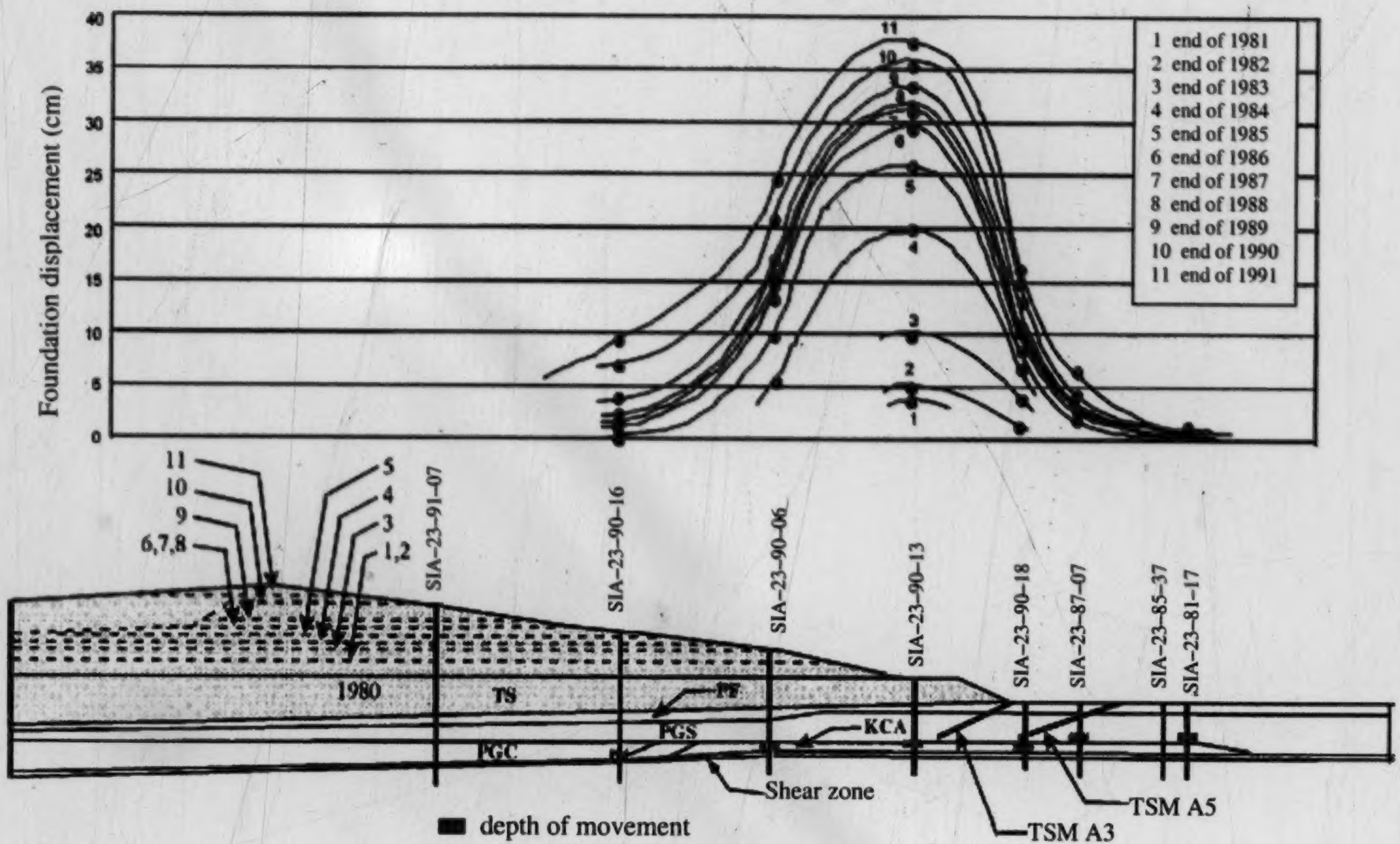

Figure 1.5 Shear zone and slope inclinometer displacement at section 53+00E, cell 23 in the Syncrude lease(after Wadage et al.,1998)

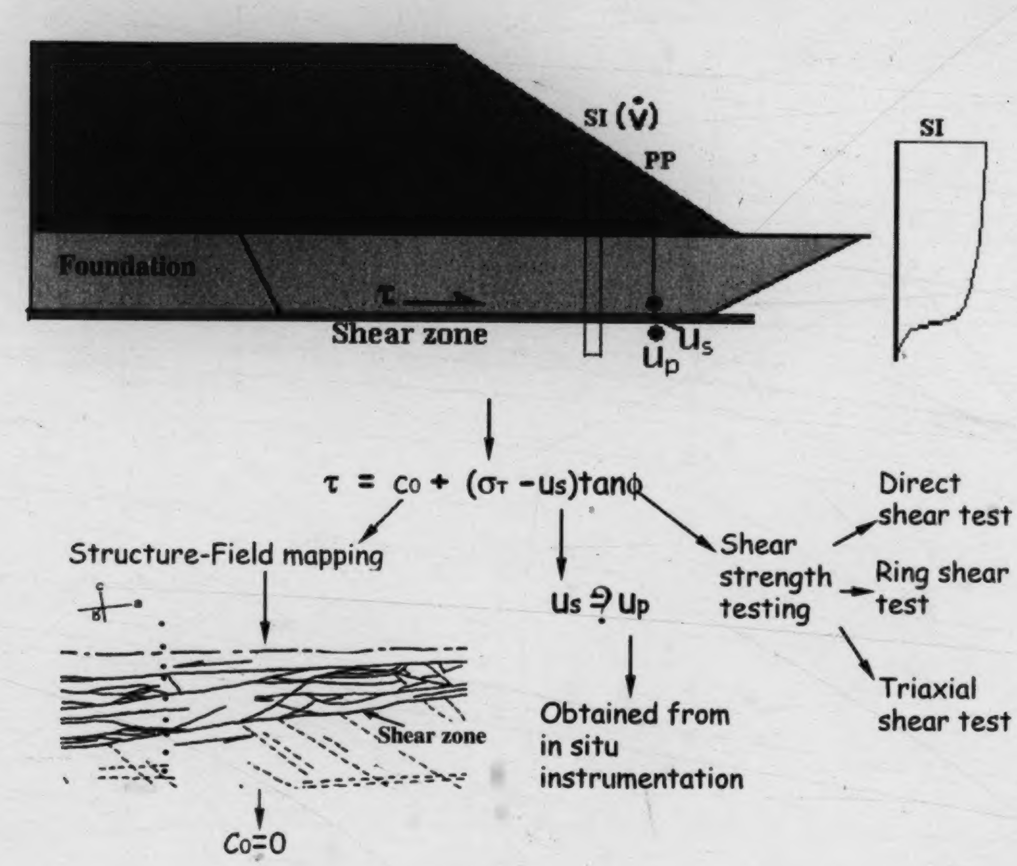
SI ($\dot{V}$)
PP
SI
Foundation
τ
Shear zone
u_s
u_p
$\tau = c_0 + (\sigma_T - u_s)\tan\phi$
Structure-Field mapping
Shear zone
$C_0=0$
$u_s \overset{?}{=} u_p$
Obtained from in situ instrumentation
Shear strength testing
Direct shear test
Ring shear test
Triaxial shear test

Figure 1.6 Scenario of shear zone geotechnics

CHAPTER 2 LITERATURE REVIEW

2.1 INTRODUCTION

Natural deposits often contain shear-induced structures such as shear zones or discontinuities that are related to changes of the stress field caused by geological events or engineering works. Often, locations and features of such structures are unknown, and their complex internal fractures and geometries pose a challenge for geotechnical analysis and projects. Since the 1960's, geotechnical researchers have been examining shear zones. Field mapping yields evidence for laboratory investigations, while these investigations provide some insights into the mechanisms leading to the generation of such structures. This research has focused mainly on three aspects:

1) naturalistic studies of joints and shear zones in the field, such as field observation, field mapping, description of shear zones and their physical properties, and investigations of the fabric of clays, especially sheared clays.
2) the formation and development of shear zones by model tests on clays in the laboratory.
3) measurements of the strength and stress-strain characteristics along discontinuities in a shear zone and, for comparison, in the adjacent 'intact' clay.

2.2 FIELD OBSERVATIONS AND DESCRIPTIONS OF SHEAR ZONES

Skempton (1964, 1966), Fookes (1965), Fookes and Wilson (1966), Skempton and Petley (1967), Fookes (1969), and Skempton et al. (1969) studied both joints and shear zones in the field. In the paper "Some observations on tectonic shear zone", Skempton (1966) introduced a new terminology to describe the classic type of shear zones, which had been rarely recognized in the previous literature. Skempton's study became a landmark in the description of shear zones in the geotechnical field. He provided some definitions and defined the various features of shear zones. As a result, Skempton gave subsequent authors a methodology for describing shear zones. The general features of a shear zone and reference axes are shown in Figure 2.1. The reference axis a is the direction of movement, b lies in the plane of the shear, and c is at right angles to the ab plane. A displacement shear (D shear) is a slip surface that lies parallel or sub-parallel to the ab plane and is denoted by the letter D. A Riedel shear (R shear) is a slip surface lying typically *en échelon*, inclined at 10° to 30° to the ab plane, with the acute angle always pointing against the direction of the relative movement. Ideally an R shear is accompanied by a conjugate shear R′. A thrust shear is a slip surface having an orientation opposite to that of a Riedel shear, in the position approximately of a mirror image, and is denoted by the letter P. The sheared material between the boundary displacement shears is referred to as the 'shear zone', which has a sharply different fracture pattern from that of the adjacent material, even though this may contain various accommodation fractures, thrust shear joints, and so on. The combined effect of the various sets of slip surfaces is to divide the shear zone into numerous lenses. Characteristically, the lenses are bounded by R and D shears and display an approximately rhombic section in the ac plane. At an advanced stage of shearing, the lenses may become distorted into a sigmoidal section. Thus, sigmoidal or highly distorted lenses indicate that a large displacement occurred in a shear zone. In Skempton's paper, two shear zones, which developed at Lough Fee, Ireland and at Jari, West Pakistan, were well mapped and described in detail by the author. The field observations showed that the shear zones had several features in common, and most of their essential characteristics can be observed in laboratory experiments on clay (Riedel, 1929; Skempton, 1966). Describing the Jari shear zone, Skempton pointed out, "Not all the clays are sheared, but all the shear zones are in clay beds and generally in those parts of a clay bed with the highest percentage of clay particles"(p.334). Skempton (1985) and Su et al. (2002) later verified this point.

Morgenstern and Tchalenko (1967a) investigated the microstructures of clays, especially sheared clays, by using an optical microscope and thin sections prepared by the Carbowax technique. These microstructures have an important effect on the mechanical behaviour of clays (Skempton, 1964). According to the author's observations of several shear zones of slips, a shear zone was always characterized by the presence of continuous shear planes in the direction of movement, which were typically close to, or formed, the boundaries of the shear zone, and of many discontinuous shear planes which were inclined to the continuous shear planes. The continuous shear planes are the *principal displacement shears,* and the discontinuous families are *Riedel shears* or *thrust shears* (Skempton, 1966). Usually, they are between 10 and 100μ in width, but exceptionally up to 300μ. A shear zone's details obtained from a study of a thin section are shown in Figure 2.2. The authors (Morgenstern and Tchalenko, 1967) found that a shear zone in a thin section had the same geometry as a shear zone at a site and contained a shear matrix with a strong degree of orientation approximately in the direction of movement.

2.3 SHEAR-ZONE-FORMING PROCESS IN LABORATORY INVESTIGATION

As Picarelli et al. (1998) pointed out, the described mechanism leading to the formation of a slip surface is not possible when displacement is allowed only along an imposed plane having a direction different from that predicted by the Mohr-Coulomb theory. This mechanism becomes possible only after a rotation of principal stresses that gives rise to the formation of a shear surface coinciding with the imposed plane of rupture. This situation is typical of direct shear tests (Morgenstern and Tchalenko, 1967b).

Cloos (1928) and Riedel (1929) first described such a process, which had been observed during a kind of shear test on a clay specimen.[1] Vallejo (1982) and Walters and Thomas (1982) investigated shear-zone development in clays and granular materials during direct shear tests. Skempton (1966) redid the Riedel test and described the shear-zone formation. Morgenstern and Tchalenko (1967b) investigated the microstructures and their formation in kaolin subjected to direct shear. According to Riedel and Skemptons' observations (Figure 2.3), when a clay is subjected to a simple shear, five successive stages can be recognized as the deformation increases. During the first stage, before the peak is reached, continuous non-homogeneous strain due to strain localization occurs. The second stage, which occurs at or just before the peak, is characterized by the initial formation of single separate shear surfaces called 'Riedel shears'. They lie *en echelon* at an inclination usually between 10° and 30° to the direction of the general movement (the a axis), and conjugate shears R′ are sometimes seen. With further movement, a third stage is reached, at which slip along the Riedel shears is no longer kinematically possible, and the clay is compelled to develop new slip surfaces ('displacement shear') parallel or sub-parallel to the a axis. With greater movements, displacement shears extend and eventually, in the fourth stage, some of them link up to form a 'principal displacement shear' or 'slip surface.' This is undulated since the shears involved were not originally all in line. 'Thrust shears,' typically inclined at about 160° to the a axis, also tend to develop in the third and fourth stages. The third and fourth stages are linked to the material's post-peak strength. In the fifth stage, the slip surface undergoes appreciable flattening as a result of still greater movements and is linked to the material's residual strength. Tchalenko (1970) also described these stages in detail by considering the shear zones' specific positions in the stress-displacement curve (see Figure 2.4). Laboratory tests have indicated that different shear-zone structures form in different stages under different deformations. A larger deformation generally forms a shear zone with significant displacement shear(s) and sigmoidal shear lenses, while a smaller deformation may form only a shear zone without significant displacement shear(s) and with shear lenses in rhombic shape. Thus, the detection of a specific shear-zone structure can help researchers to qualitatively judge the displacement that has occurred during the formation of such a shear zone even if no marker layer has been sheared through.

---

[1] As Tchalenko(1970) pointed out, Fath(1920) and Fujiwhara(1924,1925) performed similar experiments, but did not describe the details of the shear-zone structure.

2.4 SIMILARITY OF SHEAR ZONES

Tchalenko (1970) revealed that shear zones in different scales have similar shear-zone structures by comparing the shear-zone geometries generated in direct shear tests, Riedel tests, and earthquakes, in different stages (Figure 2.5). All shear zones contain a characteristic structure consisting of one or several parallel principal displacement shears in the general direction of movement and some minor shears, which are Riedel- and conjugate Riedel-, thrust-, and displacement shears of limited extent. The similarities in structure have been interpreted as indicating similarities in the deformation mechanism (Tchalenko, 1970). At the peak stage, the mechanism is essentially of the simple shear type, whereas at the post-peak stage, it is governed by the kinematic restraints inherent in the strain field, and at the residual stage, it is of the direct-shear type. Information from other studies (Skempton, 1966; Archambault et al., 1990; Su et al., 2002) indicates that shear zones have the same characteristics (see Figures 2.6 and 3.9). Shear-zone similarity is one of shear zones' most important characteristics and provides some basic information for studying shear zones' mechanical properties.

2.5 PHYSICAL PROPERTIES OF SHEAR ZONES

Shearing in geomaterial generates changes in fabric and structure. Such changes are often concentrated in a narrow zone (strain localization) due to the effect of the small heterogeneities of the material or of the stress field. As shearing continues, a shear surface forms, which represents a physical discontinuity in the material. If drainage is permitted, shear strain localization is associated with contractancy in normally consolidated clays and with dilatancy in highly overconsolidated clays. All these processes will cause changes in physical properties.

When shear zones develop, the water content will change due to changes in the material's fabric and structure. An increase or decrease in the water content will depend on the state of the geomaterial and the drainage condition. If drainage is allowed, dilation occurs when shearing takes place in stiff, overconsolidated material, and as a consequence, an increase occurs in the water content in the shear zone or on the shear surface. Figure 2.7, showing a water-content profile across the shear surface of a London Clay landslide (Henkel, 1956), represents an example of shearing dilatancy. In this case, as often occurs in such landslides, the shear zone is quite thin, although the water content substantially increases from about 28% up to a maximum of 37%.

Hicher et al. (1994), who performed drained tests on normally consolidated and overconsolidated reconstituted clays, observed local changes in the clay fabric due to localization. After the test, local measurements of water content and density revealed changes in a very thin zone around the slip surface. In normally consolidated specimens, the density increased, whereas in overconsolidated specimens, it decreased. Guerrier et al. (1993) found that an increase in the local values of the water content around the slip surface formed in an overconsolidated clay (see Figure 2.8). As well, Su et al. (2002) found that the water content increases in the field shear zones formed in soft rocks in the Fort McMurray area (Figures 3.18 and 3.19). In the reverse case, contraction occurs when shearing takes place in normally consolidated material or sensitive clays. The consequence is a decrease in the water content in the shear zone or on the shear surface (Lefebvre, 1981; Chandler et al., 1998) (see Figure 2.9). Water-content change not only reflects changes in the fabric and structure of geomaterial, but also helps in identifying the thickness of a shear zone in some cases (Picarelli et al., 1998). The water content in overconsolidated materials gradually increases from the boundaries of the shear zone towards the sliding surface inside such a zone, where it reaches its maximum value.

Su et al. (2002) pointed out that the grain size of the material within a shear zone is smaller than that of the adjacent unsheared material (Figure 3.19). Archambault et al. (1990) indicated that when shear zones form under high stresses, dilatancy is inhibited, and the material experiences intense comminution and destruction, causing grain-size reduction. Through microscopic observations, Hicher et al. (1994) also noticed a breaking up of the particles in the shear zone. Consistent with the water-content increase and grain-size decrease of the material in the shear zone, the Atterberg limits (W_l, W_p, and PI) of the material in the shear zone are significantly higher than those of the adjacent unsheared material (Su et al., 2002). Chandler et al. (1998) reported that the opposite occurs when shear zones develop in normally consolidated materials.

2.6 MECHANICAL PROPERTIES OF SHEAR ZONES

Less information is available on the strength characteristics of shear zones due to the lack of well-documented shear zones. Skempton (1964), Skempton and Petley (1967), D'Elia et al. (1977), Dounias et al. (1987), Tika et al. (1996), and Chandler et al. (1998) made measurements of the strength or stress-strain characteristics along the principal slip surface of the following landslides or shear zones: Walton's Wood landslide, Guildford landslide, Guildford Dedham Sudbury Hill landslide, Sevenoaks landslide, and Jari Mangla dam shear zone, and, for comparison, of the adjacent 'intact' clay in the same places. These researches provided a clear framework for understanding the strength characteristics and deformation mechanisms of intact material and pre-existing slip surfaces. Some conclusions are

- In most shear zones, large movements have taken place, principal slip surfaces are polished and subplannar, with striations in the direction of movement. The clay particles are strongly oriented along the slip surface, practically in the direction of movement.
- The strength along a principal slip surface is at or very close to the residual strength, and it may be much lower than the intact clay's peak strength.
- After displacements of several centimeters, the intact clay's strength falls approximately to the residual value.
- For shear zones in the third stage of development or, perhaps in places, just entering the fourth stage (Figure 2.3), the strength is clearly greater than the residual.

The typical stress-strain curves in tests on principal slip surfaces and on intact clay are presented in Figure 2.10. A slip surface with full-particle orientation is expected to have a stress-strain curve of the type shown by line (1) in Figure 2.10. This curve shows no peak and at a small displacement, reaches the residual strength. Quite often, however, the test shows a small peak as shown by line (2) in Figure 2.10 due to the following factors (Skempton and Petley, 1967): (i) the slip surface is not planar or may have some asperities; (ii) all the clay particles may not be fully oriented; (iii) some 'bonding' effect may have developed during the period since movement last occurred; (iv) some clay pellets are left on the slip surface; and (v) inaccurate results have been obtained from errors in setting up a specimen or in applying shear movements in the wrong direction.

The post-peak strength of a shear zone is a very important characteristic, and a shear zone's residual strength is an important parameter for geotechnical design. Skempton (1985) investigated the post-peak features and residual strength of clays in landslides, folded strata, and the laboratory. He concluded that the post-peak drop in the drained strength of an intact overconsolidated clay may be considered as being due, firstly, to an increase in water content (dilatancy) and, secondly, to the reorientation of the clay particles parallel to the direction of shearing. At the end of the first stage, the 'fully softened' or 'critical state' strength is reached. At larger displacements, when reorientation is complete, the strength falls to and remains constant at the residual value (see Figure 2.11). If the clay fraction is less than about 25%, the second stage scarcely comes into operation; the clay behaves much like a sand or silt, with angles of residual-shearing resistance typically greater than 20°. Conversely, when the clay fraction is about 50%, the residual strength is controlled almost entirely by the sliding friction of the clay minerals, and a further increase in the clay fraction has little effect. When the clay fraction lies between 25% and 50%, a 'transitional' type of behaviour occurs, and the residual strength depends on the percentage of clay particles as well as on their nature (see Figures 2.12 and 2.13). The displacements for mobilizing different strengths of clays are tabulated in Table 2.1 (Skempton, 1985) and also shown in Figure 2.14. After the strength of a clay reduces to the 'fully softened' or 'critical state' value, a large displacement is needed for a further minor change in strength. This finding probably implies that small changes in strength can cause large changes in displacement for a reactivated slide. At a high pressure, the particle orientation, and therefore the fall to residual strength, can be expected to be completed at a small displacement. Sinclair & Brooker's (1967) study supports this conclusion. For the clay shale in Edmonton, with σ' = 100kPa, the strength was still falling after displacements of 60 mm, but when σ' = 200kPa, the residual was reached at about 25 mm. One study of Lower Oxford Clay found that the angle of shearing resistance fell to within 2° of the residual after displacements of only 4mm and almost to the residual itself at little more than 10 – 20 mm (Burland et al., 1977). However, the residual strength for a fully developed slip or shear surface is recovered at virtually zero displacement, which is called the 'field residual strength' and, according to the case records of some English clays, can be determined by the back analysis of reactivated landslides and slip surface tests.

The rate of displacement is an important factor for residual-strength research on pre-existing shear surfaces/shear zones. As Tika et al. (1996) concluded, all the investigators agree that the effect of the rate of shearing on the ultimate strength of granular soils is negligible. Tests on the clays over a range of speeds from about 100 times slower to 100 times faster than the usual (slow) laboratory test rate (0.002-0.01mm/min) showed a negligible effect (change in strength is less than 2.5% per logarithmic cycle) (Skempton, 1985). Some of these results are shown in Figures 2.15 and 2.16. Therefore, for the slow-rate laboratory test or back analysis, rate correction on the residual strength or the so-called 'static residual strength' (Skempton, 1985) is not necessary, but at a fast rate (>400mm/min), a clay's residual strength will increase significantly, probably due to the disturbance of the originally ordered structure and pore pressure changes (Skempton, 1985). In contrast, in a low-clay-fraction clay siltstone, no qualitative change occurs at rates even as high as 800mm/min, whereas for an intermediate material with about 25% clay fraction, the residual strength shows a decrease (see Figure 2.17). La Gatta (1970) found that increasing the shear displacement rate from 0.006 to 0.6 mm/min increased the residual strength of Cucaracha Shale (with liquid limit of 65%, plasticity index of 20%, and clay faction of 48%) by 35%. Wedage et al. (1998a, 1998b) pointed out that the apparent residual friction angle of Clearwater clay shale increases linearly with the logarithm of the shear strain rate for the range of strain rates considered (0.01/day to 0.7/day).

2.7 PORE PRESSURE RESPONSE OF SHEAR ZONES

The pore-pressure response of a shear zone may be totally different from that of the intact material, which has the same composition as the shear zone. Pore-pressure measurement on a shear plane is a difficult problem because of the limitation of the piezometers and their installation. No report about the pore-pressure measurement of shear zones or discontinuities, both in the laboratory and in the field, has been published, except for a study on *in situ* pore-pressure measurements on a shear zone during a controlled displacement-rate *in situ* shear test carried out in 1985 at a dam site in western Canada (Shuri et al., 1985). The rock at this site is a Cretaceous shale containing a thin clay seam tentatively identified as a bedding-plane shear zone. Two large blocks of shale were sheared along the clay seam. These tests were conducted under a strictly controlled rate of shear displacement and the monitoring of pore pressures throughout the test. Several constant displacement rates ranging from 0.025 to 25 mm/h were used during the tests. A stiff, low-volume, and high-air-entry piezometer was used to measure pore pressure. Three piezometers were installed in each block. They were equally spaced along the center line in the first block and placed in a triangular configuration in the second. The sensor's ceramic face was smeared with clay seam material and was pressed directly into contact with the undisturbed seam. Two of the test results were that during the shearing, the pore pressure measured was not uniform along the shear zone and the highest pore pressure (334 kPa) was measured at the highest shear rate (25mm/h), and the shear strength was increased approximately 3% by each order-of-magnitude increase in the rate of shear.

2.8 HYDRAULIC CONDUCTIVITY OF SHEAR ZONES

The hydraulic conductivity of shear zones is one of the main hydraulic parameters, having a great influence on these zones' pore pressure. Shear zones in clay can either enhance or retard fluid flow, depending on the clay content and the composition of the sheared sediments and their states before shearing (normally consolidated or over-consolidated). Dewhurst et al. (1996a, 1996b) measured the hydraulic conductivity of a sheared clay, and for comparison, of a consolidated clay. The shear zone was formed during ring shear tests of a silty clay. The hydraulic conductivities in shear-parallel and shear-normal to the shear zone were measured. Figure 2.18 schematically shows the shear-parallel, shear-normal and oedometric hydraulic conductivities in a sheared clay specimen. The results showed that the hydraulic conductivity of shear zones is anisotropic. For any given load or void ratio, the shear-parallel hydraulic conductivity is slightly lower than the oedometric hydraulic conductivity. The shear-normal hydraulic conductivity is distinctly and consistently lower than either the shear-parallel or the oedometric hydraulic conductivity, and the clear trend is for the difference in conductivity to increase with a decreasing void ratio. The oedometric hydraulic conductivity is larger than both the shear-parallel hydraulic conductivity and the shear-normal hydraulic conductivity, probably because in normal consolidated material, the shear zones' hydraulic conductivity is lower than that of the unsheared material because shear contractancy occurs in the formation of shear zones. However, for a shear zone that has developed in an over-consolidated clay, the shear-parallel hydraulic conductivity will be larger than the hydraulic conductivity of the unsheared material because of shear dilatancy, while the relationship between the shear-normal hydraulic conductivity and the hydraulic conductivity of unsheared materials is more complex and will depend on the clay content and shear modes (Lupini et al., 1981). After further research, Dewhurst et al. found that a shear zone's hydraulic conductivity was a function of the sheared material's microfabric, so that the development of an anisotropic fabric resulted in anisotropic hydraulic conductivity. Strong fabric-related anisotropy of hydraulic conductivity became increasingly well developed as the change to sliding-shear behavior occurred. Intense parallel grain alignment occurred at or close to the main slip surface in the sliding-shear direction, while highly deformed, chaotic fabric development occurred above the slip surface compared with that below it. This parallel grain alignment at the main slip surface resulted in the lower shear-normal hydraulic conductivity.

2.9 CONCLUSIONS AND COMMENTS

The literature has been reviewed to investigate the previous work related to this research project. The information obtained from the review indicates that a framework for understanding a shear zone's characteristics and mechanical properties has been established. As well, the methods for carrying out field investigations, detailed mapping, and laboratory tests, and for identifying *in situ* physical properties, have also been determined. The following conclusions and comments are based on this review:

- Laboratory tests indicate that the formation of a shear zone in a laboratory is possible under either a simple shear test or a direct shear test or even under a triaxial shear test provided that the kinematic or boundary conditions allow for such a formation. These kinematic or boundary conditions include the rotation of principal stresses in the direct shear and a large enough ratio between the length L and the diameter D of the specimen in the triaxial test. The laboratory observations of shear zones seem to be consistent with *in situ* observations even though a shear zone generated in a laboratory has a different origin from one in nature.
- Although numbers of well-documented shear zones are limited, some common features have been observed in the field. Shear zones are generally developed in those parts of a clay bed with the highest percentage of clay particles, and all shear zones seem to have a similarity in their shear-induced structures, which are characterized by the presence of various minor shears and main slip surfaces (D shears), along which, the clay particles are more or less oriented depending on the clay content and sheared displacement. The geometrical arrangement of such discontinuities is complex, and the original fabric and structure between shears are generally disturbed.
- Many laboratory tests on shear discontinuities, shear zone materials, and adjacent intact materials have provided a clear framework for understanding a shear zone's strength characteristics and deformation mechanism. In fact, the strength along a principal slip surface is at or very close to the residual value. The peak strength of specimens taken from the shear zone is very close to the critical value, and the

intact clay's strength falls approximately to the residual value in a displacement of several centimeters.

- As a result of strain localization, shear zones generally develop in weaker layers with a high clay content. These high clay content layers often have low permeability, and the clay particles are more or less orientated along the slip surface, depending on the displacement which has occurred. Such an orientation of the clay particles causes a shear zone to have an even lower permeability, especially in the shear-normal direction. This low permeability results in exceptionally low rates of the dissipation of the excess pore pressure resulting from the soil structure construction. Thus, the combination of a shear zone's low shear strength and high pore pressure leads to the prediction of low factors of safety. In addition, the basal failure zone developed in clay-rich sediments could enhance the prospects of developing perched aquifers within a landslide since such a zone would greatly restrict vertical drainage and increase the likelihood of reactivated slope failure as a result of the extra mass and reduced effective stress on the slide's base.
- A shear zone's pore pressure is a vital parameter for the stability and performance of a slope or foundation that either is founded on or located in such a shear zone. However, the pore pressure obtained from the *in situ* instrumentation is often that of the area adjacent to the shear zone. No research has been published about the issue of whether this instrumented pore pressure is a good representative of the shear zone's pore pressure. In addition, nothing has been published about a shear zone's pore-pressure response, or about that of a pre-existing slip surface during the practical deformation rates. No matter the pore pressure generated on a slip surface is high or low, this pressure will have a big influence on the stability and safety of a geotechnical work either founded on or located in a shear zone.
- The previous research focused on specific areas and materials. In the Athabasca Oil Sands area near Fort McMurray, more and more shear zones have been found during recent site investigations, but shear zones have not been well documented. With the expansion of the Oil Sands industry, more and more tailings structures such as tailings dykes will be built on these shear zones. The designers of such

structures must consider a shear zone's pore pressure and strength characteristics. A thorough understanding of the material behavior and detailed geometry of the shear zone itself is essential, so the detailed mapping of it is necessary and beneficial.

- The experience from the deformation of some big tailing dykes construction in the Athabasca Oil Sands area highlighted the limitations of the design based on factor of safety considerations alone (Fair and Handford, 1986; Morgenstern, 1987, 1999; Morgenstern and Scott, 1997). A design that considers the deformation represents great progress. Today, estimating the deformation of a geotechnical project is not difficult with the help of some commercial numerical software. The challenge, now, is to determine what properties to assign for the analysis and how to describe the deformation and failure process, especially when a project is founded on a shear zone. To overcome this challenge, we must study not only a shear zone's strength properties such as peak and residual strength, but, more importantly, also study its post-peak strength characteristics and stress-strain relationship.

Table 2.1 Typical displacements at various stages of shear in clay having CF> 30% (Skempton, 1985)

Stage	Displacement: mm	
	O-C	N-C
Peak	0.5 – 3	3 - 6
Rate of volume change approximately zero	4 - 10	
At $\phi_r + 1°$	30 - 200	
Residual ϕ_r	100 - 500	

Intact clays, with $\sigma' < 600$ kPa

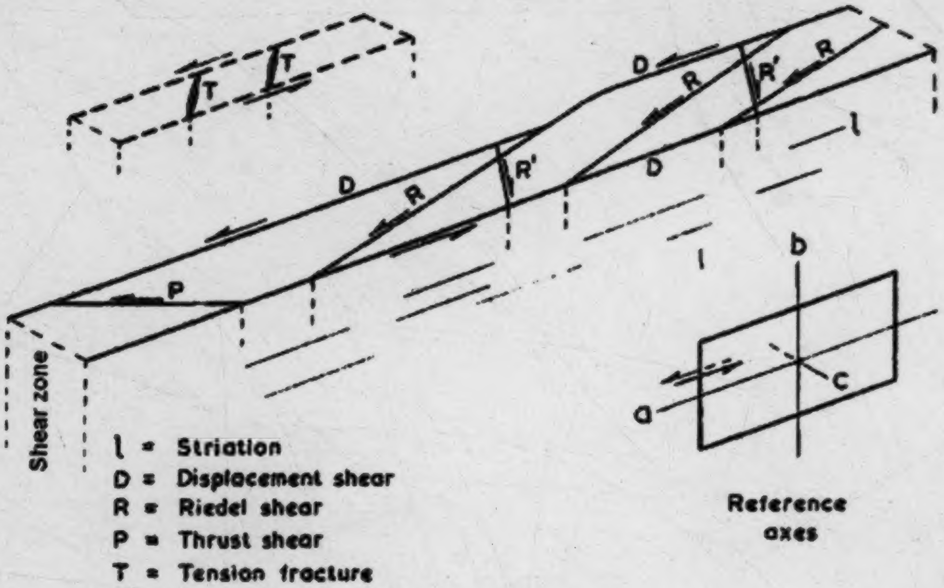
T
T
D
R
R'
R
D
R
R'
D
P
l
l
b
c
a
Shear zone
l = Striation
D = Displacement shear
R = Riedel shear
P = Thrust shear
T = Tension fracture
Reference axes

Figure 2.1 General features in a shear zone and reference axes (modified from Skempton 1966)

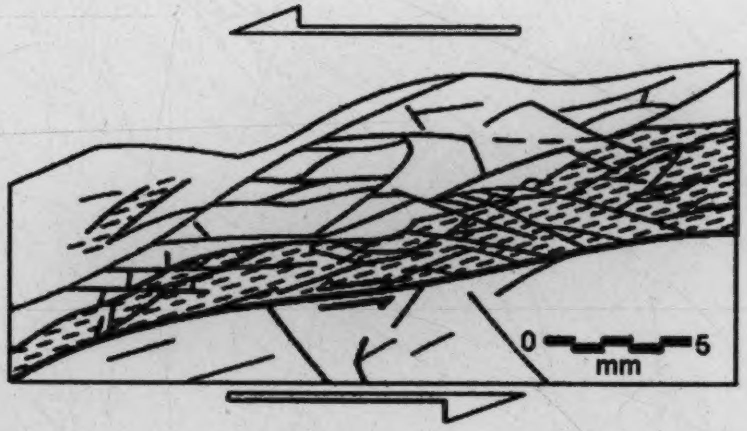

Figure 2.2 Details of Geildford shear zone in a thin section. (after Morgenstern and Tchalenko, 1967)

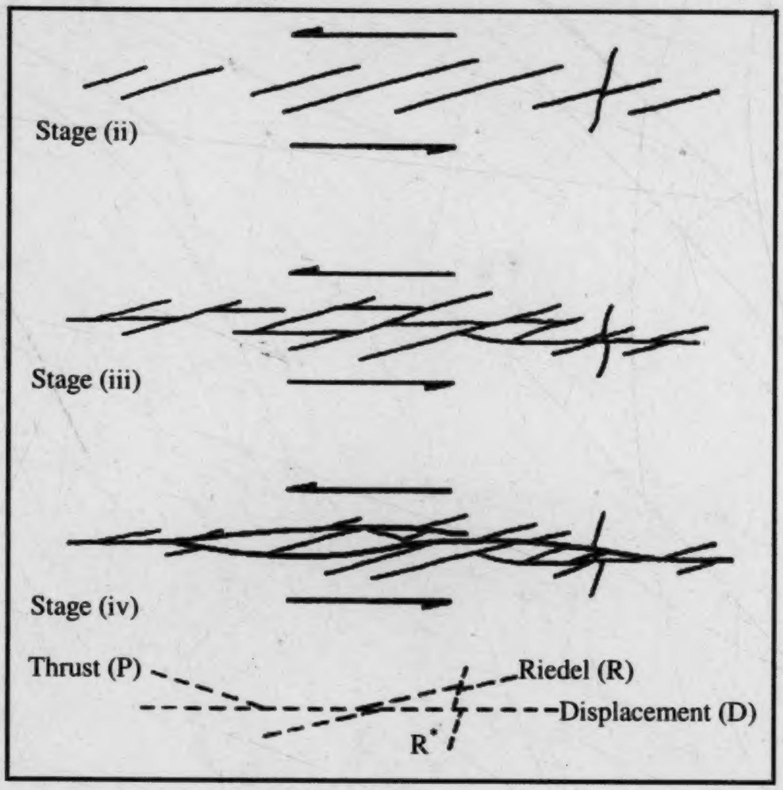
Stage (ii)
Stage (iii)
Stage (iv)
Thrust (P)
Riedel (R)
Displacement (D)
R'

Figure 2.3 Successive stages in the development of a shear zone in clay, from laboratory tests (modified from Skempton 1966).

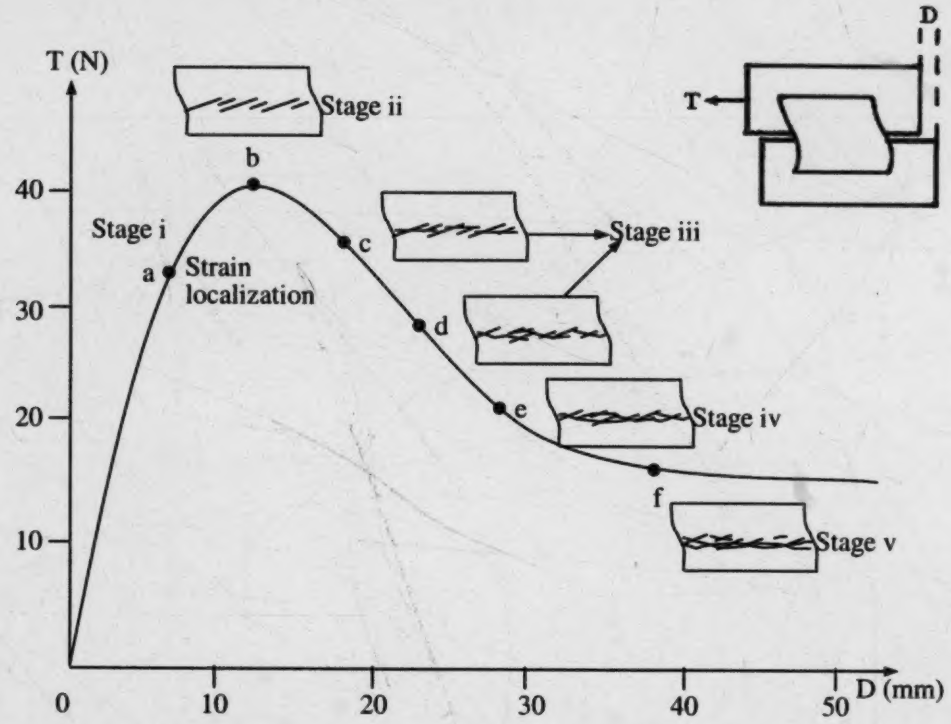

Figure 2.4 Stress-displacement curve and shear zone development (modified from Tchalenko 1970)

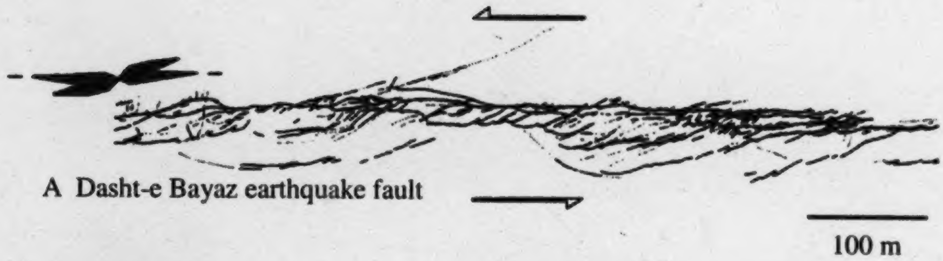
A Dasht-e Bayaz earthquake fault

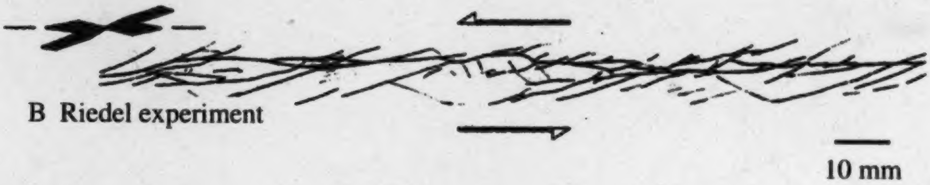
B Riedel experiment

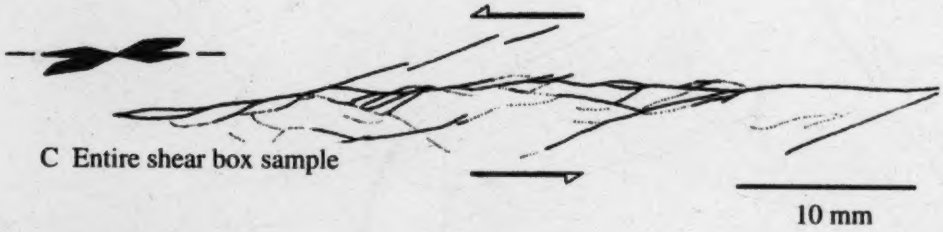
C Entire shear box sample

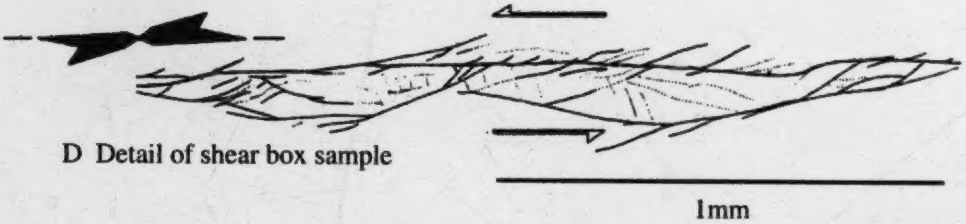
D Detail of shear box sample

Figure 2.5 Similarity of shear zones in different scales (modified from Tchalenko, 1970)

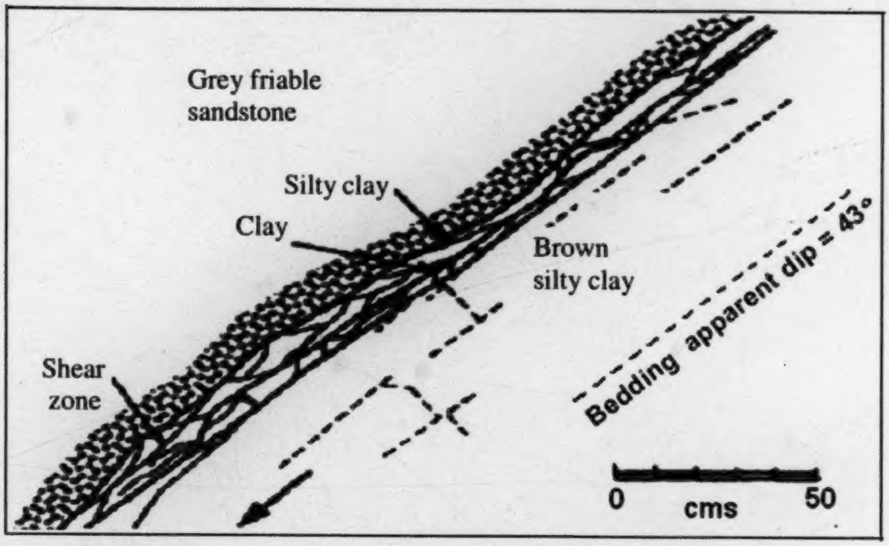
Grey friable sandstone
Silty clay
Clay
Brown silty clay
Shear zone
Bedding apparent dip = 43°
0
cms
50

Jari Pakistan (modified from Skempton and Petley, 1966)

(a)

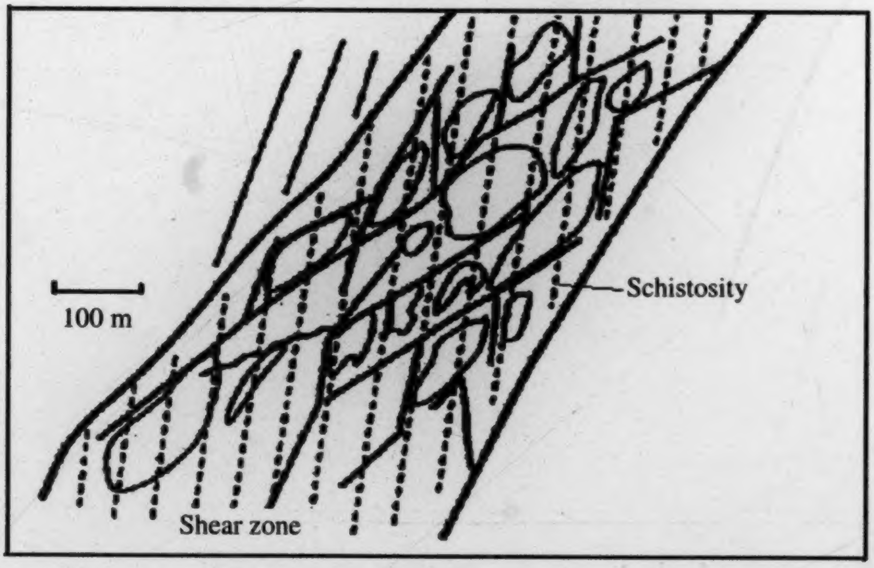
100 m
Schistosity
Shear zone

Abitibi belt, Quebec (modified from Archambault et al., 1990)
(b)

Figure 2.6 Shear zones developed in folded (a) and faulted (b) layers

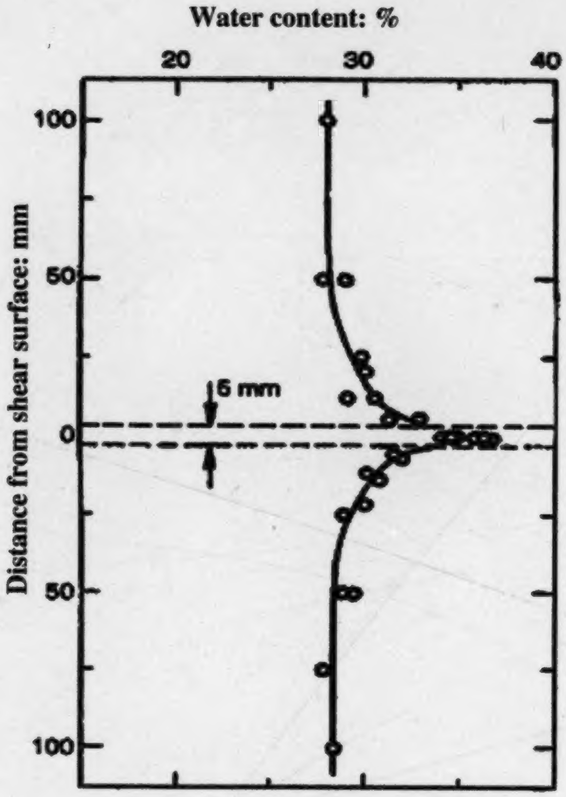

Figure 2.7 Water content profile across basal shear surface of a London clay landslide (modified from Henkel, 1956)

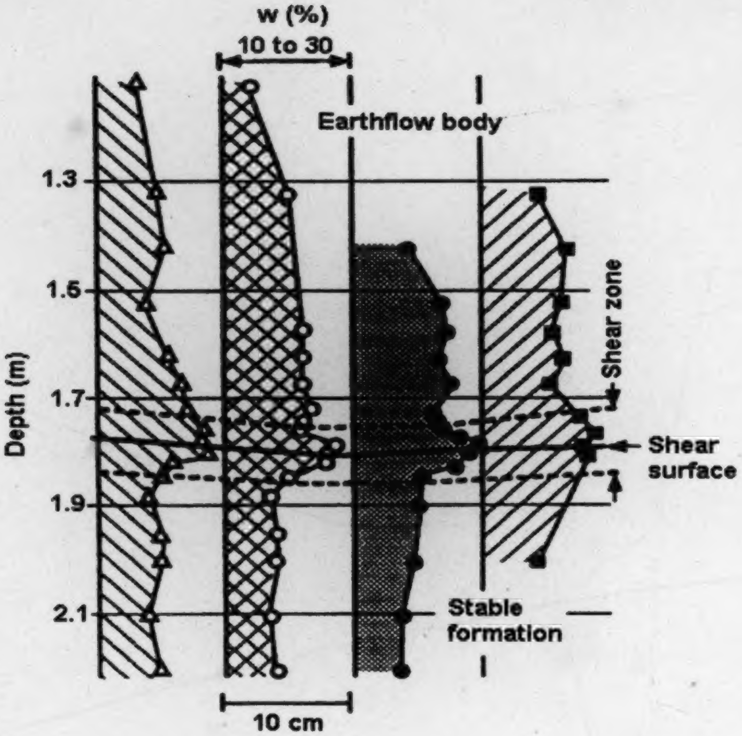

Figure 2.8 Water content profiles of a shear zone found at the base of earthflows in the Basento Valley, Italy (modified from Guerrier et al., 1993)

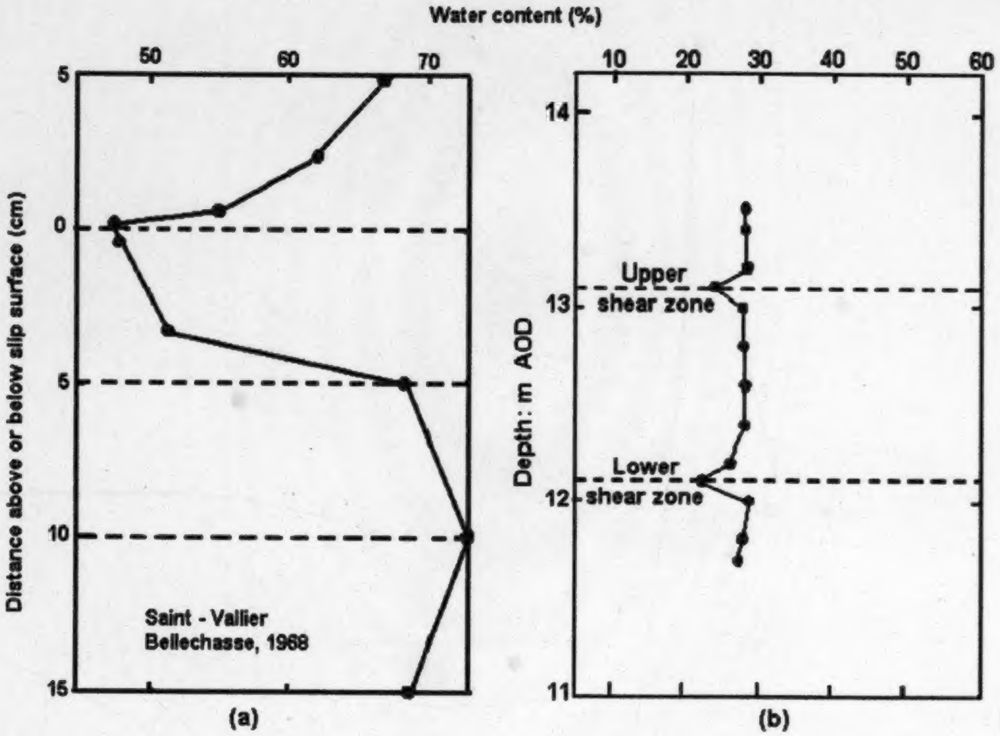

Figure 2.9 Water content profiles around shear zones in sensitive clay (a) (modified from Lefebvre, 1981) and in London clay (b) (modified from Chandler et al., 1998).

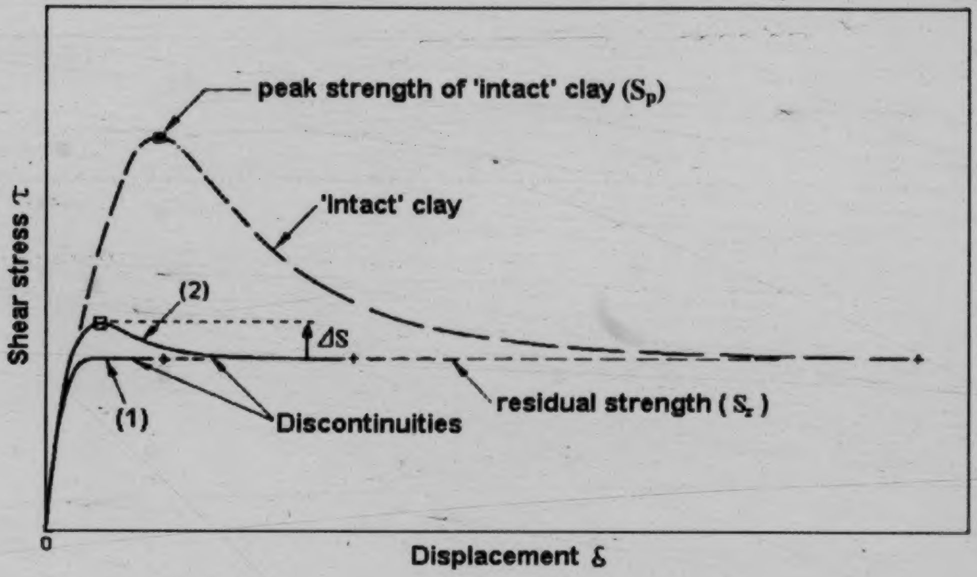

Figure 2.10 Typical stress-displacement curves on a principal slip surface and on intact clay (modified from Skempton and Petley, 1967)

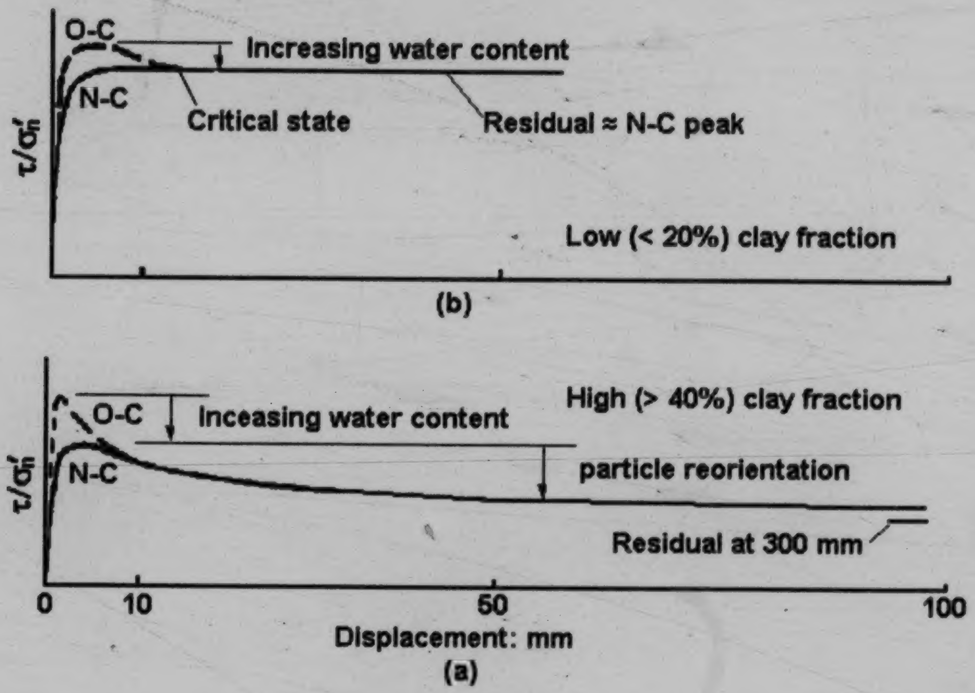

Figur 2.11 Stress-displacement curves and post-peak features at constant σ_n' (Modified from Skempton, 1985)

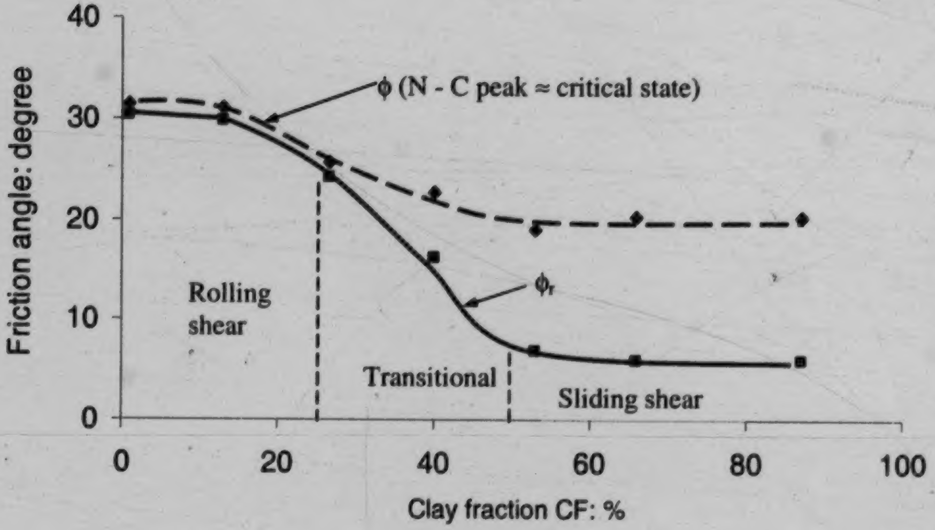

Figure 2.12 Ring shear tests on sand-bentonite mixtures (modified from Lupini et al., 1981)

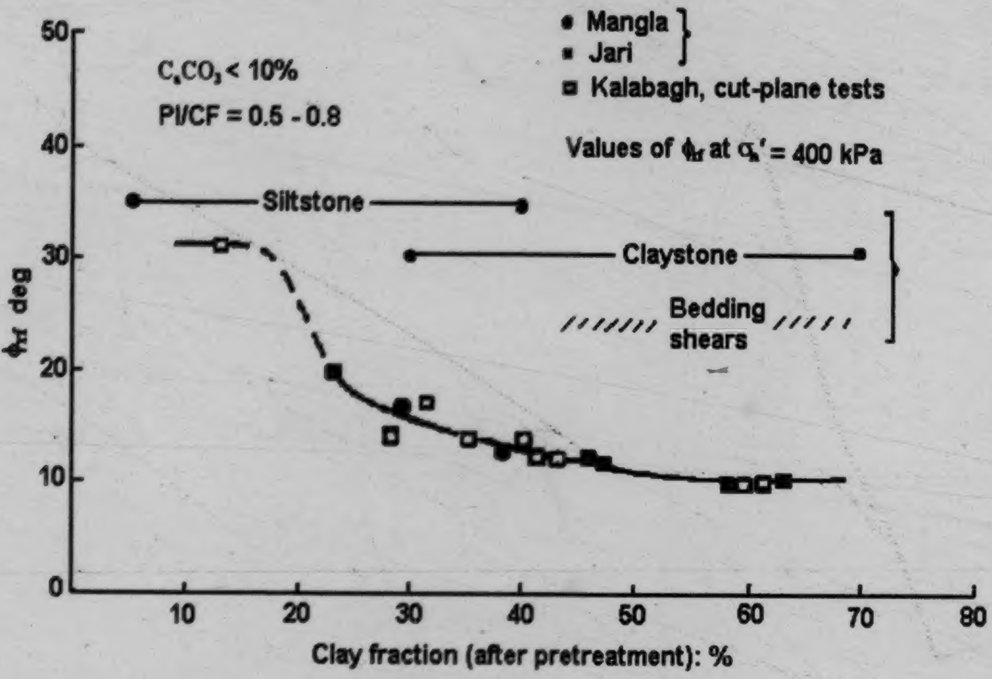

Figure 2.13 Field residual and ring shear tests on sands, kaolin and bentonite (after Skempton, 1985)

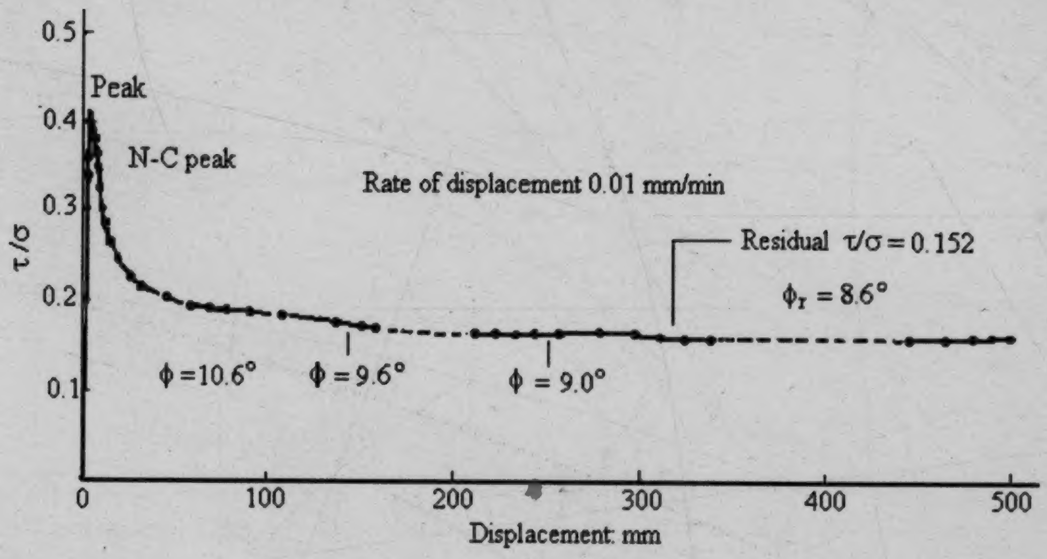

Figure 2.14 Mobilized strengths of a clay at different displacements (modified from Skempton, 1985)

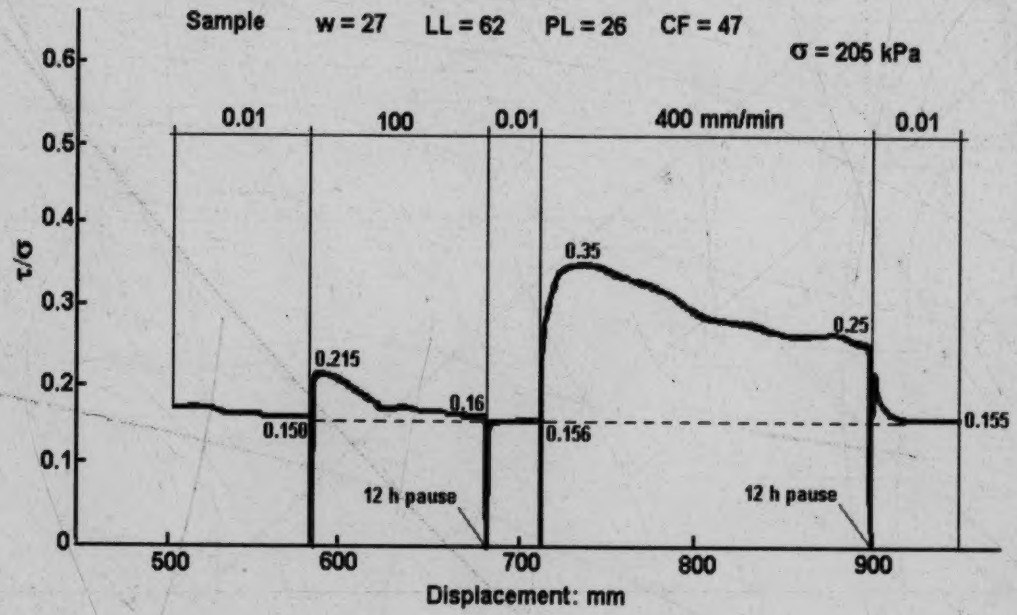

Figure 2.15 Shear strength of a clay at different rates of displacement (after Skempton, 1985)

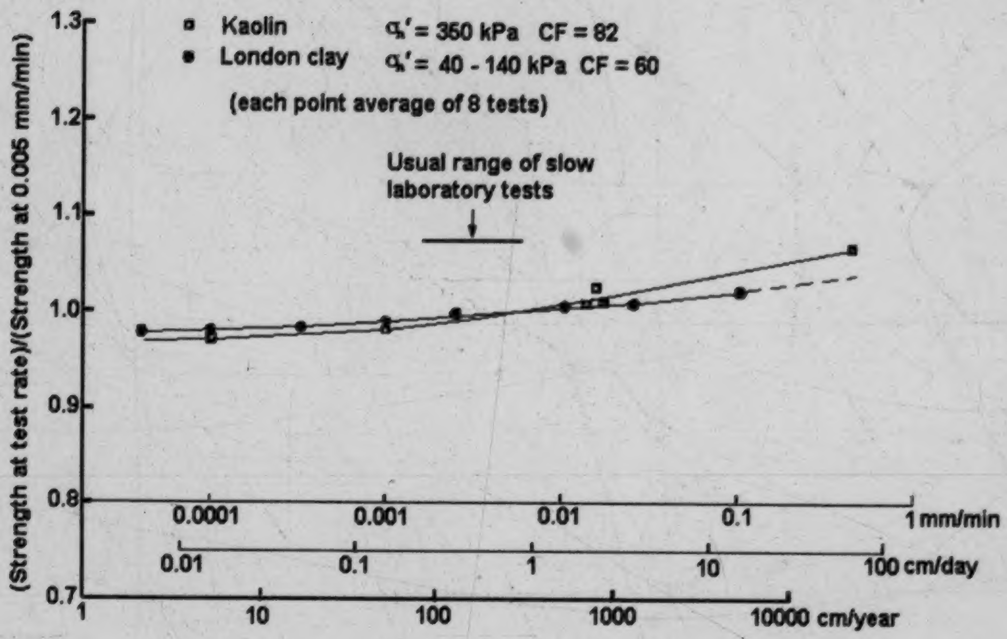

Figure 2.16 Variation in residual strength of clays at slow rates of displacement (after Skempton, 1985)

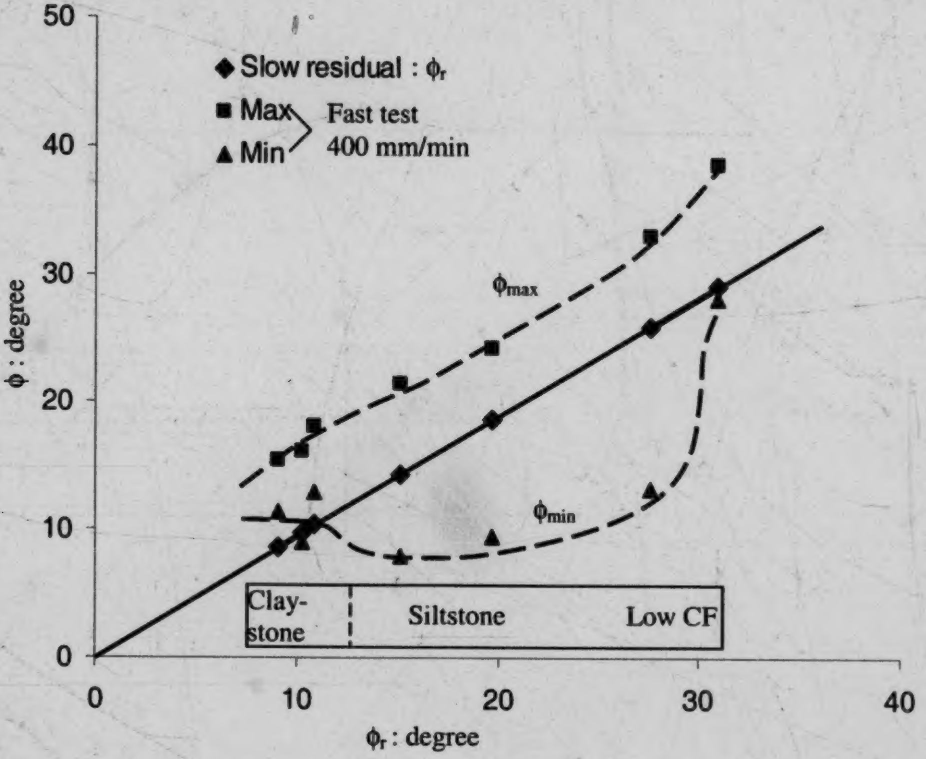

Figure 2.17 Summary of ring shear tests for Kalabagh Dam, June 1984 (modified from Skempton, 1985)

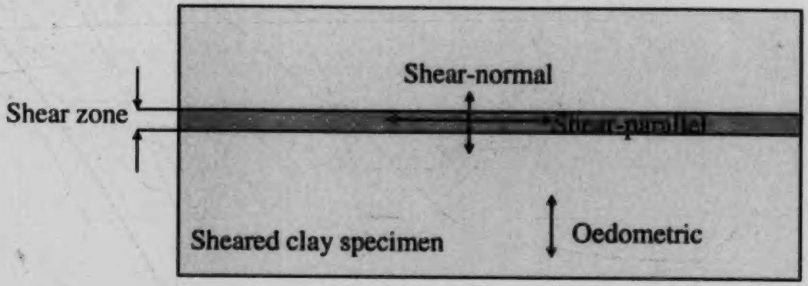
Shear-normal
Shear zone
Shear-parallel
Sheared clay specimen
Oedometric

Figure 2.18 Sketch shows the shear-parallel, shear-normal and oedometric hydraulic conductivities in a sheared clay specimen

CHAPTER 3 FIELD INVESTIGATION OF SHEAR ZONES IN WEAK ROCKS

3.1 INTRODUCTION

The determination of the shear strength of intact weak rock and discontinuities is quite straightforward. However, for jointed weak rocks or a discontinuous shear zone in weak rocks, the available shear strength can range from the peak strength of the intact material to the residual strength of the high-strain slip surface. Engineered structures founded on these weak zones demand a thorough understanding of the material's behaviour and the detailed geometry of the zone itself. The pore-pressure characteristics of shear zones are important for the stability and performance of a structure either founded on or located in a shear zone because it is a much weaker zone than the rest of a slope or foundation. The pore-pressure response of a shear zone may be quite different from that of its adjacent material due to the shear zone's internal fractures. Therefore, knowledge of a shear zone's geometry is necessary for measuring the zone's pore pressure and investigating its pore-pressure response under practical displacement rates of the potential failure slope or foundation.

A major expansion of Oil Sands projects for Suncor Energy Inc. is now under way. Several big tailings ponds are either being constructed or planned. The site investigations for these projects found many shear zones or shears developed in clay-rich beds such as clay shale, pond mud, basal clay, Paleosol, and heavily weathered limestone (Figure 3.1). These apparently weak strata clearly posed a potential hazard for the stability of subsequent tailings dykes founded on these strata, so investigating the shear zones' *in situ* properties and geometry were necessary. This work was done by detailed field mapping during the excavation of two shear keys for the construction of the Suncor tailing dykes.

3.2 INVESTIGATION METHOD

For many years, researchers have been extensively investigating the discontinuities developed in geomaterials, including their geometric states and mechanical properties. The International Society for Rock Mechanics Commission on Standardization of Laboratory and Field Tests (1978) produced the "suggested methods for the quantitative description of discontinuities in rock masses" (hereafter "suggested methods"), which supply a "standard" method to describe discontinuities in the field. Documentation of discontinuities is generally done by either field mapping (Hodgson, 1961; Nickelsen and Hough, 1967; Snow, 1968; Fookes, 1969; Skempton et al., 1969; Babcock, 1973; Priest, 1993), photogrammetry (Savage, 1965; Rangers, 1967; Wickens & Barton, 1971; Ross-Brown et al., 1973), or drill-core description (Deere, 1963; Geological Society Engineering Group, 1970; Rankilor, 1974; South African Core Logging Committee, 1976). Skempton (1966) introduced a new terminology to describe shear zones in the field and mapped several shear zones in detail, providing a methodology for subsequent authors to use to describe shear zones. In this thesis, the author will use Skempton's terms to describe shear zones, and the baseline and network method was used for the detailed field mapping. The baseline and network method sets up baselines and/or a network on a selected outcrop or excavated slope to copy the shear zone geometry and related discontinuities, to a certain scale, in an engineering form.

3.2.1 Equipment

In order to map shear zones in the field, the following equipment is necessary, which include a compass, a half- or one-meter ruler, a large set-square (triangle), a 5- or 10-meter measuring tape, red paint, several pins, a geological hammer, and a shovel. Of course, a pencil with eraser, small triangles, a protractor and a small ruler are necessary to copy the shear zone, to a certain scale, in an engineering form. A camera is useful to record the interesting spots and the environment. All equipment used during the field mapping is shown in Figure 3.2.

3.2.2 Procedures

The procedures for mapping shear zones in the field are as follows:

1. Selection of a satisfaction outcrop or slope. A "outcrop or slope" is an outcrop or slope that contains an interesting shear zone and that is fresh, or without the interference of weathering fissures. If the outcrop or slope is not fresh, clean-up with a hammer or shovel is needed to present the original structures.
2. Set-up of a horizontal baseline. According to the size and shape of a selected outcrop or slope, a horizontal baseline position is determined. It is best located at the bottom or at a suitable height if this line cannot be placed on the bottom due to frozen talus, which is difficult to remove, on the slope. After the position is determined, the compass and the ruler are used to draw the initial part of this horizontal baseline. If the length of the outcrop or slope is greater than 2 meters, the measuring tape is used to extend the baseline to the required position, and red paint is used to draw this baseline on the outcrop or slope.
3. Establishment of vertical baselines and network. After the horizontal baseline is set up, one or more vertical baselines will be set up which are perpendicular to the horizontal baseline. If the number of the vertical baseline is more than one, the interval between any two adjacent baselines should be equal, and 0.5 meters is recommended. If the height of the slope is greater than 1 meter, another 1 or 2 horizontal baselines should be drawn. The interval between these horizontal baselines is also recommended to be 0.5m. In this case, a network with 0.5m by 0.5m squares has been established. Red paint is used to draw these baselines on the slope. The scenario is shown in Figure 3.3.
4. After the baselines or network are set up, the detailed mapping can be undertaken. Such mapping should include all the shear zone's information such as its length, thickness, waviness, internal fractures, and constituent materials. The lithological components of the outcrop or slope, particularly the marker horizon and their contacts, should be mapped.

5. The orientation of main discontinuities, the slope section, and any striations are measured with a compass and marked on the map. After the mapping and measurement are done, photos should be taken to support the mapping.
6. Field descriptions record the shear zone's important phenomena and any interesting points.
7. Some disturbed samples should be taken with a tube sampler for some specific purposes such as the measurements of the water content and index properties. High-quality block samples could be taken on the outcrop or slope by using specific tools if needed.

3.2.3 Presentation of the Mapping

After the field investigation is finished, the primary field mappings should be processed into drawings in different scales. The scale is determined by the demands. Generally, a large scale such as 1:20 and a small scale of 1:100 are basic demands. The field mapping can be first redrawn on another sheet of an engineering form with the required scale, and then can be traced exactly on a transparent paper. After the marking of important information such as the orientation of some main discontinuities and sampling points on this drawing, it can be scanned or input into a computer to form an image file, or be digitized into an image file by using a digitizer. This file can then be edited and put in a paper, thesis, or report or printed out for use.

3.3 LOCATION AND GEOLOGY OF THE MAPPING SITES

Suncor Energy Inc. operates a mine in the Athabasca oil sands about 40 km north of Fort McMurray in northern Alberta, (see Figure 3.4). The Athabasca oil sands comprise the Cretaceous McMurray Formation. The McMurray Formation was deposited in a tidal environment, and the sediments originated from successive deposition in fluvial, estuarine tidal conditions where tidal flats developed without strong waves. Overlying the McMurray Formation is the Cretaceous Clearwater Formation, which forms the reservoir cap for the oil sands and consists primarily of laterally extensive, flat-lying clay-shale, clay silts and fine-grained sands deposited in a shallow marine environment (Kosar 1992). Underlying the McMurray Formation is the Devonian Waterways Formation, which consists of Paleosol, a waxy, slickensided, greyish green or greenish grey clay or silty clay, situated on top, and some weathered and unweathered interbedded massive and argillaceous limestone below. Figure 3.5 shows the stratigraphic sequence for the project's area.

A significant challenge associated with the oil-sand mining is the construction of dykes to retain tailings. To obtain a steeper dyke slope, two shear keys were constructed. They are located in dyke 10 of pond 7 and dyke 11 A of pond 8A, respectively. Pond 8A is situated between Leggett Creek and McLean Creek, while pond 7 is about 5 km north of pond 8A (see Figure 3.6).

3.4 DESCRIPTION AND MAPPING OF THE SHEAR ZONES

The general features of a shear zone and reference axes are shown in Figure 2.1. Skempton (1966) provided some associated definitions. Following his terminology, some shear zones observed in the field are described as follows.

3.4.1 Shear Zone ("Shear Zone I" hereafter) at Dyke 11A

Dyke 11A is the west dyke of pond 8A, which is situated north of McLean Creek and south of Leggett Creek (Figure 3.6). Dyke 11A's shear key is about 700m long and between 70m and 150m wide. The strata at the location consist of the Clearwater Formation (clay shale) and upper McMurray Formation (Marine Shore Facies and Tidal Flat Mud), dipping in a southerly direction at 5° to 10°. During the shear key's excavation, field mapping of discontinuities on the pit's east wall was done. One shear zone that had developed in the MSF (Marine Shore Facies) was well exposed on the wall. The relationship between the shear zone and the strata is shown in Figure 3.7. The detailed mapping of this shear zone was done at two positions (positions A and B) on the wall (Figures 3.8 and 3.9). The following features were observed:

- The thickness of the shear zone is about 5 ~ 20 cm. Almost its whole length includes a principal slip surface (basal D shear). It is not strictly planar over its full extent and is developed along bedding.
- A wavy displacement shear occurs at the top of the zone and deviates from the a axis by low angles.
- Many minor shears (R shear, P shear, and short D shear) have developed in the shear zone.
- The zone includes many characteristic shear lenses with a sigmoidal shape.
- The adjacent rocks have almost no accommodation fractures.

The existence of the principal slip surface and the shear lenses with a sigmoidal shape means that this shear zone probably underwent a relatively large displacement.

3.4.2 Shear Zones at Dyke 10

One proposed shear key is located at the west dyke 10 of pond 7. The strata in this shear key are bitumen-rich and locked sand (K_m), underlying water sand that is overlying the paleosol, while argillaceous limestone (D_w) is underlying the paleosol. Some argillaceous limestone is highly weathered. In order to examine the distribution of the weak paleosol layer, several test pits were excavated within the proposed shear key. Another pit, pit 18, is located about 150m northwest of the shear key. Detailed mapping in some of the pits was carried out (Figure 3.10), and several shear zones were discovered.

3.4.2.1 Shear zone ("shear zone II" hereafter) in pit 18

This shear zone occurs in weathered argillaceous brownish grey limestone, which dips in a westerly direction at about 15°. The zone is grey to dark grey, which is a different color from that of the adjacent rock. A pocket knife can be inserted into the zone, but cannot be inserted easily into the unsheared adjacent rock. The relationship between the shear zone and adjacent rock, and the form of the shear zone, are shown in Figure 3.11 and Figure 3.12.

The shear zone is bounded by two main slip surfaces (D shears), which can be traced as a gently undulating, smooth surface over the entire length of the exposed pit wall. The thickness of the shear zone is about 15 ~ 30 cm. The interior of the shear zone is dominated by the R and D shears, forming a complex pattern of shear lenses. These lenses are not distorted enough to have sigmoidal shape, but have more of a rhombic shape. In the south end are several conspicuous thrust shears. A few striations were seen on the basal D shear with a plunge of 15° and trend to the northwest (320°), but the movement's magnitude is not indicated. The rhombic-shaped shear lenses may indicate that a relatively small displacement occurred during the shear zone's formation. The rock below the shear zone contains numerous accommodation fractures, and some developed along bedding.

3.4.2.2 Shear zone ("shear zone III" hereafter) in pit 26

A shear zone has developed on the top of the weathered argillaceous limestone, with an increase of calcium carbonate content downward. The calcium carbonate occurs in pockets and strips and is white in colour. A photograph and a drawing of the shear zone are shown in Figures 3.13 and 3.14, respectively. The shear zone consists mainly of several subhorizontal D shears, which apparently run parallel to the bedding and are highly polished, planar, and shiny. All these shears have a high degree of continuity. This zone only has a few minor shears, so it has few shear lenses. Instead, the thin shear slices are the main feature (see Figure 3.13). Note that an unweathered limestone relic has interrupted several D shears.

3.4.2.3 Shear zone ("shear zone" IV hereafter) in pit 20

In the east end of pit 20, paleosol was found, which is a waxy, slickensided, greyish green or greenish grey clay or silty clay. The contact between paleosol and limestone is complex. The top contact between the paleosol and the Oil Sands was excavated during the mining. Detailed mapping of the paleosol on the pit's two sidewalls was conducted. Two drawings of the shear zone are shown in Figures 3.15 and 3.16. It has no obvious principal shears. All shears have a low degree of continuity and intersect each other to form a complex pattern of shear lenses. Figure 3.17 shows the combination of these lenses and the minor shears, which occur in different patterns. Some shear surfaces are rough, and striations are common (see Figures 3.18 and 3.19). Several sets of striations in different orientations are present in the shear zone, and sometimes this phenomenon occurs in the block samples in the pit's dump. This phenomenon was also observed during the site investigation (AGRA 1999). The material within the shear zone has probably undergone complicated movements such as translation and rotation during the formation of the shear zone.

3.5 PHYSICAL PROPERTIES OF SHEAR ZONES

3.5.1 Water Content

The observation of the water content around the slip surfaces developed in overconsolidated clays and clay shales will detect a local increase in the water content (see Figures 2.7). This increase can be related to the dilatancy induced by shearing (Henkel, 1956; Skempton, 1964; Chandler et al., 1998). In this case, although the shear zone is quite thin, the increase in water content is substantial, from about 28% up to a maximum of 37%.

During the field mapping of shear zones II and III, water-content samples were collected by using a tube sampler (Figures 3.11 and 3.14), and the water contents were measured. The results are shown in Figures 3.20 and 21 and presented in Table A1. In zone II, the water content increases from about 7% in the unsheared rock to about 13% in the shear zone. In zone III, the water content increases from about 12% in the unsheared rock to about 15% in the shears. This increase probably means that dilatancy occurred when shearing took place. Although the water content in shear zone I was not measured, this water content can be expected to have increased after shearing since a volume increase was observed after shearing due to some minor shear surfaces opening.

3.5.2 Grain-size Distribution

Hydrometer tests were used to measure the grain-size distribution for the shear zone material, and this distribution was compared with that of the adjacent unsheared material. The results are shown in Figure 3.22. The test data are presented in Tables A2 and A3. In shear zone I, the sheared material is mainly clay particles, which are about 86% of the total material, while in the unsheared material, the clay content is only about 21% of the total material, a percentage which is much less than that in the shear zone. In shear zone II, the clay fraction is about 42% within this zone, while outside it, the clay content is about 23%. In short, the grain size of the material within the shear zone is smaller than that of the material outside the shear zone. This result is consistent with the results of Skempton's (1985) and Archambault et al. (1990) investigation.

3.5.3 Atterberg Limits

The Atterberg limits of the material in the shear zone were measured to compare them with those of the material outside the shear zone. The results are presented in Table 3.1, and the test data are presented in Tables A4 to A6. The Atterberg limits in the shear zone are much higher than those outside the zone. Within zone I, the liquid limit increases from 34.8, outside the shear zone, to 101 within the shear zone, while the plastic limit increases from 25.0 to 47.6, and the associated plastic index increases from 9.8 to 53.5. In zone II, the liquid limit increases from 24.7 to 39.9, while the plastic limit increases from 14.7 to 19.6, and the plastic index increases from 10 to 20.3. In short, the Atterberg limits increase within the shear zone. This result is consistent with the shear zone's water content and grain-size distribution. Within the shear zone, the water content is higher and the grain size is smaller, so the Atterberg limits are higher.

3.6 CONCLUSIONS

Four shear zones of varying complexity were mapped in the weak Cretaceous mudstone and the weathered argillaceous Devonian Waterways Formation. From the mapping and laboratory analysis, the following conclusions can be made:

1. Shear zones are common phenomena in the Athabasca Oil Sands area. They often develop in clay beds with high clay content such as clay shale, basal clay, Paleosol, pond mud, and the highly weathered limestone. These shear zones make the weak clay beds have much weaker behavior than the rest of the materials.
2. Shear zones have a fracture pattern sharply different from that of the adjacent rock. This pattern is strongly related to the amount of deformation that has occurred in geological events. The one or more principal D shears in the shear zone and its minor shears make the shear zone more complex. The D shears are the weakest place in the shear zone.
3. The shear zone's water content is markedly higher than that of the adjacent unsheared material.
4. The grain size of the material within the shear zone is much smaller than that of the adjacent unsheared material since some of the bigger particles were comminuted into smaller ones during the shear zone's formation.
5. The Atterberg limits of the material within the shear zone are significantly larger than those of the adjacent unsheared material.

The magnitude of the past shear displacement is an important factor for determining a shear zone's strength parameters. Unfortunately, without a reference or marker horizon that was sheared through, determining shear displacement magnitudes in the field is difficult. For the mapped shear zones, we can infer that shear zone I underwent a relatively large displacement because of the sigmoid shape of its shear lenses and the large differences between the water content, particle size, and Atterburg limits of the sheared material and its adjacent material, while shear zone II at pit 18 underwent a relatively small displacement because this shear zone has different characteristics than those of shear zone I.

Table 3.1. Atterberg limits inside and outside the shear zones

	Shear zone I (Dyke 11A)		Shear zone II (Pit 18)	
	Inside	Outside	Inside	Outside
Wl	101	34.8	39.9	24.7
Wp	47.6	25.0	19.6	14.7
PI	53.5	9.8	20.3	10

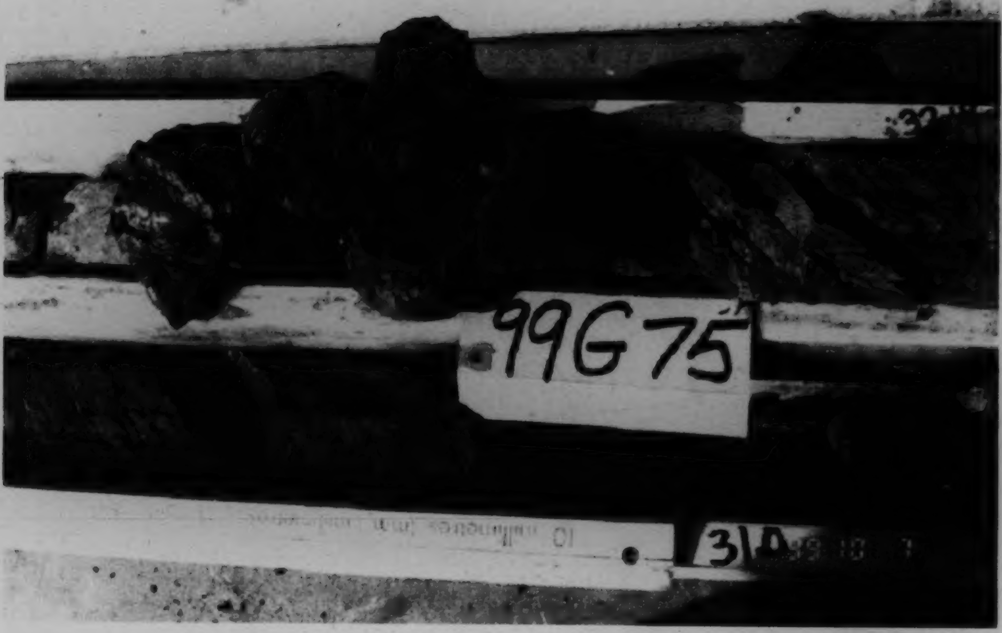

Figure 3.1 Photograph showing the slickensided basal clay (after McRoberts, 2001)

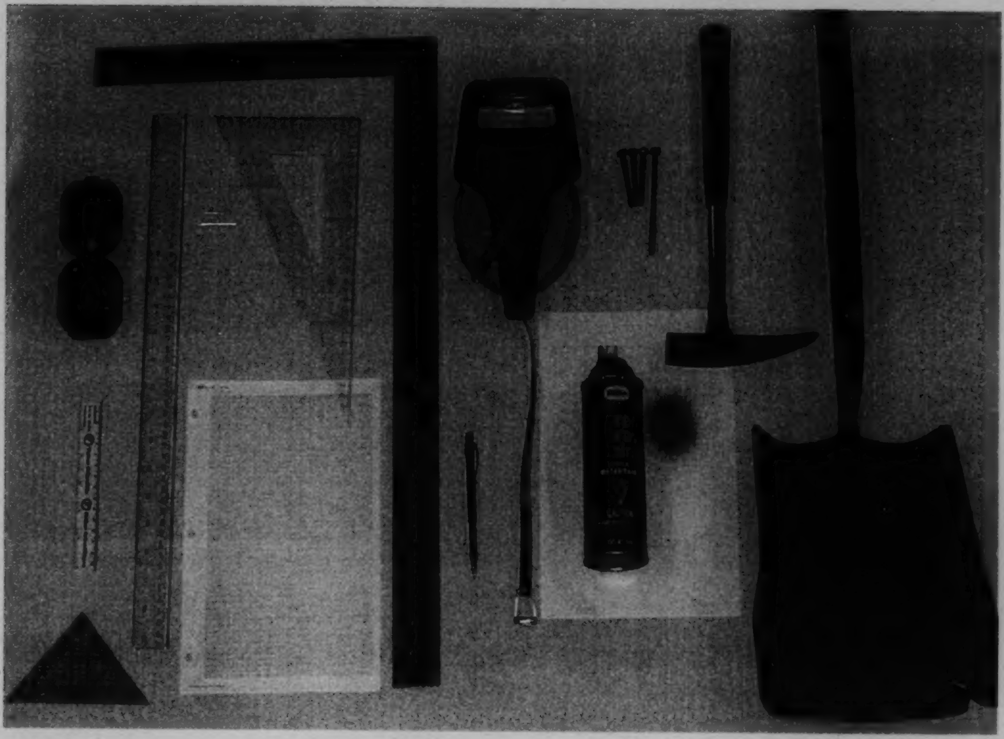

Figure 3.2 Photograph of the mapping tools

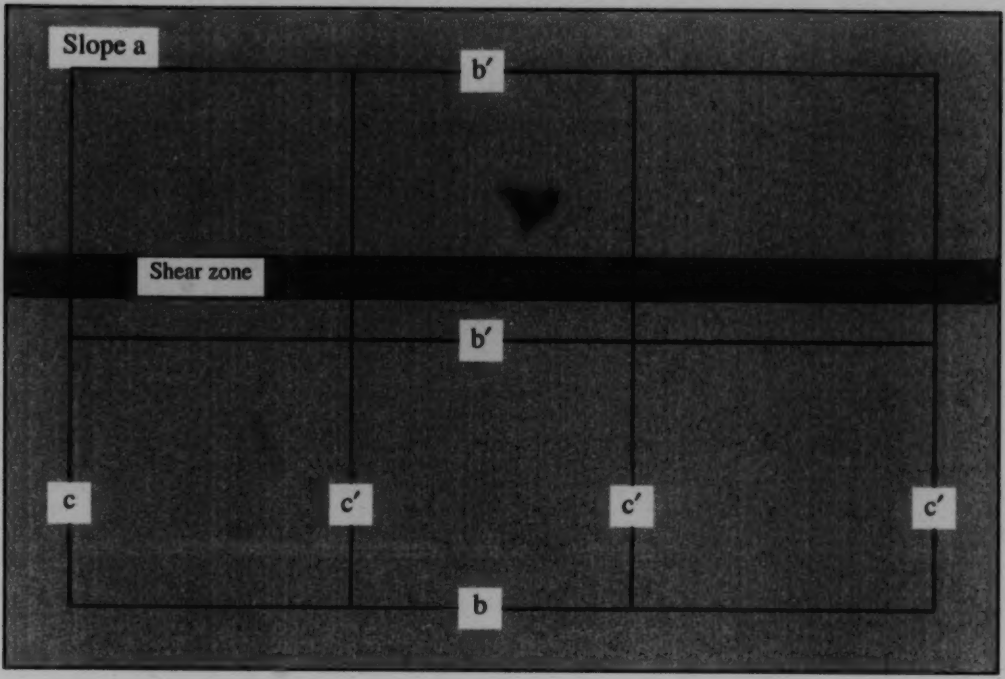
Slope a
b′
Shear zone
b′
c
c′
c′
c′
b

Figure 3.3 A scenario of the shear zone mapping slope; b is a primary horizontal baseline, b′ is a secondary horizontal baseline; c is primary vertical baseline, c′ is a secondary vertical baseline; b, b′, c, and c′ constitute a network

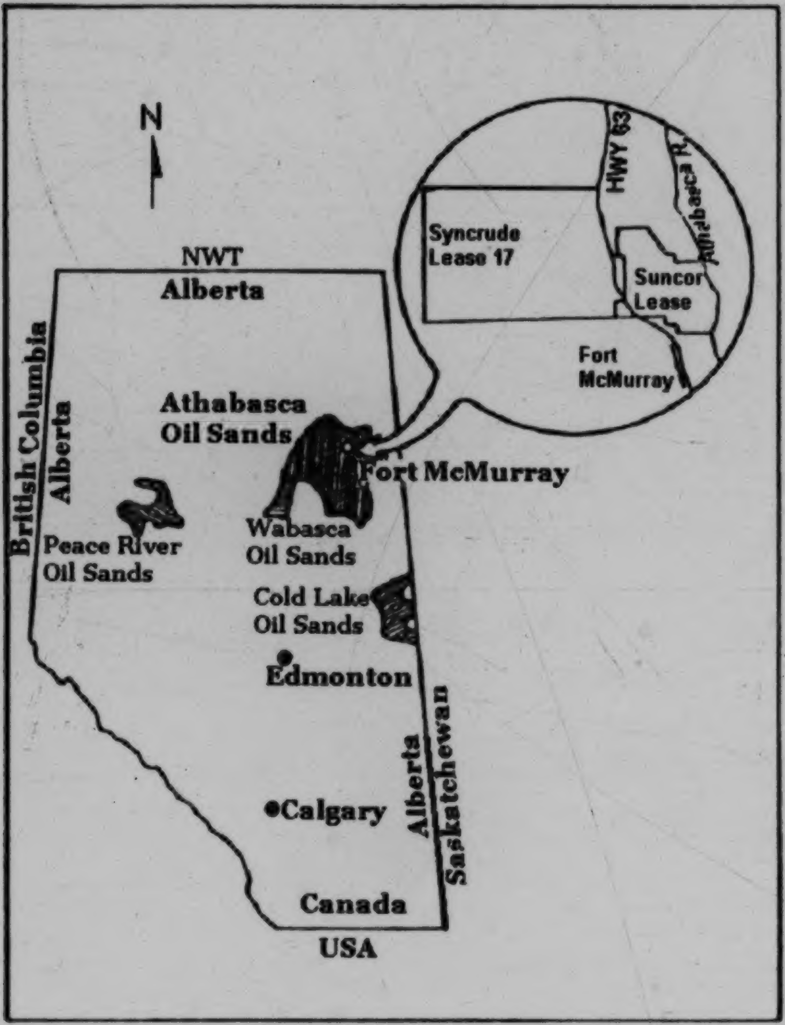
N
NWT
Alberta
British Columbia
Alberta
Athabasca Oil Sands
Fort McMurray
Peace River Oil Sands
Wabasca Oil Sands
Cold Lake Oil Sands
Edmonton
Calgary
Alberta
Saskatchewan
Canada
USA
HWY 63
Athabasca R.
Syncrude Lease 17
Suncor Lease
Fort McMurray

Figure 3.4 Location of Suncor Energy Inc. mine site

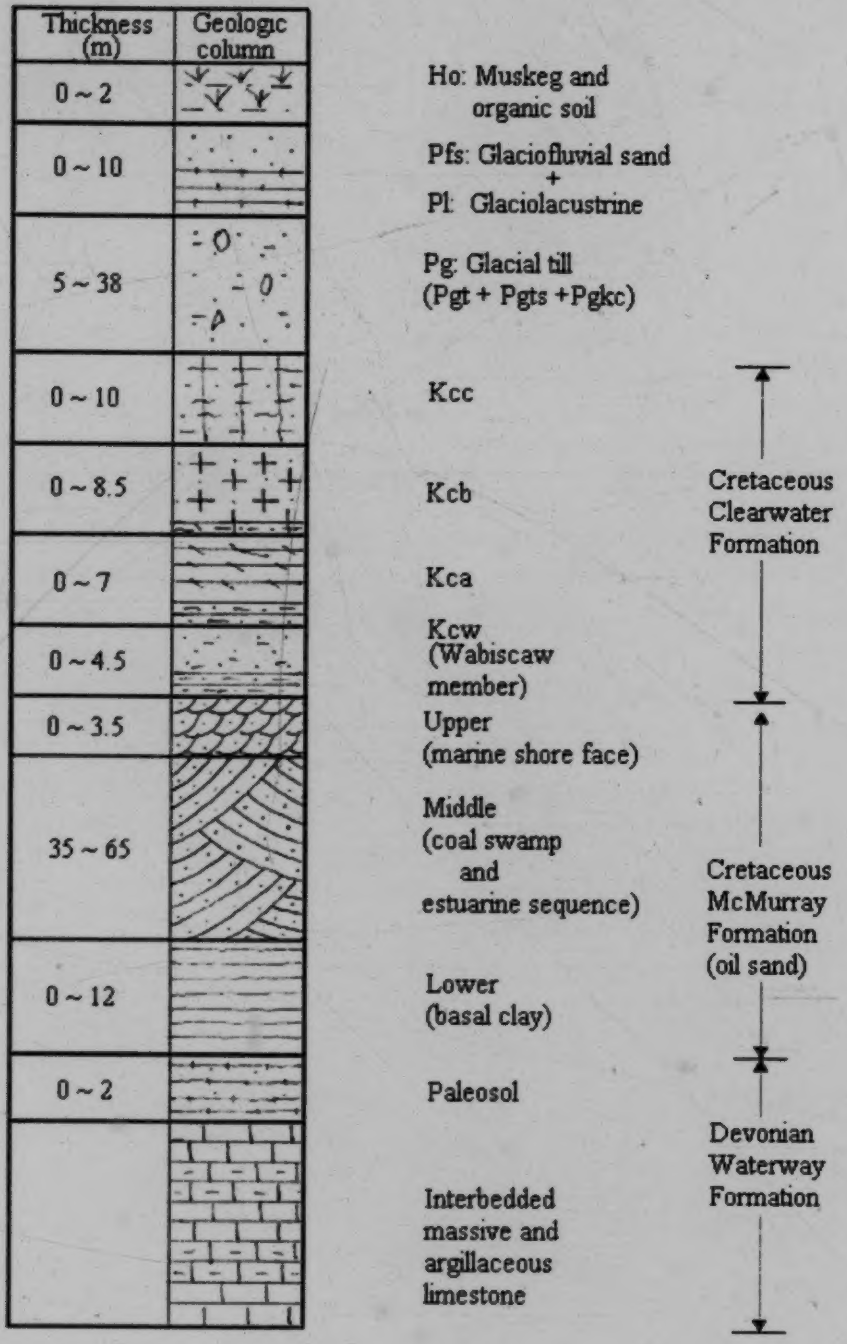
Thickness (m)
Geologic column
0 ~ 2
0 ~ 10
5 ~ 38
0 ~ 10
0 ~ 8.5
0 ~ 7
0 ~ 4.5
0 ~ 3.5
35 ~ 65
0 ~ 12
0 ~ 2
Ho: Muskeg and organic soil
Pfs: Glaciofluvial sand
+
Pl: Glaciolacustrine
Pg: Glacial till
(Pgt + Pgts +Pgkc)
Kcc
Kcb
Kca
Kcw
(Wabiscaw member)
Upper
(marine shore face)
Middle
(coal swamp and estuarine sequence)
Lower
(basal clay)
Paleosol
Interbedded massive and argillaceous limestone
Cretaceous Clearwater Formation
Cretaceous McMurray Formation (oil sand)
Devonian Waterway Formation

Figure 3.5 Stratigraphic sequence in the project's area (AGRA 1999, Carrigy 1966, Kosar 1992, and Dewar 1996)

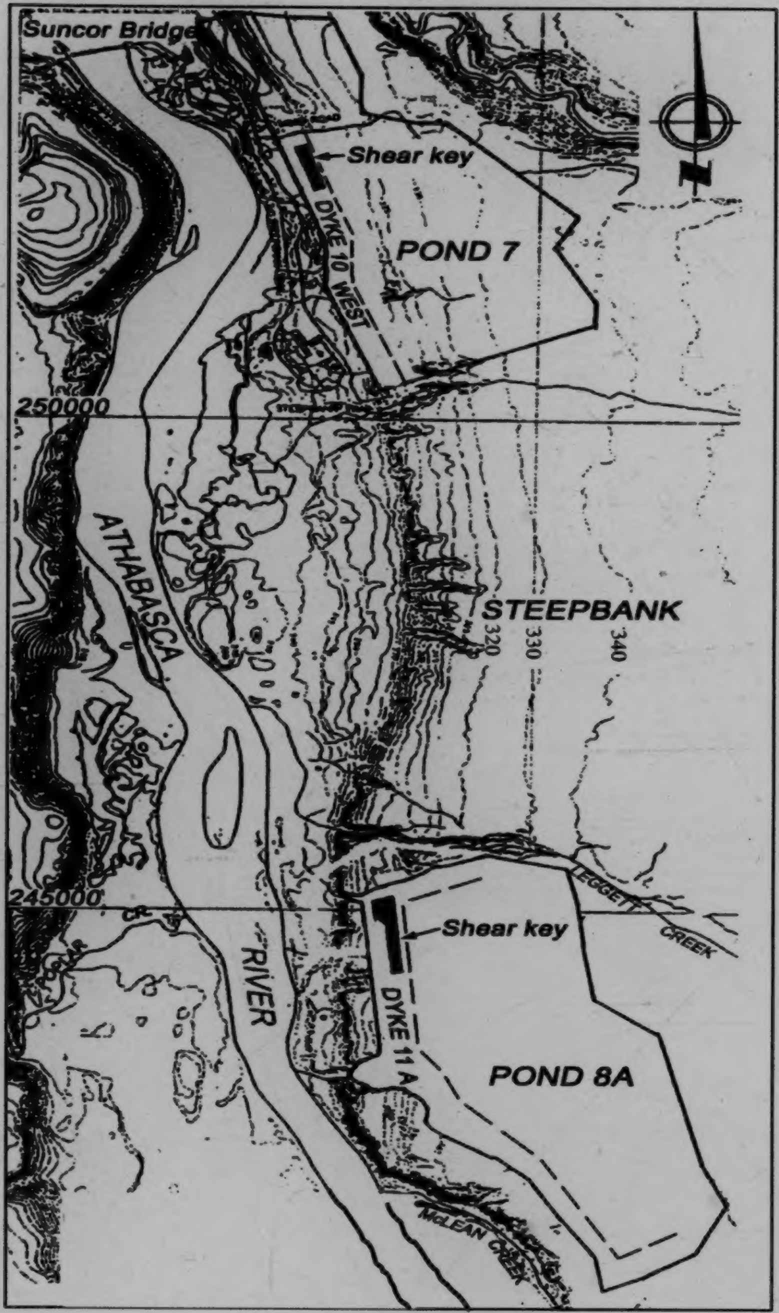
Suncor Bridge
Shear key
DYKE 10 WEST
POND 7
250000
ATHABASCA
STEEPBANK
320
330
340
RIVER
245000
LEGGETT CREEK
Shear key
DYKE 11A
POND 8A
McLEAN CREEK
N

Figure 3.6 Location of the shear keys (Scale 1:62500)

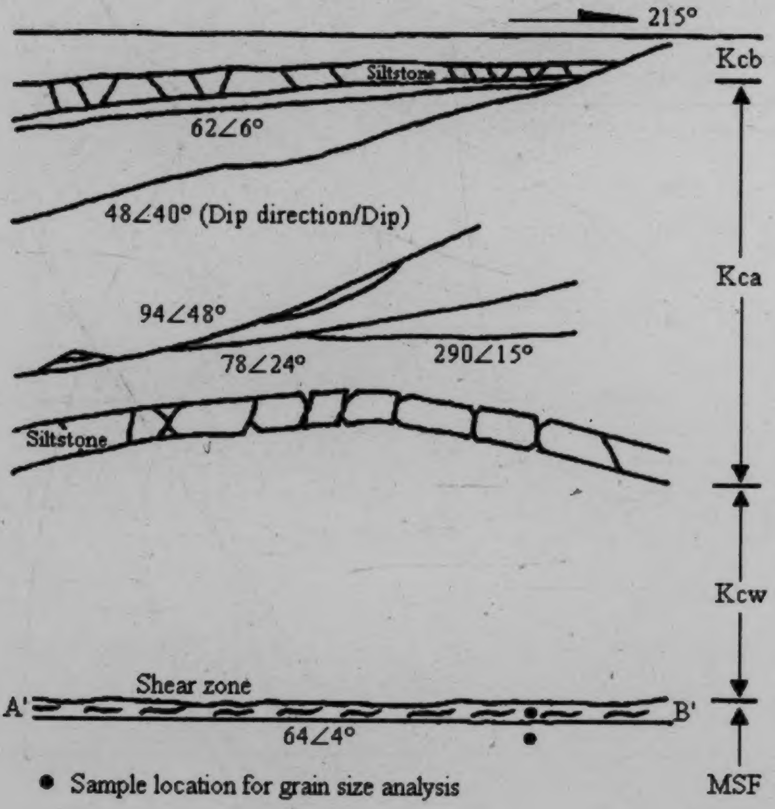
215°
Kcb
Siltstone
62∠6°
48∠40° (Dip direction/Dip)
Kca
94∠48°
78∠24°
290∠15°
Siltstone
Kcw
Shear zone
A'
B'
64∠4°
MSF
● Sample location for grain size analysis

Figure 3.7 Relationship between shear zone and adjacent rock (not to scale, but vertical about 4m)

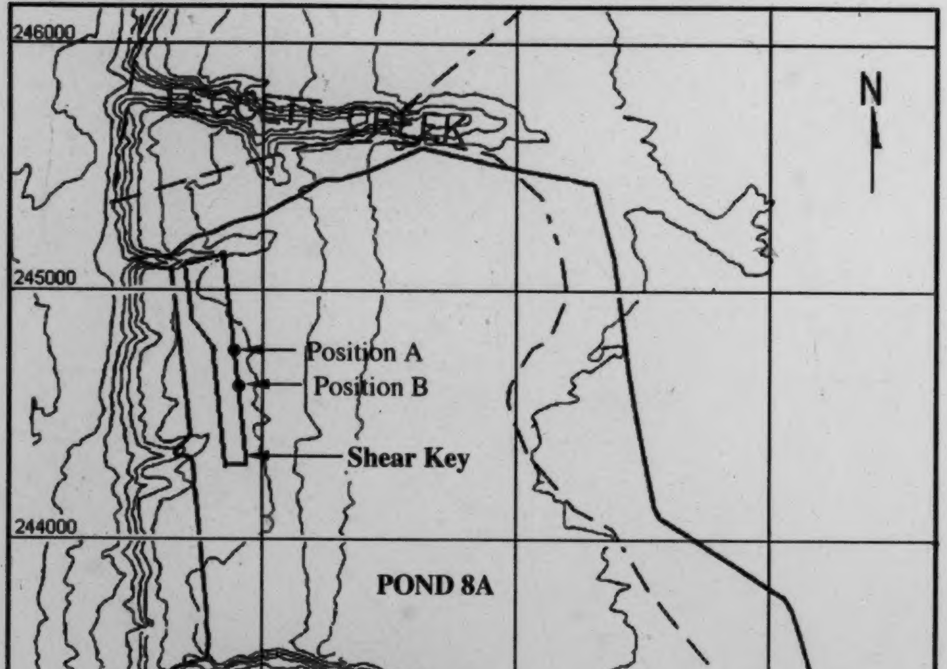
246000
245000
244000
243000
242000
241000
148000
149000
150000
151000
N
BECOTT CREEK
Position A
Position B
Shear Key
POND 8A
WOOD CREEK
MCLEAN CREEK

Figure 3.8 Mapping positions (A and B) at the shear key in dyke 11A of Pond 8A (scale 1:25000)

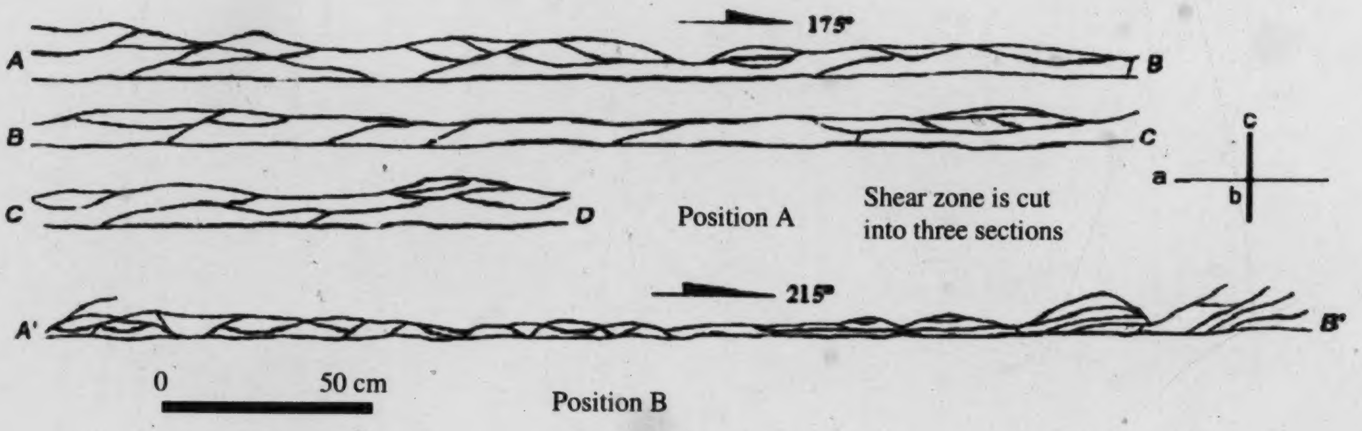
175°
A
B
B
C
C
D
Position A
Shear zone is cut
into three sections
c
a
b
215°
A'
B'
0
50 cm
Position B

Figure 3.9 Shear zone in the marine shore face silty clay at dyke 11A (direction of the sections is 175° and 215°, respectively. Position B is about 110 m south of position A)

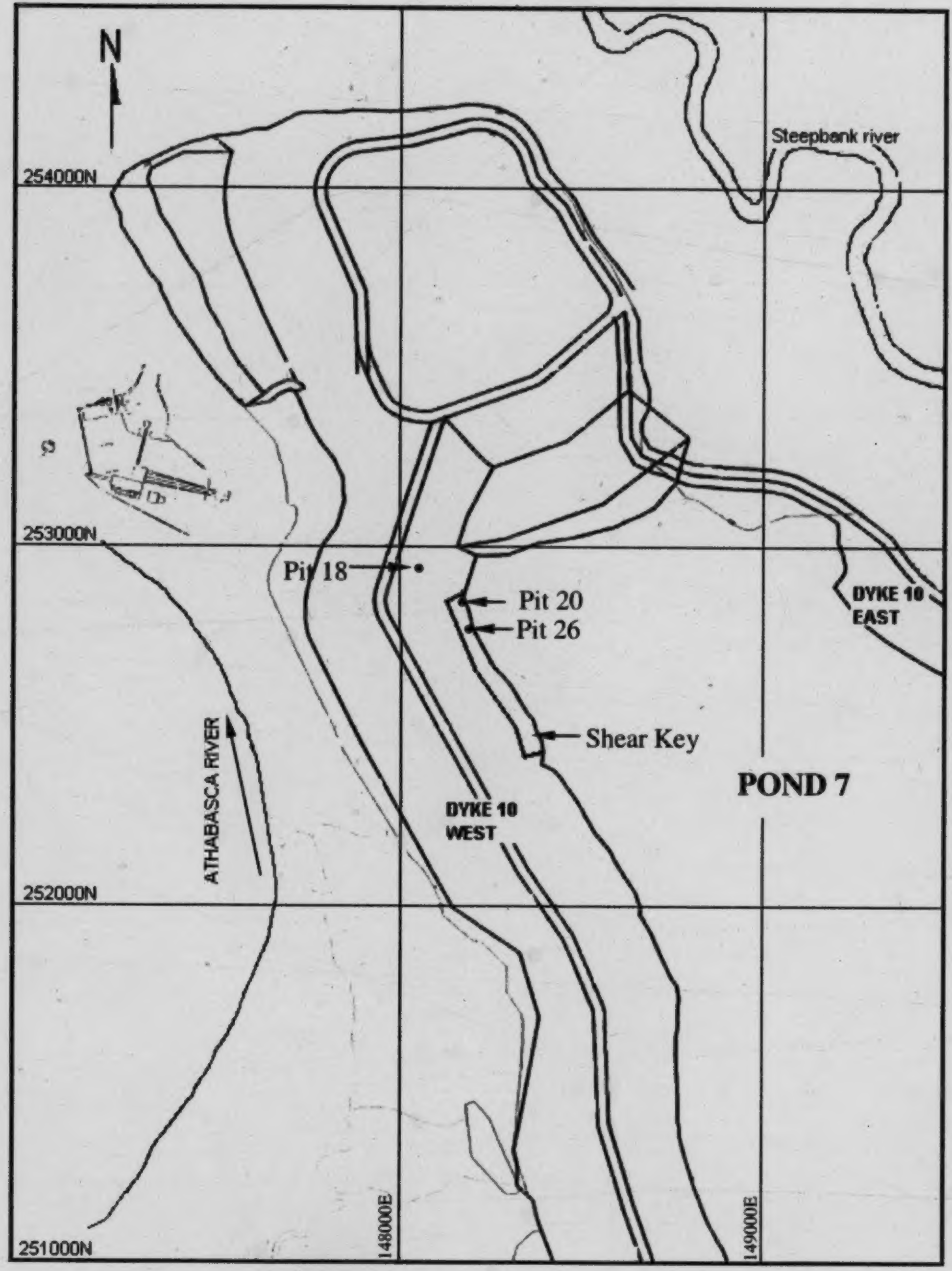
N
Steepbank river
254000N
253000N
252000N
251000N
148000E
149000E
Pit 18
Pit 20
Pit 26
Shear Key
POND 7
DYKE 10 EAST
DYKE 10 WEST
ATHABASCA RIVER

Figure 3.10 Mapping locations (Pits 18, 20, and 26) in dyke 10 west of Pond 7 (scale 1:17000)

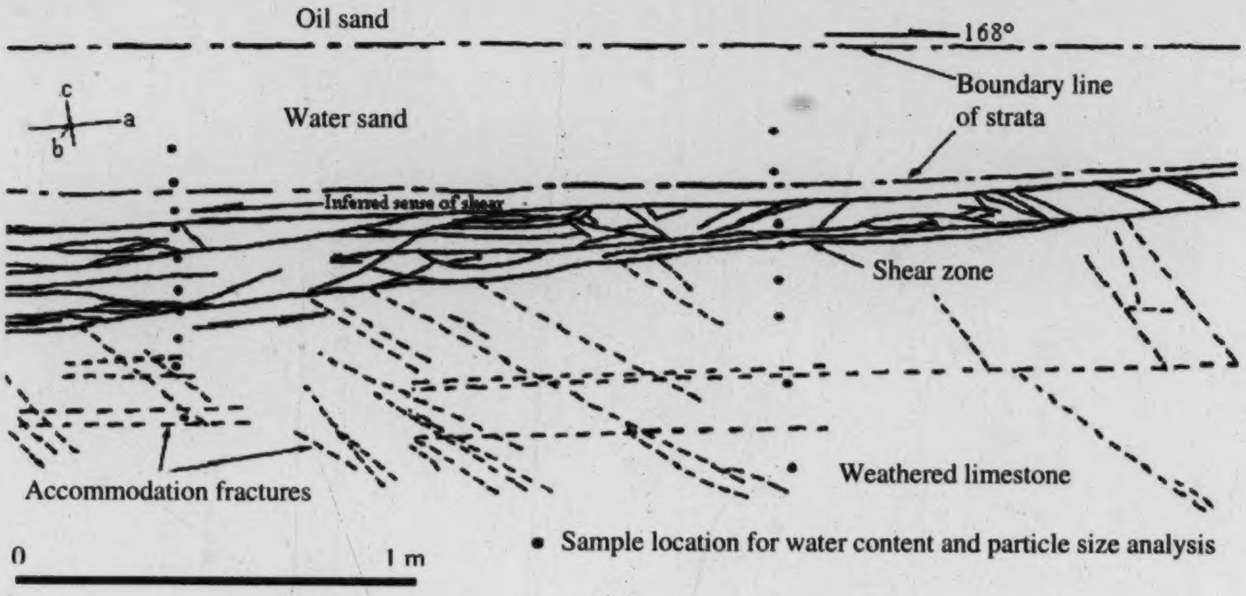
Oil sand
168°
Boundary line of strata
c
a
b
Water sand
Inferred sense of shear
Shear zone
Weathered limestone
Accommodation fractures
0
1 m
• Sample location for water content and particle size analysis

Figure 3.11 Shear zone in the weathered limestone at pit 18

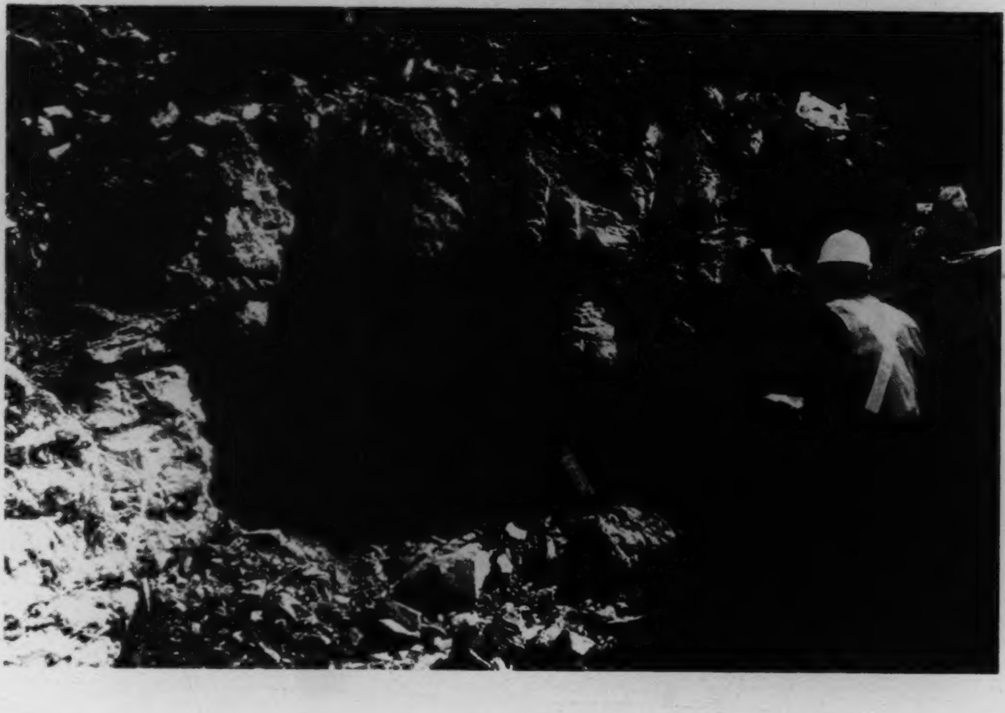

Figure 3.12 Photograph of the shear zone at pit 18

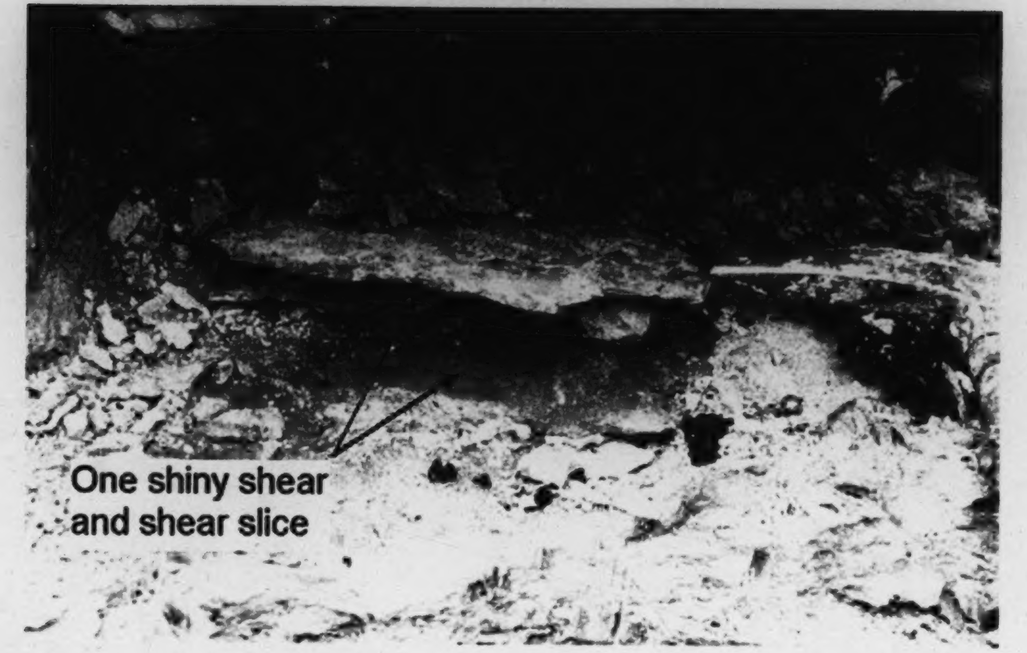
One shiny shear
and shear slice

Figure 3.13 Photograph of the shear zone at pit 26

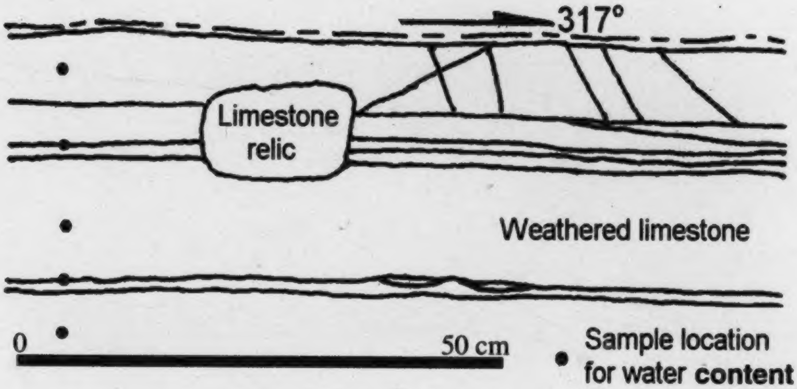
317°
Limestone relic
Weathered limestone
0
50 cm
Sample location for water content

Figure 3.14 Shear zone in the weathered limestone at pit 26

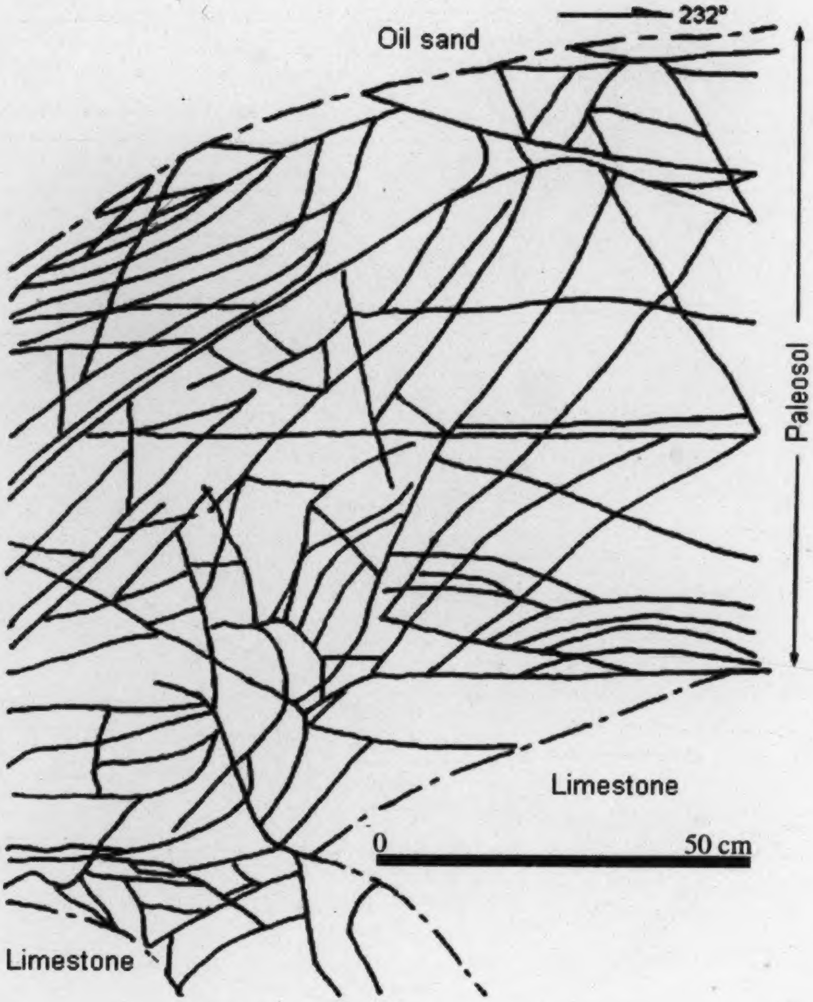
232°
Oil sand
Paleosol
Limestone
0
50 cm
Limestone

Figure 3.15 Shear zone in Paleosol mapped on south sidewall at pit 20 (lines are discontinuities)

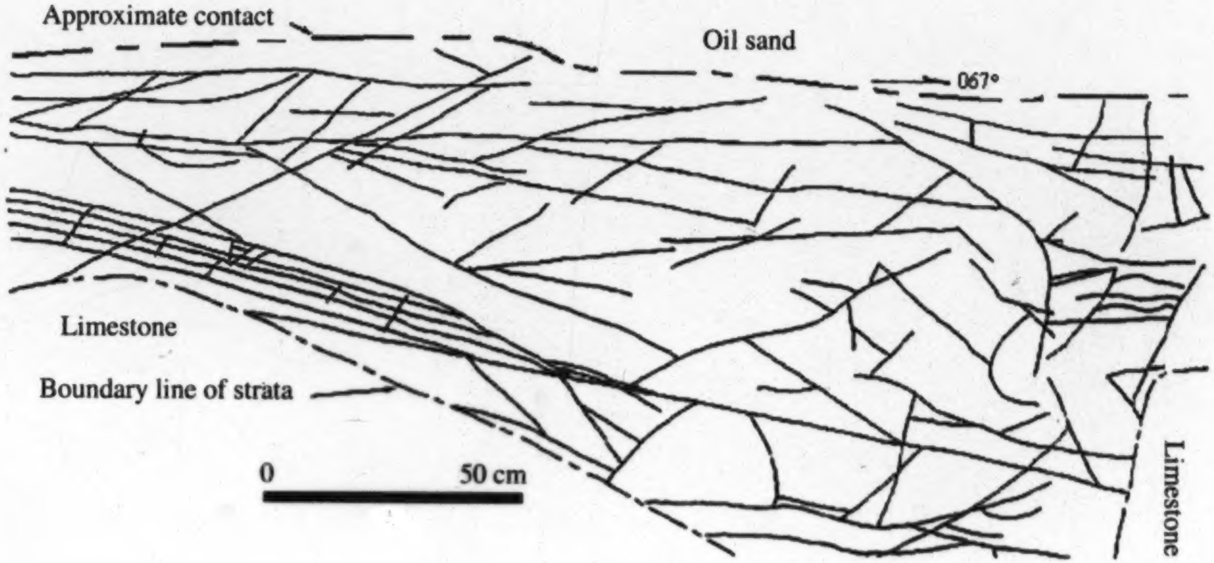
Approximate contact
Oil sand
067°
Limestone
Boundary line of strata
0
50 cm
Limestone

Figure 3.16 Shear zone in Paleosol mapped on north sidewall at pit 20 (direction of the section is 067°)

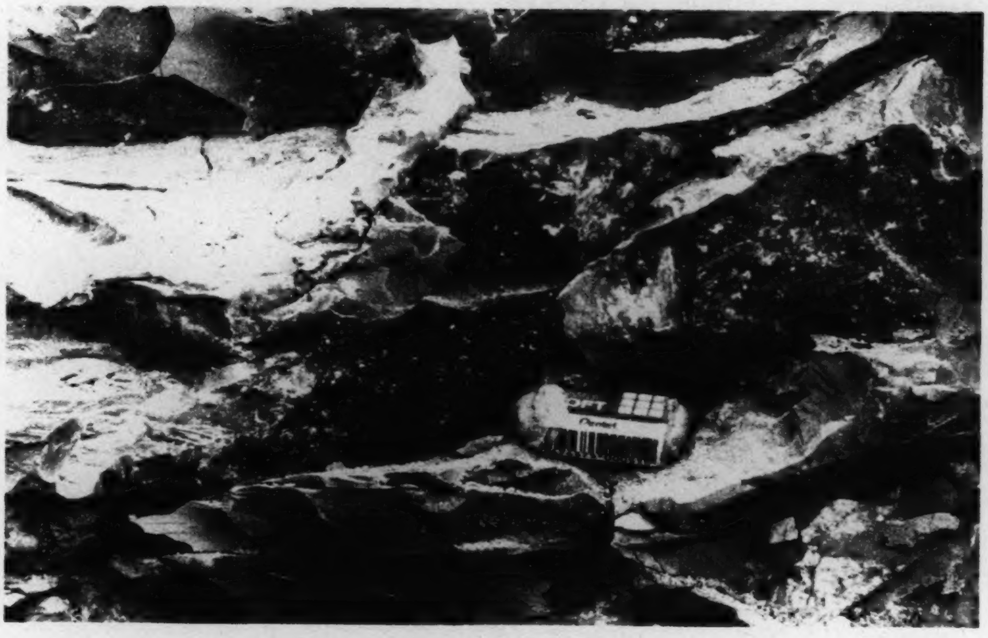

Figure 3.17 Photograph showing the shear lenses and minor shear occurrence (length of the eraser is about 3 cm)

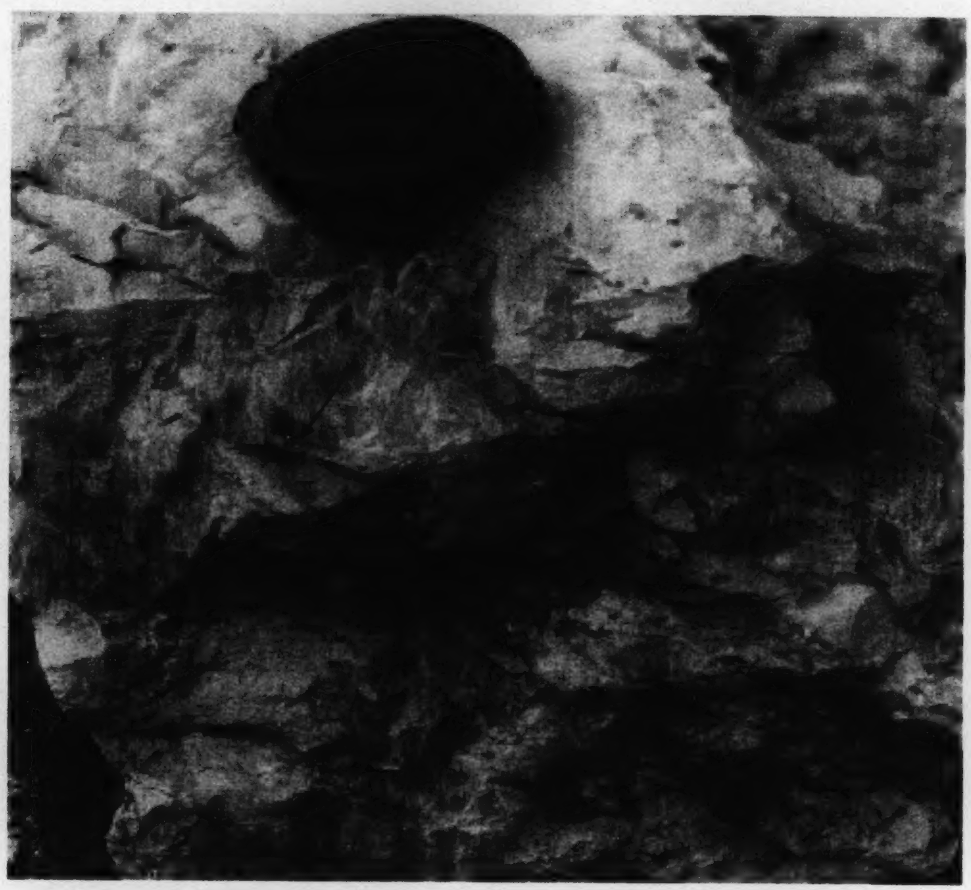

Figure 3.18 Photograph showing different directions of the striations (diameter of the camera lens cap is about 5cm)

(a)

(b)

Figure 3.19 Two photographs showing rough shear surface (a) and striation (arrow) (b) (diameter of Canadian one-dollar is about 2.6cm)

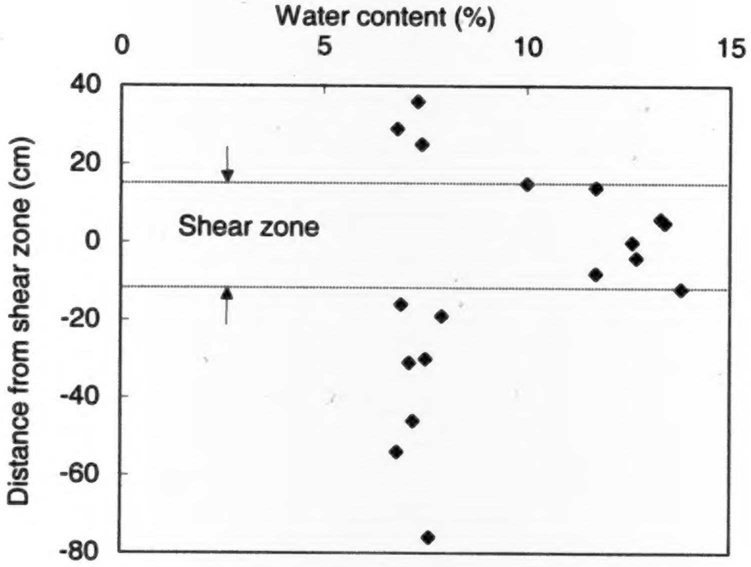

Figure 3.20 Water content profile across shear zone II at pit 18

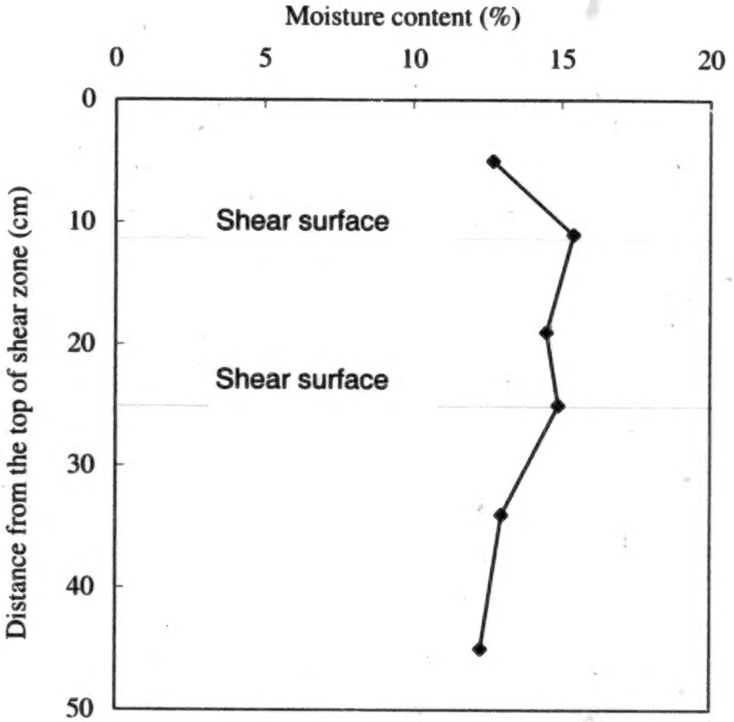

Figure 3.21 Water content profile across shear zone III at pit 26

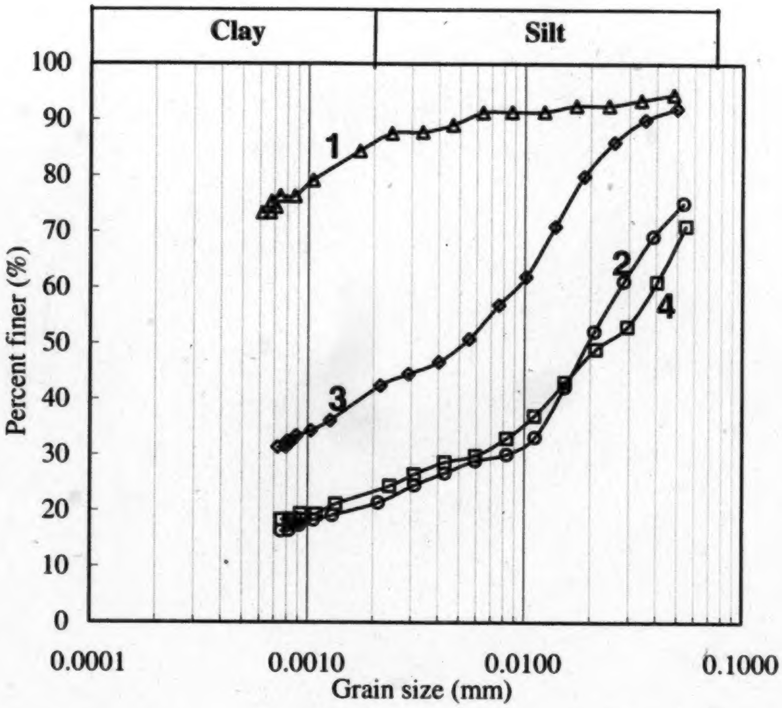

Figure 3.22 Grain size distribution (1 within shear zone, 2 out of shear zone at dyke 11A; 3 within shear zone, 4 out of shear zone at pit 18)

CHAPTER 4 MECHANICS OF SHEAR RESISTANCE OF SHEAR ZONES AND PARAMETRIC SENSITIVITY ANALYSIS

4.1 INTRODUCTION

The exact determination of a shear zone's shear strength is quite difficult because of the zone's complex fractures and the amount of deformation that has occurred. A shear zone's strength could be expressed in terms of cohesion and friction. Generally, a shear zone in the field well developed is assumed to have no cohesion because of the existence of a discrete slip surface and a friction angle that may be 1° to 3° higher than the residual friction angle, depending on the amount of deformation that has occurred. In this chapter, the Edgerton landslide is used to investigate the effect of a minor change in the residual shear strength on a slope's stability and the associated deformations. The analyses show that a minor change in the friction angle has a great influence on a slope's stability and movement. The pore-water pressure in a shear zone is also important, so the influence of a minor change in the pore pressure on a slope's stability and the associated deformations is also examined in this chapter.

4.2 SHEAR-RESISTANCE CHARACTERISTICS OF SHEAR ZONES

The shear resistance of soils and rocks is made up basically of cohesion, structural resistance, and frictional resistance. Cohesion arises from intermolecular attractive forces (bonds—primary valence bonds and chemical bonds or cementation). Structural resistance is due to the interlocking of the soil particles, and frictional resistance depends on the nature of the material itself and the magnitude of the effective normal stress on a potential shear plane in the material. If a material is loaded, it deforms until rupture failure takes place—manifesting itself in the ruptured surface of a shear (Aydan et al., 1993). In this case, the cohesion and structural resistance will be lost along this surface and frictional resistance will reduce from its peak to its residual strength. A shear zone has no cohesion and structural resistance on the principal slip surface (the D shear), which is the weakest place in a shear zone. If an engineered structure is founded on or located in such a shear zone, the frictional resistance is the only source of zone's shear strength when shearing occurs along such a principal slip surface. Generally, a shear zone's shear strength is in its post-peak state and depends on the displacement that has occurred. If potential shearing develops along the main slip plane (the D shear), a flattened principal slip surface in which the particles have attained their maximum degree of orientation must possess the minimum possible shear resistance, or residual strength (Skempton, 1985). Its magnitude depends on the effective normal pressure ($\sigma_T - u$) and the amount and the nature of the clay minerals present (Skempton, 1964; Kenney, 1967). If the slip surface is not too flat and has some asperities, or the particles are not fully oriented, this surface's shear strength may have a minor peak (see Figure 2.10). Therefore, a shear zone's shear strength depends on the nature of the clay minerals and the amount of displacement that has occurred along the slip plane.

4.3 EFFECT OF RESIDUAL STRENGTH AND PORE PRESSURE ON SLOPE STABILITY AND MOVEMENT

4.3.1 Effect of Residual Strength on Slope Stability

Skempton (1964) showed that soil's shear strength was a function of shear displacement. In some cases, the friction angle of slip surface is only 1-3° different from the residual value or just at the residual value depending on the displacement that has occurred in the shear zone. Sometimes, even when the strength is at its residual value, we often cannot obtain its exact value due to the sampling disturbance, test errors, other random factors (El-Ramly, 2001), and the selection of the test method (Dounias and Potts, 1993). Therefore, a 1° to 2° or 3° shift from the *in situ* value of the friction angle selected for evaluating a project can occur. In order to explain the impact of this minor change in a shear zone's friction angle on a project founded on or located in a shear zone, the case history of the Edgerton landslide will be examined.

The Edgerton landslide, which occurred about 48km northeast of Wainwright, Alberta, is typical of natural slope instability in the soft bedrock deposits of the central places of North America. Tweedie (1976) and Thomson and Tweedie (1978) delineated this landslide's features and geological condition and carried out stability analyses. Figure 4.1 presents a cross-section of the slide and the interpreted failure surface and Table 4.1 lists the characteristic soil properties used in their stability analysis. Slope/W (version 5.0) was used to evaluate the sensitivity of the slope stability by varying the friction angle 7, 8, 9 and 10° with cohesion $c' = 0$. A residual friction angle of 8° was chosen as the "nominal" residual friction angle. In the probabilistic analysis, 1° and 2° standard deviation (SD) were used.

Figures 4.2 typically show the deterministic result with friction angle of 8 degrees. Figure 4.3 presents the relationship between the factor of safety and the friction angle. The linear relationship is because the total resistance against sliding is derived along the basal slip plane on which there is no cohesion and the friction angle is small. The factor of safety will change by 8.43% when the friction angle changes by 1°. Figures 4.4 and 4.5 show the landslide's failure probability at a friction angle of 8° with 1°or 2° of standard deviation. Figure 4.6 summarizes the results of using the probabilistic method to determine the relationship between the failure probability and the friction angle. Figure 4.6 also shows that the landslide's failure probability decreases linearly with an increase in the friction angle. The failure probability of the Edgerton landslide will decrease by about 28% for 1° of standard deviation and 18% for 2° of standard deviation when the friction angle increases by 1°. Therefore, the above analyses show that a minor change in the residual friction angle has a significant impact on the stability of a slope that might potentially fail.

4.3.2 Effect of Residual Strength on Slope Movement

The Edgerton landslide was also used for this analysis, but some simplifications were made to facilitate the calculations. The analysis was carried out by using the FLAC 4.0 (Fast Lagrangian Analysis of Continua) (Itasca 2000) code with the Mohr-Coulomb model and the parameters from Table 4.1. The friction angles of the failure surface that were used in the stability analyses were used in this analysis. The FLAC analysis formulation is presented in Appendix B. The results are presented in Figure 4.7, which shows that when the friction angle equals 8° (the residual value), the landslide has a large movement because the landslide is unstable in this case. When the friction angle is even 1° larger than the residual value, the landslide's movement is greatly reduced. However, when the friction angle is 1° less than the residual value, the landslide's movement is much greater, so a minor change in the residual strength has a large influence on the slide's movement. Analysis of a rock slope by Corkum and Martin (2002) revealed a similar mechanism (Figure 4.8). The above analyses also mean that friction angle even only 1° larger than the real friction angle of a potential sliding shear zone will not only influence the stability evaluation of a project either founded on or located in a shear zone, but also will cause a much smaller predicted displacement than would have occurred otherwise.

4.3.3 Effect of Pore Pressure on Slope Stability and Movement

Pore pressure has a very significant influence on the stability of the earth structure (Bishop and Morgenstern, 1960). Figure 4.9 shows the linear relationship between the factor of safety, F, and the pore pressure ratio, r_u. Iverson (1991) evaluated the sensitivity of slope-stability analysis to groundwater data for an infinite slope and found that in some cases, the effects of groundwater on slope stability are particularly important and can even exceed those of friction. The analysis of the Edgerton landslide by using Slope/W revealed a linear relationship between the factor of safety and the phreatic surface (pore pressure) (see Figure 4.10). The analysis of the Edgerton landslide by using FLAC 4.0 showed that the slope movement is greatly influenced by the phreatic surface's position (see Figure 4.11). The movement is much greater when the position of the phreatic surface is higher than that of the *in situ* one (i.e. higher pore pressure). In both Figures 4.10 and 4.11, the 0 meter refers to the *in situ* phreatic surface; the positive value means that the supposed phreatic surface is higher than *in situ* one; the negative value means that the supposed phreatic surface is lower than *in situ* one.

Figures 4.10 and 4.11 indicate that the factor of safety has a linear relationship with the pore pressure, but that the movement of a landslide whose FOS = 1 will increase greatly with an increase in pore pressure. This finding means that pore pressure has a very significant influence on the stability and performance of a potential slope failure.

Kawabe (1991) carried out an experiment on the artificial occurrence of a landslide on a natural slope to investigate the influence of pore-water pressure on a landslide's land deformation and established the relationship between the strain rate and the pore-water pressure as

$$\ln \dot{\gamma} = 0.581 \cdot u - 19.8 \qquad [4.1]$$

Figures 4.12 and 4.13 show the measured data for the pore-water pressure and the ground deformation and the relationship between the pore-water pressure and the strain rate.

After carrying out field experiments on the Salledes landslide, Faure et al. (1991) reported on the relation between pore pressures and displacements. They found that a slide is triggered suddenly when the pore pressure exceeds a specific level. If the pore pressure on the sliding surface is less than 35 kPa, no displacement occurs. Between 35 and 50 kPa, displacement rates are small, and over 50 kPa, the displacement becomes quite significant (see Figure 4.14).

The results from both Kawabe's and Faure's studies also showed that pore-water pressure has a very significant influence on a landslide's movement.

4.4 CONCLUSIONS

The shear-resistance characteristics of shear zones are delineated based on these zones' internal fractures and geometries. The influence of a minor change in the residual friction angle and the pore pressure on the stability and movement of a slope founded on or located in a shear zone has been analyzed by using data from the well-defined Edgerton landslide. The following conclusions are drawn from this study:

- In a shear zone, no cohesion and structural resistance are present on the principal slip surface (the D shear), and the frictional resistance is the only source of a shear zone's shear strength when shearing occurs along this surface. A shear zone's shear strength is at its post-peak state and depends on the displacement that has occurred.
- The factor of safety and the failure probability along a shear zone or slip surface are linearly related to the friction angle. Based on the Edgerton landslide, the factor of safety increases 8.43% when the friction angle increases by 1°, while the failure probability will reduce by about 28% for 1° of standard deviation and 18% for 2° of standard deviation when the friction angle increase by 1°.
- A minor change in the residual strength in a slip surface has a large influence on a slide's movement.
- Pore pressure has a very significant influence on the stability and performance of a slope that might potentially fail. The factor of safety has a linear relationship with pore pressure, while the movement of a landslide will increase exponentially with an increase in pore pressure.

The analyses above show that for soil structures founded on or located in a shear zone, a minor change in the residual strength and the pore pressure on the potential slip surface have a very significant influence on the stability and performance of such structures. Therefore, obtaining or predicting the exact pore pressure and shear strength parameter is necessary for evaluating a shear zone's role in a geotechnical project.

Table 4.1 Summary of soil properties used in stability analysis (Thomson & Tweedie 1978)

Material	Wet density (kN/m^3)	Saturated density (kN/m^3)	Measured strength parameters				Parameters used in stability analysis	
			Peak		Residual			
			C'(kPa)	ϕ' (deg)	C'(kPa)	ϕ' (deg)	C'(kPa)	ϕ' (deg)
Till	18.83	20.40	600	24			0	24
Brown weathered silty clayshale	17.55	18.83	70	23	0	10	0	23
Stiff grey silty clayshale	19.81	19.81	160	41	0	19	0	23
Bentonitic clayshale (failure surface)	21.97	21.97			0	8	0	8

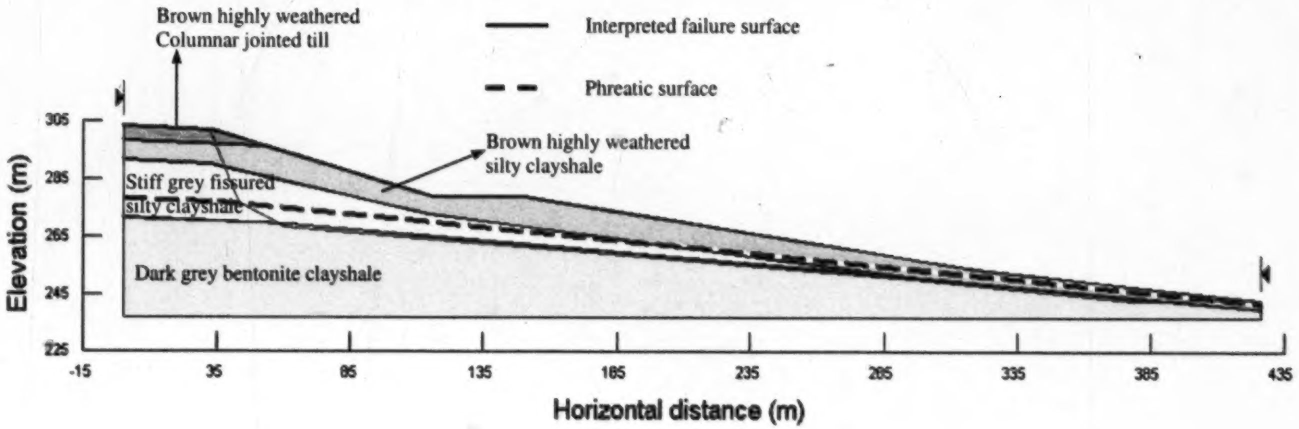
Brown highly weathered
Columnar jointed till
Interpreted failure surface
Phreatic surface
Brown highly weathered
silty clayshale
Stiff grey fissured
silty clayshale
Dark grey bentonite clayshale
Elevation (m)
305
285
265
245
225
-15
35
85
135
185
235
285
335
385
435
Horizontal distance (m)

Figure 4.1 Section of the Edgerton landslide with stratigraphic layers and interpreted failure surface

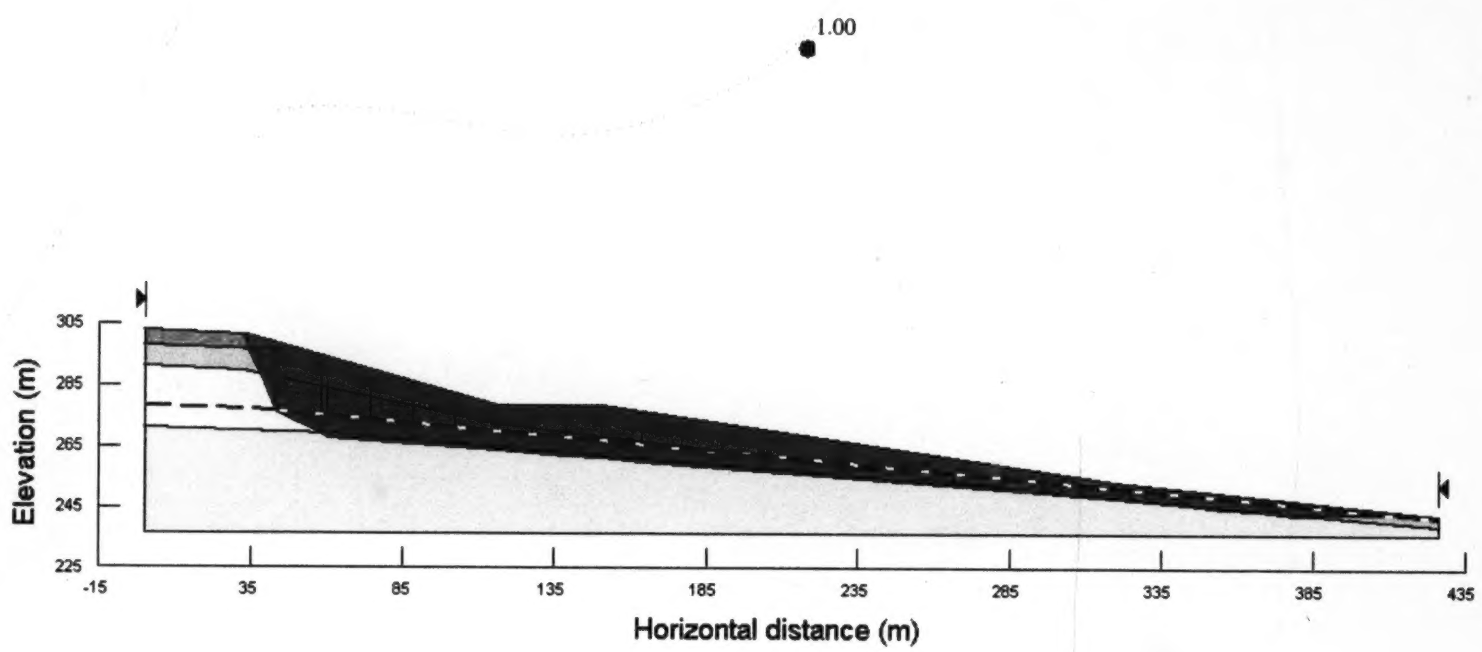

Figure 4.2 Factor of safety in the nominal friction angle of 8°

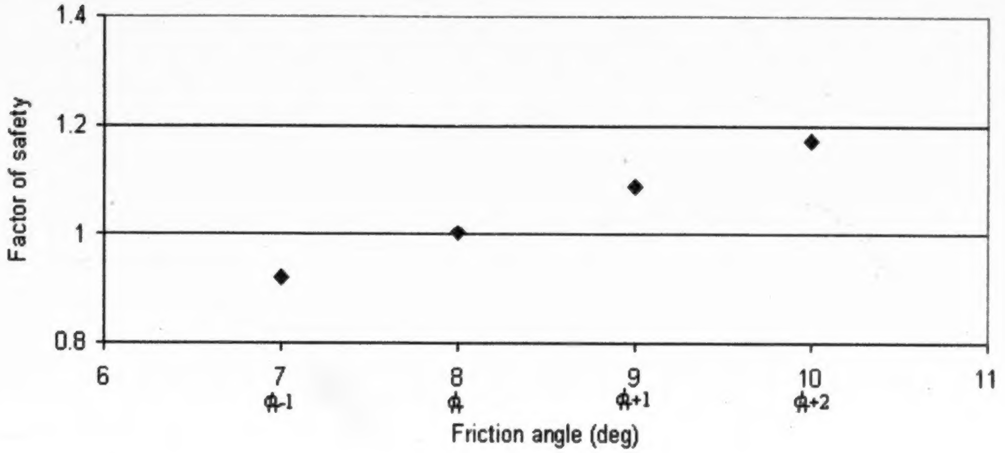

Figure 4.3 Relationship between factor of safety and friction angle

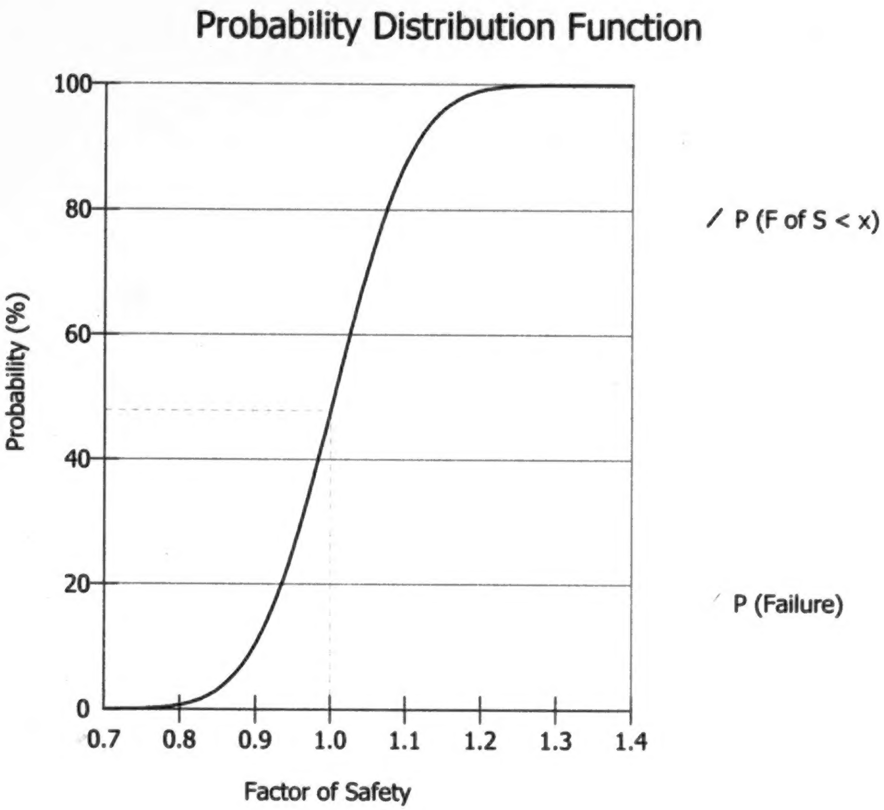

Figure 4.4 Failure probability in the nominal residual friction angle of 8° with 1° of standard deviation

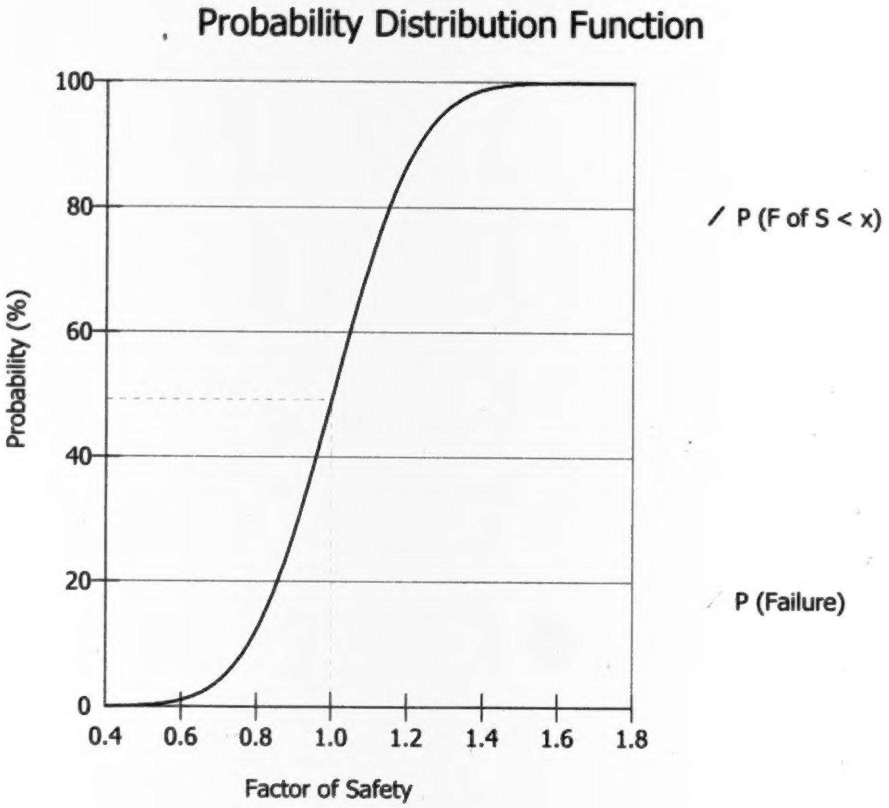

Figure 4.5 Failure probability in the nominal residual friction angle of 8° with 2° of standard deviation

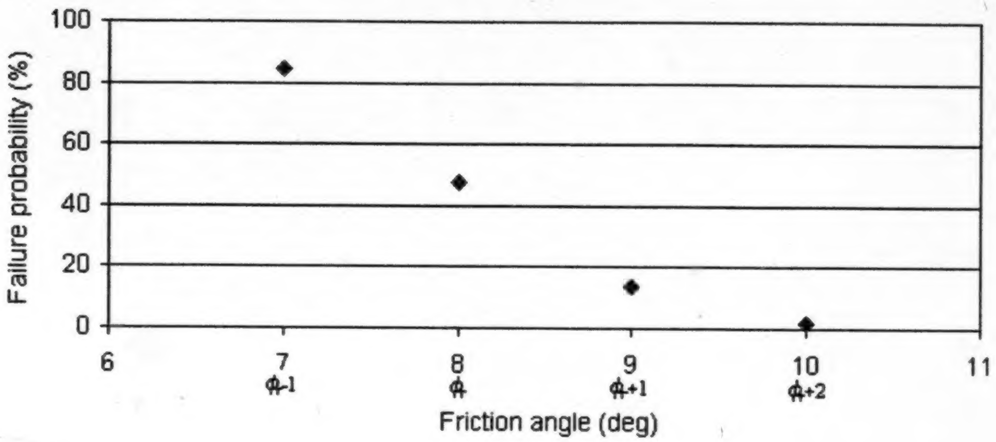

(a)

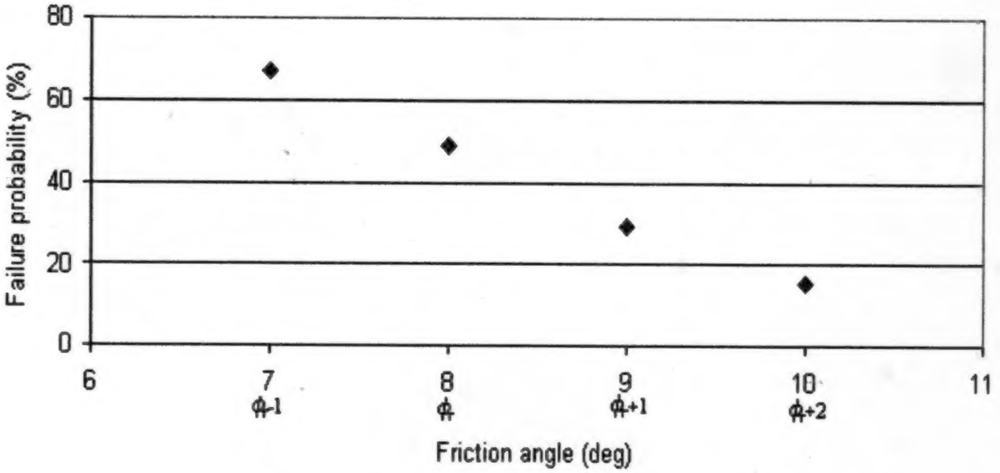

(b)

Figure 4.6 Relationship between failure probability and friction angle in SD = 1° (a) and SD = 2° (b)

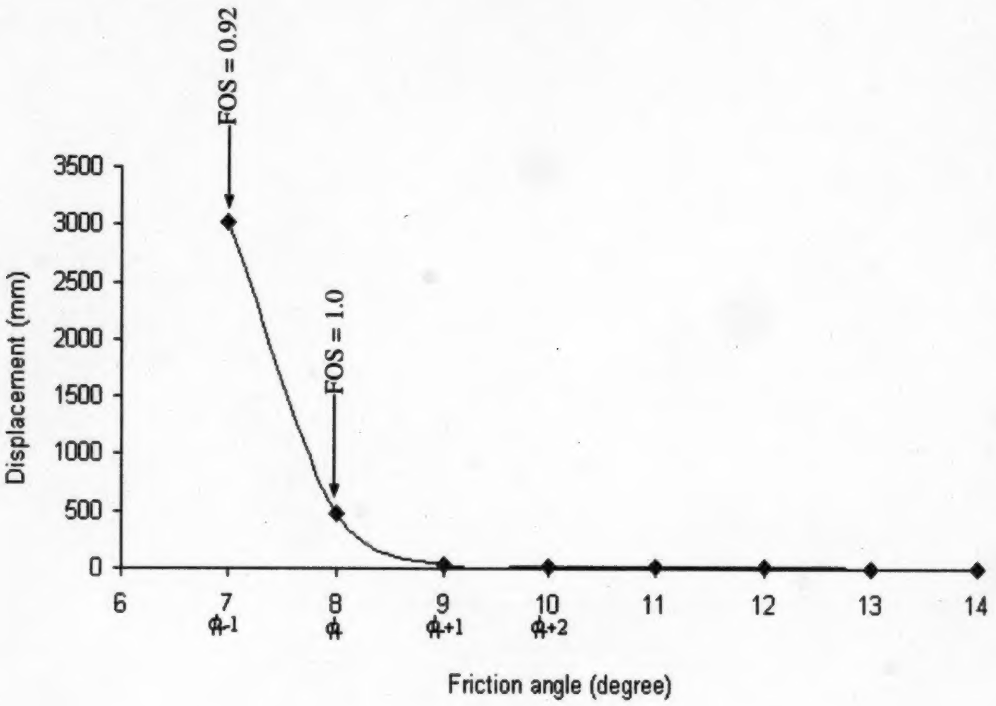

Figure 4.7 Relationship between movement of the landslide and friction angle of potential failure surface

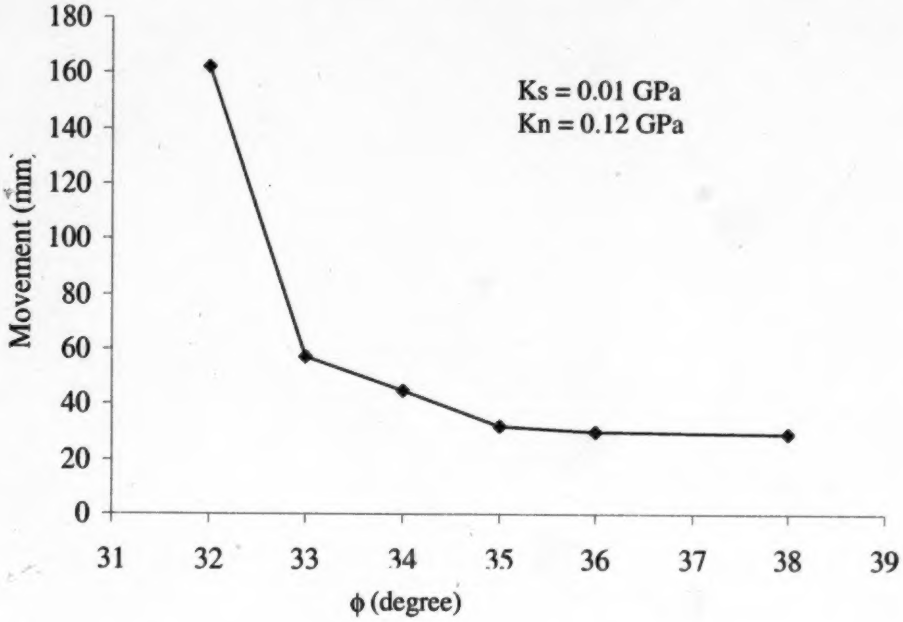

Figure 4.8 Relationship between movement and friction angle for a large rockslide (after Corkum and Martin, 2002) (Ks is the shear stiffness of the slip plane and Kn is the normal stiffness of the slip plane)

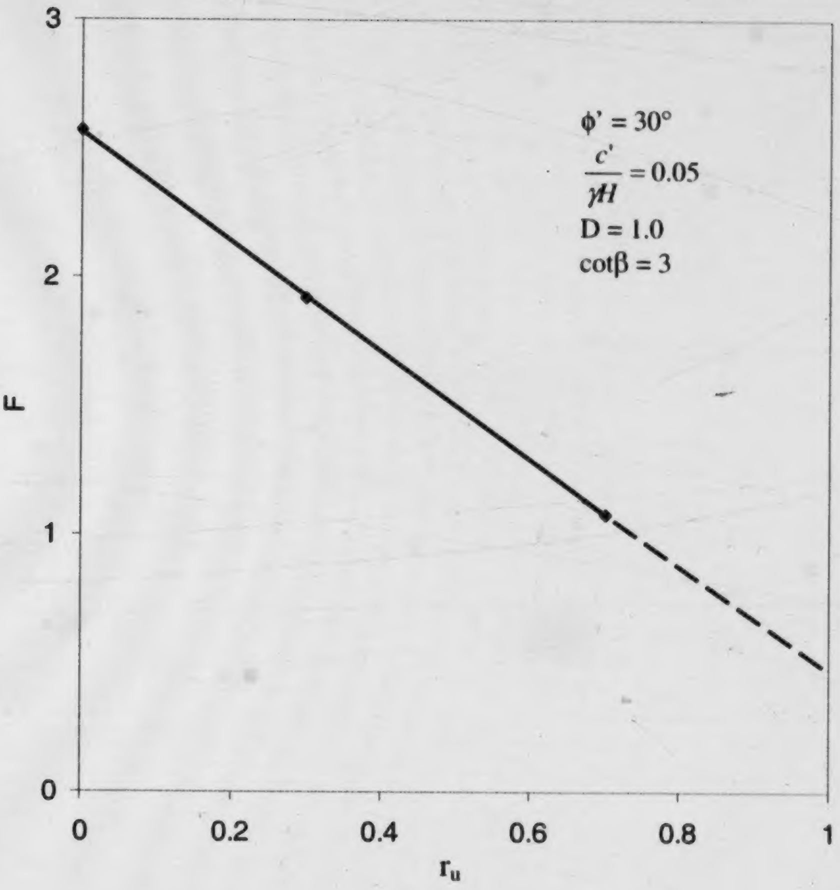

Figure 4.9 Linear relationship between factor of safety, F, and pore pressure ratio, r_u (after Bishop and Morgenstern, 1960)

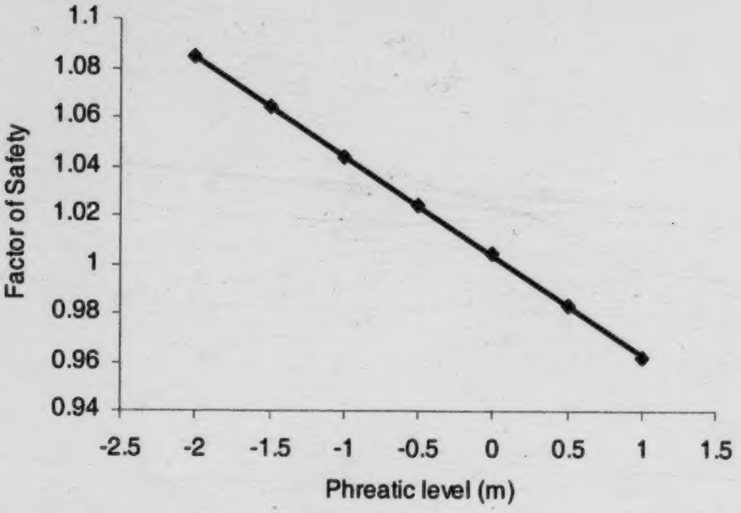

Figure 4.10 Linear relationship between factor of safety and positions of the phreatic surface level (0 meter refers to the *in situ* phreatic level)

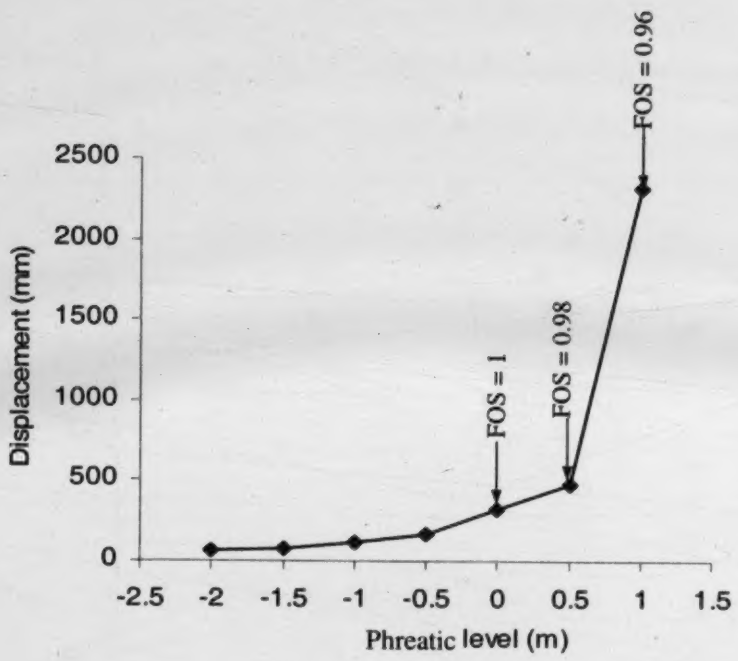

Figure 4.11 Relationship between the slide's movement and the phreatic surface level (0 meter refers to the *in situ* phreatic level)

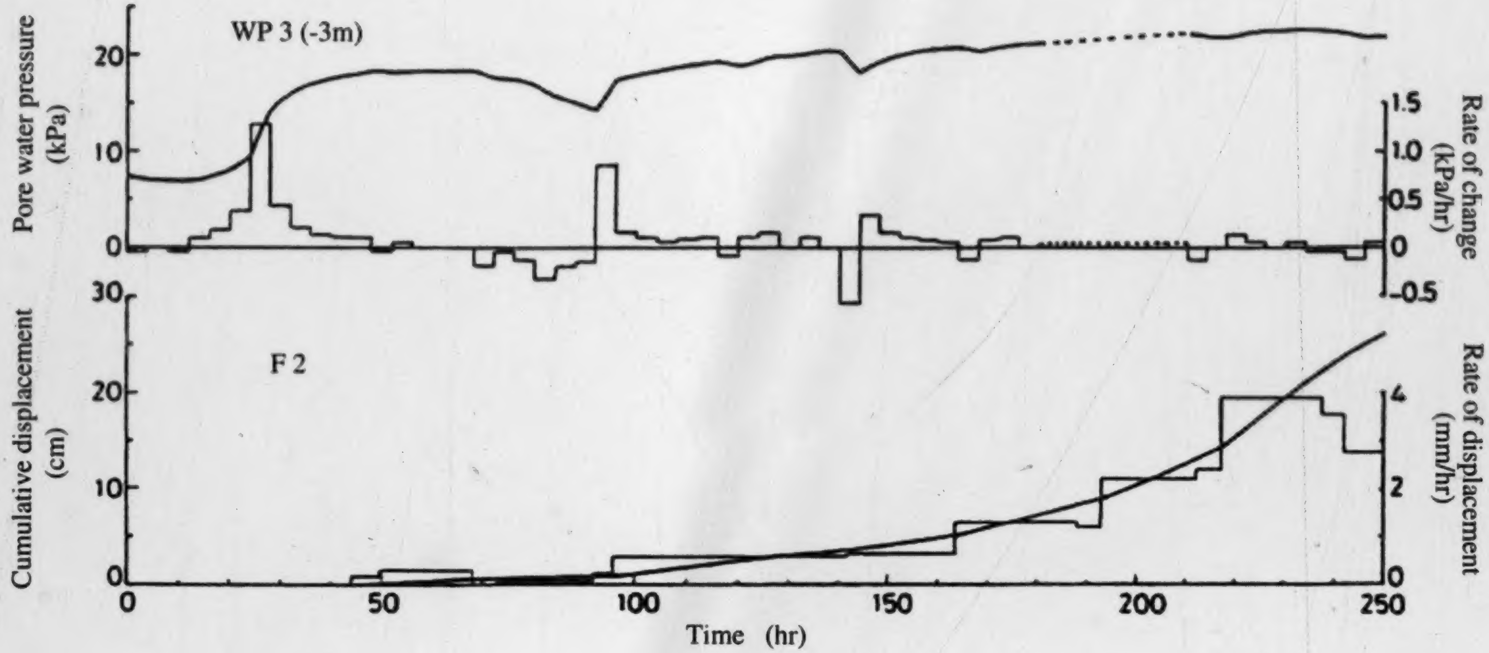

Figure 4.12 Change in pore water pressure and displacement with time (after Kawabe, 1991)

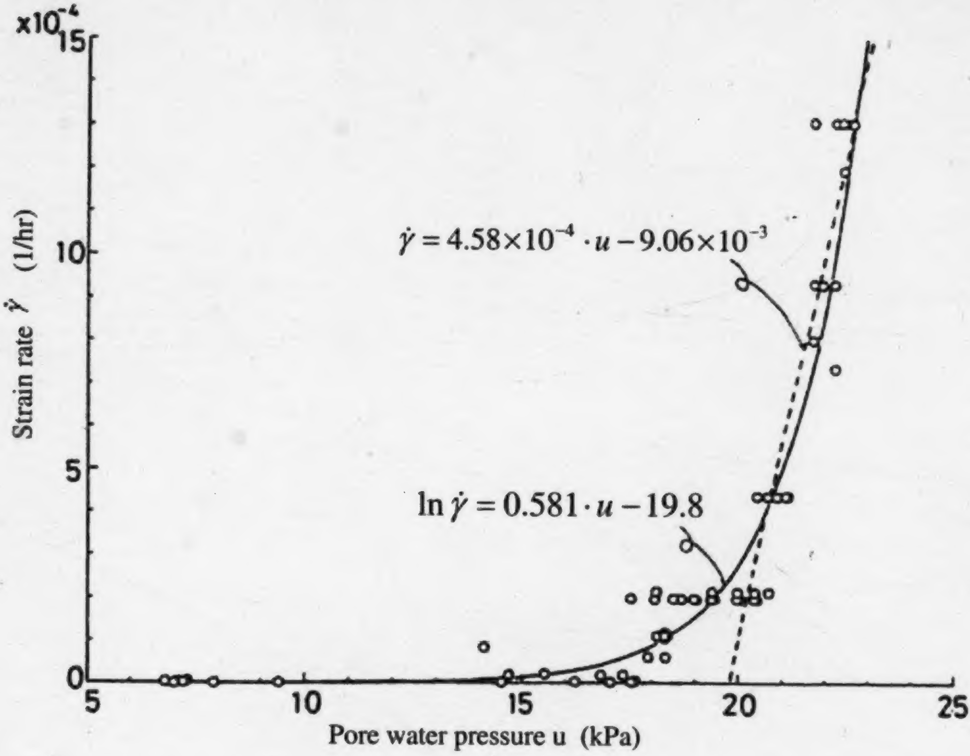

Figure 4.13 Relationship between the strain rate and the pore-water pressure (after Kawabe, 1991)

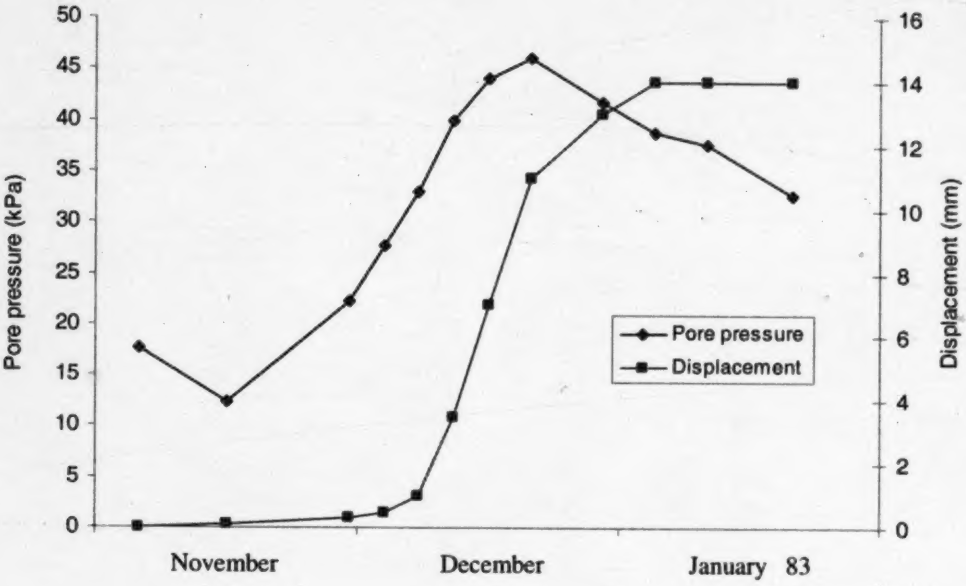

Figure 14 Pore pressure and displacements versus time (modified from Faure et al., 1991)

CHAPTER 5 DEVELOPMENT OF TEST EQUIPMENT

5.1 INTRODUCTION

The triaxial test is probably the most common and versatile experiment used in the laboratory for determinating stress-strain properties. The main advantages of the triaxial test include the control of drainage conditions and the measurement of pore pressure, the ability to perform both stress-controlled and strain-controlled tests, and the different stress paths that can be followed.

The type of triaxial test most commonly used in research and in routine testing is the cylindrical compression test. Generally, tests are classified into three types according to the conditions of drainage during the application of all-round pressure and the deviator stress (Bishop and Henkel, 1962):

1. Undrained test. No drainage, and hence no dissipation of pore pressure, is permitted during the application of both the all-round stress and the deviator stress.
2. Consolidated-undrained tests. Drainage is permitted during the application of the all-round stress, and the sample is fully consolidated under this pressure. No drainage is allowed during the application of the deviator stress and pore pressure can be measured.
3. Drained tests. Drainage is permitted throughout the test, so that full consolidation occurs under the all-round stress, and no pore pressure is set up during the application of the deviator stress.

One of this study's main objectives was to measure the pore pressure on a shear zone/plane under different displacement rates, so the consolidated-undrained test was chosen to perform this study. In the conventional consolidated-undrained triaxial test, pore pressure is generally measured at the base of the specimen. For tests on low permeability material, depending on the shearing rate and end platens, the pore pressure in the specimen may be non-uniform. The pore pressure on the shear zone/plane may not be same as that on the base where the measurement is made. In this case, the pore-pressure measurement should be carried out right on the plane. When shearing is along a pre-existing shear plane in a large sample, an internal LVDT (Linear Variable Displacement Transducer) is used to measure the relatively large shear displacement, which requires a large cell. In addition, testing on the undisturbed sample requires larger consolidation pressure that equals to the *in situ* overburden pressure. In this case, the conventional triaxial cell may not satisfy the requirements. A more suitable triaxial apparatus is needed in which the pore pressure along a pre-existing shear plane can be measured, a large specimen may be used, and the high consolidation pressure can be applied.

A new triaxial testing system with the capabilities to continuously measure the pore pressure on a shear plane under different loading rates, to use large specimens, and to apply large consolidation pressure was developed for this study. The laboratory facility included the following major components:

- Triaxial compression cell and axial loading system
- Triaxial pressure panel system
- Pore-pressure measurement system
- Displacement measurement system
- Data-acquisition system.

This chapter describes the design of thus new test equipment.

5.2 TRIAXIAL COMPRESSION CELL AND AXIAL LOADING SYSTEM

5.2.1 Triaxial Compression Cell

The triaxial cell was designed to test samples 100mm in diameter by 200mm high. Through the use of the different optional specimen caps, specimens ranging in size from

50mm to as large as 200mm in diameter can easily be tested. The cell was constructed from precision-machined extruded aluminum alloy material with four components: (i) cell body and top, (ii) cell base (pedestal); (iii) loading piston, and (iv) loading caps. The back pressure, the confining pressure drainage ports, and the basal pore-pressure measurement port access the interior of the triaxial cell through pressure-sealed fittings in the cell base and the no-volume change valves. The wires of the internal LVDT lead to the outside of the triaxial cell through a port in the pedestal and are sealed with a male connector and a nut. The internal pore pressure transducer leads to the outside of the triaxial cell through a borehole in the base cap and pedestal and is sealed with a male connector, O-rings, ferrule, and a union nut. A post inside the cell for supporting the LVDT was screwed into the pedestal. Figure 5.1 schematically shows details of the triaxial cell. Figure 5.2 shows the triaxial cell's appearance.

5.2.1.1 Cell body and top

The cell body and top consist of a single unit. The cell body, a cylinder 338mm in inner diameter, 405mm in outer diameter, and 33.5mm in thickness, was made from acrylic plastic transparent material and reinforced by two 51mm metal bands enabling the cell to withstand pressures up to 3000kN/m^2. The transparency of the acrylic plastic material enables sample examination during a test. A thick O-ring was used to seal the cell wall through pressure on the pedestal. Figure 5.3 shows the structure of the triaxial cell. The cell top, 508mm (20″) in diameter and 76mm (3″) thick, was machined with an aluminum alloy and pressure-sealed with a single O-ring. The cell top was fitted with an air-release valve and a pressure gauge. The brass bush was fixed in the center of the cell-top. Four quick-release tie rods were used to attach the cylinder and cell top assembly to the wall base. Details of the cell top are given in Figure 5.4. Two eyebolts were screwed on two tie rods (Figure 5.2). A steel chain was used to connect these two eyebolts, which were used to install and uninstall the cell body.

5.2.1.2 Cell base

The cell base (pedestal), 508mm (20″) in diameter and 70mm (2.75″) thick, was also machined with an aluminum alloy and pressure-sealed with a single O-ring. The pedestal had six inflow and outflow ports. Each port terminated at a screwed socket on the edge of the cell pedestal, into which could be fitted a valve or a blank plug if the line was not used. Four ports connected to the appropriate pressure/drainage or specific measurement lines. The four ports were (i) the cell-chamber connection for filling, pressurizing and emptying the cell; (ii) the connection to the sample's top cap, for application and drainage of back pressure to the specimen; (iii) the connection to the base porous stone for the base pore-pressure measurement; and (iv) the seal of the local displacement measurement cord. Another two valves were sealed off and can be used when needed. The top surface of the pedestal was smooth to allow for less likelihood of trapping air. In the centre of the cell base, a large hole was bored to pass through the tubing of the internal pore-pressure transducer and contain the sealing parts of the tubing. Four capscrews were used to attach the lower loading cap to the cell base (see Figure 5.5).

5.2.1.3 Loading piston

The loading piston was made from stainless steel and had a high-quality honed finish with brass bushing on the top. The piston was 70mm (2.75″) in diameter and was fitted with a stainless steel ram float 102mm (4″) in diameter. The lower end of the piston was a plane for easy loading on a ring bearing resting on the upper loading cap during the tests. The piston was pressure-sealed with a pair of rubber O-rings, which were placed in the annular-coned recesses around the bushing. The final assembly included the use of a special silicone lubricant to reduce friction to an absolute minimum and prevent any water leakage. Figure 5.6 shows the details of the triaxial cell piston, bushing, and ram float.

5.2.1.4 Loading caps

The loading from the piston was transmitted to the sample through the top loading cap. It was made of a stainless steel and perforated with an eccentric small-diameter hole to which a drainage connection could be fitted. The surface of the top cap was smooth to allow for resting a stainless steel ring bearing which fit the lower end of the cell's loading piston (see Figure 5.7). Such a bearing permitted relative movement between the bearing and the surface of the top cap, and the lower end of the loading piston to eliminate friction. The lower cap was also made of stainless steel and perforated with two eccentric small-diameter holes, to one of which a base pore-pressure measurement was connected, and a centered small hole (3.2mm) to which the tubing of the internal pore-pressure transducer was fitted. The small center hole was enlarged in its lower part so that a 6.35mm NPT (national pipe thread) could be screwed in. This NPT and an O-ring and a ferrule were used to seal the transducer's tubing. Four capscrews attached the lower cap to the cell base (see Figure 5.8).

5.2.2 Axial Loading System

5.2.2.1 Loading frame

The loading frame was made with a C310 × 45 steel trough. Figure 5.9 gives its dimensions and parameters. The vertical steel trough columns were 1448mm (57″) high and were welded on a stiffened frame base 610mm (24″) in length. On the upper part of each loading frame column, 14 holes were bored in two columns. The interval between them was 184mm (7.25″), and the space between any two closed holes in a column was 102mm (4″). The diameter of the hole was 27mm (1-1/16″). The stiffened frame top could be bolted on these columns through these holes, and its height was adjustable to match the cell body. The frame top was stiffened with two lateral steel plates. Another two steel plates were welded onto the two ends, on which four boreholes were bored into each plate. These holes had the same diameter and spacing as those in the frame columns and were used to bolt the frame top to the columns. The center of the frame top was threaded for the hydraulic jack, which passed the load to the loading piston. The details of the loading frame are shown in Figures 5.10 and 5.11.

5.2.2.2 Hydraulic jack

The hydraulic jack used for passing the load to the loading piston was an Enerpac RC-1510 single-acting cylinder. This cylinder has a large stroke to satisfy the requirement of the large vertical displacement. Its threaded end enabled easy fitting on the frame top (see Figure 5.12).

5.2.2.3 Loading equipment

A ISCO Series D (model 100DX) single syringe pump, consisting of a controller and a pump module, was used to apply an axial load to a sample in a strain-controlled mode, in which the constant flow rate could provide a predetermined constant rate of displacement, or strain rate, and the resulting axial load was measured by using a load cell. The rate of displacement can be calculated as in the following equation:

$$D = 10Q/S, \qquad [5.1]$$

where

D is the rate of displacement (mm/min);
Q is the Syringe pump flow rate (ml/min); and
S is the Hydraulic cylinder effective area (cm^2).

A Syringe pump 100DX, has a capacity of 103ml with a maximum flow rate of 60ml/min and a minimum flow rate of 0.00001ml/min. From Equation 5.1, the rate of displacement in the system is then in the range of 0.000005mm/min to 29.6mm/min. These rates can satisfy most test requirements. The pump can supply a maximum pressure of 68.95MPa (10000psi). Figure 5.13 shows such a pump. The load cell used was an ALD-COMP load cell with a capacity of 222.4kN (50klb) and 63.5mm outside diameter and 50.8mm in height, and can perfectly match the hydraulic cylinder and the loading piston. This load cell is a compact reliable sensor for accurate and repeatable measurements of static and dynamic compressive loads. Electrically, this load cell is a full Wheatstone Bridge with four arms. The strain-sensitive elements were bonded to the load column and sealed with a moisture-proof coating to shield them from a harsh environment. Figure 5.14 shows this load cell's dimensions.

5.3 TRIAXIAL PRESSURE PANEL SYSTEM

Figure 5.15 shows the layout of the triaxial pressure panel system used for this equipment. This panel consists of a back-pressure system and a cell-pressure system. The cell pressure system consists of a compressed air cell-pressure subsystem and a syringe pump cell-pressure subsystem. For the maximum pressure needed when either of the back pressure or cell pressure was less than or equal to 800kPa, a compressed air supply of 900kPa was used as the source for increasing the pressure and venting into atmosphere to decrease the pressure. Pressures up to a maximum 1800kPa were anticipated to be needed to apply the confining pressure. Since this maximum was above the pressure usually provided by conventional air compressors in a soil mechanics laboratory, an ISCO Series D (model 500D) single syringe pump, consisting of a controller and a pump module, was used to supply the confining pressure during the consolidation and shearing stages. This syringe pump has a 507 ml capacity, a flow rate range of 0.001ml/min to 204ml/min, and a 25.8MPa (3750psi) pressure rating. The pump was operated in a constant pressure mode. The standard pressure accuracy is 0.5% FS. The system was operated in the following manner.

During the saturation of samples, the back pressure was anticipated to be below or equal to 800kPa, and the compressed air pressure was used as both back pressure and cell pressure. In this case, Valves b, d, and e were closed, while valves a and c were opened (see Figure 5.15). During the consolidation, 1700~1800kPa confining pressure was used to consolidate the samples, which was much higher than the compressed air pressure. In this case, the back pressure still used compressed air because the back pressure remained constant during the consolidation, while confining pressure was supplied by the syringe pump. At this time, valves b, c, and d were closed, while valves a and e were opened. This subject is described in detail in Chapter 6.

5.4 PORE-PRESSURE MEASUREMENT SYSTEM

The pore pressure measurement involved in the tests included base pore-pressure measurement and shear plane pore-pressure measurement. The pore-pressure measurement on the base of a specimen is relatively straightforward and conventional (Bishop and Henkel, 1962; Head, 1986), but pore-pressure measurement on a shear plane is quite challenging due to the transducer's proximity to the shear plane and lack of referenced (related) experience. The measurement of the failure plane's pore pressure could be compromised if the transducer were located too far away from such a plane.

After considerable discussions and trial tests, the problem of the transducer's proximity for pore-pressure measurement on a shear plane was overcome by developing a new transducer. This transducer was made by potting an ultra-small pressure sensor into a brass cylinder 13.7mm in diameter and 25.4mm in length with an inclined end surface that had the same angle as that of the shear plane. The surface of the pressure sensor was parallel to the inclined end surface. Figure 5.16 shows the structure of the brass container. A tubing 3.2mm(1/8″) in diameter was connected to this sensor to hold the coated wires with flexane 80. The pressure sensor was a Kyowa Model PS-10KB pressure sensor (Figure 5.17). This model has a range of 0 – 1000kPa. Pressure sensors with a large range are available for high-pressure measurements. The small size and the inclined end surface permitted the mounting of the transducer right onto the face of the shear plane without any fittings between it and the inclined transducer face to measure the pore-pressure response during the tests. Figure 5.18 shows this pore-pressure transducer. Figure 5.19 shows the mounting of the pore-pressure transducer in a sample.

The key concern when measuring the pore pressure on a shear plane is the development of the internal pore-pressure transducer. Two points need special attention when making the transducer. Firstly, a gap between the porous stone and the sensor's face is needed so that the measurement obtained from the transducer is the pore pressure and not the loading force passed from the porous stone. Secondly, the porous stone's surface should be at the same level as that of the inclined plane of the transducer holder. If the pore stone's surface is higher or lower than that of the inclined plane, either the sample material will be pressed into the holder's hole, or the porous stone will be pressed into the sample when testing on the reconstituted clay sample. As a result, the measured deviator stress will be affected.

5.5 DISPLACEMENT MEASUREMENT SYSTEM

Displacement measurements include the overall vertical displacement measurement and the local shear displacement measurement. The former is straightforward and is conducted with a LVDT set up on the cell top, but the latter measurement along the pre-existing or pre-cut shear plane is difficult. In the newly developed large cell, considerable space is available to install a submersible Schaevitz LVDT. This LVDT was held on a post screwed inside the cell into the base. The LVDT's movable bar was rested on a right-angled steel plate attached to the sample wall by two magnets (see Figure 5.1). This process is described in detail in Chapter 6. The modified conventional triaxial cell does not have enough "space" for a submersible LVDT, so the electrolytic level was used to make the transducer measure the local displacement along a pre-existing shear plane. Burland and Symes (1982) used the electrolytic level in an inclinometer for piles in the field and introduced this level into the local strain measurement. Jardine, Symes and Burland (1984) described a modified version for use with 38mm diameter samples. These previous studies influenced the author of this present study to select an appropriately small electrolytic level to make a "tilt" transducer to measure the local shear displacement.

5.5.1 Principle of the Electrolytic Level

The Fredericks Company's electrolytic level provides an output voltage proportional to the tilt angle, and a phase indicative of the tilt direction when connected in an appropriate electrical circuit. It consists of a tubular glass envelope partially filled with an electrolytic fluid which contacts the metal electrodes. The desired operating characteristics can be achieved by varying the envelopes, electrolytes, and electrode configurations. When the level is connected in the appropriate test circuit and leveled, an equal impedance to the common electrode will exist, and the digital voltmeter will indicate a minimum (null) output. Tilting the level will cause an unbalanced impedance to the common electrode, and the output voltage will increase. This voltage is the usable output of the sensor and is proportional to the tilt angle. In these tests, the model 0725 level and model 0729 signal conditioner were the instruments of choice. The model 0725 level is a proportional linear sensor with an 80° operating range (see Figure 5.20), while the 0729 signal conditioner delivers versatile electronic drive requirements for one dual-axis, or two single-axis Fredericks levels, and all from one compact unit (see Figure 5.21). This simple connection configuration is ideal for mass assembly. The surface-mounted components enhance the compact design and ensure greater in-field durability. The 0725 level was wired into the electronics board and remotely mounted to provide an exact tilt measurement in a flexible, compact package that would fit into almost any design. The system required 2 levels for forming a transducer to properly monitor the required displacements.

5.5.2 Make-up of the Tilt Transducer

The 0725 level is just 12.7 mm in diameter and 5.3 mm in width and wired with Teflon-coated leads. The small size allowed these levels to be potted into small pressure-proof brass "containers" that would fit between the cell wall and the sample. The Teflon leads facilitated the connection from the transducers inside the cell and the signal conditioner outside the cell. One end of each level was fixed to a telescoping bar. The two bars were hinged at one end, which was attached to an "ideal" point on the sample, while the other end of this "tilt" transducer was connected to a post mounted inside the triaxial cell. The connection to the sample was done through two magnets. One was fixed or epoxied on the sample wall, and the other was placed just outside the membrane that had been glued at the hinged end of the sensor. Doing so allowed the integrity of the membrane to be maintained. The signal conditioner selected has two channels available on board. Figure 5.22 shows the appearance of the "tilt" transducer.

5.5.3 Principle of the Tilt Transducer

Figure 5.23 shows the principle of the "tilt" transducer. When a sample is sheared along the pre-existing shear plane (assuming a rigid block movement), the "ideal" point A will move to A′ in the direction parallel to the shear plane. The angle change α is measured by level 1, while the angle change β is recorded by level 2. Then the local vertical displacement (D_v) from the movement along the shear plane is

$$D_v = \frac{L \cdot \tan\theta \cdot \tan\beta}{\tan(\theta+\alpha) - \tan\beta} , \qquad [5.2]$$

where

L is the initial distance between the sample wall and the post,
θ is the initial angle between the two telescoping bars,
β is the change of the angle between the post and the lower telescoping bar,
α is the change of the angle between the post and the upper telescoping bar, and
D_v is the vertical displacement of the shear plane.

From the local vertical displacement, the displacement along the shear plane, S, can be calculated from the equation below:

$$S = \frac{D_v}{Sin\,\psi} , \qquad [5.3]$$

where

ψ is the inclination of the shear plane.

When comparing this local displacement measured by either internal LVDT or "tilt" transducer with the overall displacement measured by external LVDT, one can find that the local displacement is smaller than the overall displacement. Figures 5.24 to 5.26 typically show the displacements measured by both internal LVDT or "tilt" transducer and external LVDT for three types of samples. For the test on Athabasca clay, the overall displacement includes not only the local displacement, but also includes the error from compliance (bedding error) and the compressive strain of a sample (Burland, 1990). Therefore, the difference in displacements measured by external LVDT and internal LVDT or "tilt" transducer increases with the test time due to the compressive deformation of a relative soft Athabasca clay sample. For Highvale mudstone and weak rocks taken near Fort McMurray, they are stiff enough to have no compressive strain during the test. The difference in displacements measured by external LVDT and internal LVDT or "tilt transducer keeps almost constant with the test time, which mainly reflects the bedding error. Therefore, the displacement measured by the internal LVDT or "tilt" transducer reflects the real displacement along the shear plane, while the internal straining of the sample will not affect such a displacement.

5.6 DATA ACQUISITION SYSTEM

The typical measurements made during a test included

- Cell pressure (by using a pressure transducer)
- Back pressure (by using a pressure transducer)
- Axial load (by using a load cell)
- Basal pore pressure (by using a pressure transducer)
- Shear plane pore pressure (by using a pressure transducer)
- Overall vertical displacement (by using a LVDT)
- Local displacement (by using a submersible LVDT or a "tilt" transducer)

- Volume change (by using a electric volume change reservoir)

Figure 5.27 shows the layout of the measurement devices. Outputs from the monitoring transducers were connected to a computer-controlled data-logging system. Figure 2.28 shows the schematic representation of the data processing and control system. A Data Dolphin data logger and software, or Agilent 34970A Data Acquisition/Switch Unit and HP Benchlink Data logger software, were used to automatically monitor and control the laboratory processes.

The Agilent 34970A consists of a three-slot mainframe with a built-in 6 ½ digit DMM. Each channel can be configured independently to measure one of 11 different functions. The built-in signal conditioning measures thermocouples, thermistors, ac/dc volts, current, resistance, frequency, and period. 50k readings of non-volatile memory can hold data when power is removed. With a different modular, 34970A can use 20 to 120 channels to log data. Its reading rates can be up to 600 readings per second on a single channel, and the scan rates can be up to 250 channels per second. The 34970A is well suited for high displacement (loading) rate tests. With Agilent Benchlink Data Logger II software, one can easily set up a test, acquire and archive measurement data, and perform real-time display and analysis of the measurements, but during the data logging, the reading rates cannot be changed without restarting.

A familiar spreadsheet environment makes configuring and controlling the tests easy, and for analyzing and displaying the data. The Agilent BenchLink Data Logger II can easily move data to other applications for further analysis or for inclusion in presentations and reports. Figure 5.29 shows an Agilent 34970A Data Acquisition/Switch Unit, which was used for the tests using the large cell.

The Data Dolphins have 4 "standard inputs," 8 "precision inputs" and 3 frequency-based inputs. The standard inputs record the voltage, counts, or a simple on-off status with 10 bits of precision. The 8 precision inputs have an extra 16 bits of precision (total of 24), which allow voltage measurements to be taken into the mv range, and most sensors to be directly connected without any signal conditioning. The data recorded by the Data Dolphin are stored on an erasable memory chip. Each record is time-stamped and stored in the card in a normalized database fashion, which allows different inputs to be turned on and off without restarting the Data Dolphin. Even the sample rate can be changed without restarting. Data collecting, programming, and viewing are simple with the Data Dolphin Software. It allows one to view the current status, set up the logger, and generate graphs. One can also export data to other programs for more detailed analysis and presentations. Unfortunately, Data Dolphin cannot perform real-time display, and its reading rates are relatively slow, so that this software is relatively less useful for a high loading rate test. Figure 5.30 shows a Data Dolphin data logger, which was used for the tests using the modified conventional triaxial cell.

5.7 MODIFIED CONVENTIONAL TRIAXIAL EQUIPMENT

Before developing the large triaxial equipment for the measurement of the pore pressure on the shear plane, a modified conventional triaxial equipment was used for this test. Bishop and Henkel (1962) and Head (1986) had previously described the conventional triaxial equipment. The modifications included installing an internal pore-pressure transducer inside into a specimen to measure the pore pressure on the shear plane and a "tilt" transducer inside the cell to measure the displacement along the shear plane. The internal pore-pressure transducer and the "tilt" transducer are described in Sections 5.4 and 5.5. A 3.2mm (1/8″) hole was bored through the lower cap and cell base in the centre to lead the internal pore pressure tubing out, and the cell base was over-bored to contain the tubing's sealing parts. A steel post was screwed into the cell base inside the cell to hold the "tilt" transducer. Its wires were led to the outside of the cell through a spare port and were sealed with a gland screw. A ring bearing was placed between the sub-top loading cap and the top-loading cap to eliminate friction. The sub-top loading cap had a polished top surface and was hard enough to support the bearing. The top-loading cap, placed on the bearing, was also hard enough and had a polished bottom surface. The top surface of the top-loading cap had a coned recess to rest a ball to fit the hemispherical recess on the lower end of piston. The Data Dolphin software automatically monitored and controlled the laboratory processes, and two Data Dolphin data loggers logged the data. Figure 5.31 schematically shows the set-up of such a modified cell.

5.8 SUMMARY

- A newly developed large dimensional triaxial apparatus and a modified conventional triaxial apparatus were used for the triaxial compression test on different materials with the pore-pressure measurement on a shear plane. The apparatus are described in detail.

- The apparatus can be used with various pressure-control systems. A compressed air-water system and a syringe pump were used for the pressure system. The axial load was applied by a syringe pump for the large cell. Data Dolphin software and Agilent Benchlink Data Logger II software were used to create the data logging.

- A special pore-pressure transducer and a "tilt" transducer were developed to measure the pore pressure on the shear plane and the local displacement along the shear plane. Their designs and principles were described.

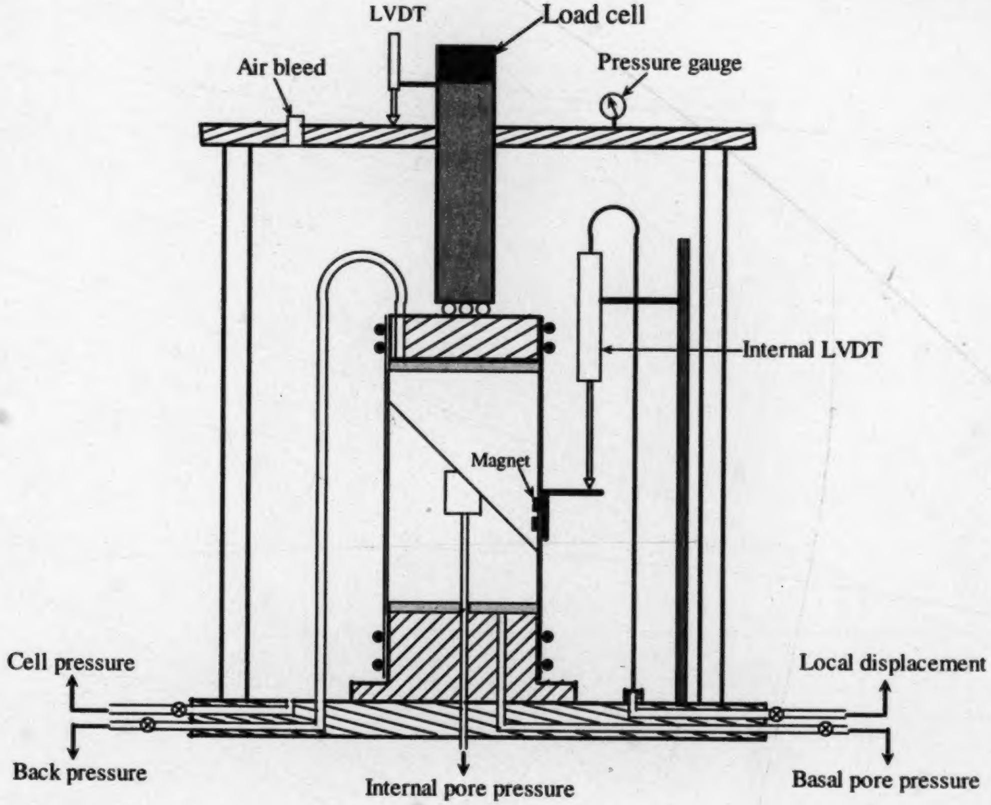
LVDT
Load cell
Air bleed
Pressure gauge
Internal LVDT
Magnet
Cell pressure
Local displacement
Back pressure
Internal pore pressure
Basal pore pressure

Figure 5.1 Sketch of the set-up of the large triaxial cell (not to scale)

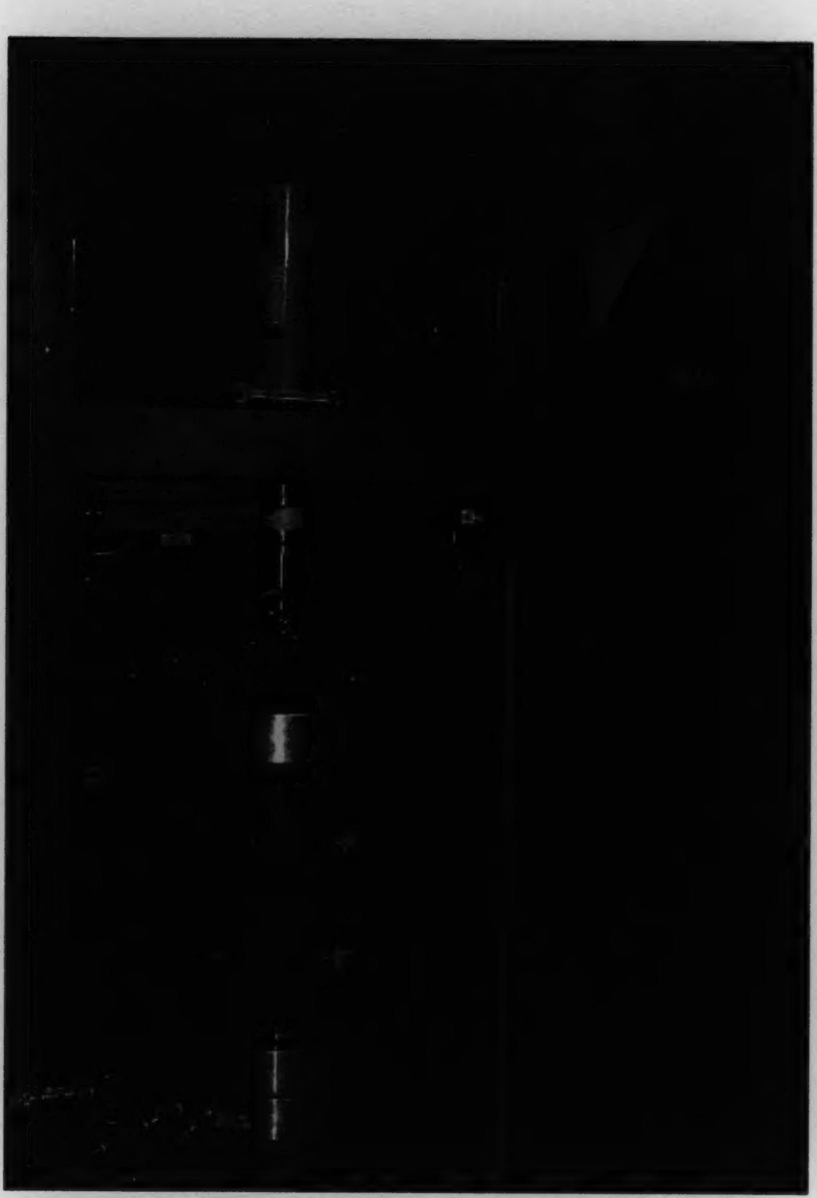

Figure 5.2 Photograph showing the large triaxial cell and the loading frame

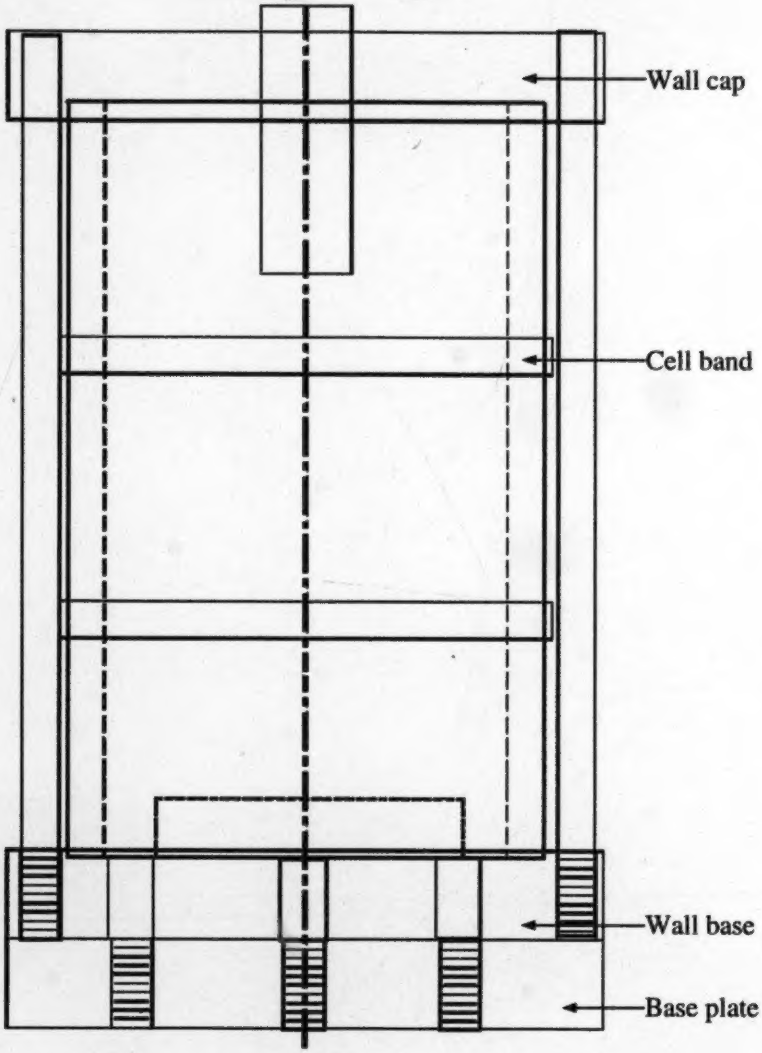
Wall cap
Cell band
Wall base
Base plate

Figure 5.3 Structure sketch of the large diameter triaxial cell

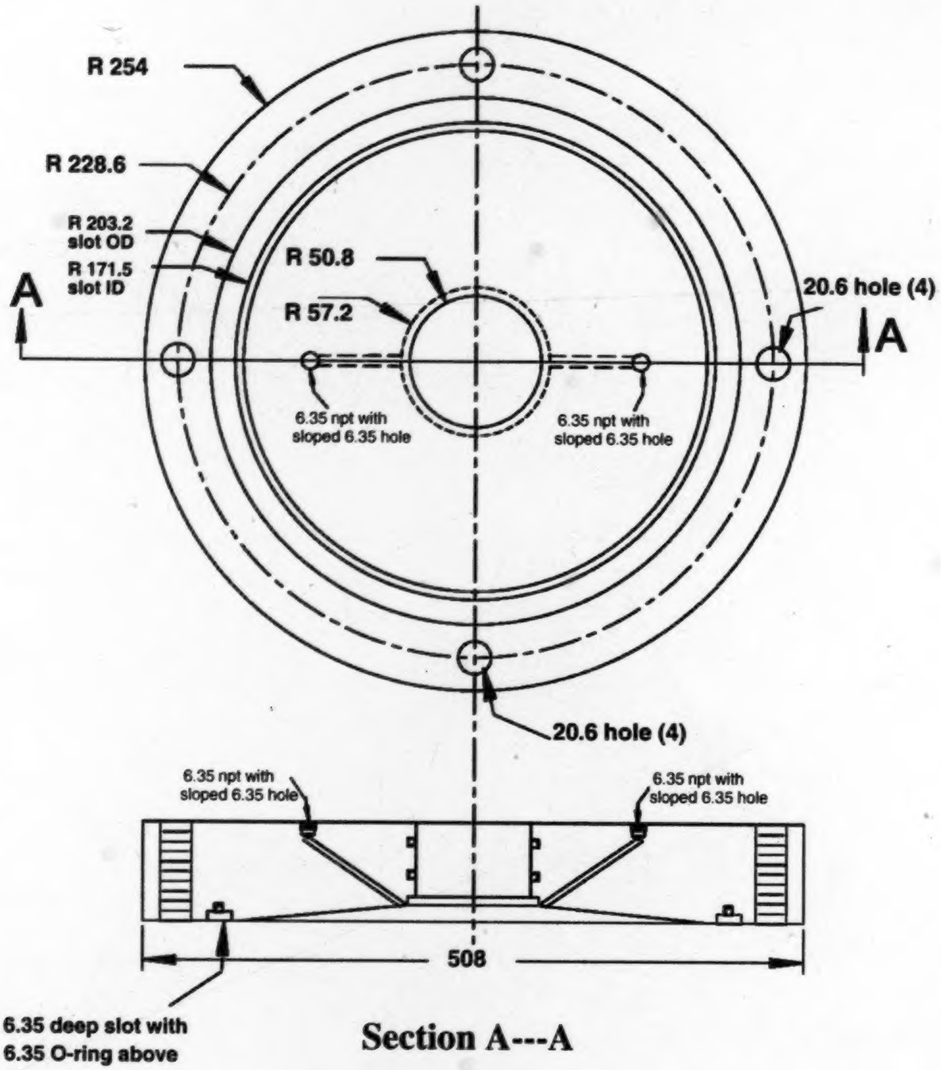
R 254
R 228.6
R 203.2
slot OD
R 171.5
slot ID
R 50.8
R 57.2
A
A
20.6 hole (4)
6.35 npt with
sloped 6.35 hole
6.35 npt with
sloped 6.35 hole
20.6 hole (4)
6.35 npt with
sloped 6.35 hole
6.35 npt with
sloped 6.35 hole
508
6.35 deep slot with
6.35 O-ring above
Section A---A

Figure 5.4 Details of the triaxial cell top (unit: mm)

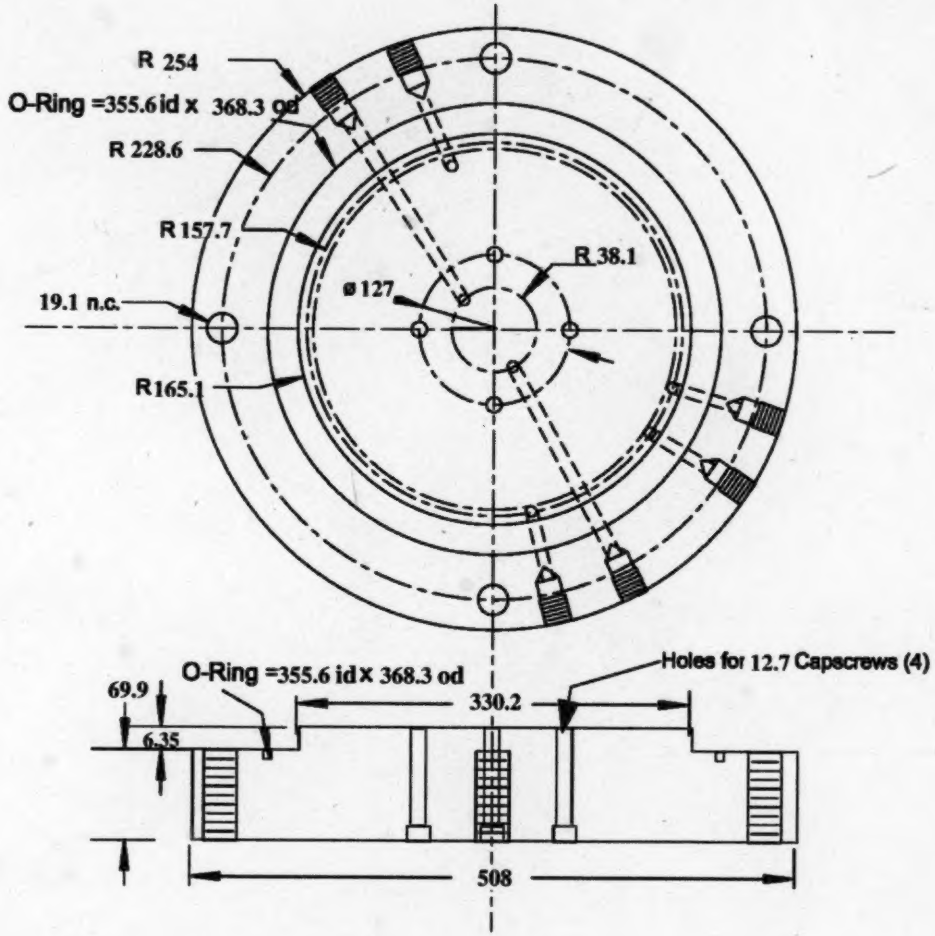
R 254
O-Ring =355.6 id x 368.3 od
R 228.6
R 157.7
R 38.1
ø 127
19.1 n.c.
R165.1
O-Ring =355.6 id x 368.3 od
Holes for 12.7 Capscrews (4)
69.9
330.2
6.35
508

Figure 5.5 Details of the triaxial cell base (unit: mm)

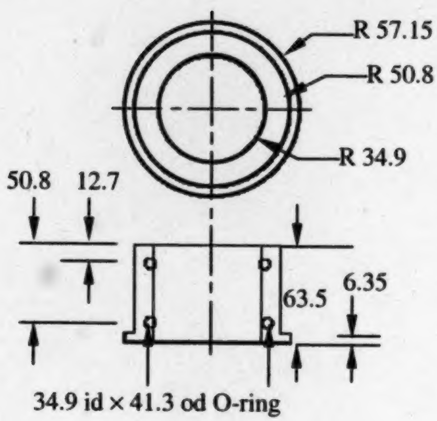
R 57.15
R 50.8
R 34.9
50.8
12.7
63.5
6.35
34.9 id × 41.3 od O-ring

Cell bushing in brass

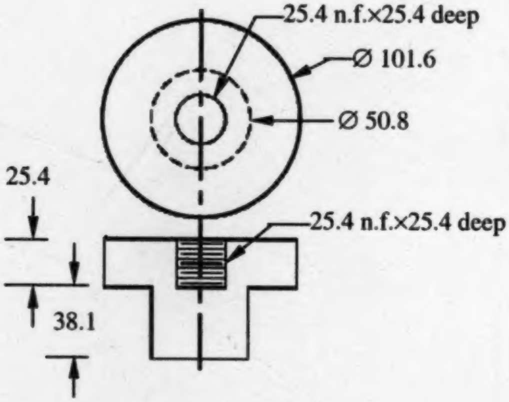
25.4 n.f.×25.4 deep
Ø 101.6
Ø 50.8
25.4
25.4 n.f.×25.4 deep
38.1

Ram float in stainless steel

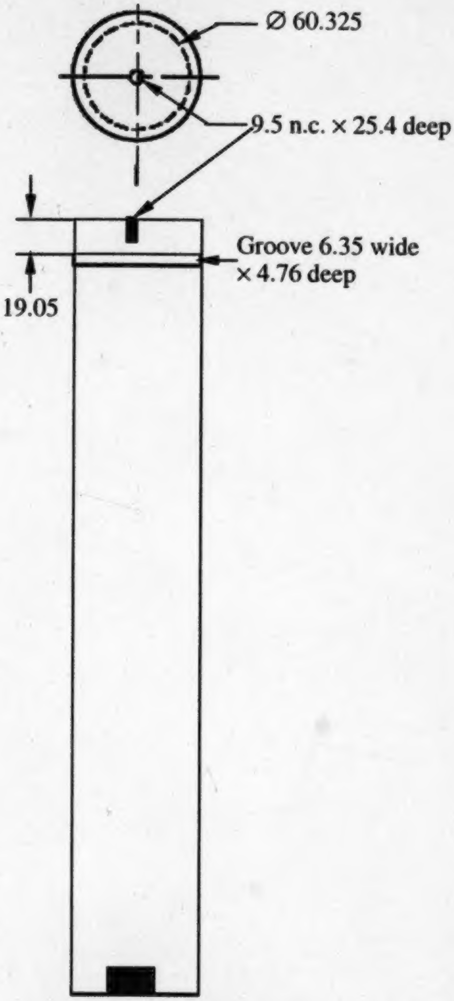
Ø 60.325
9.5 n.c. × 25.4 deep
Groove 6.35 wide × 4.76 deep
19.05

Piston in stainless steel

Figure 5.6 Details of the large triaxial cell bushing in brass, piston and ram float in stainless steel (unit: mm)

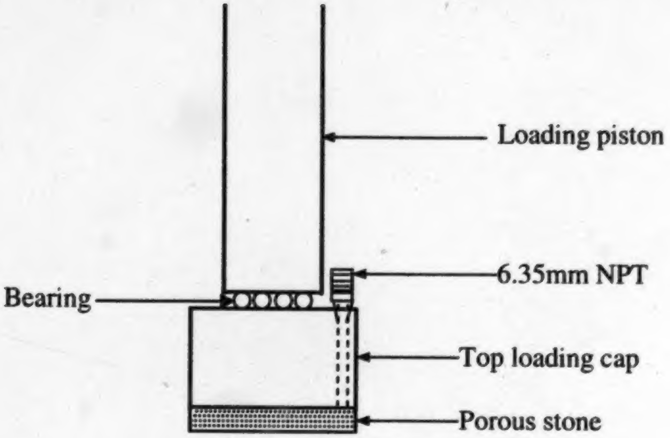
Loading piston
6.35mm NPT
Bearing
Top loading cap
Porous stone

Figure 5.7 Top loading cap and its relationship with bearing and loading piston

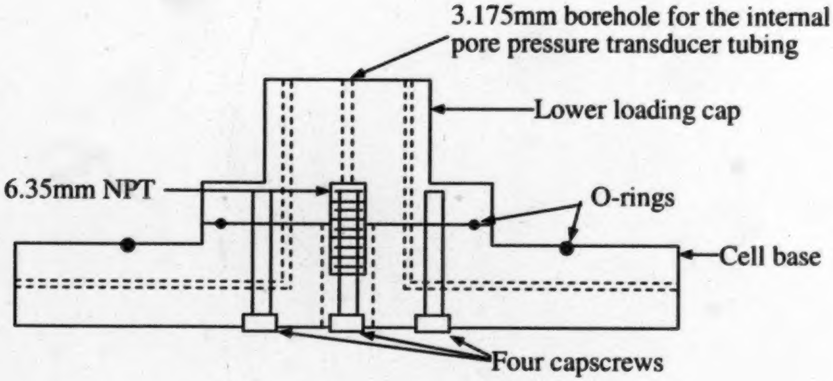
3.175mm borehole for the internal pore pressure transducer tubing
Lower loading cap
6.35mm NPT
O-rings
Cell base
Four capscrews

Figure 5.8 Attachment of the lower loading cap to the cell base

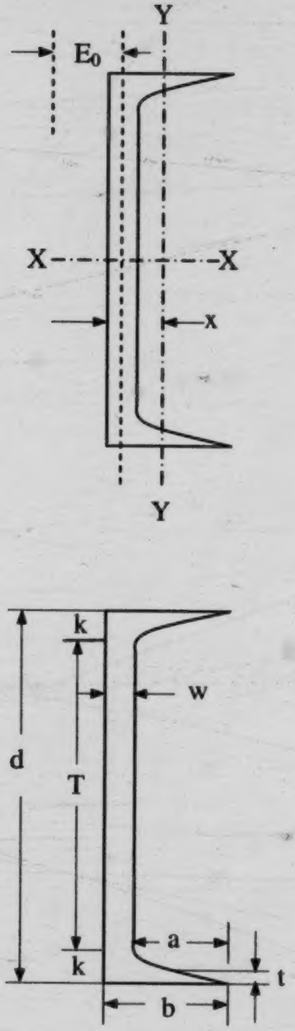

Dead load: 0.438 kN/m

Total area: 5690 mm^2

I_y: 2.12x10^6 mm^4

S_y: 33.6x10^3 mm^3

r_y: 19.3 mm

x : 17.0 mm

Shear center E_0: 21.9 mm

Torsional constant J: 363x10^3 mm^4

Warping constant C_w: 39.9x10^9 mm^6

Nominal mass: 45 kg/m

Depth d: 305 mm

Width b: 80 mm

Mean thickness t: 12.7 mm

Web thickness w: 13.0 mm

Distance:

a: 67 mm

T: 250 mm

k: 28 mm

Surface area: 0.904 m^2/m

Figure 5.9 Basic dimensions and properties of the steel trough C310 x 45

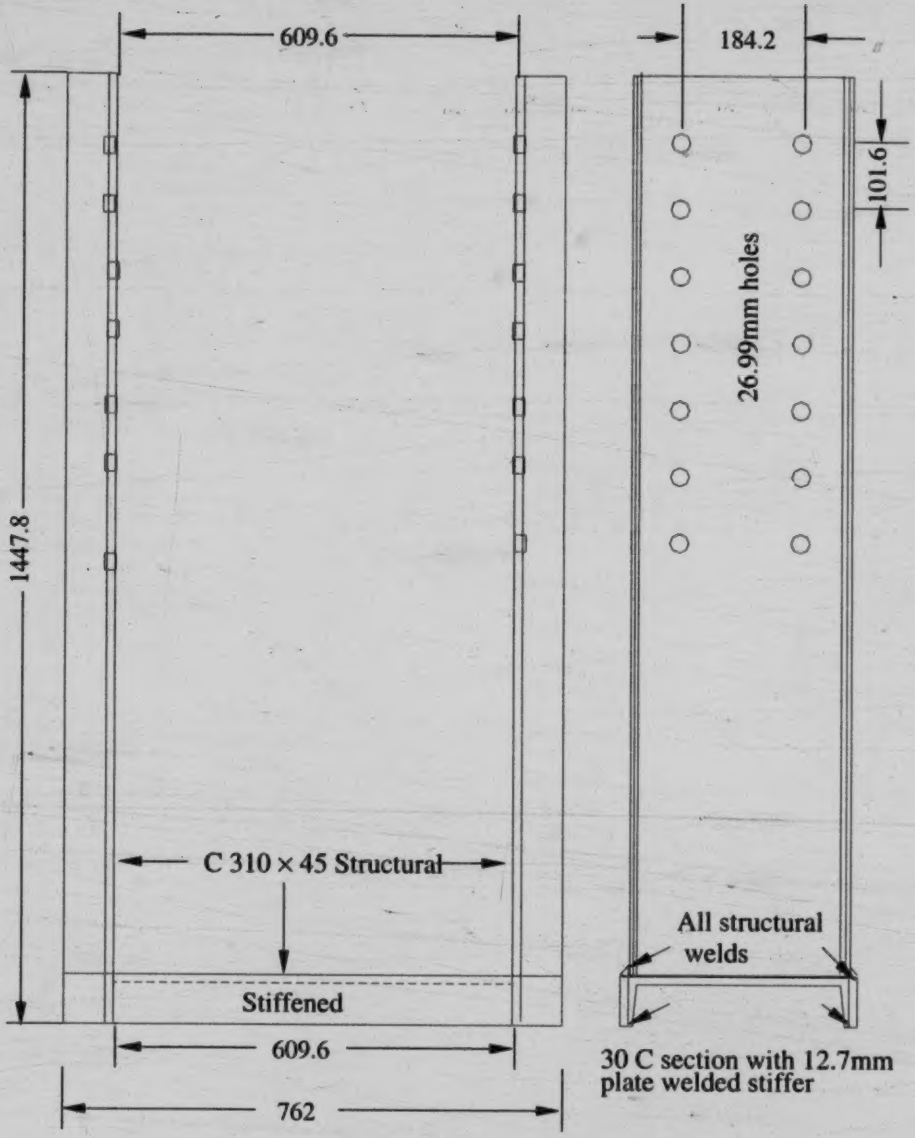
609.6
184.2
1447.8
101.6
26.99mm holes
C 310 × 45 Structural
All structural welds
Stiffened
609.6
762
30 C section with 12.7mm plate welded stiffer

Figure 5.10 Details of the C310 x 45 structural loading frame (unit: mm)

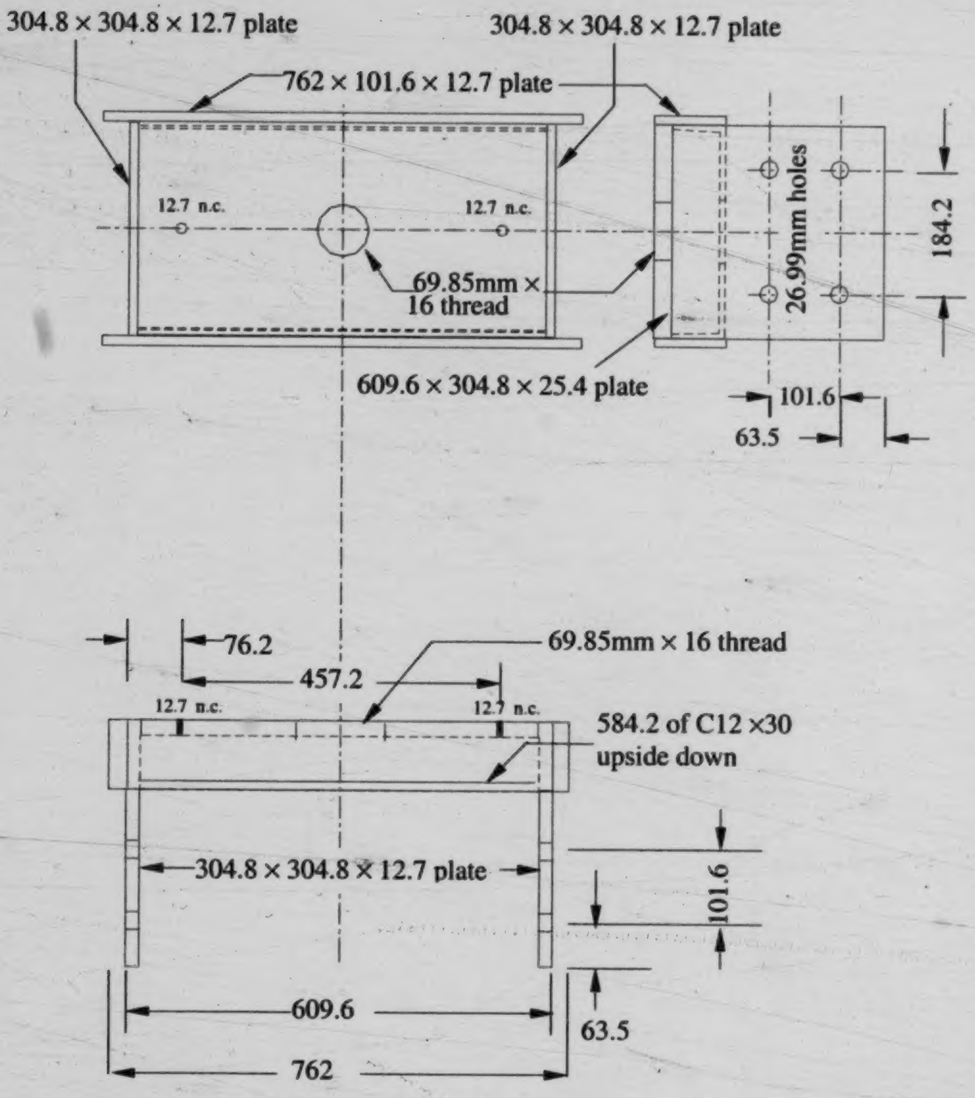
304.8 × 304.8 × 12.7 plate
304.8 × 304.8 × 12.7 plate
762 × 101.6 × 12.7 plate
12.7 n.c.
12.7 n.c.
69.85mm × 16 thread
26.99mm holes
184.2
609.6 × 304.8 × 25.4 plate
101.6
63.5
76.2
457.2
69.85mm × 16 thread
12.7 n.c.
12.7 n.c.
584.2 of C12 ×30 upside down
304.8 × 304.8 × 12.7 plate
101.6
609.6
63.5
762

Figure 5.11 Details of the C310 x 45 structural loading frame top (unit: mm)

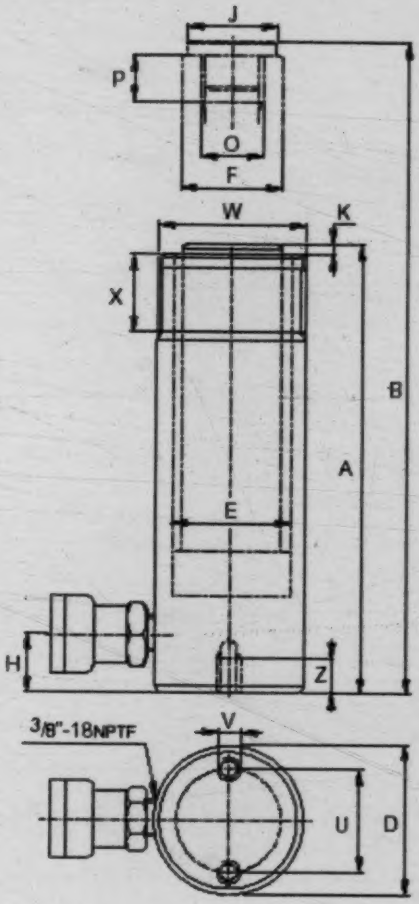

Basic dimensions:

Cylinder capacity (tons): 15
Stroke (mm): 254
Cylinder effective area (cm^2): 20.26
Oil capacity (cm^3): 514.88
Collapsed height A (mm): 373.1
Extended height B (mm): 627.1
Outside diameter D (mm): 69.9
Cylinder bore diameter E (mm): 50.8
Plunger diameter F (mm): 41.4
Base to average port H (mm): 25.4
Saddle diameter J (mm): 38.1
Saddle protrusion from plunger K (mm): 9.65
Plunger internal thread O (mm): 25.4mm- 8
Plunger thread length P (mm): 25.4
Base Mounting Hole
    Bolt circle U (mm): 47.8
    Thread V (mm): 9.5mm- 16UN
    Thread depth Z (mm): 12.7
Collar thread W (mm): 69.85- 16

Collar thread length X (mm): 30.2
Weight (kg): 9.53

Figure 5.12 Details of the hydraulic cylinder Enerpac RC-1510

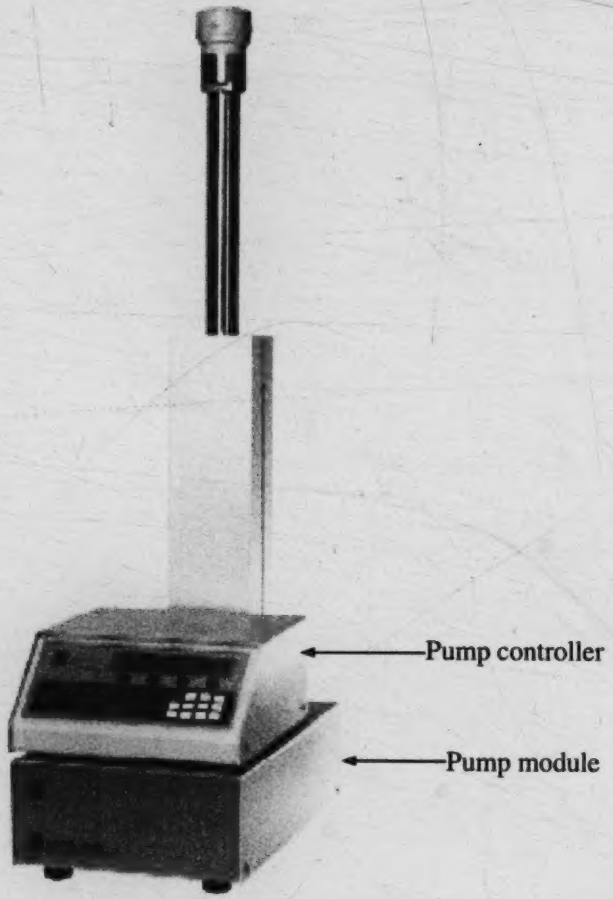
Pump controller
Pump module

Figure 5.13 ISCO Series D Model 100DX syringe pump

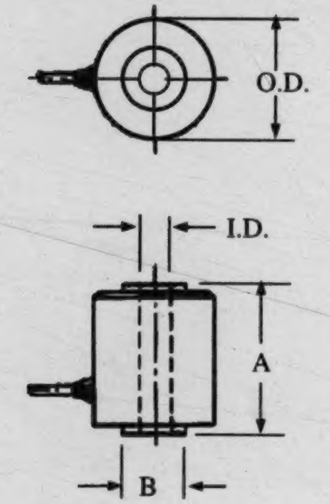

O.D. = 63.5mm I.D. = 25.4mm

A = 50.8mm B = 44.45mm

Output resistance: 700 Ohms

Input resistance: 350 Ohms

Excitation: 10 V DC or AC

Sensitivity: 2 MV/V

Non-linearity: ±0.15% F.S.

Hysteresis: ±0.15% F.S.

Compensated temperature range: 15°F - 150°F

Zero balance: better than 1% F.S.

Figure 5.14 Dimensions and properties of 50klb Ald-Comp load cell

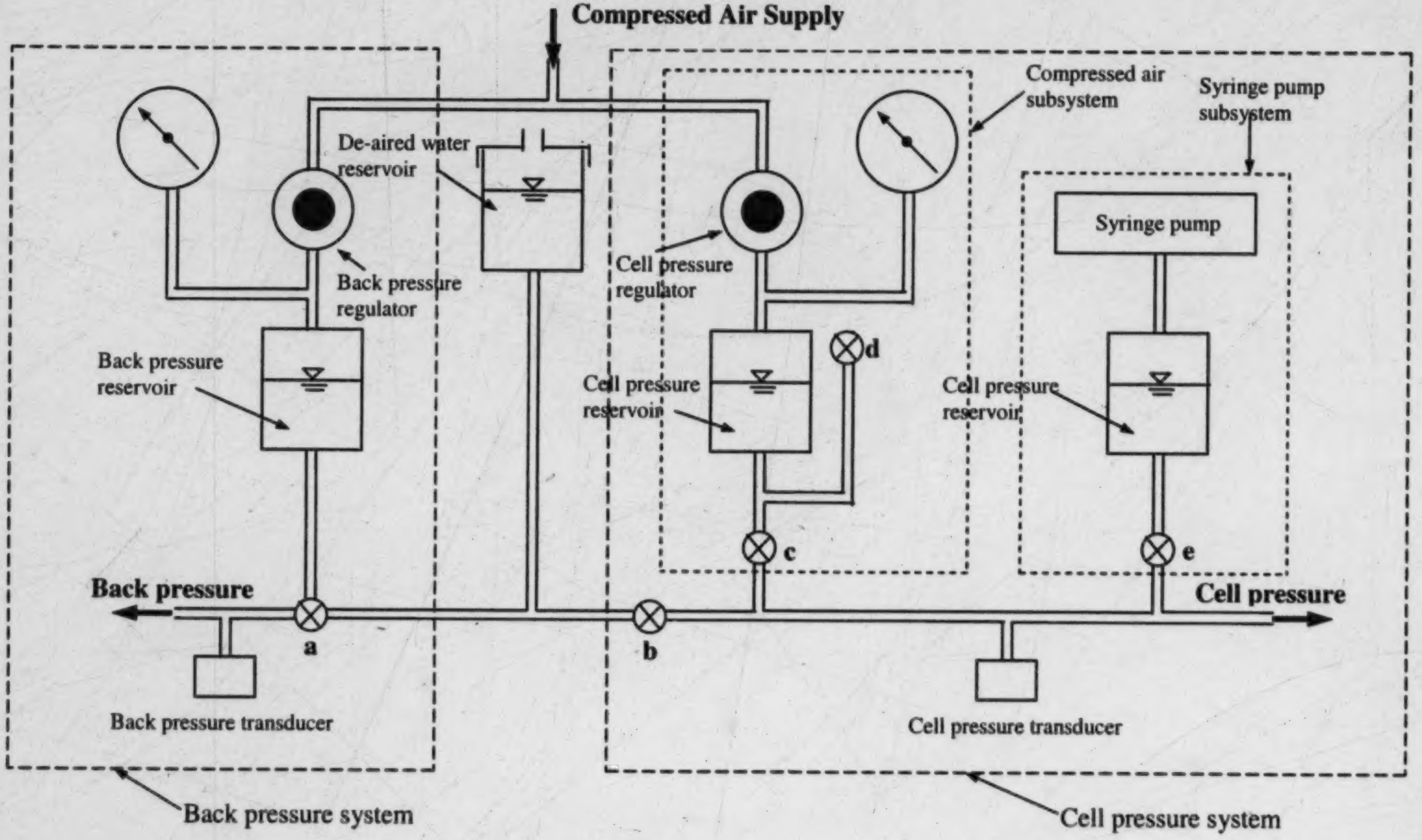
Compressed Air Supply
De-aired water reservoir
Back pressure regulator
Back pressure reservoir
Back pressure
a
Back pressure transducer
Back pressure system
Cell pressure regulator
Cell pressure reservoir
d
c
b
Compressed air subsystem
Syringe pump subsystem
Syringe pump
Cell pressure reservoir
e
Cell pressure
Cell pressure transducer
Cell pressure system

Figure 5.15 Layout of triaxial panel system

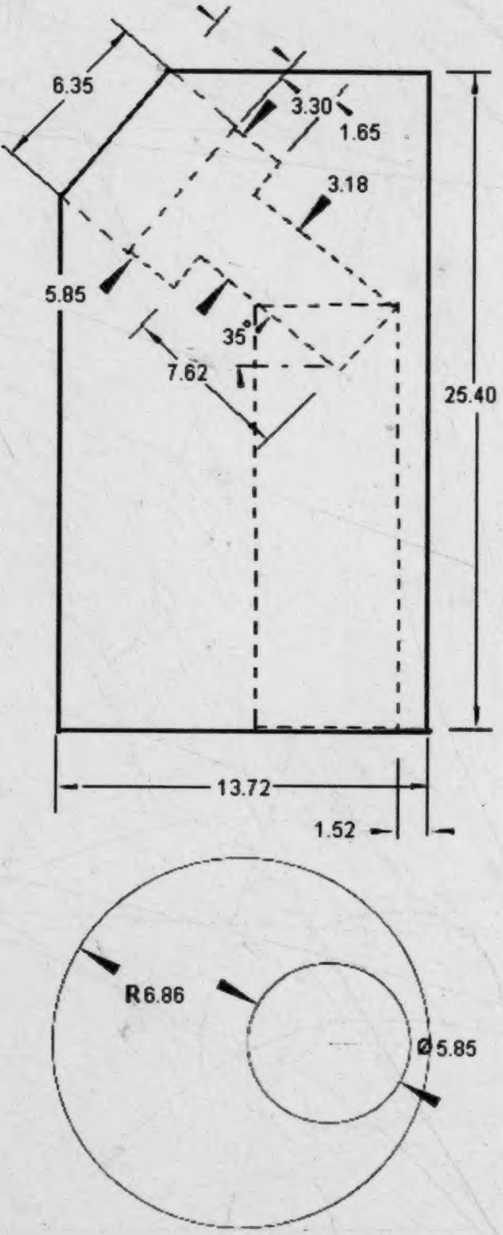
6.35
3.30
1.65
3.18
5.85
35°
7.62
25.40
13.72
1.52
R6.86
Ø5.85

Figure 5.16 Design of pore pressure transducer brass container (unit: mm)

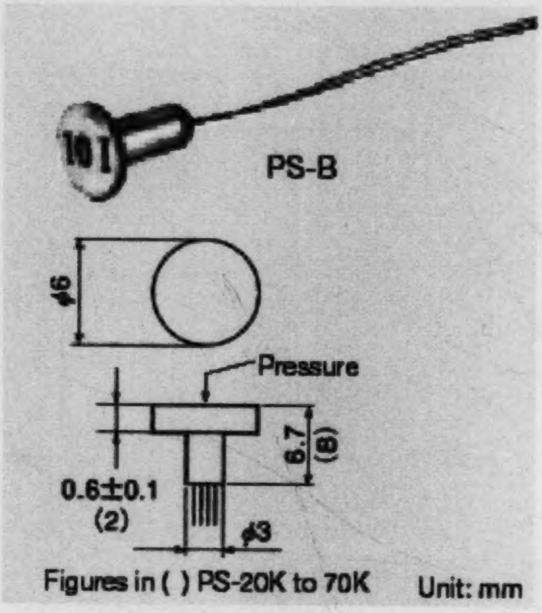
101
PS-B
ϕ6
Pressure
6.7
(8)
0.6±0.1
(2)
ϕ3
Figures in ( ) PS-20K to 70K
Unit: mm

Figure 5.17 Kyowa Model PS-10KB pressure sensor

Figure 5.18 Photo of the pore pressure transducer

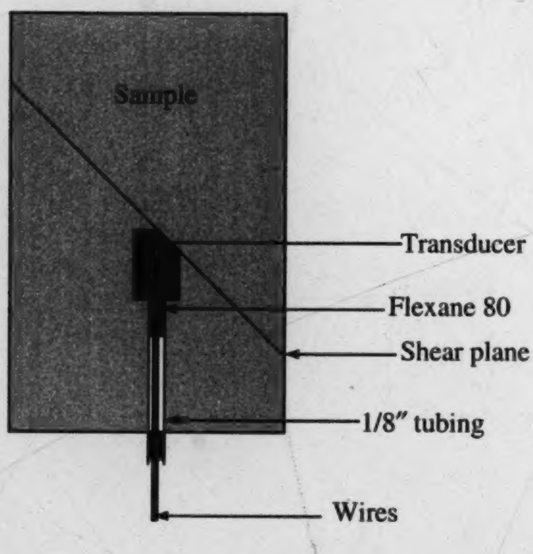
Sample
Transducer
Flexane 80
Shear plane
1/8″ tubing
Wires

Figure 5.19 Mount of the pore pressure transducer in a sample

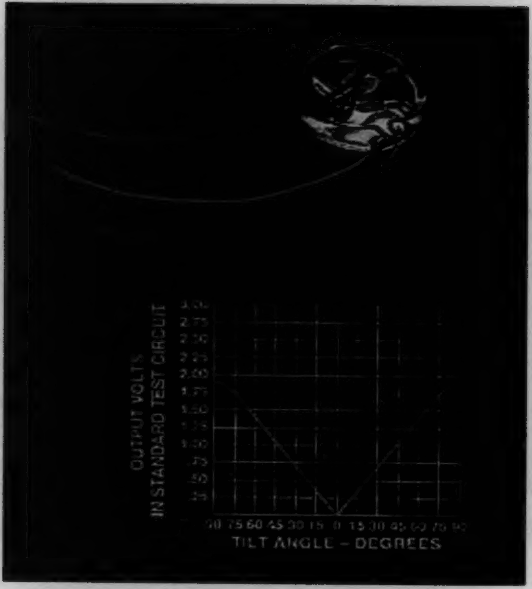
OUTPUT VOLTS
IN STANDARD TEST CIRCUIT
3.00
2.75
2.50
2.25
2.00
1.75
1.50
1.25
1.00
.75
.50
.25
90 75 60 45 30 15 0 15 30 45 60 75 90
TILT ANGLE – DEGREES

Figure 5.20 0725 tilt sensor and its linear output

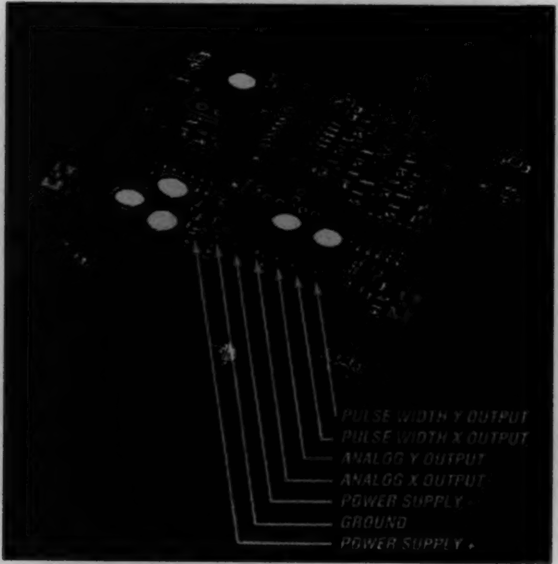
PULSE WIDTH Y OUTPUT
PULSE WIDTH X OUTPUT
ANALOG Y OUTPUT
ANALOG X OUTPUT
POWER SUPPLY -
GROUND
POWER SUPPLY +

Figure 5.21 0729 signal conditional

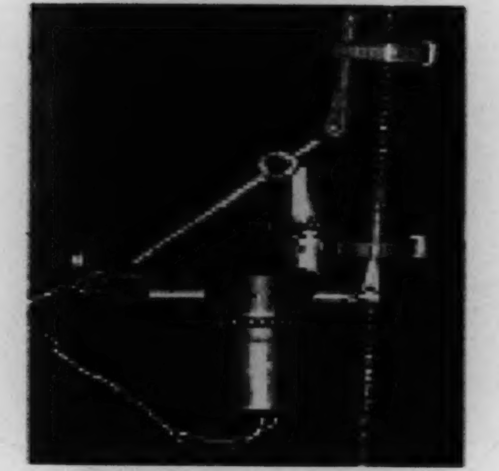

Figure 5.22 Photograph showing the appearance of the tilt transducer

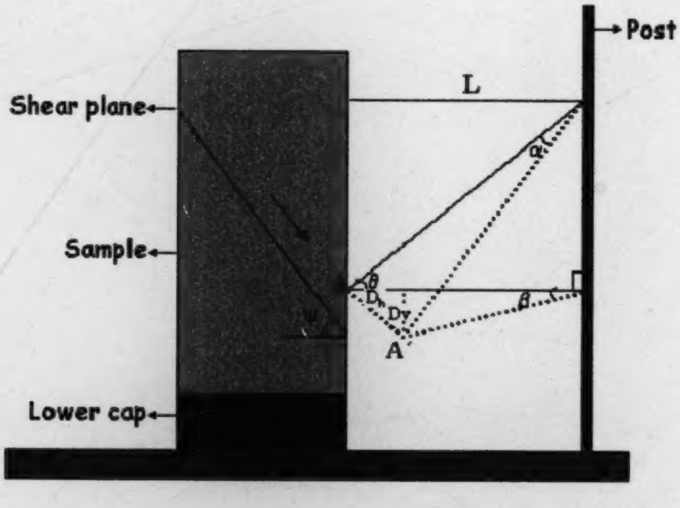
Post
L
Shear plane
Sample
Lower cap
α
θ
D
Dv
β
ψ
A

Figure 5.23 Principle of the tilt transducer (assuming a rigid block movement)

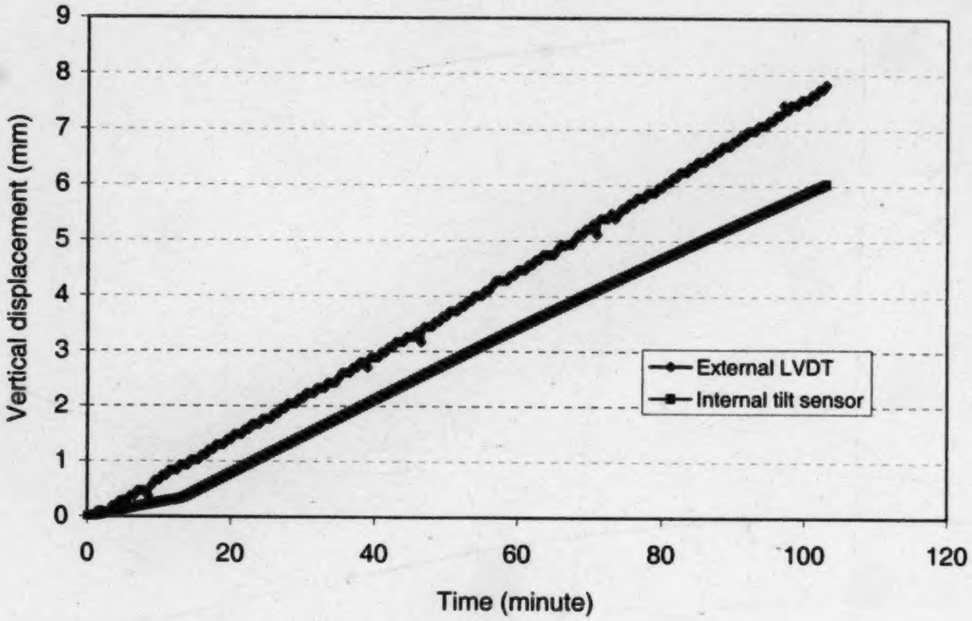

Figure 5.24 Typical vertical displacements measured by external LVDT and internal "tilt" sensor for an Athabasca clay sample

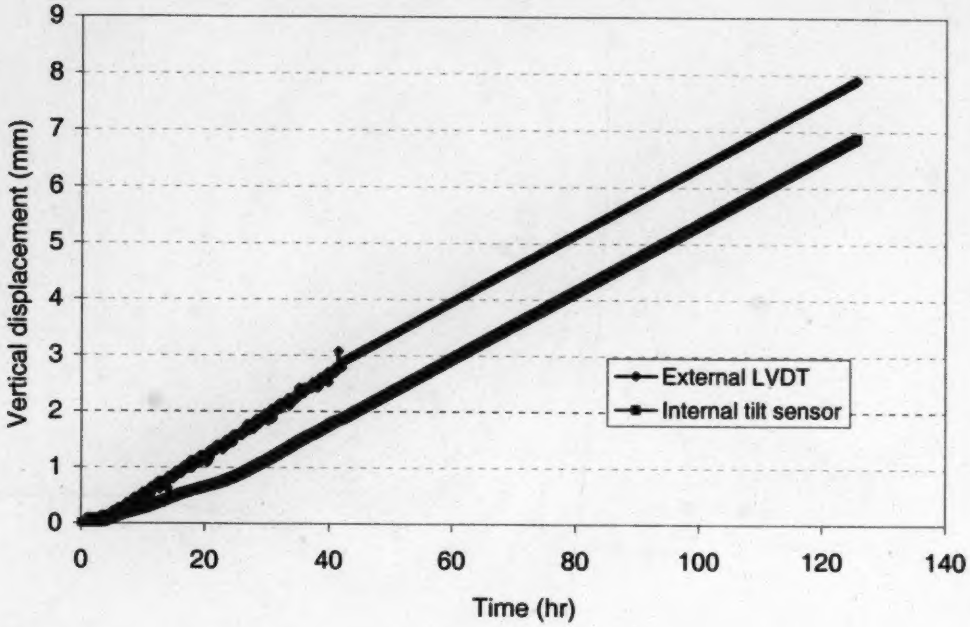

Figure 5.25 Typical vertical displacements measured by external LVDT and internal "tilt" sensor for a Highvale mudstone

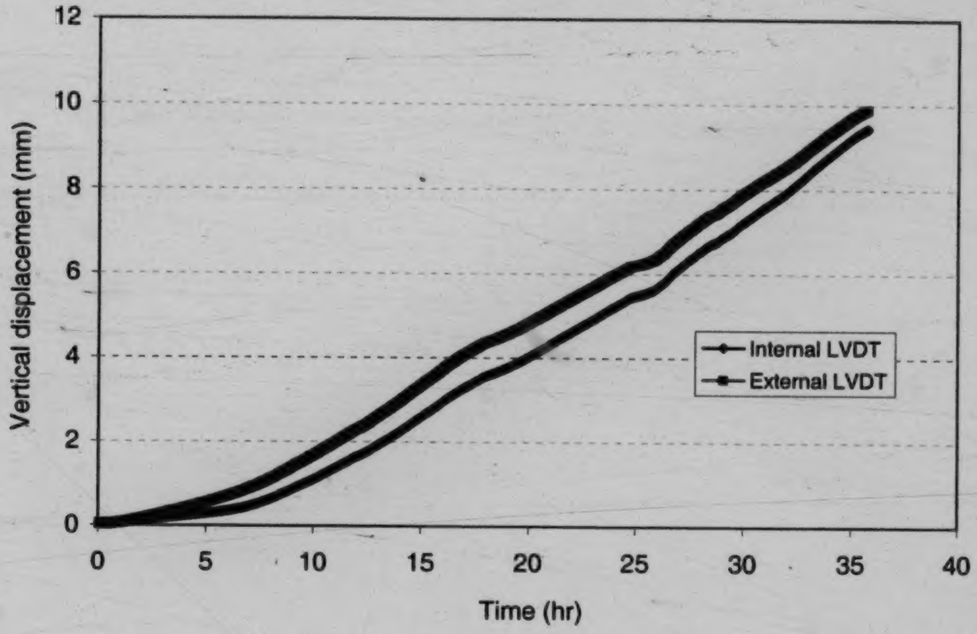

Figure 5.26 Typical vertical displacements measured by external LVDT and internal LVDT for a Suncor weak rock sample

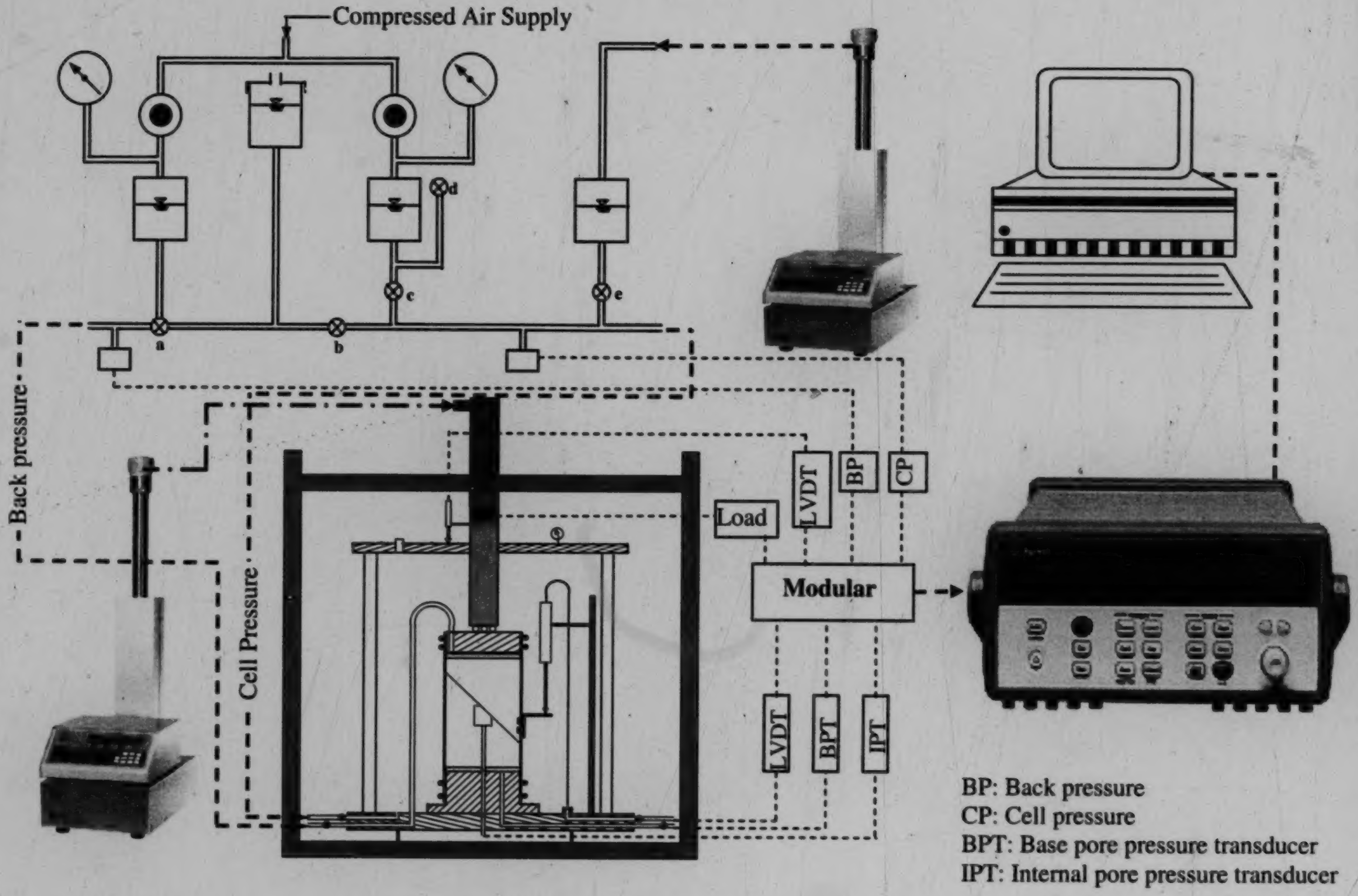
Compressed Air Supply
a
b
c
d
e
Back pressure
Cell Pressure
Load
LVDT
BP
CP
Modular
LVDT
BPT
IPT
BP: Back pressure
CP: Cell pressure
BPT: Base pore pressure transducer
IPT: Internal pore pressure transducer

Figure 5.27 layout of the measurement system

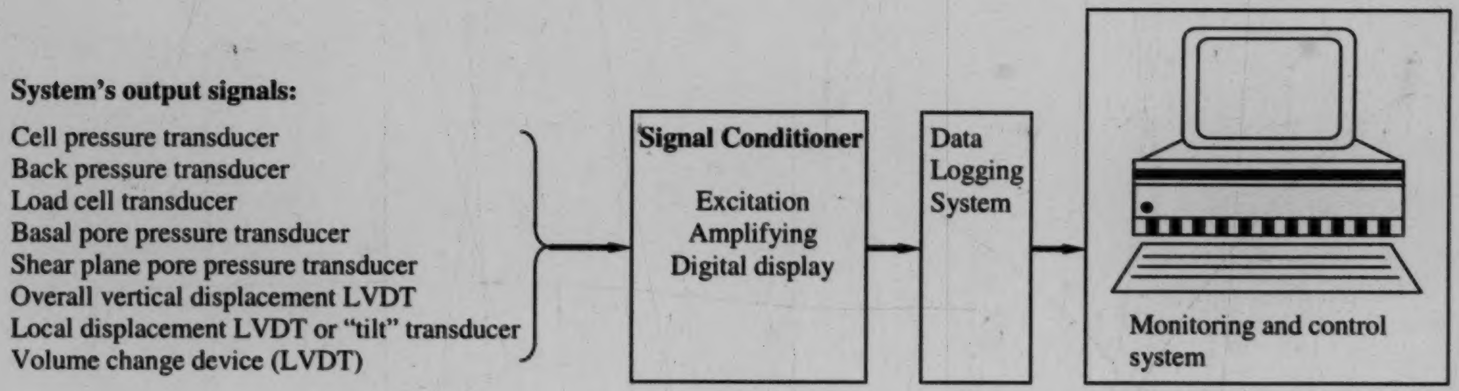
System's output signals:
Cell pressure transducer
Back pressure transducer
Load cell transducer
Basal pore pressure transducer
Shear plane pore pressure transducer
Overall vertical displacement LVDT
Local displacement LVDT or "tilt" transducer
Volume change device (LVDT)
Signal Conditioner
Excitation
Amplifying
Digital display
Data
Logging
System
Monitoring and control
system

Figure 5.28 Schematic representation of data logging and control system

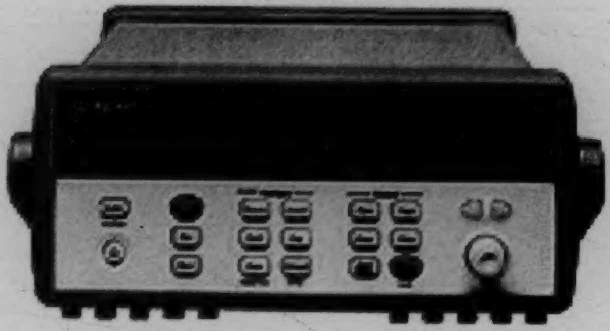

Figure 5.29 Agilent 34970A Data Acquisition/Switch Unit

Figure 5.30 Data Dolphin data logger

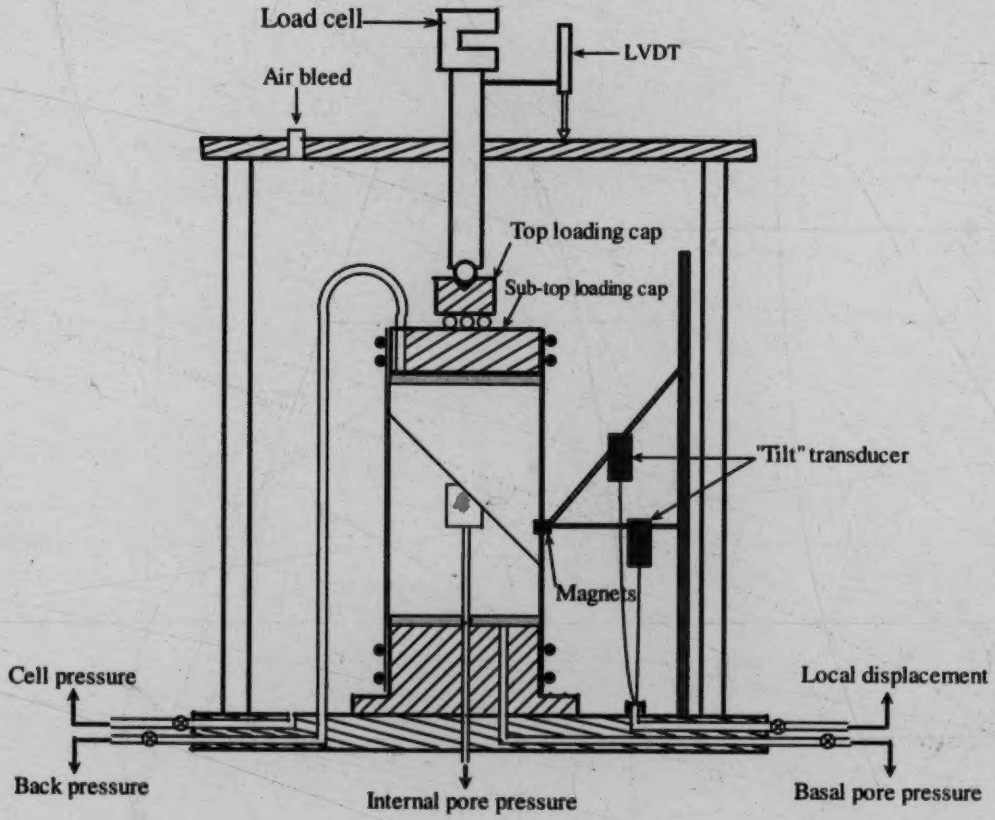
Load cell
LVDT
Air bleed
Top loading cap
Sub-top loading cap
"Tilt" transducer
Magnets
Cell pressure
Local displacement
Back pressure
Internal pore pressure
Basal pore pressure

Figure 5.31 Sketch of the set-up of the modified triaxial cell (not to scale)

CHAPTER 6 TESTING PROCEDURES FOR CONSOLIDATED UNDRAINED TRIAXIAL TESTS WITH PORE-PRESSURE MEASUREMENTS ON A SHEAR PLANE

6.1 INTRODUCTION

This chapter describes the test procedures adopted for consolidated undrained triaxial tests with pore-pressure measurements on a shear plane. The equipment calibration, specimen preparation, saturation techniques, consolidation, and data-analysis procedures are discussed. Procedures for installing the internal pore-pressure transducer and setting up the local displacement transducer are also explained.

6.2 CALIBRATION OF MEASUREMENT INSTRUMENTS

Instrument calibration is the determination of the relationship between an observed reading and the physical quantity being measured. The calibration of instruments and equipment is an essential factor in maintaining a high standard of reliability in the laboratory. Calibration data should always be readily available for reference or displayed alongside fixed instruments such as transducers. Re-calibration or additional regular checks will be necessary for items used intensively. Items that have been misused, or which are suspected of giving erroneous results, should be re-calibrated immediately. For some transducers, the data logger system during the tests should be same as that in the calibration for the specific excitation voltage. Calibrations, in this test program, were required for the following electronic monitoring devices:

- 3 – 3447.5kPa (500psi) strain gauge pressure transducers
- 2 – 1034kPa (150psi) strain gauge pressure transducers
- 1 – volume change device LVDT (DC type)

- 2 – triaxial cell external LVDTs (DC type)
- 1 – triaxial cell internal submersible LVDT (AC type)
- 3 – 1MPa internal pore pressure transducers
- 2 – 2MPa internal pore pressure transducers
- 3 – 3MPa internal pore pressure transducers
- 1 – "tilt" transducer for the local displacement measurement
- 1 – 8.9kN (2klb) load cell for the modified triaxial cell
- 1 – 222.4kN (50klb) load cell for the large triaxial cell

The calibration of the strain gauge pressure transducers was carried out by using a DPI 603 pressure calibrator and a Data Dolphin data logger and software or a voltmeter. The transducer used for measuring the load or pressure should have a clearly defined "fixed zero" point, which is obtained before applying any load or pressure. The maximum load or pressure used for calibration should be very close to the maximum load or pressure used for the tests.

The LVDT in the volume change device was calibrated against a graduated burette for volume response and against a micrometer scale for linear displacement compliance. Similarly, the triaxial cell LVDTs were calibrated against a micrometer scale.

The internal pore pressure transducer was calibrated by using a DPI 603 pressure calibrator, a gas collector, and Data Dolphin data logger and software. The "zero" point was obtained after filling water into the gas collector but before applying any load or pressure. The maximum load or pressure used for calibration should be very close to the maximum load or pressure used for the tests.

The "tilt" transducer's levels were calibrated by using a Universal Bevel projector set and data logger system. This projector can move in two opposite directions to check the output from the level.

An external load cell, of 8.9kN (2klb) capacity, for the modified triaxial test apparatus was calibrated against the proving rings of compatible load capacity. The proving ring calibration was checked against another hydraulic loading system gauge at the University of Alberta. This gauge had been calibrated independently in order to verify the accuracy of the proving rings. An external load cell of 222.4kN (50klb) capacity was calibrated against a Tinius Olsen compression test machine, which was calibrated by Cal-Chek Canada – a factory-trained service and calibration company.

6.3 TEST MATERIALS AND SAMPLE PREPARATION

6.3.1 Test Materials

Laboratory tests were scheduled on reconstituted Athabasca clay samples, disturbed mudstone samples, and high-quality undisturbed weak rock samples. Athabasca clay is a dark brown silty clay (CL). The mudstone was taken from the Highvale coal mine, west of Edmonton. The high-quality undisturbed weak rocks were taken from Athabasca Oil Sands projects near Fort McMurray, northern Alberta. These weak rocks included Peleosol and highly weathered limestone. The detailed characteristics of these materials will be described in Chapter 7.

6.3.2 Sample Preparation

6.3.2.1 Reconstituted Athabasca clay samples

The reconstituted clay samples were made by compacting Athabasca clay with a Modified Proctor hammer under a moisture content about 3~5% wet of the optimum moisture content. The use of a high moisture content gives the samples a high initial degree of saturation and thereby reduces the time needed for saturation under certain back pressures during the tests (Black and Lee, 1973) and makes cutting a plane on the sample easy. The compaction was conducted in accordance with the standard procedures in ASTM D-1557. Firstly, the air-dry clay material was thoroughly mixed to the required moisture content using a Hobart soil mixer. Then the mixed soil was compacted in a split mould with a diameter of 100mm and a volume of about 944cm^3 by using a 4.5kg rammer falling 45mm. The soil was compacted in 5 layers, with each layer receiving 25 blows from the rammer. The compacted samples were then wrapped with plastic wrap and aluminum foil and placed in the moisture room for one week to 10 days for maturing. After a sample had matured, it was taken out to be trimmed to the required dimensions (about 67mm in diameter) by using a sample trimmer. The length of the samples used for the tests was about 140mm. The trimmed sample was then cut to form a shear plane. According to the Mohr-Coulomb criterion, a sample should be sheared along a plane inclined at an angle of $45°+\phi/2$ to the major principal stress plane during the triaxial test. Figure 6.1 shows that the lowest strength occurs when a discontinuity's normal is inclined at an angle of $45°+\phi/2$ to the major applied principal stress (Hudson and Harrison, 1997). This figure also specifies that if a sample has a discontinuity which is inclined at an angle βw, $\beta_1 < \beta_w < \beta_2$ (Figure 6.1), to the major principal stress plane, the sample will fail along this discontinuity during a triaxial test under this applied stress state. Assuming the friction angle of a shear plane in Athabasca clay was around 20°, then the angle of the cut plane in the reconstituted clay sample was about 55°. The sample was cut in a wooden trough, which had a pre-cut plane of 55°, by using a wire saw.

6.3.2.2 Highvale mudstone samples

The cylindrical mudstone samples in the required diameter, which were used for the tests, were cored from the mudstone blocks by using a Milwaukee Dymodrill and a core barrel. The bored samples were then wrapped with plastic wrap and aluminum foil and placed in the moisture room. For the same reason that a shear plane was cut into the reconstituted clay sample, a 55° shear plane was cut in mudstone sample by using a mechanical saw. A wood wedge with an inclined plane of 55° was made in advance and placed on the saw's supporting plane to assure the sample was cut at 55°. Tap water was used to cool and clean up the sample during the cutting. In order to eliminate the influence of a cut plane's roughness on the pore pressure on such a plane, the cut plane in each sample was polished by using fine sandpaper. Figure 6.2 shows a cut plane before and after polishing.

6.3.2.3 Undisturbed weak rock samples from Suncor sites

The undisturbed block samples with dimensions of about (250~300) × (250~300) × (250~300) mm^3 containing a shear zone were taken from Suncor test pits in the field by using a chain saw. One sample from test pit 18, 3 samples from pit 26, and 3 samples from pit 20 were taken. Before the samples were taken, the test pits' slope surface was cleaned by using an excavator, and the upper part of the slope was excavated to expose the fresh material. The block samples were then cut from this slope's fresh area (see Figure 6.3). Figure 6.4 shows a cut block sample. After being cut, these block samples were immediately wrapped with two plastic bags and gauze. These wrapped samples were then put into pre-prepared wood boxes. Some plastic foam was placed around each sample. The samples were then coated with paraffin wax on site. These coated samples were shipped to Edmonton and stored in a moisture room.

The cylindrical samples for the laboratory tests were bored from these block samples in the laboratory and required a shear zone/plane at about 55° to the horizontal plane. Generally, the shear zone/plane in the block samples was not in this direction. Therefore, directly coring the block samples was not possible without first rotating the blocks. A block sample was first unpacked from the wooden box, and then placed into a dismountable mould. After rotating the sample in the mould to let the main displacement shear be about 55° to the horizontal plane and marking the drilling position on the mould, the space between the mould and the sample was filled with a wet mixture of plaster and sand in a ratio of 1:2 (see Figure 6.5). The sample was stored in a moist room one to two days for plaster hardening. After the plaster had hardened, a cylindrical sample was bored by using a fly-auger type core barrel. This barrel can bring the debris out with its flying wing, but no both water and air were used, so the sample was not disturbed. Figure 6.6 shows the 100mm core barrel used for sample coring.

6.4 SAMPLE MOUNTING PROCEDURES

6.4.1 Installation of the Magnet Pieces

In order to measure the local displacement along the shear plane in the reconstituted clay samples, a pair of magnets was used to connect the "tilt" transducer to an "ideal" point on the sample wall (see Figure 5.21). One magnet was placed inside the sample, while another was epoxied on the "tilt" transducer. After several trials, a Rare-Earth 99K31.01 magnet was chosen for this test. This magnet is 6.35mm in diameter by 2.54mm thick and can lift a 1.134kg block of steel. A magnet that is either too big (strong) or too small (weak) is not good for the test. If the magnet is too strong, the one inside the sample will be pulled out by the other one during the installation of the transducer. If the magnet is too weak, the attraction between the two magnet pieces will not be strong enough to hold them together, thereby influencing the test results. The "ideal" point at which a magnet is installed should be in the maximum shear plane inclination profile, and such a point was located about 2.5 to 3cm above the lowest point of the shear plane (see Figure 6.7). Before the magnet was placed into a sample, a small steel pin was placed into the hole for the magnet. The pin's end that was in contact with the magnet had the same diameter as the magnet. The function of this steel pin was to pull the magnet toward the sample to protect this magnet from being pulled out by another magnet on the transducer.

For the tests on the undisturbed Suncor samples, a submersible LVDT was used to record the displacement along the shear plane. This LVDT was supported by a small right-angled steel strip fixed on the sample wall by 4 magnets, which were divided into two groups to be placed into two holes in the sample (see Figure 6.8). The magnets used were the Rare-Earth 99K32.03, which is 9.5mm in diameter and 2.54mm thick and stronger than the one used in the clay samples. Like the "ideal" points in the clay samples, the "ideal" points at which magnets are installed also should be in the maximum shear plane's inclination profile.

6.4.2 Placement of the Internal Pore-pressure Transducer

The inclined end face of the pore-pressure transducer has the same angle as that of the shear plane, so the transducer can be placed right on the shear surface. Because the tubing connected to the transducer has a smaller diameter than that of the transducer, a small hole with the same diameter as the tubing was bored first from the sample base to the shear plane, and then this small hole was over-bored in the diameter of the transducer on the shear surface. For clay samples, these holes were drilled by hand by using drilling bits, but the holes for the mudstone samples and the undisturbed samples were drilled by a machine. The length of the over-bored hole was slightly shorter than that of the transducer for the clay samples so that the transducer had to be pushed into the samples to avoid water leakage (flow) along the tubing. But for the mudstone samples and the undisturbed samples, the length of the over-bored hole was slightly longer than that of the transducer so that a small amount of mud could be placed under the transducer to avoid water leakage (flow) along the tubing. After the hole had been bored, the pore-pressure transducer was placed from the shear plane down to the sample base. First, the wires and tubing were put through, and then a hard push was used to place the transducer into the hole. A syringe needle was used to fill the gap between the porous stone and the gauge surface with distilled water, and then the saturated porous stone was put into the transducer holder. The small vacancy above the transducer was filled with clay. After the pore-pressure transducer had been placed into position, the top half of the sample was put back and taped in place with grey tape. The area around the tubing on the clay sample's base was smeared by using a knife, while for the mudstone samples and undisturbed samples, the mud made from the sample material was used to fill the small gap between the tubing and the hole wall to avoid water seepage along the tubing. All these processes are shown in Figure 6.9. Note that the procedures described above were for the first-time use of an internal pore-pressure transducer. After the first sample was tested, the transducer was taken out and put into distilled water to maintain its saturation for direct use in the second and following samples.

6.4.3 Sample Mounting

After the pore-pressure transducer had been placed in the sample, the sample was placed upside down on a table to install the lower porous stone and the lower cap. The tubing of the transducer was sealed with an O-ring, a ferrule, and a nut (see Figure 6.10). The lower cap and sample were then mounted on the pedestal by using 3 cap-screws (4 cap-screws for the large cell) after the sample had been adjusted to keep the magnet exactly facing the tilt transducer (or the submersible LVDT). The tape securing the sample was then taken off, and the upper porous stone and the upper cap were put in place. The side surfaces of both the lower and top caps were coated with a thin layer of silicone grease. Side drains of filter paper were fitted around the sample and upper porous stone and about 5mm above the lower porous stone to make sure the filter paper does not connect upper and lower porous stones. The rubber membrane was extended laterally by using a membrane stretcher to facilitate insertion of the sample. O-rings were then fixed on the lower and upper caps.

After tape had been removed from the mudstone samples, the upper halves would not stay in place. As a result, the upper half of each sample was taken off first, and the filter paper side drains and the rubber membrane were put in place. After fixing the lower end of the rubber membrane on the lower cap, the membrane was rolled down to the lower end of the shear plane. The upper half of the sample was then placed on the lower half, and the membrane was rolled back to hold the whole sample and the upper cap. This process is shown in Figure 6.11.

The tilt transducer, held on a post inside the cell, was correctly connected to the "ideal" point (magnet) and adjusted to the required position. In the large cell, the right-angle steel strip was adjusted to the right position to support the LVDT that was being held on a post. After connecting the drainage line and placing the steel ball or ring bearing on the upper cap, the cell top and cell wall were lowered over the pedestal and assembled on it by using six tie rods (four strong tie rods for the large cell). The cell wall was sealed by using a thick O-ring to apply pressure to the pedestal. The triaxial cell and sample were then held up and placed in the loading frame. For the large cell, the cell base with the mounted sample was placed in the loading frame first. The cell wall was then carefully placed on the cell base by using a crane (see Figure 6.12) and sealed by using a thick O-ring to apply pressure on the pedestal. The frame top was also installed by using a crane (see Figure 6.13) and was fixed on the frame columns with six strong screws. The wires of the internal pore-pressure transducer were led to the outside through a trough in the base of the pedestal. The final step of the sample mounting involved in filling the cell with water and connecting the cell-pressure system, the back-pressure system, the pore-pressure-measurement system, the external LVDT, and the load cell.

6.5 TESTING PROCEDURES

Prior to conducting test, all the tubings were flushed with de-aired water, and the pressure in the compressed air-water reservoirs was reduced to atmospheric pressure. A series of readings was performed for the pressure transducers. The average value of these readings corresponded to the zero reading of the pressure transducers.

6.5.1 Saturation

In triaxial tests on saturated soils, saturation is normally carried out as a first step. The most usual method in practice is to apply back pressure to the pore fluid incrementally, alternating with increments of confining pressure. The back pressure is always a little less than the confining pressure to ensure that the effective stress remains positive.

6.5.1.1 Rationale for testing under conditions of complete saturation

The saturation of the testing specimens is very important for taking pore-pressure measurements on a shear plane. Athabasca clay is classified as silt clay (CL) according to the United Soil Classification System (USCS). This type of clay's saturation is about 95% when it is compacted at its optimum moisture content (Craig, 1987). The specimens used for this test were compacted at 3-5% wet of the optimum moisture content, so it is reasonable to say that their saturation was over 95%. Even so, 3-5% air still remained in the sample. In addition, although careful laboratory procedures were followed to saturate the test cell and drainage lines by using water to displace the air in the system, a small amount of air, i.e., up to about 10 ml, which was less than one percent of the system's total fluid volume, was found to be present in the apparatus after mounting each sample (Agar, 1984). Henry's coefficient of the volume solubility of air in water is 0.026 (Fredlund, 1976), which implies that approximately one atmosphere (100kPa) back pressure is required to dissolve each 2.6 percent of initial air saturation. Full saturation or a level of saturation very close to full saturation is a must for this test in order to obtain reasonably accurate test results. A common procedure for increasing the rate of air sorption in laboratory samples is to apply an elevated back pressure.

Entrapped air bubbles in the system can significantly influence the pore-pressure response in undrained tests because of the relatively high compressibility of air. Despite the relatively high back pressure used in this research, it was deemed necessary to establish some quantitative evaluation of the degree of saturation achieved.

6.5.1.2 Saturating specimens by back pressure

The advantages of using an elevated back pressure to obtain full saturation are summarized as follows:

- Air in the void spaces within the specimen is forced into solution under the applied pressure when full saturation is reached.
- Any air trapped between the membrane and the specimen is also dissolved.
- Any air bubbles remaining in the drainage line and pore-pressure connections, which could not be flushed out, are eliminated. This result improves the response time of the pore pressure and avoids the risk of air bubbles impeding the drainage to the back pressure.

- Reliable pore-pressure measurements and permeability measurements can be made on soil in which saturation was achieved by applying back pressure (Head 1986)

Lowe and Johnson (1960) showed that the theoretical back pressure required to bring a specimen from an initial degree of saturation, S_i, to a final degree of saturation, S, by both compression and solution of the pore air is

$$P = P_i \frac{(S - S_i)(1 - H)}{1 - S(1 - H)}, \qquad [6.1]$$

in which

P is the change in pressure required to increase saturation from S_i to S,

P_i is the initial absolute pressure corresponding to S_i, and,

H is Henry's constant, which at normal room temperature is approximately equal to 0.02 cc of air per 1 cc of water.

For complete saturation, S = 1, Equation 6.1 reduces to

$$P_{100} = 49 P_i (1 - S_i), \qquad [6.2]$$

in which P_{100} represents the back pressure required to provide 100% saturation.

If the initial pressure, P_i, is atmospheric, by substituting a standard atmosphere of 101.32 kPa and assuming that a degree of saturation of 90% is reached after the specimen is flushed, the required back pressure, P_{100}, is calculated to be 497kPa.

During the course of this study, a minimum back pressure of 500kPa was maintained on the reconstituted-clay specimens and mudstone specimens at all times, and 800kPa was maintained on the undisturbed samples.

When pressured deaired water is introduced into the void spaces in a specimen, an immediate increase in the degree of saturation occurs due to the compression of air in accordance with Boyle's law. Assuming that none of the free air goes into solution in the pore water, from Boyle's law it follows that the degree of saturation, S, resulting from an applied back pressure, P, is (Black and Lee, 1973)

$$S = 1 - \frac{1}{49R + \frac{1}{1 - S_i}} , \qquad [6.3]$$

where, $R = P/P_{100}$.

The application of P_{100} to any specimen will immediately produce a condition of 98% saturation or greater. However, to increase S to 99% requires twice the back pressure, and to increase S to 99.8% requires 10 times P_{100} unless the initial degree of saturation is already close to or greater than these final amounts.

The time required for saturation under the appropriate back pressure ($P = P_{100}$) depends on the initial degree of saturation of the specimen, and whether a degree of saturation of 100% must be obtained or whether a slightly lower value is acceptable. The theoretical times for final saturation values of 99%, 99.5% and 100% are plotted graphically in Figure 6.14 (Black and Lee, 1973). The time required appears to be greatest when the initial saturation lies in the range of 75 to 85%. This time decreases dramatically when the initial saturation exceeds 95%. A substantial saving of time results if 99.5% or 99% saturation can be accepted.

6.5.1.3 B value

The pore-pressure response of most saturated sands and clays to an undrained isotropic stress increment can be expressed as the equation below (Bishop, 1966)

$$B_{100} = \frac{1}{1 + nC_w / C_s}. \qquad [6.4]$$

where

B_{100} is pore-pressure parameter for a fully saturated specimen,

C_w is the compressibility of the pore water,

C_s is the compressibility of the soil skeleton,

n is the porosity of the soil.

The value of the pore-pressure parameter B, for saturated Athabasca clay at room temperature, is very closed to unity, but for intact mudstone may range from about 0.35 to 0.85. Therefore, the common criterion used to test compressible soil samples for full saturation, i.e., a B value approaching unity, applies to only Athabasca clay, and is clearly not valid for low-compressibility intact mudstone samples.

However, after a plane was cut on a mudstone sample, this plane could not be fully closed after the cut sample was put back together. This is equivalent to a great increase in the compressibility of the soil skeleton, C_s. In this case, the B value for a cut mudstone sample was much greater than that of an intact mudstone sample and was verified by tests to be close to 1. Similarly, for the undisturbed weak rock samples with a shear zone or shears, the compressibility of the skeleton, C_s, is much greater than that of the unsheared weak rock, and the B value is close to 1. Therefore, B-value criteria can be used to evaluate the saturation of both mudstone samples and the undisturbed samples, which have either cut planes or shear zones.

Black and Lee (1973) developed the following expression, based on the pore-pressure parameter B, for calculating the initial degree of saturation of a sample:

$$S_i = \frac{1 - Z(1 - B)}{1 - ZQ}, \qquad [6.5]$$

where

$$Z = \frac{C_s \Delta\sigma_3 / n_i}{1 - P_i / (P_i + B\Delta\sigma_3)}, \quad Q = Bn_i \frac{C_w}{C_s},$$

in which

n_i is the initial porosity, and

$\Delta\sigma_3$ is the change in confining pressure.

For a fully saturated specimen, $S_i = 1$, Equation 6.5 converts to the Bishop equation for B_{100}, Equation 6.4.

In deriving equation (6.5), Black and Lee (1973) assumed that Henry's coefficient was H = 0, since very little time is allowed for air exsolution during a "B" test. During the tests in this study, the clay samples were saturated at a back pressure of about 500kPa for about 48 hours or more, and the mudstone samples were saturated at a back pressure of about 500kPa for about 24 hour or more, while the undisturbed samples were saturated at a back pressure of about 800kPa for more than 100 hours throughout the laboratory investigation.

6.5.1.4 Evaluating degree of saturation --- B-test

During triaxial testing, the commonly used procedure for assessing the degree of saturation of samples and apparatus is summarized by Bishop and Henkel (1962) and Head (1986). The procedure involves shutting off the drainage line to the sample, then applying increments of isotropic confining pressure (cell pressure) and measuring the undrained pore-pressure increase with each increment of the confining pressure. The ratio of the pore-pressure increase to the confining pressure increment is the B value. The main disadvantage of using the standard B-test procedure is that the effective confining stress increases, thereby recompressing the test materials prior to performing other strength or compression tests (Agar, 1984).

Wissa (1969) described an alternate procedure for evaluating the B parameter and degree of saturation for soils of low compressibility. His method is based on the fact that the pore-pressure response in fully saturated soils is independent of the magnitude of the back pressure, whereas in unsaturated soils, the pore pressure varies with the back pressure. The following steps were followed in computing the B parameter:

1) Before applying the increments of confining pressure, the initial readings of the confining pressure, back pressure, and pore pressure were recorded.
2) With pore-pressure fluid drainage prevented, a 50kPa increment of isotropic confining pressure was applied.
3) The pore-pressure response was measured, and the B value was calculated as a ratio of the resulting increase in the pore pressure to the cell-pressure increment.
4) The pressure in the back-pressure system was increased the same amount as the increment in the cell pressure (50kPa). The pore fluid drainage valves were opened to the back-pressure to restore the initial effective stress.
5) With the new back-pressure level, steps 2, 3, and 4 were repeated. These incremental B-tests were conducted for at least three pressure levels to ensure that the pore-pressure response had stabilized.

6.5.2 Consolidation

The standard consolidated undrained triaxial test is a compression test in which the specimen is first consolidated under an equal all-round pressure and is then caused to fail by increasing the axial stress under the condition of no drainage (Bishop and Henkel, 1962).

During the consolidation, the drainage of the excess pore pressure took place from the upper end of the sample. The vertical filter-paper side drains, which were fitted around the sample and upper porous stone and about 5mm above the lower porous stone, also allowed drainage from the radial boundary and speeded up the consolidation of the sample (see Figure 6.15). Measurement of pore pressure was made on both the shear plane and the base. Bishop and Henkel (1962) and Head (1986) detailed the procedures.

The drainage of the pore water resulted in a decrease in volume and an increase in the effective stress, which, after consolidation, was equal to the difference between the confining pressure and the mean pore pressure remaining in the sample. The consolidation of a sample was judged from the pore-pressure dissipation, U, at any time, which is expressed as follow

$$U = \frac{u_0 - u}{u_0 - u_b} \times 100\%, \qquad [6.6]$$

where

u_0 is the initial pore water pressure immediately before consolidation,
u_b is the back pressure, which is a constant during the consolidation, and
u is the measured pore pressure either on the shear plane or on the base.

The effective stress selected for consolidation is related to the in-situ conditions. For the test on the remoulded sample, the unique effective stress selected was about 100kPa because of no referenced in-situ condition. For the undisturbed samples, the *in situ* stress is about 950kPa. During the consolidation, the excess pore pressure was difficult to completely dissipate due to the friction between the rubber and the groove in the wall of the volume change reservoir and the time limitation. A 95% dissipation of the excess pore pressure at the base can be considered as an acceptable threshold value and may allow the tests to be completed more quickly than they could be by attempting to achieve 100% dissipation. Another function of the consolidation in this test is that the consolidation pressure can close the cut shear plane so that the pore-pressure measurement is more accurate.

6.5.3 Shearing of Samples

The displacement-control method was used to load a sample to fail in this program. In conventional triaxial tests, the selection of the deformation rate depends on the type of test (drained or undrained), type of soil, size of sample, and side drains used (Head, 1986).

In this study, the objective was to measure the pore-pressure response of a shear zone/plane related to practical projects, so the selection of the deformation rate was based on engineering practices and limitations of time. Millimeter per day probably is the permitted maximum value for most projects. Therefore, 0.0007%/min (1.44mm/day vertical displacement rate) to 0.014%/min (28.8mm/day) strain rates were used for the reconstituted samples and the mudstone samples, and 0.001%/min (2.88mm/day) to 0.005%/min (14.4mm/day) strain rates were used for the undisturbed samples. In order to investigate the influence of a high strain rate on the pore pressure on the shear plane, a strain rate of up to 1.43%/min (2880mm/day) was used for the tests on the reconstituted samples.

It is needed to know that membrane penetration around the corner of a sample block at the tip of the shear plane will greatly affect the pore pressure response during shearing. Therefore, the amount of the displacement along the shear plane should be controlled during shearing to avoid membrane penetration at the tip corner of a shearing block. Fortunately, the membrane used in the tests can accommodate quite a large shear deformation and the shear displacement is not so big during this test. The membrane penetration can be neglected.

6.6 ANALYSIS OF DATA

After the end of each test on the reconstituted specimens the specimen was cut into slices which were parallel to the shear plane and then oven-dried overnight to measure the water content. To judge the water transmission, this water content can be compared with the water content before the test.

The cell pressure, back pressure, and pore pressure values were obtained through the readings of corresponding transducers. These readings were corrected for the zero readings. The cell pressure was also corrected for the use of latex rubber membrane in the triaxial test.

The axial load was corrected for the friction and the weight of the loading ram. During the triaxial test, the cross-section area of the specimen was different at different time, so an area correction was needed. The conventional filter-paper side drains applied an additional stress to the deviator stress, so side-drain correction was applied. All these corrections are detailed in the section be[illegible].

The zero reading for the axial strain was the moment that the specimen started taking the axial load. Therefore the axial load must be obtained first and then the axial strain calculated. The shear displacement along the shear plane was calculated according to the vertical displacement measured from the local displacement transducer (the "tilt" transducer or submersible LVDT).

6.6.1 Axial Load Correction

Piston friction reduces the magnitude of the axial load applied to a triaxial sample and is dependent upon the confining pressure and axial stress (Agar, 1984). Internal load cells are generally preferred in geotechnical testing since they directly measure the axial load on the sample, independently of piston friction. An external load cell was used in this experiment, so quantifying the piston friction was necessary. Because the piston friction is confining-pressure and axial-stress dependent, it was measured under the confining pressure that was used in the test. This test was performed by mounting a 222.4kN (50 klb) external load cell and a 17.8 kN (4klb) internal proving ring that had been calibrated in advance. The piston friction, the difference between the internal and external load measurements, was found to be a linear function of the axial stress. The calibration coefficient was 0.045kN/kN.

When a sample fails by sliding along a single plane, as occurred in this study, lateral forces, which can appreciably increase the bushing friction, are introduced. The correction needed also depends on the axial strain, and a deduction of about 1% of the measured load for every 2% strain from the start of slip seems appropriate (Head, 1986). This correction can be applied for the tests on the reconstituted samples and the undisturbed samples. However, for the Highvale Coal Mine mudstone samples, the piston friction introduced by lateral forces appeared to be great. It could not be fully eliminated by using a ring bearing placed on the upper cap. The correction of the piston friction was not practical in this case. Using an internal load cell to measure the axial load was preferable.

6.6.2 Area Correction

When failure occurs by sliding along a surface, the effective plane area, used for calculating the axial stress, decreases as movement takes place. The mechanism is illustrated in Figure 6.16. The axial stress will increase because the effective shear area decreases with the vertical strain. A correction factor, f_s, should be multiplied by the value calculated by using the initial shear area. If θ lies between 27° and 35°, and ε_s does not exceed 15%, an approximate correction factor, f_s, (Head, 1986) is recommended as follows:

$$f_s = \left[1 + \left(0.06\theta \times \frac{\varepsilon_s\%}{100}\right)\right], \qquad [6.7]$$

in which

θ is the inclination of the slip surface relative to the sample axis,

ε_s is the axial strain measured from the start slide

The term "strain" is used above for mathematical convenience and does not have the same meaning as the definition of "strain" after the start of the slide, because the "strain" in the above equation is not dependent on the sample's length. The magnitude of the displacement is more relevant.

6.6.3 Membrane Correction

The restraining effect of the rubber membrane enclosing a triaxial specimen makes a small contribution to the resistance offered against compression. The influence of the rubber membrane on the measured strength of specimens in conventional triaxial compression tests at confining stresses greater than 100kPa is considered to be negligible (Oldakowski, 1994). However, in the case of tests with different stress paths or under high-loading-rate tests, the effective confining stress at failure was as low as several tens kilopascal. Neglecting the restraining effect of the membrane may lead to significant errors in the calculated stress ratios.

The membrane effect in slip plane deformation has been investigated by several researchers (Head, 1986), but the results were not all compatible with one another. Head suggested using La Rochelle's equation to correct the membrane effect, which is illustrated in Figure 6.17. The results were obtained under a slip plane inclined at 35° to the sample axis in a 38 mm diameter sample 76mm long fitted with a rubber membrane 0.2mm thick. For any other sample diameter (D mm), length (L mm), and rubber thickness (t mm), the values derived from the curves (see Figure 6.30) should be multiplied by $\sqrt{\frac{38}{D}\times\frac{t}{0.2}\times\frac{L}{2D}}$. If the inclination of the slip is not 35°, another correction factor, f_θ, should be multiplied.

6.6.4 Side Drain Correction

Tests to determine the correction for the side drains under conditions of single-plane slide were carried out by several workers (Head, 1986) by using 38mm diameter samples of Perspex fitted with bearings on the sliding surface. Based on data from La Rochelle (1967), the simplified drain corrections were plotted in Figure 6.18. Drain corrections for samples of any other diameter (D mm) can be obtained by multiplying the correction by 38/D.

Note that slip plane corrections for both the membrane and the side drain can be avoided by not extending a compression test to a large strain for which only the area correction need be applied (Head, 1986).

6.7 SUMMARY

- The procedures involved in preparing the reconstituted clay samples, the mudstone samples, and the undisturbed samples were described and discussed.
- An objective of this study was to measure the pore pressure on a shear zone/plane. The procedures for mounting samples, especially for the pore pressure transducer, were detailed. The saturation techniques were described.
- Full saturation is vital in a triaxial undrained test with pore-pressure measurements. In the course of this study, different techniques of specimen saturation were evaluated, and specimen saturation by back pressure was chosen. A proper B-test, an integral part of the saturation procedure, was defined.
- The required corrections and calculations in the analysis of the resulting data were described. They included the effect of the membrane and drains, the area corrections, and axial load correction

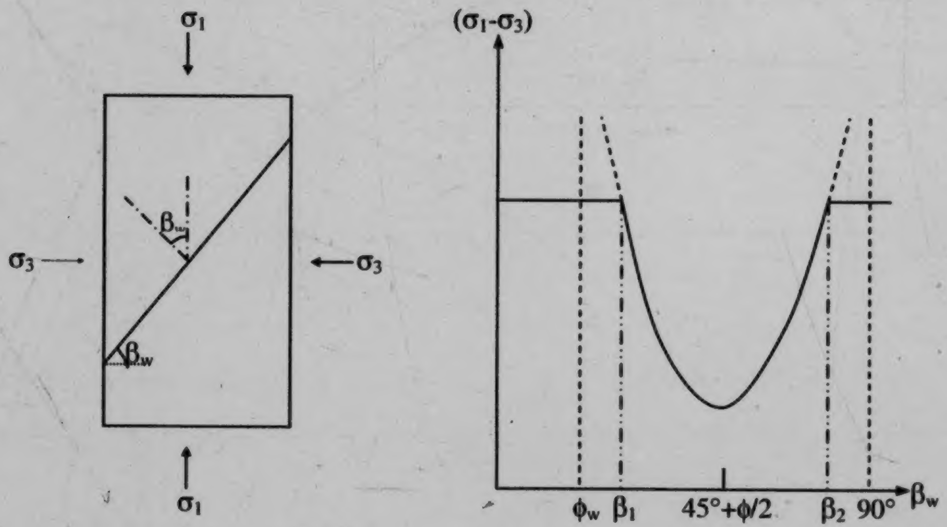

σ_1
σ_3
σ_3
β_w
β_w
σ_1
$(\sigma_1-\sigma_3)$
ϕ_w
β_1
$45°+\phi/2$
β_2
$90°$
β_w

Figure 6.1 Effect of a discontinuity on the strength and failure mode of a sample (modified from Hudson and Harrison, 1997)

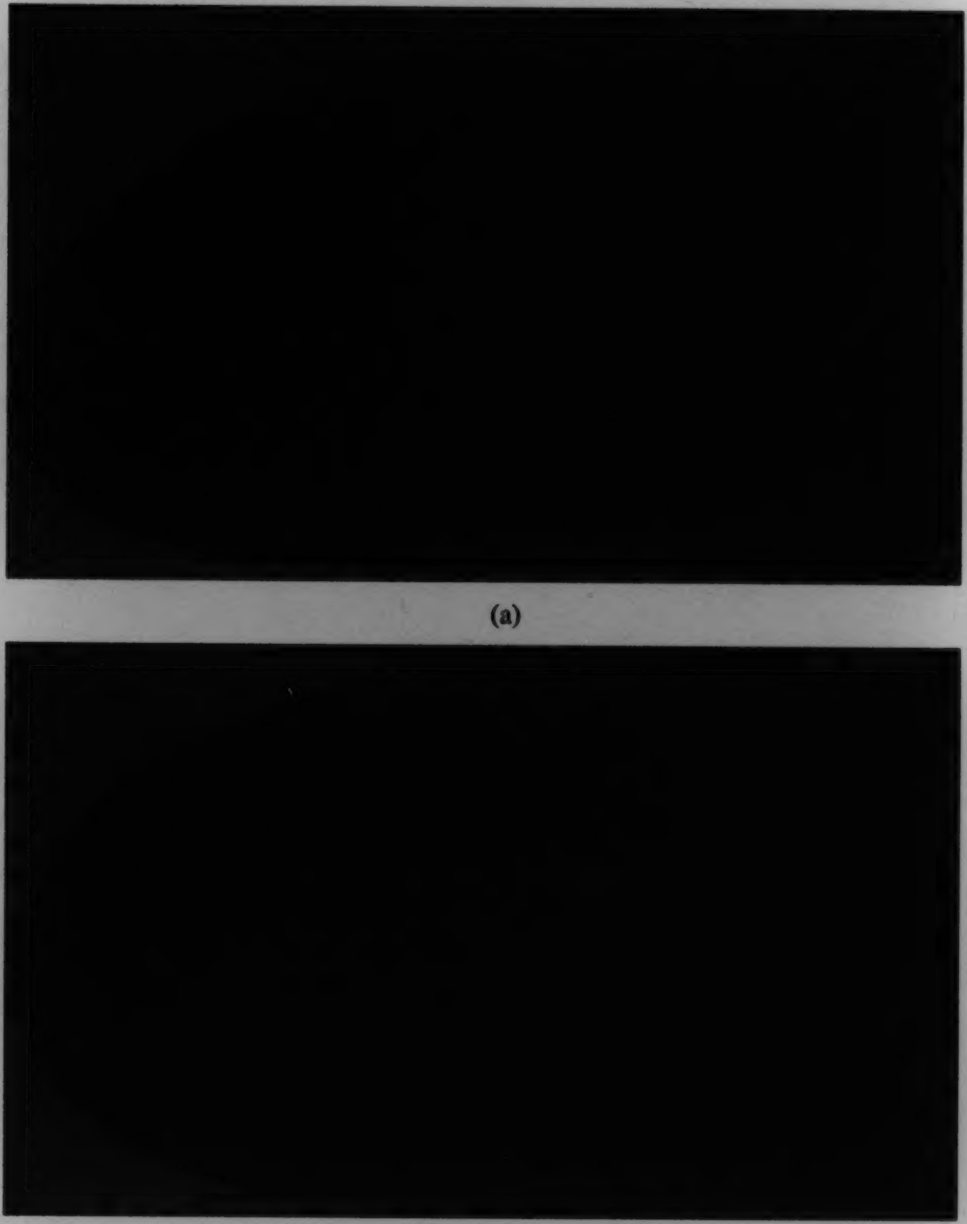

(a)

(b)

Figure 6.2 Photographs showing a cut plane before (a) and after (b) polishing

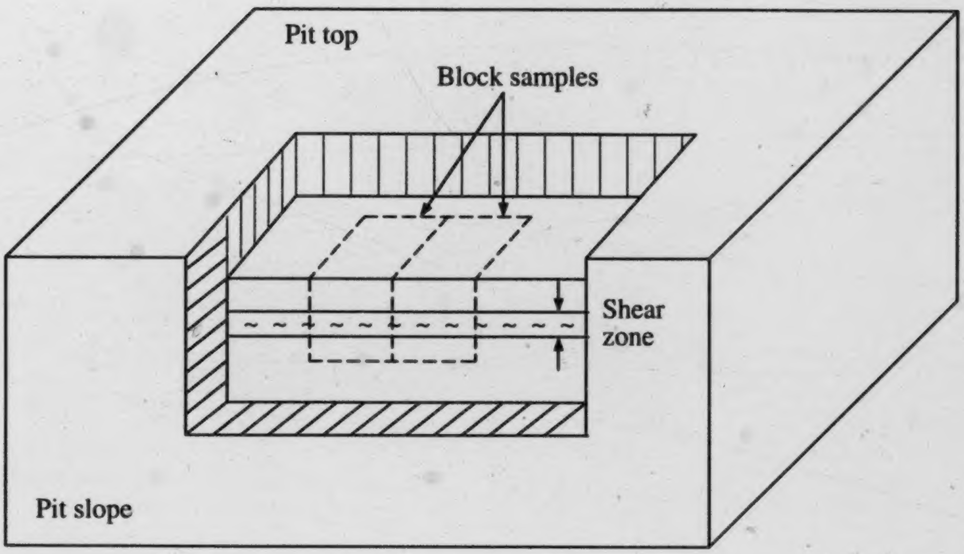
Pit top
Block samples
Shear
zone
Pit slope

Figure 6.3 Sketch of sampling of the block samples in the test pits

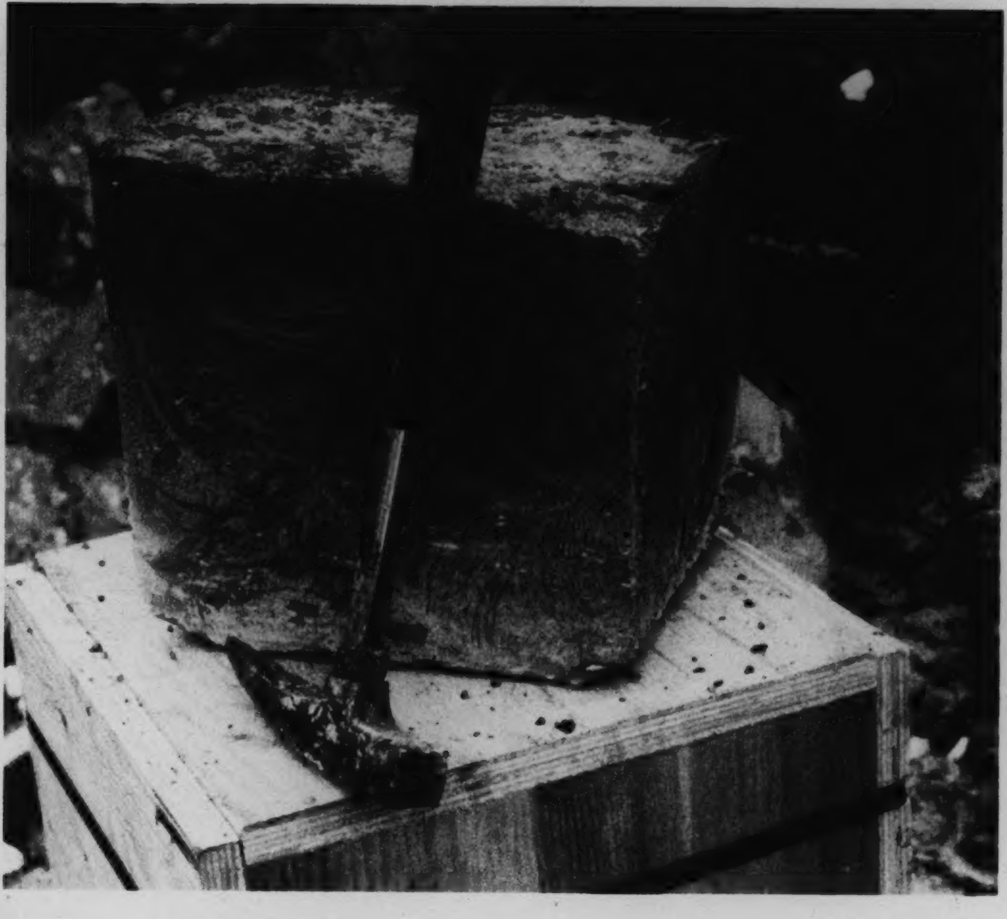

Figure 6.4 Photograph showing a block sample

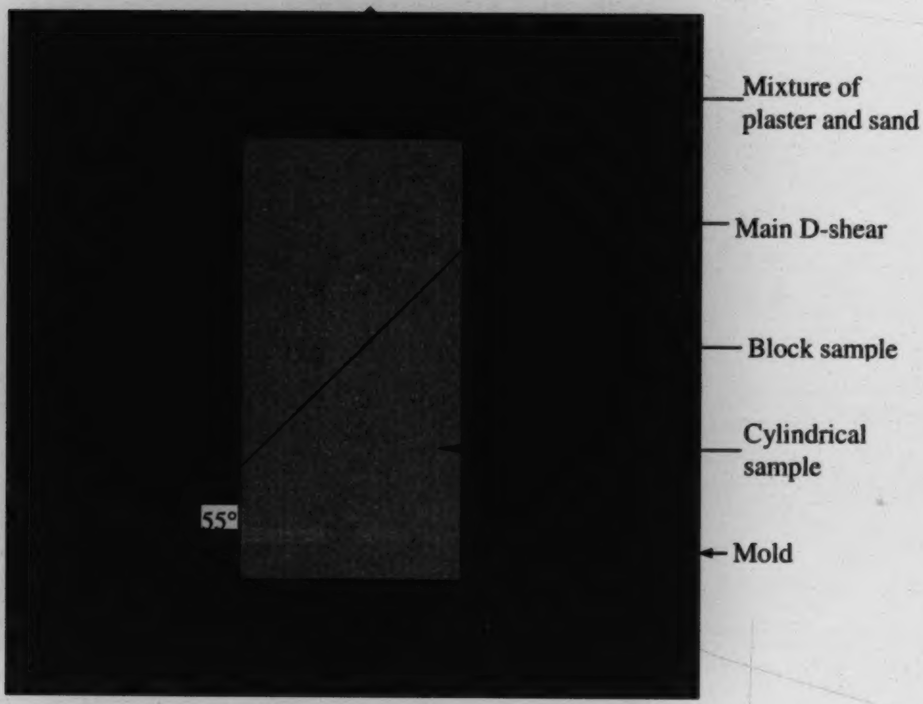
Mixture of plaster and sand
Main D-shear
Block sample
Cylindrical sample
Mold
55°

Figure 6.5 Sketch of sampling of the laboratory samples

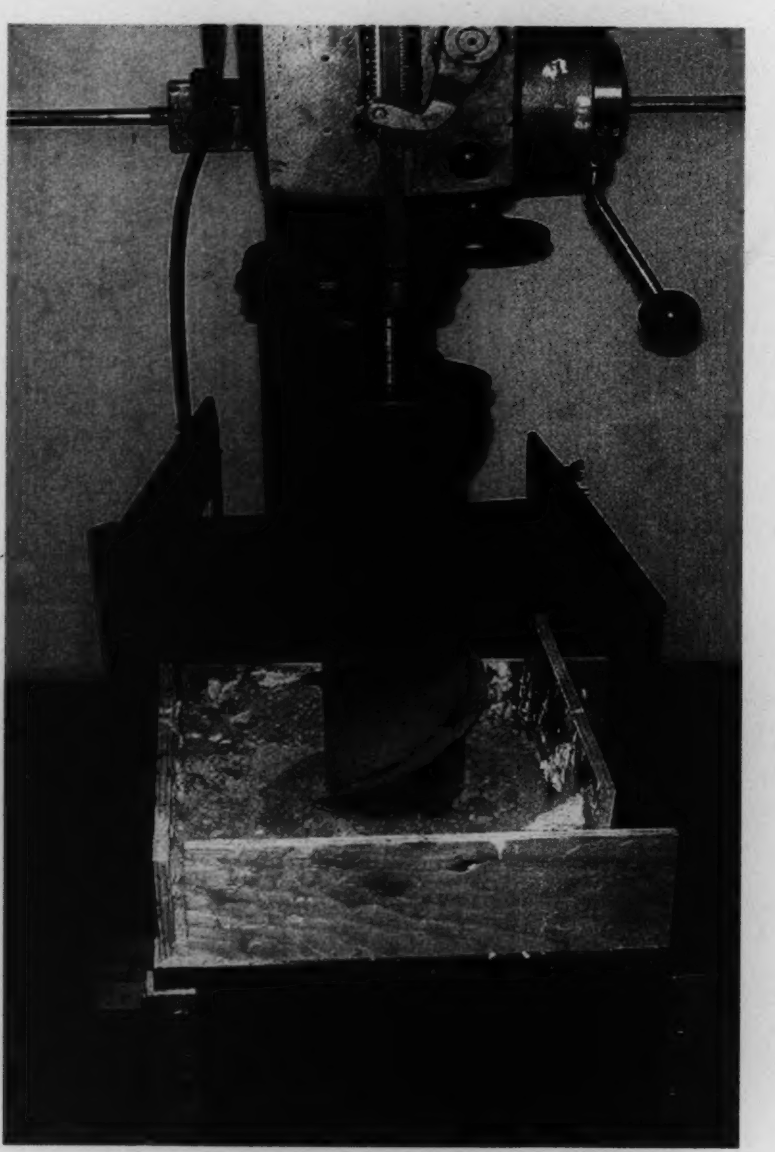

Figure 6.6 Fly-auger type core barrel used for sample coring

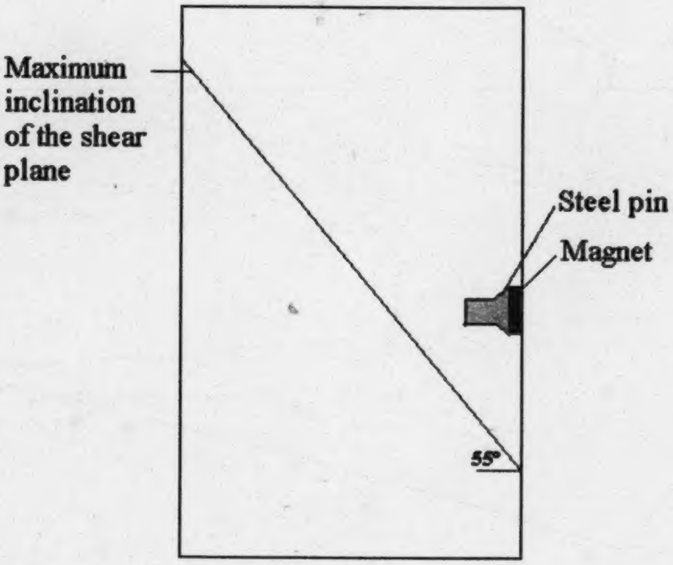
Maximum inclination of the shear plane
Steel pin
Magnet
55°

Figure 6.7 Schematically showing the position of the magnet in a sample

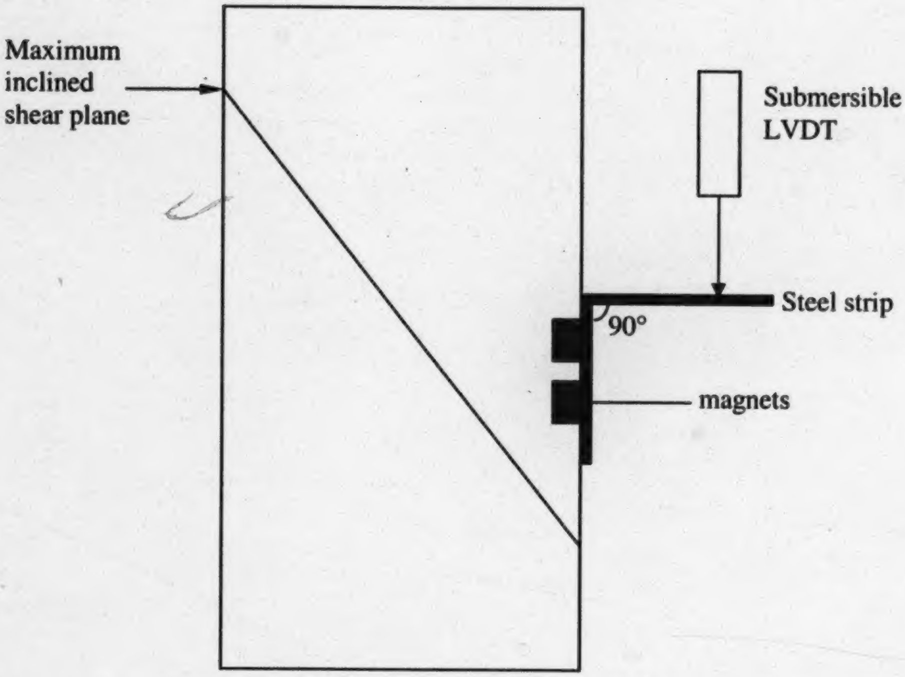
Maximum inclined shear plane
Submersible LVDT
Steel strip
90°
magnets

Figure 6.8 Schematically showing the relationship between the magnets and the sample, the steel strip, and the LVDT

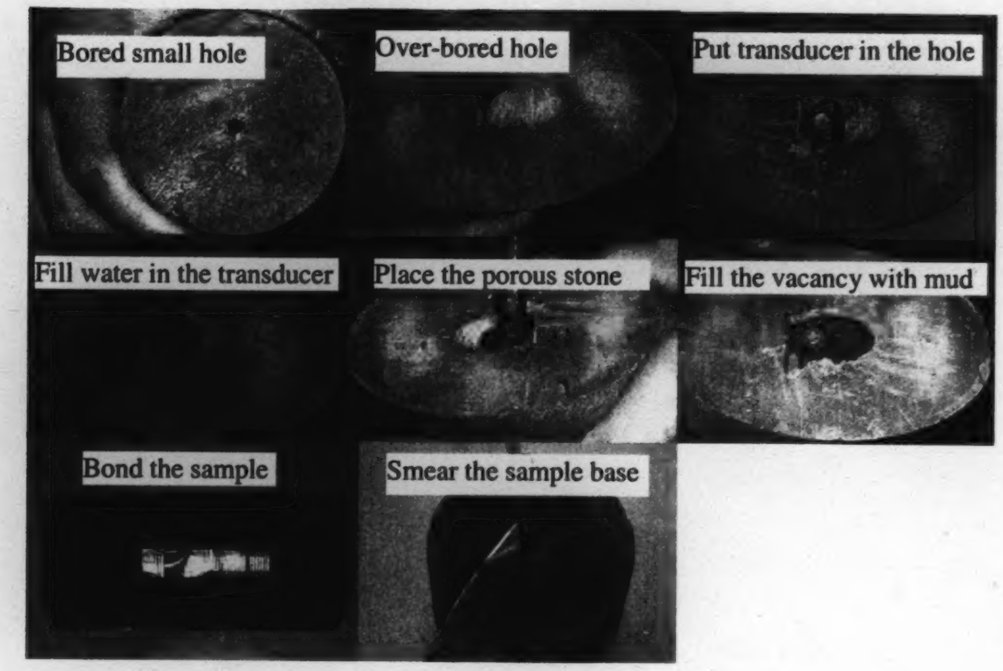
Bored small hole
Over-bored hole
Put transducer in the hole
Fill water in the transducer
Place the porous stone
Fill the vacancy with mud
Bond the sample
Smear the sample base

Figure 6.9 Photographs showing the procedures of the internal pore pressure transducer installation

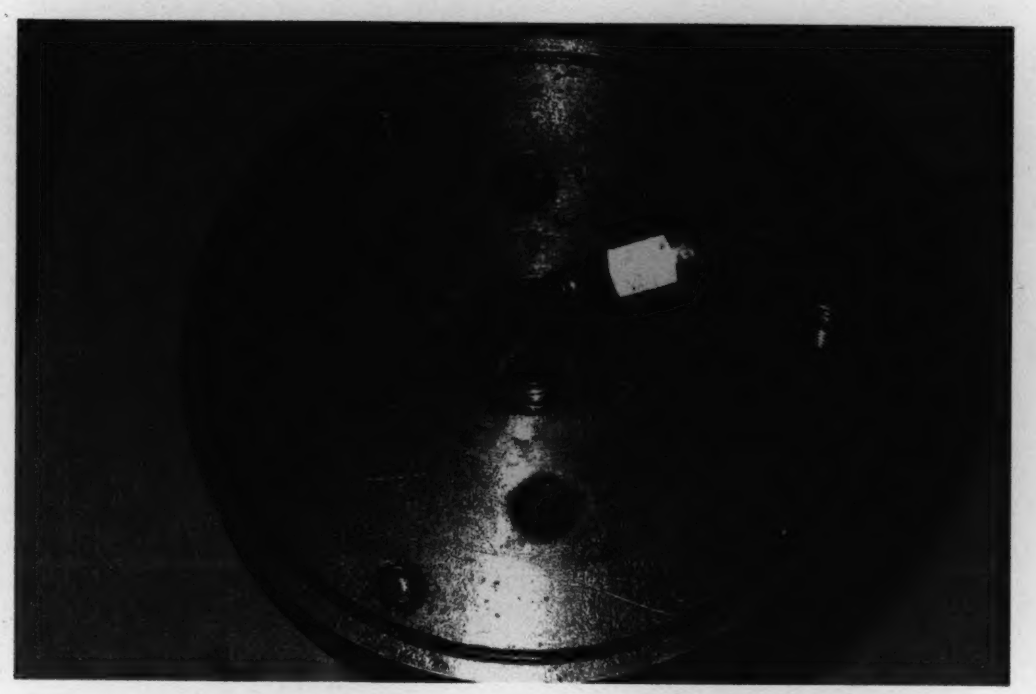

Figure 6.10 Photograph showing the seal of the transducer tubing

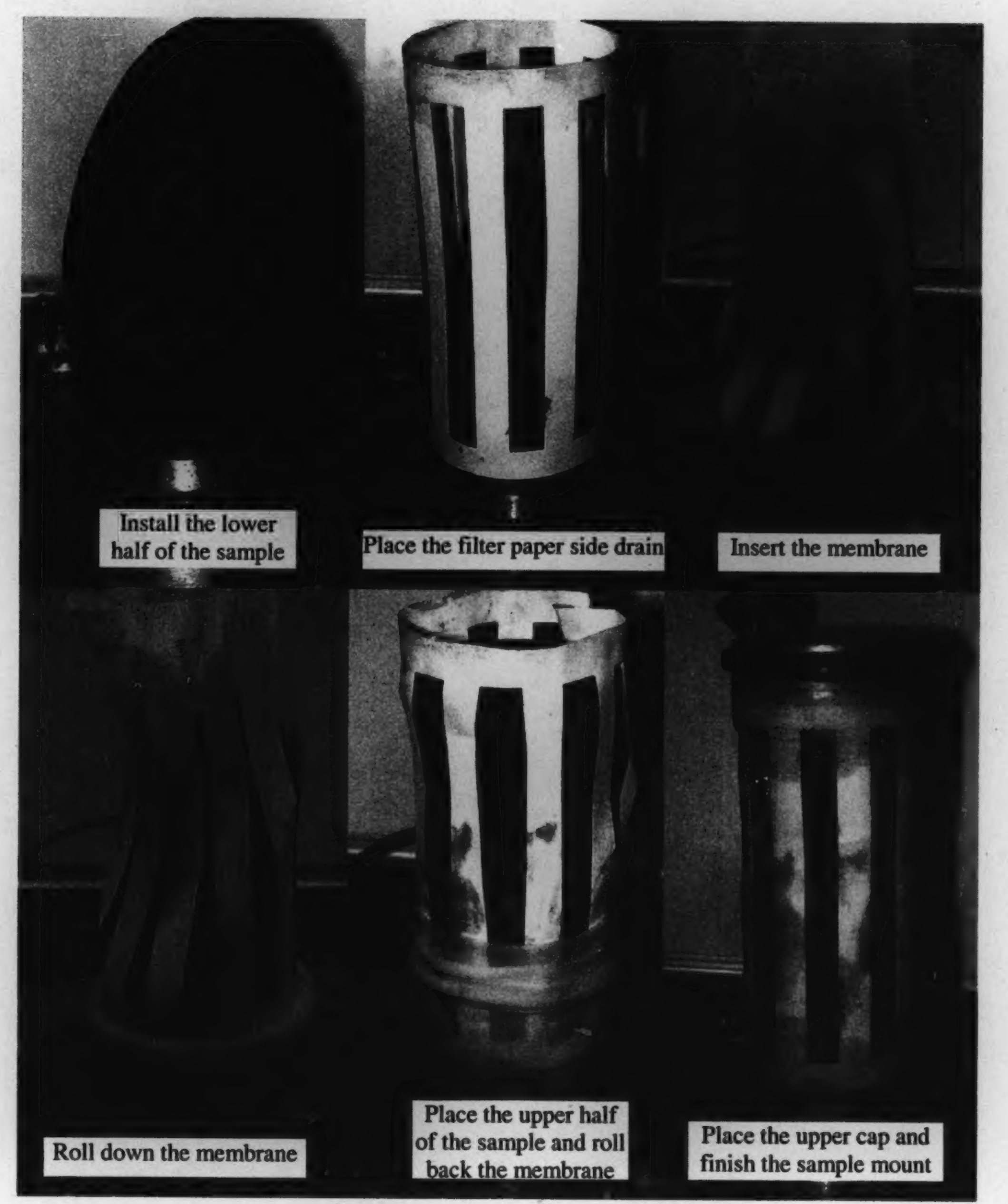
Install the lower half of the sample
Place the filter paper side drain
Insert the membrane
Roll down the membrane
Place the upper half of the sample and roll back the membrane
Place the upper cap and finish the sample mount

Figure 6.11 Set-up of a mudstone sample

Figure 6.12 Installation of the large cell wall with a crane

Figure 6.13 Installation of the frame top by using a crane

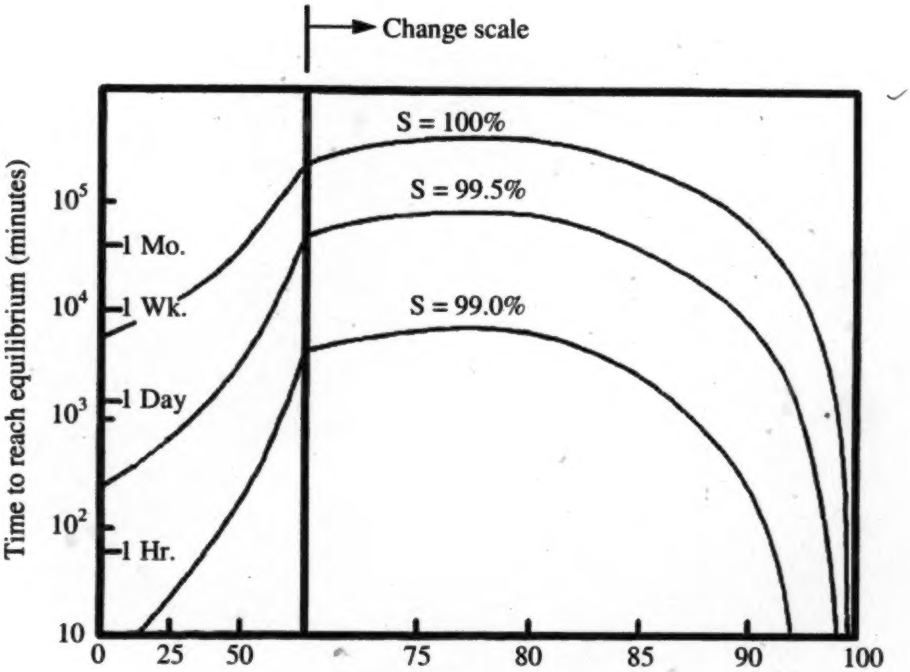

Figure 6.14 Time to reach a degree of saturation using back pressure (modified from Black and Lee, 1973)

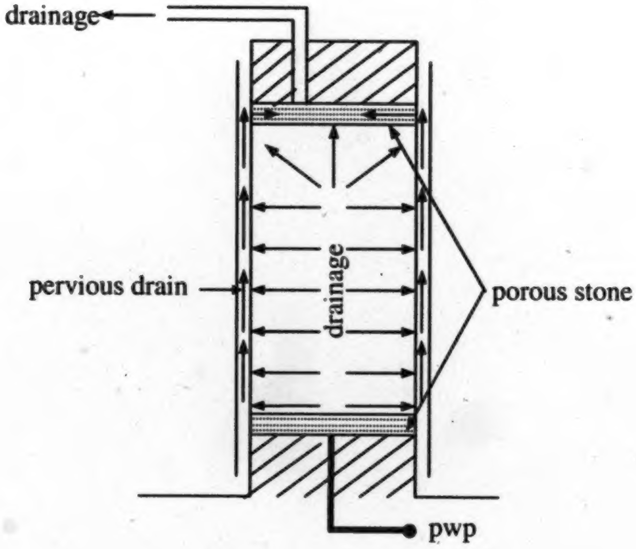
drainage
pervious drain
drainage
porous stone
pwp

Figure 6.15 Drainage from end and radial boundary during consolidation (side drains of filter paper were fitted about 5mm above the lower porous stone)

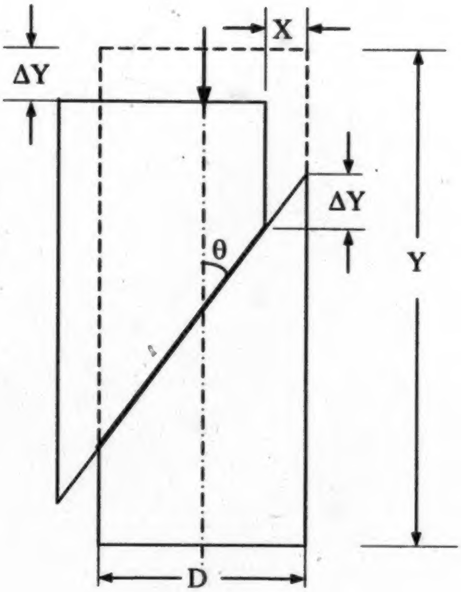

Figure 6.16 Mechanism of single-plane slip for area correction

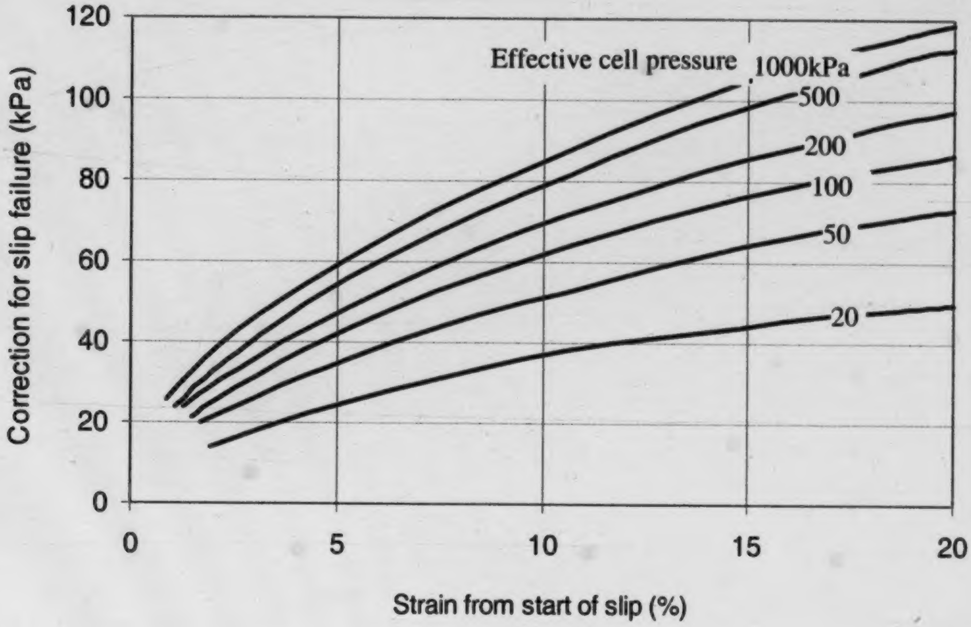

(a)

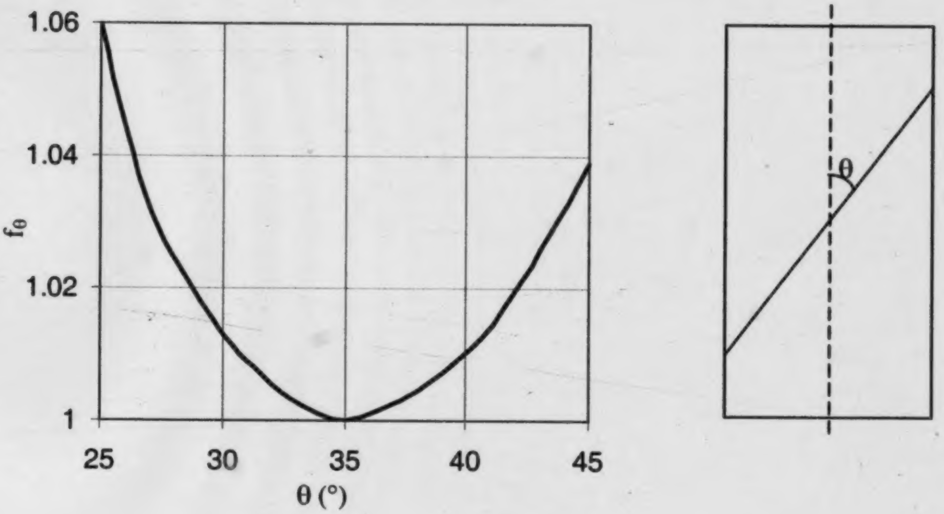

(b)

Figure 6.17 Membrane corrections for single-plane slip: (a) correction curve, (b) value of factor f_θ for various inclinations of slip plane (modified from Head, 1986)

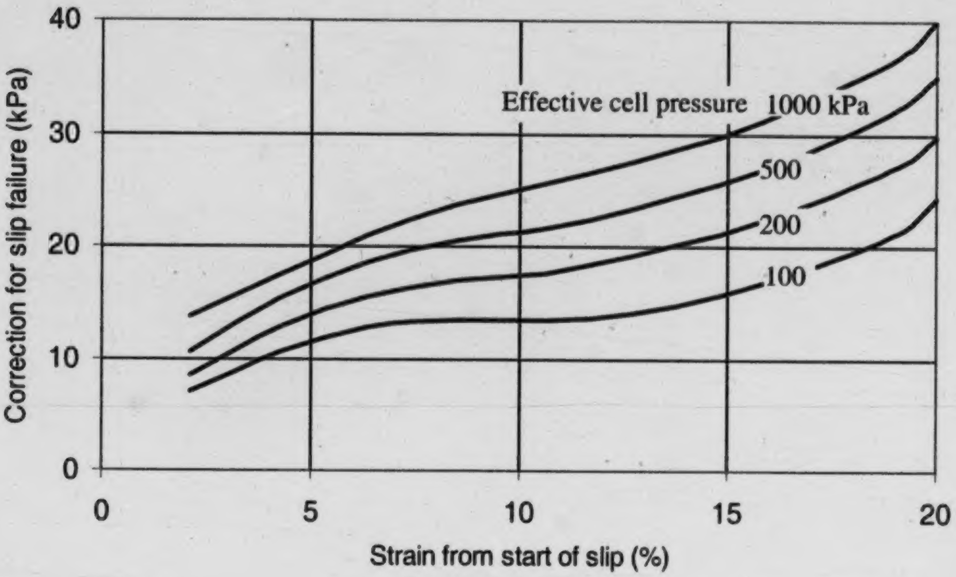

Figure 6.18 Drain correction curve for single-plane slip (modified from Head, 1986)

CHAPTER 7 PORE-PRESSURE RESPONSES AND SHEAR BEHAVIOR OF SHEAR ZONES IN THREE MATERIALS

7.1 INTRODUCTION

The design and evaluation of a soil structure located in or founded on a shear zone requires a good understanding of the zone's shear behavior and pore-pressure response. Measuring a shear zone's pore pressure in the field is very difficult, if not impossible, due to the zone's unknown position and its thinness. Laboratory tests were used to measure a shear zone's pore pressure and to obtain an understanding of the zone's pore-pressure-response characteristics under different displacement rates. The exact determination of the shear strength of a shear zone is quite difficult because of its complex fractures. This chapter presents pore pressures and shear characteristics measured on a shear plane under different loading rates and, for comparison, on the sample base for three different materials.

7.2 TEST MATERIALS

Laboratory tests were carried out on reconstituted Athabasca clay, Highvale mudstone, and Fort McMurray weak rocks. These weak rocks include Paleosol and highly weathered argillaceous limestone. According to the United Soil Classification System (USCS), Athabasca clay is a dark brown silty clay (CL). The specimens used for the tests were compacted at about 5% wet of optimum moisture content by using a Modified Proctor hammer (Chapter 6). The characteristics of Athabasca clay are presented in Table 7.1. Figure 7.1 presents its grain-size distribution. The test data are presented in Tables A7 and A8.

The mudstone taken from the Highvale coal mine is a member of the Paskapoo Formation, Tertiary to Upper Cretaceous in age (Small, 1989). The rock is indurated and cemented with montmorillonite and is highly bentonitic. Core samples and highwall mapping showed the mudstone had been crushed with jointing in numerous directions. Short, discontinuous slickensides were detected along many joint contacts (Small, 1989). The mudstone had several layers within it, varying in colors from blue-grey to brown with interbeds of clay clasts, siltstones, and coal. According to the USCS, the mudstone was described as CH: a highly plastic inorganic clay. The Liquidity Index, I_L, for the mudstone was between -0.4 and 0, indicating that it was over-consolidated. Activity for the unit ranged from 0.58 to 0.70, confirming the presence of montmorillonite. The characteristics of the mudstone are presented in Table 7.2. In this study, the intact mudstone blocks were taken from the Highvale coal mine dumps, and the cylindrical specimens were cored from these blocks (Chapter 6).

Paleosol near Fort McMurray is a waxy, slickensided, greyish green or greenish grey clay or silty clay. It also may take on a rusty orange or a whitish "bleached" soil-like appearance, or may be slightly indurated with minor development of marcasite nodules and sideritic cement (Beardow and Horne, 1987). The argillaceous limestone is one of the main mother stones to form the Paleosol. If the limestone is not fully weathered, especially by chemical weathering, the Paleosol will contain many calcium carbonate nodules. Many discontinuous shears and slickensides have developed in the Paleosol. Some shear surfaces are rough, and striations are common. Sometimes, several sets of striations in different orientations are present. The characteristics of Paleosol are presented in Table 7.3. Figure 7.2 shows its grain-size distribution. The test data are presented in Tables A7 and A9.

The highly weathered argillaceous limestone found in pit 18 is brownish grey. The shear zone developed in it is grey to dark grey. The weathered argillaceous limestone found in pit 26 is from brownish grey to whitish grey with an increase of calcium carbonate content downward. The calcium carbonate occurs in pockets and strips and is white in color. Several sub-horizontal continuous shears developed are highly polished, planar, and shiny. The characteristics of the highly weathered limestone are presented in Tables 7.4 and 7.5. Figure 7.2 shows its grain-size distribution. The test data are presented in Tables A 7 and 10. The sampling techniques are described in Chapter 6.

7.3 TEST CONDITION AND SPECIMEN INFORMATION

7.3.1 Test Condition

One of the main objectives for this study was to measure the pore pressure on the shear zone/plane and to investigate the pore-pressure response of a shear zone and its adjacent material under different displacement rates related to engineering practice. Therefore, the displacement rate is one of the important experimental parameters. In engineering practice, for both a slope and a foundation, millimeter per day probably is the maximum permitted displacement rate. Hence, a displacement rate of millimeter per day was selected for the tests. Considering the limitations of equipment and time, the displacement rates in Table 7.6 were selected for this program. One objective of the tests on the compacted Athabasca clay was to establish the test methodology, so higher displacement rates were also used for testing to investigate rate effects.

The consolidation pressure was another parameter that had to be chosen for testing. For the Fort McMurray weak rock samples, the *in situ* overburden pressure was selected as the consolidation pressure so that the sample could be restored to its *in situ* state. For the Athabasca clay samples and the mudstone samples, 100 kPa consolidation pressure was chosen for tests to investigate their pore-pressure response under different displacement rates.

7.3.2 Specimen Information

Table D1 presents the specimen information for the Athabasca clay, the Highvale mudstone, and the undisturbed Paleosol and the highly weathered limestone.

7.4 TEST RESULTS AND OVERVIEW

7.4.1 Athabasca Clay

The six CIUC (Consolidated, Isotropic, Undrained, and Compression) tests on the Athabasca clay specimens were all performed under a confining stress of 100 kPa at the axial displacement rates of 0.001, 0.005, 0.02, 0.2, 1, and 2 mm/minute by using a modified conventional triaxial testing system. The equipment and procedures used in the testing have been described in Chapters 5 and 6. Figures 7.3 to 7.10 show the test results of one sample under the axial displacement rate of 2 mm/minute. All other tests results are presented in Figures D1 to D40. Figures 7.3, 7.4, D1, D2, D9, D10, D17, D18, D25, D26, D33, and D34 show the consolidation behavior related to the volume change and the pore-pressure dissipation for 6 specimens, respectively. These figures indicate that 6 specimens had similar consolidation characteristics and that the pore-pressure dissipation rate on the plane was greater than that on the base.

Figures 7.5, D3, D11, D19, D27, and D35 present the relationship between the normalized deviator stress, $2q/\sigma'_0$, and the shear displacement at the different axial displacement rates, where q is the same as q′ and equals $(\sigma_1-\sigma_3)/2$ and is normalized with respect to the pre-shear consolidation pressure σ'_0. The comparative results are presented in Figure 7.11. When the axial displacement rate, which is denoted by $\dot{\delta}$, increases from 0.001 mm/minute to 0.02 mm/minute, the deviator stress increases. When the axial displacement rate further increases, the deviator stress decreases within the measured shear displacement. All these curves show that the material has strain-hardening behavior. However, the change in the deviator stress is not uniform for either the stress increase or decrease. When $\dot{\delta}$ increases from 0.001 to 0.005 mm/minute, the deviator stress increases quickly by about 27% at a shear displacement of 7 mm, whereas when $\dot{\delta}$ further increases from 0.005 to 0.02 mm/minute, the deviator stress increases only by 7 % at a shear displacement of 7 mm. When $\dot{\delta}$ increases from 0.02 to 0.2 mm/minute, the deviator stress decreases quickly by about 14% at a shear displacement of 7 mm, and further decreases in $\dot{\delta}$ cause only a very small decrease in the deviator stress.

Figures 7.6, D4, D12, D20, D28, and D36 indicate the change in normalized pore-water pressure $\Delta u/\sigma_0'$, where Δu is the pore-water pressure change on the shear plane or on the base, with the shear displacement at the different axial displacement rates. The comparative results are presented in Figures 7.12 (plane) and 7.13 (base). The test results show that the pore-pressure-changes at the small axial displacement rates (0.001 to 0.02 mm/minute) are almost the same, and that the pore-pressure-changes on the plane and on the base are also similar. However, the pore-pressure-change increases with a further increase in the axial displacement rate, $\dot{\delta}$, at a shear displacement of less than about 4 mm, and the rate of increase in the pore-pressure-change decreases with the increase in $\dot{\delta}$. When the shear displacement increases, the pore-pressure-change in the high $\dot{\delta}$ (0.2 to 2 mm/minute) gradually decreases to a level lower than the pore pressure obtained at the small displacement rate $\dot{\delta}$. The pore-pressure-change on the base always increase with increase in the displacement rate $\dot{\delta}$ and the shear displacement when $\dot{\delta}$ is greater than 0.2 mm/minute.

Figures 7.7, D5, D13, D21, D29, and D37 present the normalized effective stress paths q'/σ_0' versus p'/σ_0' on the plane and on the base at the different displacement rates, where $p' = (\sigma_1'+\sigma_3')/2$ is the mean effective stress. The comparative results are presented in Figures 7.14 (plane) and 7.15 (base). The effective stress paths on the plane at the high shear displacement rates appear to reach the same obliquity, whereas on the base no unified effective stress path envelope is formed in any situation.

Figures 7.8, D6, D14, D22, D30, and D38 show the relationship between the pore-pressure parameter A (on the shear plane only) and the shear displacement at the different axial displacement rates. The comparative results are presented in Figure 7.16. At any displacement rate, the pore-pressure parameter A increases first to reach its peak and then gradually drops with increase in the shear displacement. The peak pore-pressure parameter A_p decreases first and then increases with increase in the displacement rate.

Figures 7.9, D7, D15, D23, D31, and D39 show the relationship between the mobilized friction angle and the shear displacement at the different displacement rates. The comparative results are presented in Figure 7.17. When the axial displacement rate increases from 0.001 to 0.02 mm/minute, the mobilized friction angle increases. When the axial displacement rate increases further from 0.02 to 2 mm/minute, the mobilized friction angles increase quickly to reach their peak at a small shear displacement and then remain constant or slightly decrease with the shear displacement to reach the value obtained at the displacement rate of 0.001 mm/minute. The ultimate friction angle obtained at a high displacement rate is smaller than that obtained at a relatively low displacement rate

Figures 7.10, D8, D16, D24, D32, and D40 indicate the difference in pore-pressure-changes on the plane and on the base. The results indicate that the pore pressure on the base is greater than that on the plane at the small shear displacement rates, but that the difference is very small and negligible. When the shear displacement rate increases, the pore pressure on the plane is greater than that on the base at the small shear displacement but smaller than that on the base at the large shear displacement.

7.4.2 Highvale Mudstone

The three CIUC tests on the Highvale mudstone specimens were also performed under a confining stress of 100 kPa at the different axial displacement rates from 0.001 to 0.01 mm/minute. Figures 7.18 to 7.25 show the test results of one sample under the axial displacement rate of 0.01 mm/minute. All other test results are presented in Figures D41 to D57. Figures 7.18, 7.19, D41, D42, D50, and D51 show the consolidation behavior related to the volume change and the pore pressure dissipation for the 3 specimens. These figures indicate that the 3 specimens have similar consolidation characteristics and pore-pressure dissipation behaviors. The consolidation and pore-pressure dissipation for these materials are much quicker than those for the Athabasca clay. The pore-pressure dissipations on the plane and on the base are very similar.

Figures 7.20, D43, and D52 present the relationship between the normalized deviator stress and the shear displacement at the different axial displacement rates. The results show that when the shear displacement increases, the deviator stress first reaches its peak, then decreases slightly, and then continually increases again. This continuous increase in the deviator stress is caused by the friction between the ram and the bushing, which is generated from the ram deflection due to the shearing along the cut plane. Figure D49 shows that most of this friction can be eliminated by using a ring bearing on the top cap (Chapter 6), but usage of this bearing cannot eliminate all the friction. A comparison of the results from the different specimens is not meaningful and accurate because each specimen may have different friction due to the differences in each sample's installation and equipment set-up.

Figures 7.21, D44, and D53 indicate the change in the normalized pore-water pressure with the shear displacement at the different axial displacement rates. These pore-pressure response curves are similar for the axial displacement rates used, and the pore pressures measured on the shear plane and on the base are also similar. However, the pore-pressure response of the Highvale mudstone differs from that of the Athabasca clay due to its different stress history.

Figures 7.22, D45, and D54 present the normalized effective stress path on the plane and on the base. The stress paths are similar.

Figures 7.23, D46, and D55 show the relationship between the pore-pressure parameter A (on the shear plane only) and the shear displacement at the different axial displacement rates. At any displacement rate, the A parameter increases first to reach its peak and then decreases with the shear displacement to a negative value. The peak value, A_p, at the 3 different displacement rates are 0.22 (0.001 mm/minute), 0.23 (0.005 mm/minute), 0.28 (0.01 mm/minute).

Figures 7.24, D47, and D56 show the relationship between the mobilized friction angle and the shear displacement at different axial displacement rates. For each test, the friction angle reaches its peak at a very small displacement and then remains constant or decreases slightly with the shear displacement. The residual friction angle is the same as the peak or about 1° less. The friction angles for these three tests are between 28° and 32°.

Figures 7.25, D48, and D57 indicate the difference in pore pressure on the plane and on the base. The results show that the pore pressure on the base is smaller than that on the plane at these small axial displacement rates, but that the difference is small. These results are different from those obtained from the Athabasca clay, for which the pore pressure on the base is larger than that on the plane.

7.4.3 Fort McMurray Highly Weathered Limestone

The three CIUC tests on the highly weathered limestone specimens were performed under a confining stress of 900~1000 kPa at three axial displacement rates (0.002, 0.005, and 0.01 mm/minute) to investigate their pore-water-pressure response. Two of these samples were taken from the same place in pit 26, and their shear planes are comparable. The third one was taken from pit 18, and its shear plane differs from that of the other two. During the installation, each specimen was separated along its main discontinuity into two parts to install the internal pore-pressure transducer on the plane. At this point, the sample is disturbed. Figures 7.26 to 7.32 show the test results for one sample under the axial displacement rate of 0.002 mm/minute. All other tests results are presented in Figures D58 to D71. Figures 7.26, D58, and D65 show the consolidation behavior related to the pore-pressure dissipation for the 3 specimens. These figures indicate that the 3 specimens have similar consolidation characteristics and pore-pressure-dissipation behaviors. The pore-pressure dissipation on the plane is much quicker than that on the base.

Figures 7.27, D59, and C66 present the relationship between the normalized deviator stress and the shear displacement at three different axial displacement rates. The two specimens from pit 26 show no peak strength and, at a small shear displacement, reach the residual. The third curve (sample was taken from pit 18) indicates that the stress-displacement curve has a peak followed by a decrease in the deviator stress with the increase in the shear displacement.

Figures 7.28, D60, and D67 indicate the change in the normalized pore-water pressure change with the shear displacement at three different axial displacement rates. The two specimens from pit 26 have a similar pore-pressure response, but the third one has a different response, which has a significant peak value. For each sample, the pore-pressure-change on the plane is similar to that on the base. The difference is minor (see Figures 7.32, D64, and D71). The pore-pressure response of this weak rock is different from that of both Athabasca clay and Highvale mudstone due also to its different stress history.

Figures 7.29, D61, and D68 present the normalized effective stress paths on the plane and on the base at three axial displacement rates. The two specimens from pit 26 have a similar effective stress path, but the third one has a different effective stress path. These stress paths reflect that the materials are slightly over-consolidated.

Figures 7.30, D62, and D69 show the relationship between the pore-pressure parameter A (on the shear plane only) and the shear displacement at three axial displacement rates. At any shear displacement rate, the A parameter increases first to reach its peak and then decreases with the shear displacement. The two specimens taken from pit 26 have a similar pore-pressure parameter A, but the third one is different. A_p at the 3 different displacement rates is 0.32 (0.002 mm/minute), 0.37 (0.005 mm/minute), 0.56 (0.01 mm/minute).

Figures 7.31, D63, and D70 show the relationship between the mobilized friction angle and the shear displacement at three axial displacement rates. The two specimens from pit 26 show no peak. The third one shows a significant peak friction angle followed by a large drop and then a gradual decrease with the shear displacement.

7.4.4 Paleosol

The objective for testing the Paleosol was to investigate its shear behavior, i.e. its stress-displacement relationship and post-peak characteristics. Therefore, unlike the specimens tested to investigate their pore-pressure response, the Paleosol specimens could not be separated into two parts along one of the shears in the samples but had to be kept intact. For this reason, the plane of shear failure cannot be known in advance to place the pore-pressure transducer. However, the tests on Athabasca clay showed that when the axial displacement rate was less than 0.02 mm/minute, the pore pressures measured on and off the plane were similar (see Figure 7.33). Therefore, during the tests on the Paleosol specimens, the pore-pressure transducer was placed out of the possible failure zone to avoid the influence of the transducer on the shear strength (see Figure 7.34). At the same time, the pore-pressure transducer's end does not need an inclined plane but a horizontal plane (Figure 7.34). The thickness of the possible failure zone depends on the inclination of the possible failure surface, ψ. The larger the ψ, the smaller the potential failure zone and *vice versa*. In order to measure the pore pressure generated on the shear plane, a 3.18mm (1/8″) small hole was drilled through the possible failure zone and filled with sand that contacted the porous stone in the pore-pressure transducer so that it could produce a timely response to the pore pressure on the shear plane. Below the transducer, the over-cored hole was filled first with the sample material and then with wet bentonite to prevent seepage along the transducer tubing so that the pore pressure measured on the base would be accurate. A 0.01 mm/minute axial displacement was used for testing to avoid the influence of the loading rate on the pore pressure.

The three CIUC tests on the Paleosol specimens were performed under a confining stress of about 900 kPa at an axial displacement rate of 0.01 mm/minute to investigate their shear behavior. These three samples were taken from same place in pit 20, but their internal structures may not have been the same. Figures 7.35 to 7.40 show the test results for one sample. All other tests results are presented in Figures D72 to D85. Figures 7.35, D72, and D79 show the consolidation behavior related to the pore pressure dissipation for the 3 specimens. These figures indicate that the 3 specimens have similar consolidation characteristics and pore-pressure dissipation behaviors. Although the pore pressure dissipation on the plane is also quicker than that on the base, the difference is much smaller compared to that in the results from the highly weathered limestone.

Figures 7.36, D73, and D80 present the relationship between the normalized deviator stress and the shear displacement. All three specimens have different stress-displacement curves. One has a significant peak stress followed by a significant drop and a further decrease to reach the residual. Other two have no significant peak stress.

Figures 7.37, D74, and D81 indicate the changes in the normalized pore-water pressure with the shear displacement for the three specimens. Two specimens more or less have similar pore-pressure responses, but the third one has a different response, which results in a negative pore-pressure-change with the increase in the shear displacement. However, for each specimen, the pore-pressure-change on the plane is similar to that on the base. The difference is not significant (see Figure 7.41, D78, and D85). At the end of the test on sample 1, the specimen's upper shear part was moved against the right-angle steel strip that was used to support the internal LVDT (see Figure 7.41). As a result, the pore-pressure-change on the plane increased whereas the pore-pressure-change on the base did not change (Appendix D). This result plus some other phenomena observed during the tests suggest that the pore pressure on the plane was much more sensitive than that on the base.

Figures 7.38, D75, and D82 present the normalized effective stress paths on the plane and on the base. The stress paths on the shear plane and on the base for each specimen are similar except at the end of the two specimens tested. The pore pressure on the plane increases for the reason described above, which makes the effective stress path on the plane different from that on the base. All three of these tests show the material is slightly over-consolidated.

Figures 7.39, D76, and D83 show the relationship between the pore-pressure parameter A (on the shear plane only) and the shear displacement for the three specimens. The parameter increases first to reach its peak and then decreases with the shear displacement. The A_p for the 3 specimens is 0.32, 0.44, and 0.38.

Figures 7.40, D77, and D84 show the relationship between the mobilized friction angle and the shear displacement for the three specimens, under an assumption of no cohesion in the material. Although these three samples were taken from same place, the mobilized friction angles are different. One sample shows a significant peak value and the others have no significant peak.

7.5 ANALYSIS OF TEST RESULTS

This section integrates the observations from the previous sections to provide a picture of the overall pore-pressure response and the shear behavior in undrained shear for the three different materials. Where possible, comparisons with data from the literature are included to provide an overall perspective.

7.5.1 Consolidation Behavior

The consolidation of a test sample was carried out in a triaxial cell before starting an undrained compression test. The consolidation during the tests on the three materials showed that different materials have different consolidation behaviors: the Highvale mudstone consolidated very quickly and the Athabasca clay, the highly weathered limestone, and the paleosol consolidated relatively slowly. However, for all these materials, the pore pressure on the plane dissipated quicker than that on the base although their consolidation pressures were different. During the test, if a specimen was first separated along the shear plane into two parts to install the internal pore-pressure transducer and then put back together to conduct the tests, the difference between the pore-pressure dissipation on the plane and on the base was large. If a specimen was not separated into two parts to conduct a test, for example, the test on paleosol, the difference was relatively small. Therefore, the difference in the pore-pressure dissipation on the plane and on the base resulted from the existence of higher permeability along a shear zone/plane (see page 190 for resons) and can be explained by Terzaghi's one-dimensional consolidation theory.

During the consolidation, in order to increase the rate of consolidation, a vertical strip of filter-paper was placed around the sample. Side drain for a sample, hence, had drainage from the end and the radial boundary (see Figure 6.15). If the lower half of the sample along the shear plane was analyzed, the drainage was only in the radial direction (see Figure 7.42). According to Terzaghi's one-dimensional consolidation theory, the degree of consolidation at one point in a sample in terms of the pore pressures can be expressed as

$$U_z = 1 - \frac{u}{u_i}, \qquad [7.1]$$

where u_i is the initial excess pore pressure induced by the applied stress, i.e. the consolidation pressure, and u is the excess pore pressure measured at a certain time. The pore-pressure dissipation curves in this chapter and Appendix D were obtained according to this expression. The degree of consolidation can also be expressed in another format as below:

$$U_z = 1 - \sum_{n=0}^{\infty} f_1(Z) f_2(T) \qquad [7.2]$$

where $f_1(Z)$ is a function related to the considered point and geometry,
$f_2(T)$ is a function related to the time after starting consolidation,
Z is a geometry parameter, and
T is the time factor.

The internal pore-pressure transducer, point A, on the plane, and the center point B on the base in the profile in Figure 7.42 have a similar position relative to the radial drainage. In this case, the position function $f_l(Z)$ can be neglected when comparing the pore-pressure dissipation on the plane and on the base. Therefore, equation 7.2 can be rewritten into equation 7.3 below:

$$U_z \propto 1-\sum_{n=0}^{\infty} f(T) = 1-\sum_{n=0}^{\infty} f(\frac{1}{T_v}) = 1-\sum_{n=0}^{\infty} f(\frac{H^2}{C_v t}), \qquad [7.3]$$

where T_v is the time factor and equals to $C_v t/H^2$,

Cv is the coefficient of consolidation,

H is the length of the drainage path, and

t is the time.

For the points A and B in a sample (see Figure 7.42), the drainage path is same. At a specific time, the degree of consolidation can be further rewritten as

$$U_z \propto 1-\sum_{n=0}^{\infty} f(\frac{1}{C_v}), \qquad [7.4]$$

where $C_v = k/(\rho_w \cdot g \cdot m_v)$,

k is the Darcy coefficient of permeability, and

m_v is the soil's coefficient of volume compressibility.

When the pore-pressure dissipation is large, U_z is large. When the pore-pressure dissipation on the plane is larger than that on the base, U_A is larger than U_B. From the equation [7.4], C_{vA} is larger than C_{vB}; i.e.,

$$(\frac{k}{m_v})_A > (\frac{k}{m_v})_B, \qquad [7.5]$$

or $$\frac{k_A}{m_{vA}} > \frac{k_B}{m_{vB}}. \qquad [7.6]$$

If m_v is considered as a constant for a specific material under a certain stress, and C_v is large, then k is large; i.e., $k_A > k_B$. More accurately, m_{vA} is larger than m_{vB} due to the existence of the disturbed shear zone/plane in the sample. In this case, k_A is even much larger than k_B. Hence, when the pore-pressure dissipation on the plane is larger than that on the base, the permeability on the plane is larger than that on the base. This situation probably reflects the real situation. As Dewhurst et al. (1996a, 1996b) stated, for an over-consolidated material, the hydraulic conductivity in shear-parallel to the shear zone is larger than that of the material itself. For a normally consolidated material, although the hydraulic conductivity in shear-parallel to the shear zone is slightly lower than that of the material itself, a sample with a cut plane or shear, after it has been separated along such a plane into two parts and then put back together, generally cannot be restored to its original state; i.e., the cut (shear) plane cannot be fully closed. As a result, a large hydraulic conductivity occurs on the plane and then the pore pressure on the plane dissipates more quickly than that on the base. With the consolidation continuously being implemented, the shear plane will be gradually closed, and then the difference in permeability on the plane and on the base reduces with time.

7.5.2 Pore-Pressure Response

Pore-pressure measurement in a shear zone/plane and pore-pressure response at different displacement rates were not studied prior to this present study. Several studies of the intact materials have shown that the pore-pressure distribution was strain-rate dependent and not uniform in triaxial specimens in undrained tests.

For the strain-rate effects on the pore-pressure response in undrained shearing, most previous studies showed that the pore-water pressure generated in an intact specimen during shearing was higher at a lower strain rate than at a higher strain rate. Casagrande and Wilson (1951), Crawford (1959, 1963), Whitman (1960), Richardson and Whitman (1963), and Sheahan et al. (1996), among others, found that a lower strain rate resulted in higher pore pressure. Zhu et al. (1996, 2000) also found that a lower strain rate resulted in higher pore-water pressure in both the undrained triaxial compression and extension tests for normally consolidated Hong Kong marine clay. However, Alberro and Santoyo (1973) found that for Mexico City clay, the pore pressure was almost independent of the strain rate. Lefebvre and LeBoeuf (1987) indicated that for structured clay, the pore-water pressure development during shearing was not significantly influenced by the strain rate, but for normally consolidated clay, the influence of the strain-rate on the pore-water pressure was considerable. Kimura and Saitoh (1983) found that a lower strain rate resulted in higher base pore-water pressure at a small strain, but that a strain-rate increase resulted in a minor increase in the pore-water pressure at the center. Rojas (1988) reported that a lower loading rate resulted in lower pore pressure according to his tests on Mexico City clay. Fourrie and Dong (1991) indicated that a lower strain rate resulted in a lower pore-water pressure on the sample base, and that a strain rate increase resulted in a minor increase in the pore-water pressure at the mid-height. Shuri et al.(1985) also found from an *in situ* undrained shear test that a higher strain rate resulted in a higher pore-water pressure on the shear zone/plane.

Some other researchers showed that the pore-pressure distribution in a sample during the triaxial compression test was not uniform. Crawford (1963) conducted studies on Leda clay in a diameter of 36 mm with pore-pressure measurement on the base and in the center with a hypodermic needle and found that under a slow loading rate, a specimen developed higher pore pressures at its lower end than at the geometric center. Crawford indicated that this higher base pore pressure could be attributed to a disturbance caused by end restraint. Whitman (1960) reported extensive studies on undisturbed Boston clay and noted that the pore pressure at the center was higher than that at the ends. This finding correlated with the higher water content near the ends of the specimen after a test. The results also indicated that the pore pressures at the center and at the ends were similar when strain rate was less than 0.16%/minute, and therefore, that the difference was small. Bishop et al. (1960) reported the pore pressure at the base of compacted specimens to be greater than at mid-height and attributed this finding to the influence of the end restraint. Gibbs et al. (1960) described the test results on compacted clay in which the pore pressure measured in the center and at the ends were identical. Richardson and Whitman (1963) found that the pore pressure on the base was larger than that in the center at a large strain rate and were almost same at a strain rate of less than 1%/h. Kimura and Saitoh (1983) found that the pore pressure in the center was larger than that on the base at a small strain and that at a large strain, the pore pressure on the base was larger than that in the center, and that as the strain rate increased, this separating strain value also increased. Fourrie and Dong (1991) reported that the pore pressure at mid-height was smaller than that on the base and attributed this finding to the end restraint, and the difference was found to be proportional to the testing rate used.

A summary of the research on the rate effects on pore-pressure response and shear behavior is presented in Table 7.7. The observed pore pressures in a sample are complex, variable, and not all compatible with one another, and suggest uncertainties associated with any rigorous interpretation of their significance. These variations can be attributed to the variable materials used and their stress histories (OCRs), the pore-pressure measurement positions (base, center, and mid-height), the pore-pressure transducers used (porous needle and electronic sensor), the end restraints (rough and lubricated), and the strain rates used.

This present study involved an experimental study of the pore-pressure response and shear behavior of a shear zone/plane in three materials: compacted Athabasca clay, Highvale mudstone, and Fort McMurray weak rocks. A pre-existing shear zone/plane or cut plane alters the integrity of a sample and makes its pore-pressure response different from that of intact materials. For compacted Athabasca clay, Figures D4, D12, and D20 show that at an axial displacement rate of less than 0.02 mm/minute, the pore pressure measured on the shear plane and on the sample base are similar. The difference is small (see Figure D8, D16, and D24). If the 0.02 mm/minute axial displacement rate is converted into an equivalent axial "strain"[1] rate, it equals 0.85%/h in this study. Therefore, the pore pressures measured on the shear plane and on the base are the same if the "strain" rate is less than 0.85%/h. This "strain" rate is very close to the strain rate that

---

[1] The term "strain" is used here for mathematical convenience and does not have the same meaning as the definition of "strain" after the start of the slip, because the "strain" in the equation is not dependent on the sample's length.

Richardson and Whitman (1963) obtained. After their studies of Mississippi valley alluvial clay, Richardson and Whitman found that the pore pressures on the base and in the center were almost same at a strain rate of less than 1%/h. A complete equalization condition was apparently reached in tests with an axial displacement rate of less than 0.02 mm/minute for the compacted Athabasca clay. Figures D28, D36, and 7.6 show the changes in the normalized pore pressures on the shear plane and on the base at axial displacement rates of 0.2, 1, and 2 mm/minute, respectively. The pore pressures on the base and on the plane are different when the axial displacement rate is larger than 0.2 mm/minute. The pore pressure on the plane first increases to a peak value at a relatively small shear displacement, which is higher than that on the base, and then decreases with the shear displacement to a value that is lower than that on the base, whereas the pore pressure on the base continually increases with the increase in the shear displacement. The equivalent "strain" rate of 0.2 mm/minute axial displacement rate is 8.6%/h. A 0.2 mm/minute axial displacement rate also equals a 0.244 mm/minute shear displacement rate along the shear plane. This finding means that the pore pressures in the sample during tests cannot be equalized out if the shear displacement rate is greater than 0.244 mm/minute.

Figures 7.12 and 7.13 show that when the axial displacement rate is less than 0.02 mm/minute, the pore-pressure-changes on the shear plane are similar, so are the pore-pressure-changes on the base. This finding means that the pore pressures in the sample in tests are equalized out when the axial displacement rate is less than 0.02 mm/minute (shear displacement rate is 0.0244 mm/minute). When the shear displacement rate increases, the pore pressures on both the shear plane and on the base increase. This finding is different from most past researchers' results, which were obtained from studies on intact materials. However, the variation trend of the pore pressures on the plane and on the base is different. The pore pressure on the plane increases at a high shear displacement rate to reach a peak value at a small shear displacement and then reduces with the shear displacement to a value that is less than that obtained at the lower shear displacement rates. The larger the shear displacement rate, the higher the peak pore pressure. However, the rate of increase in pore pressure with an increase in the shear displacement rate decreases. The pore pressure on the base obtained at a high shear displacement rate is always higher than that obtained at a lower shear displacement rate. The pore pressure responses on the plane and on the base are different for all the shear displacement rates. Blight (1963) theoretically analyzed the pore-pressure distribution in intact material and indicated that the pore pressure at mid-height could be either greater than, less than, or equal to the values at the ends. The pore-pressure parameter measured at mid-height in a rapid test was much closer to the true value. Although Blight's analyses were on intact materials, these analyses could also be applied to the material with a shear zone/plane because the shear plane in a sample is away from the end, and the influence from the end restraint is small. Therefore, measuring the pore pressure only on the base at a high shear displacement (or strain) rate and using the measured pore pressure to analyze a problem involving pore pressure and effective stress on a shear plane may be misleading.

Table 7.8 summarizes the peak pore-pressure-changes on the shear plane, Δu_p, with different shear displacement rates. Figure 7.43 shows the relationship between the peak pore-pressure-changes, Δu_p, and the shear displacement rates in the Cartesian coordinates. Figure 7.44 shows the relationship between the peak pore pressure changes, Δu_p, and the shear displacement rates in a half-logarithmic scale. The equations for the best-fit lines are also shown in Figures 7.43 and 7.44. If one unique equation is used to express the relationship between the pore-pressure-change and the shear displacement rate, as is shown in Figure 7.43, the correlation is not very close, especially at the lower shear displacement rates. If the peak pore-pressures changes are divided into two groups to establish the relationship between the peak pore-pressure-change and the shear displacement rate, as is shown in Figure 7.44, the correlation is much better. The relationships indicate that at low shear displacement rates, the peak pore-pressure-change is almost constant, whereas at high shear displacement rates, the pore-pressure-change increases in a logarithmic mode. The two best-fit lines intersect at the shear displacement of 0.062 mm/minute; i.e., when the shear displacement rate is lower than 0.062 mm/minute, the peak pore-pressure-change is a constant, and when the shear displacement rate is higher than 0.062 mm/minute, the peak pore-pressure-change varies in a logarithmic mode. Therefore, the pore pressure response of a shear zone/plane in the Athabasca clay can be expressed in the equations below:

$$\begin{aligned} &\Delta u_p = 51 \text{ (kPa)} && \text{when } \dot{\delta} \le 0.062 \text{ mm/minute} \\ &\Delta u_p = 3.8768 Ln(\dot{\delta}) + 60.413 \text{ (kPa)} && \text{when } \dot{\delta} > 0.062 \text{ mm/minute,} \end{aligned} \qquad [7.7]$$

where Δu_p is the peak pore-pressure-change on the shear plane, kPa, and

$\dot{\delta}$ is the shear displacement rate, mm/minute.

If the normalized pore-pressure-change is used to set up the relationship, the best-fit equations are as expressed below:

$$\begin{aligned} &\frac{\Delta u_p}{\sigma_0} = 0.51 && \text{when } \dot{\delta} \le 0.062 \text{ mm/minute} \\ &\frac{\Delta u_p}{\sigma_0} = 0.037 Ln(\dot{\delta}) + 0.6073 && \text{when } \dot{\delta} > 0.062 \text{ mm/minute,} \end{aligned} \qquad [7.8]$$

where σ_0' is the pre-consolidation pressure.

The shear displacement rate of 0.062 mm/minute is a critical value for the pore-pressure response of a shear zone/plane in the Athabasca clay. When the shear displacement rate along a shear surface is lower than 0.062 mm/minute, the change in pore pressure on such a shear surface is negligible; i.e., the pore pressure generated in the sample during the shearing can equalize out. 0.062 mm/minute of the shear displacement rate equals an axial displacement rate of 0.0508 mm/minute in this test. If it is included in the calculation for the "equivalent strain rate," this "equivalent strain rate" is 2.15%/h. This value is very close to the strain rate (2%/h) recommended by Bishop and Henkel (1962) for the satisfactory measurement of pore-water pressure for intact material by using the side drains in a undrained test and is also similar to the results obtained by Crawford (1959).

Several studies have explained the mechanism of pore-pressure generation and response. Crawford (1959) suggested that a breakdown in the soil structure determines the level of pore pressure and used this suggestion to explain why greater pore pressure develops in slow tests in the intact sample. This mechanism probably is one of the reasons for pore-pressure generation and response in intact material. However, in this study, a pre-existing shear zone/plane or cut plane in a sample plus its installation procedure (i.e., the sample was separated first into two parts along the shear plane to install the internal pore-pressure transducer, and then the sample was put back together), caused the soil structure along the shear zone/plane to break down before tests. Therefore, the mechanism of a breakdown in the soil structure cannot be applied to explain the pore-pressure response of a shear zone/plane. Whitman (1960) pointed out that the strain rate has two possible effects on the pore pressure. One possibility is that the mineral skeleton may, under rapidly applied loads, have a resistance to compression, approaching that of water. Such a behavior would be the result of structural viscosity. If so, then the excess pore pressure set up during undrained shear in soft, saturated soils would decrease as the strain-rate increases. This possibility was also suggested by Casagrande and Wilson (1953), as Whitman pointed out. However, this possibility is not also applicable to this present study because the resistance of the mineral skeleton is very small on a shear plane, and also because no viscosity from the structure was found during the tests. The results from a test by Whitman on a remoulded backswamp clay indicated no tendency for the amount of pore pressure developed to depend upon the structural viscosity. Another possibility is that as the strain-rate increases, gradients of pore pressure will occur within a triaxial sample which is sheared undrained, and hence, the pore pressure within the central zone may be time-dependent. If one were testing a soft, saturated clay in axial compression, it would be expected that, if anything, the pore pressures in the central zone would increase as the strain-rate increased. Crawford (1959) and Whitman (1960) found gradients in the pore pressure existed in a sample. After each clay sample was tested in this study, the water contents in different positions (see Figure 7.45) in the sample were measured, and the measurements are presented in Table 7.9.[2] Gradients in the pore pressure were found in the samples tested at the high displacement rates. For the samples tested at the low displacement rates, the gradient was not significant. Therefore, a possible explanation for the pore pressure behavior is that when a triaxial compression test takes place, the pore-pressure response depends on the state of the geomaterial and the drainage condition. If drainage is allowed, contractancy occurs when shearing takes place in soft, saturated, normal consolidated material. If drainage is not allowed, volume change is not permitted, and this contractancy (hereafter called "shear contraction potential") will cause a pore-pressure increase (Wang et al., 2003). The larger the shear contraction potential, the larger the pore pressure generated. In the analysis of pore-pressure generation during slope failure and sliding, Iverson and Lahusen (1989) and Iverson et al. (1997) pointed out that the pore-pressure build-up depends mainly on the rate of landslide motion and soil deformation as well as the permeability of the soil. During an undrained situation, the rate of motion and the soil deformation (dilation or contraction) are the main factors in the pore-pressure build-up. For the undrained triaxial shearing, the larger the displacement rate, the larger the shear contraction potential, and then the larger the pore pressure.

The pore-pressure response of a sample during an undrained triaxial test is the response of the pore pressure to the applied stress, which can be described in pore pressure parameter A.

$$A = \frac{\Delta u - \Delta\sigma_3}{\Delta\sigma_1 - \Delta\sigma_3}, \qquad [7.9]$$

where Δu is the change in pore pressure due to $\Delta\sigma_3$, the change in the confining pressure, and $\Delta\sigma_1$, the change in the compression pressure. Figure 7.16 shows the relationship between the pore-pressure parameter A (on the shear plane) and the shear displacement at different displacement rates. Figure 7.46 shows the relationship between the peak pore pressure parameter A_p and the shear displacement rates. When the axial displacement rate

---

[2] The water content before testing is larger than that after testing because the water content before testing was obtained during the sample's trimming, and after the sample was trimmed, some of the water content was lost during the sample installation, which took a relatively long time.

is lower than 0.02 mm/minute, the peak pore-pressure parameter A_p reduces with the increase in the axial displacement rate because the pore pressure generated from shearing does not increase with the increase in the displacement rate, but the deviator stress (see next section) increases with the increase in the displacement rate, and then A_p decreases. This finding that A_p decreases with increase in the displacement rate is similar to the results obtained by Crawford (1959), Blight (1963), and Nakase et al. (1983), who did tests on intact clay samples. However, when the axial displacement rate is higher than 0.2 mm/minute, A_p increases with an increase in the shear displacement rate because the pore pressure on the plane increases as the displacement rate increases, but the deviator stress decreases (see next section).

The pore-pressure responses of the Highvale mudstone under the axial displacement rate of 0.001, 0.005, and 0.01mm/minute are presented in Figures D44, D53, and 7.21. These figures show that the pore-pressure response of Highvale mudstone is totally different from that of Athabasca clay. The pore-pressure-change on the shear plane in such a material increases first with the shear displacement to reach a positive peak value and then decreases to a negative value because the Highvale mudstone is an over-consolidated geomaterial. The pore-pressure-change increases in the small shear displacement is attributed to the cut plane in the sample, which may not be fully closed during the consolidation. Therefore, during shearing, the shear contractancy potential occurs first to cause the pore-pressure-change to increase under the undrained condition. With further shear displacement, shear dilatancy potential occurs in such an over-consolidated material, so that the pore-pressure-change decreases under an undrained condition. When the axial displacement rate is lower than 0.01 mm/minute, the pore-pressure-change on the shear plane and on the base is similar. The difference is small (see Figures D48, D57, and 7.25). Therefore, when the axial displacement rate is lower than 0.01 mm/minute, the pore pressure generated in a sample during shearing can equalize out. The pore-pressure parameter A_p at these three shear displacement rates is 0.22 (0.00122 mm/minute), 0.23 (0.006 mm/minute), and 0.28 (0.0122 mm/minute), indicating that the shear planes in Highvale mudstone are slightly over-consolidated (Skempton, 1953).

The pore-pressure responses of the highly weathered limestone at three different axial displacement rates are presented in Figures 7.28, D60, and D67. According to these results, the pore-pressure response of such a highly weathered limestone differs from that of both Athabasca clay and Highvale mudstone. The two samples taken from pit 26 have similar characteristics in the shear planes, which are polished, planar, and shiny. Their pore-pressure responses are similar at the displacement rates used. The pore-pressure-change reaches a peak at a small shear displacement and then gradually decreases with the shear displacement. The pore pressures on the plane and on the base for both samples are similar, and the difference is small (see Figures 7.32 and D64), so that the pore pressure generated in a sample can equalize out when the shear displacement rate is lower than 0.012 mm/minute. The third sample taken from pit 18 has a different pore-pressure response from the other two. The pore-pressure-changes on the shear plane and on the base both have a significant peak value followed by a pronounced drop. This behavior may be attributed to the shear plane's roughness and some small asperities on the plane. At a shear displacement rate of 0.012 mm/minute, the pore-pressure-changes on the plane and on the base are also similar and the difference is small (see Figure D71). This behavior also indicates that the pore pressure generated in the sample at a shear displacement rate of 0.012 mm/minute can equalize out during shearing. The peak pore-pressure parameter A_p at these three shear displacement rates is 0.32 (0.0024 mm/minute), 0.37 (0.006 mm/minute), 0.56 (0.012 mm/minute), also indicating that the shear zone/plane in the highly weathered limestone is slightly over-consolidated (Skempton, 1953). The high A_p value for the third sample may be attributed to the plaster-sand mixture, that the specimen contains due to the directional drill sampling and the lack of a central shear plane in the block sample (Chapter 6).

7.5.3 Shear Behavior

Table 7.7 also briefly tabulates the results of past research on the strain-rate effects on undrained shear strength by using undrained triaxial compression tests on intact materials. Most studies showed that a high strain rate resulted in a higher undrained shear strength. Casagrande and Wilson (1951) suggested that the strain-rate dependency of undrained strength might be caused by a change in the excess pore-water pressure generated during the shearing process. Richardson and Whitman (1963) and Sheahan et al. (1996) believed that a decrease of pore pressure was the primary mechanism of strength increase with increasing strain rate. Crawford (1959) inferred from his research that slow straining appeared to destroy the additional strength developed by pre-consolidation.

Skempton (1964), Skempton and Petley (1967), D'Elia et al. (1977), Dounias et al. (1987), Tika et al. (1996), and Chandler et al. (1998) measured the strength or stress-strain characteristics along the principal slip surface of some landslides or shear zones. These researchers found that the strength along a principal slip surface was at or very close to the residual strength and much lower than the intact clay's peak strength. The stress-strain curve in tests on principal slip surfaces depends on the surface characteristics and the prior shear displacement that has occurred. A planar and shiny slip surface with full-particle orientation is expected to have a stress-strain curve that shows no peak and, at a small displacement, that reaches the residual strength. Quite often, however, the test shows a small peak due to the slip surface roughness, clay particles on slip surface that are not fully oriented, the bonding effect, clay pellets left on the surface, and sometimes, errors. This small peak will drop to residual with a small further displacement.

The rate effects on the residual shear strength of a pre-existing shear surface/shear zone depends mainly on the material's components. Most studies showed that the effect of the rate of shearing on the ultimate strength of granular soils is negligible. Tests on the clays over a range of speeds about 100 times slower to 100 times faster than the usual (slow) laboratory test rate (0.002-0.01mm/min) showed negligible effect (Skempton, 1985). However, at a fast rate (>400 mm/minute), the rate effects depended on the clay fraction. A clay's residual strength will increase significantly at such a fast rate, probably due to the disturbance of the originally ordered structure and pore pressure changes (Skempton, 1985). In contrast, in a low-clay-fraction clay siltstone, no qualitative change occurs at rates even as high as 800mm/min. All these studies were carried out in drained or partially drained conditions. No undrained results are available.

The present study involved an experimental study of the shear behavior of a shear zone/plane in three materials: compacted Athabasca clay, Highvale mudstone, and Fort McMurray weak rocks in an undrained condition. For the compacted Athabasca clay, shear displacement rates from 0.0012 mm/minute to 2.44 mm/minute were employed to investigate its strength behavior and rate effects. For the Highvale mudstone and Fort McMurray weak rocks, however, small displacement rates, which have more practical implications, were used for testing. Figure 7.11 shows the normalized deviator stresses versus shear displacement at six axial displacement rates. At the low displacement rates from 0.001 to 0.02 mm/minute, the deviator stress increases with the shear displacement, but the pore pressures remain almost constant. This behavior may be attributed to the increase in inter-particle friction. Figure 7.17 indicates that the mobilized friction angle increases with increase in displacement rate that is within a low range. When the displacement rate further increases, the deviator stress, on the contrary, decreases, and correspondingly, the mobilized friction angle also decreases to the value similar to the friction angle obtained at the axial displacement rate of 0.001mm/minute. Such a decrease in the deviator stress occurs because the pore-water pressure increases with increase in the displacement rate (Figure7.12). Higher excess pore-water pressure results in a lower deviator stress. However, if the rate of the deviator stress increment, $\Delta\dot{q} = \Delta q / \Delta\delta$, as is shown in Figure 7.47, is considered, one can find that the rate of deviator-stress-increment for the axial displacement rates of 0.001, 0.005, and 0.02 mm/min decreases with the shear displacement, whereas for a displacement rate of 0.2 mm/minute, the rate of deviator-stress-increment is almost constant or has a minor decrease, and for the axial displacement rates of 1 and 2 mm/minute, the rate of deviator-stress-increment is constant or has a minor increase after the shear displacement is greater than 3 mm. This behavior means that after certain shear displacements, the deviator stresses at the axial displacement rates of 0.2, 1, and 2 mm/minute may increase to a value that is higher than that at the axial displacement rates of 0.001, 0.005, 0.02 mm/minute. This behavior probably results from the decrease, after the peak, in the pore pressure with shear displacement at the axial displacement rates of 0.2, 1, and 2 mm/minute (see Figure 7.12). Figure 7.14 shows the normalized effective stress paths (ESPs) on the shear plane for this test series. As the displacement-rate increases, the friction angles reduce to a similar value, and the ESPs reach the same obliquity. This result may also indicate that the changes in the deviator stress result from the changes in the pore-water pressure. However, the ESPs on the base have no such consistency (See Figure 7.15) due to the different pore-pressure response at the high axial displacement rates.

Figures D43, D52, and 7.20 show the relationship between the normalized deviator stress and the shear displacement for a polished shear plane in the Highvale mudstone samples at the axial displacement rates of 0.001, 0.005, and 0.01 mm/minute, respectively. The friction between the ram and the bushing, which is caused by the ram deflection due to the upper half of the sample moving along the shear plane, could not be fully eliminated even when a ring bearing was used for the tests (see Chapter 6). The stress-displacement curve in this situation does not reflect the characteristics of such a polished plane. However, the pore-pressure-response curve, the pore-pressure-parameter A curve, and the mobilized friction angle curve, suggest that although different samples may have different frictions due to the sample's installation and equipment set-up, and that because of such different frictions, the comparison of the results from different samples may be meaningless, for a specific sample, the influence of such a friction on the deviator stress and pore pressure is, to a certain degree, simultaneous and equal.

As is stated in Section 7.3, axial displacement rates of 0.002, 0.005, and 0.01 mm/minute, which equal the shear displacement rates of 0.00244, 0.0061, and 0.0122 mm/minute, or 3.51, 8.64, and 17.28 mm/day, were used to do the experiments on the Fort McMurray weak rocks. The effect of such displacement rates on the shear strength of the shear plane is negligible (Skempton, 1985). The shear planes of two highly weathered limestone samples taken from the pit 26 may not be from same main D-shear, but they have similar characteristics and are polished, planar, and shiny (see Figure 3.11). Such a shear plane plus the large displacement that has occurred infers full-particle orientation on the slip surface. Their stress-displacement curves show no peak and at a small shear displacement (about 1 to 1.5 mm), reach the residual strength (see Figures D59 and 7.27). The mobilized friction angle (Figures D63 and 7.31) has similar characteristics to the stress. At a small shear displacement (about 1 to 1.5 mm), the friction angle reaches about 18°, and with further shear displacements, it keeps almost constant or has a minor drop. The third highly weathered limestone sample was taken from pit 18, and its slip surface is not so planar and shiny but rough. Field mapping suggested that the prior displacement for the shear zone is small (Chapter 3). Its stress-displacement curve shows a significant peak and then a pronounced drop follows with further shear displacement (Figure D66). A large displacement is needed to drop its strength from peak to residual. The mobilized friction angle also shows a peak value at 26° at a shear displacement of about 5 mm, followed by a drop in the friction angle. Its residual friction angle of about 14° can be inferred from the mobilized friction angle curve, and a large displacement is needed to reach such a residual friction angle. Therefore, in the tests on the three highly weathered limestone samples, although their physical properties and grain-size distribution were not significantly different, their stress-displacement curves and the mobilized strength parameters (ϕ_p' and ϕ_r') were totally different due to their different slip surface characteristics and the *in situ* shear displacements that had occurred.

Three Paleosol samples were taken from pit 20. The field mapping (Chapter 3) stated that no significantly continuous D-shear exists in the Paleosol, but that minor shears are common. Such minor shears are discontinuous with different modes of occurrence. Some of the minor shears are sub-planar and moderately rough, and others are very rough with striations on them. It is expected that their shear behavior such as the stress-displacement curve and shear parameters will differ. Tests on the three samples were conducted at an axial displacement rate of 0.01 mm/minute, and their relevant shear displacement rates are 0.017 mm/minute, 0.014 mm/minute, and 0.0125 mm/minute due to their different slip angles. Two samples' shear planes are sub-planar and moderately rough (see Figure 7.48 and 7.49), and their stress-displacement curves show a minor peak in shear stress followed by a minor decrease with further shear displacement. The residual strength for both samples was not reached under the tested displacement. The mobilized friction angles, under an assumption of no cohesion, are quite high. Although the many calcium carbonate nodules (see Figure 7.50) in Paleosol will give it a high strength (Hawkins, 1996), a peak friction angle of about 32° is still too high. Therefore, it is not reasonable to consider that this weak rock has no cohesion. Shearing in a test occurs not only along one single minor shear but through the rock bridges. The test on the third sample shows that the stress-displacement curve has a significant peak in shear stress followed by a notable drop with further shear displacement (Figure 7.37). Figure 7.51 shows that one minor shear in this sample is rough and striated. Observation of the sheared sample found that shearing through a rock bridge between some minor shears happened. This shearing resulted in the shear dilation potential and the relevant pore-water-pressure-change decreasing to a negative value with further shear displacement. Under an assumption of no cohesion in the sample, the mobilized friction angle is shown in Figure 7.40. A peak friction angle of 28° is reached at the shear displacement of about 4 mm, and the residual friction angle of about 20° is reached within the testing displacement. Therefore, the tests on the three Paleosol samples show that even though they might be taken from same place, different samples may have different internal structures. Such different structures will determine whether the shearing is along a single minor shear or along a combination of different minor shears and rock bridges, and then will determine the sample's shear behavior (stress-displacement curve and post-peak features). The calcium carbonate content and rock-bridge component (clay or calcium carbonate nodule) will determine the magnitude of the shear strength. When the shearing along a combination of different minor shears and rock bridges, the shear strength could be a linear combination of the minor shears' shear strength and the rock bridges' shear strength according to their area ratio on the shear plane (Su et al., 2003)

7.6 SUMMARY AND CONCLUSIONS

A total of 15 consolidated-undrained triaxial tests on Athabasca clay, Highvale mudstone, and Fort McMurray weak rocks were carried out at different displacement rates. These materials have different physical and mechanical behavior and different stress histories. The pore water pressure on each shear plane was measured in either a modified conventional triaxial cell or a newly developed large triaxial cell, and their pore-pressure responses and shear behavior were investigated.

The following conclusions can be drawn from this study:

1. Pore pressures measured on the shear plane and on the base are identical provided that the displacement rate used is in the slow range (less than 14.4 mm/day) no matter whether the material is normal-consolidated or over-consolidated. This implies that the pore pressure measured in the shear zone or on the shear plane is the same as the pore pressure measured at a nearby location for any material provided the soil structure founded on such a shear zone moves slowly. Therefore, at slow movement, the pore pressure obtained from the *in situ* instrumentation by using piezometers, whose tips may be located adjacent to the shear zone, can be viewed as representative of the shear zone's pore pressure.
2. The pore-pressure responses differ for different materials with different stress histories (OCRs)
3. If the shear displacement rate is less than about 0.062 mm/minute, the pore pressure on the shear plane of Athabasca clay has no rate effect; i.e., the pore pressure remains identical at any shear displacement rate less than this critical value. If the shear displacement rate is higher than about 0.062 mm/minute, the peak pore pressure on the shear plane increases with an increase in the shear displacement rate, and at a specific rate, the pore pressure increases first to reach its peak, followed by a gradually decrease with further shear displacement to a value that is even lower than the pore pressure obtained at a low displacement rate. The pore pressure response for a shear zone/plane in Athabasca clay can be expressed as either equations 7.7 or 7.8.
4. Athabasca clay's deviator stress increases with an increase in the shear displacement rate if such a rate is less than 0.0244 mm/minute. This behavior may be attributed to the increase in inter-particle friction and the subsequent mobilized friction angle increases. At a small shear displacement, the deviator stress decreases with further increase in the shear displacement rate and is less than those obtained at the small displacement rates. With further shear displacement, the deviator stress obtained at a high displacement rate may increase to a value that is higher than those obtained at a low displacement rate. The change of the

deviator stress at a high displacement rate results from the pore-pressure-change; i.e., a higher pore pressure results in a lower deviator stress, and *vice versa.*

5. The effective stress paths on the shear plane and on the base differ for Athabasca clay at high shear displacement rates. The effective stress paths on the shear plane trend to an identical obliquity and then result in an identical friction angle.
6. The pore pressure on the shear plane dissipates quicker than that on the base, because of the larger permeability on the shear plane.
7. Even in shear zones developed in the same material, their shear behaviors (stress-displacement curve, post-peak characteristics, and strength parameters) may not be identical due to the different shear-surface features and pre-existing shear displacements that have occurred. The stress-displacement curve of a polished shiny planar shear surface in the highly weathered limestone with a relatively large pre-existing shear displacement shows no peak, and at a small displacement, reaches the residual strength. Conversely, a rough shear surface with small pre-existing shear displacement has a significant peak followed by a decrease in the strength with further shear displacement. A large displacement is needed to reach residual strength.
8. Paleosol contains many minor shears. Its internal structure, i.e., the minor shears geometric arrangement, controls its shear behavior. When the shearing is along different minor shear combinations, different stress-displacement curves, post-peak characteristics, and shear strength parameters result.

The pore-pressure response of a shear zone/plane in an over-consolidated material lacks results at the high displacement rates. The shear behavior of the Fort McMurray weak rocks was investigated in relation to the practical displacement rates (mms/day). The effects of high displacement rates on their shear behavior are not clear. The pore-pressure response and shear behavior of the Athabasca clay at the large shear displacement are also not clear because the tests could not accommodate large shear displacement due to the limitations of the equipment. The conventional triaxial equipment caused limitations and even errors in the results from the tests on the indurated Highvale mudstone with a shear plane. However, this study has contributed to developing innovative instrumentation to measure pore pressure on a shear zone/plane and their pore pressure response. Further experimental work and research are necessary to obtain a better understanding of the rate effects and stress history (OCR) influences for different materials and loading modes (compression and extension).

Table 7.1 Characteristics of Athabasca clay

Composition (%)			Atterberg Limits			Optimum moisture content (%)	Permeability (m/s)*	Void ratio e^*
Sand	Silt	Clay	W_l	Wp	I_p			
10	45	45	41	22.9	18.1	17 (modified proctor)	10^{-11}	0.67

* Permeability and void ratio obtained from samples with moisture content of about 22.5%.

Table 7.2 Characteristics of mudstone from the Highvale coal mine (after Small 1989)

El. (m)	M.C (%)		Avg. γ_t (kn/m^3)	Avg. γ_d (kn/m^3)	W_p	W_l	I_p	CF (%)	A
	Rg.	Avg.							
719~725	16.9~23.0	19.6	19.8	16.6	21~38	58~74	34~43	55~65	0.58~0.70

Table 7.3 Characteristics of Paleosol from dyke 10 at pit 20

Composition (%)			Atterberg Limits			Specific gravity	Water content
Sand	Silt	Clay	W_l	Wp	I_p	Gs	(%)
0	61	39	32.2	20.9	11.3	2.71	15

Table 7.4 Characteristics of the highly weathered limestone in pit 18

Composition (%)			Atterberg Limits			Specific gravity	Water content
Sand	Silt	Clay	W_l	Wp	I_p	Gs	(%)
8	50	42	39.9	19.6	20.3	2.75	13.3

Table 7.5 Characteristics of the highly weathered limestone in pit 26

Composition (%)			Atterberg Limits			Specific gravity	Water content
Sand	Silt	Clay	W_l	Wp	I_p	Gs	(%)
0	56	44	40.8	21.4	19.4	2.78	14.1

Table 7.6 Displacement rates used for tests

Material	Axial displacement rate: mm/min.					
Athabasca clay	0.001	0.005	0.02	0.2	1	2
Highvale mudstone	0.001	0.005	0.01			
Weathered limstone	0.002	0.005	0.01			
Paleosol (shear behavior testing)			0.01			

Table 7. 7 Summary of tests on rate effects and pore-pressure measurements (modified from Sheahan et al., 1996)

Reference	Soil tested	Test type (OCR)	Diameter of sample (mm)	Rate($\dot{\varepsilon}_a$) range (%/h)	With increase $\dot{\varepsilon}_a$		Pore pressure measurement position
					Δu	ϕ_p' or q	
Crawford (1959)	Leda clay (N)[a] [39][b]	CIUC (1)	35.6	0.008 - 10	↓[c]	↑	Base
Crawford (1959)	Leda clay (N) [39]	CIUC (1)	35.6	0.008 - 10	↓, $\Delta u_b > \Delta u_c$	↑	Base and center (needle)
Bishop et al. (1960)	Compacted shale	CIUC (1)	100	0.17, 2.5	$\Delta u_b > \Delta u_m$		Base and center (needle)
Gibbs et al. (1960)	Compacted Sc-CL soil		80		$\Delta u_b = \Delta u_c$		Base and center (needle)
Richardson and Whitman (1963)	Mississippi valley alluvial clay (RM)[38]	CIUC (1)	35.6	0.12, 60	↓, when rate < 1%/h, $\Delta u_b \equiv \Delta u_c$	↑	Base and center (needle)
Richardson and Whitman (1963)	Mississippi valley alluvial clay (RM)[38]	CIUC (16)	35.6	0.12, 60	↓	↓ but c↑	Base and center (needle)
Alberro and Santoyo (1973)	Mexico city clay (N) [279]	CIUC (1.8)		0.045 - 94	-[d]	↑	
Kimura and Saitoh (1983)	T.I.T mixture [10,20,30]	CK_0UC (1)	75	3.9, 9.74, 19.44	u_p minor↑ at small strain; u_b↓ at small strain; $u_p > u_b$ at small strain, $u_b > u_p$ at large strain,		Base and center (electronic sensor)
Shuri et al. (1985)	clay seam (in situ) [29]		0.7*0.7*0.4 m^3	0.1, 0.5, 5, 25(mm/h)	↑	↑	shear zone
Nakese and Kamei (1986)	T.I.T mixture [10,15,30]	CK_0UC (1)	75	0.42, 4.2, 42	↓(large I_p) - (small I_p)	↑	
Levebvre and LeBoeuf(1987)	Various clay (N)[10-40]	CIUC, CAUC (1)	35.6	0.05 - 132	↓	↑↓	
Fourie et al. (1991)	Black clay[63], Kaolin [35] Coal tailings [20] (RM)	CIUC (1)	38	0.0012, 0.012, 0.12 (mm/min)	u_b↑; u_p minor↑ or similar; $u_b > u_p$	↑	Base and mid-height (electronic sensor)
Sheahan et al. (1996)	Boston blue clay (RM) [24]	CK_0UC (1,2,4,8)	36	0.05, 0.5, 5, 50	↓	↑	Base and mid-height (needle)
Jun-Gao Zhu et al. (2000)	Hong Kong marine clay (RM) [32]	CIUC (1,2,4,8)	50	0.15, 1.5, 15	↓	↑	Base

[a](N) = natural, (RM) = remoulded; [b][] = plastic index, %; [c]↓ = parameter decreased with increasing strain rate; and [d]- = parameter do not change significantly with strain rate change

Table 7.8 Peak pore-pressure-changes at the different shear displacement rates

Shear displacement rates (mm/minute)	0.00122	0.0061	0.0244	0.244	1.22	2.44
Peak pore- pressure change (kPa)	51.0	50.5	51.0	55.5	61.5	64.0

Table 7.9 Water contents in an Athabasca clay sample before and after testing

No. of sample	Displacement rate (mm/minute)	Water content (%)			
		Before test	Plane	Close to plane	Away from plane
1	0.001	22.8	21.76	22.01	21.83
2	0.005	23.1	22.63	22.33	22.18
3	0.02	22.0	21.72	21.97	21.72
4	0.2	22.4	21.35	21.41	21.59
5	1	23.2	22.06	22.19	22.41
6	2	22.2	21.14	21.32	21.40

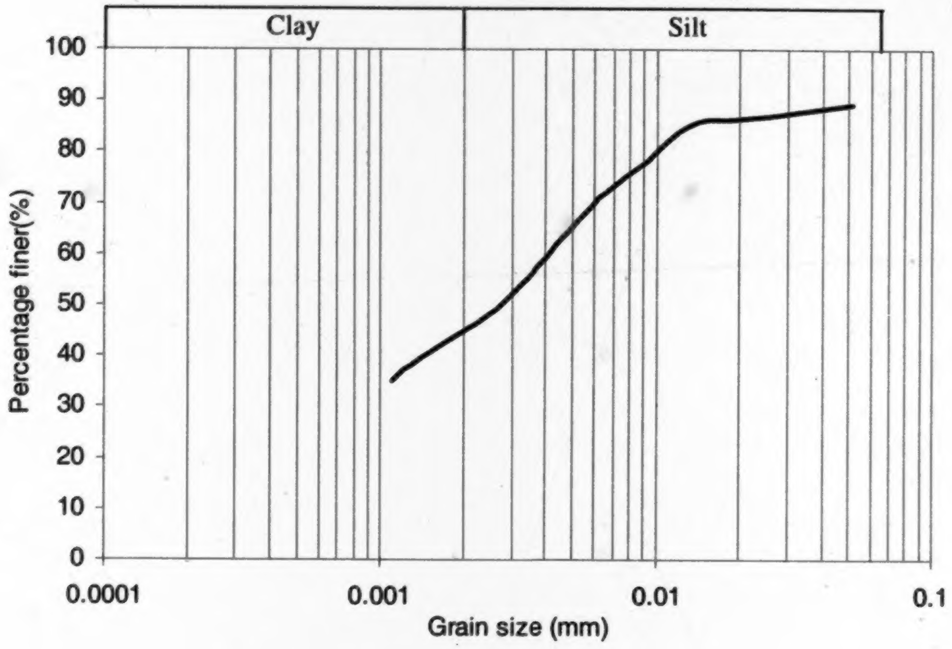

Figure 7.1 Grain-size distribution of Athabasca clay

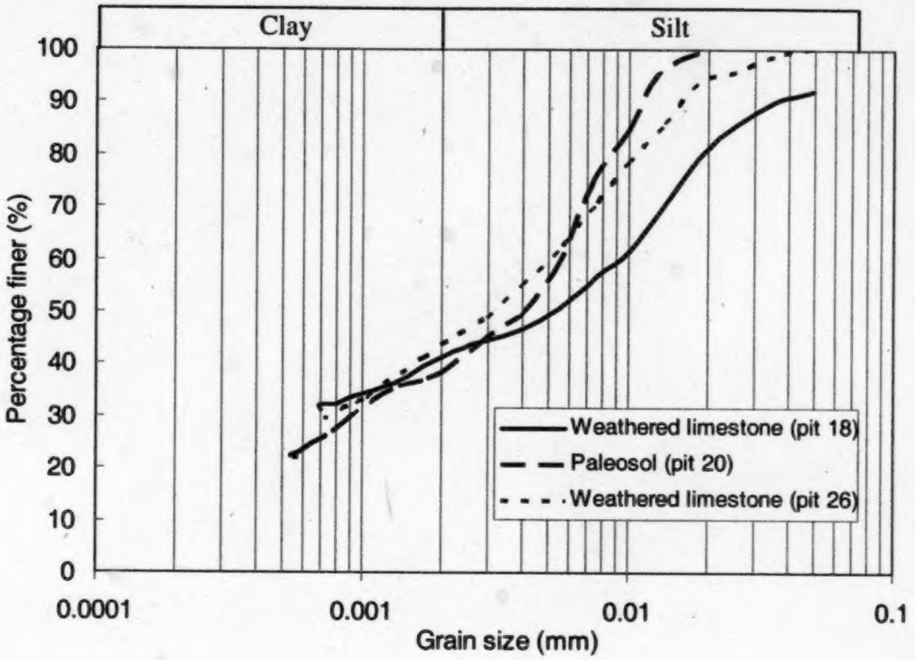

Figure 7.2 Grain-size distribution of Fort McMurray weak rocks

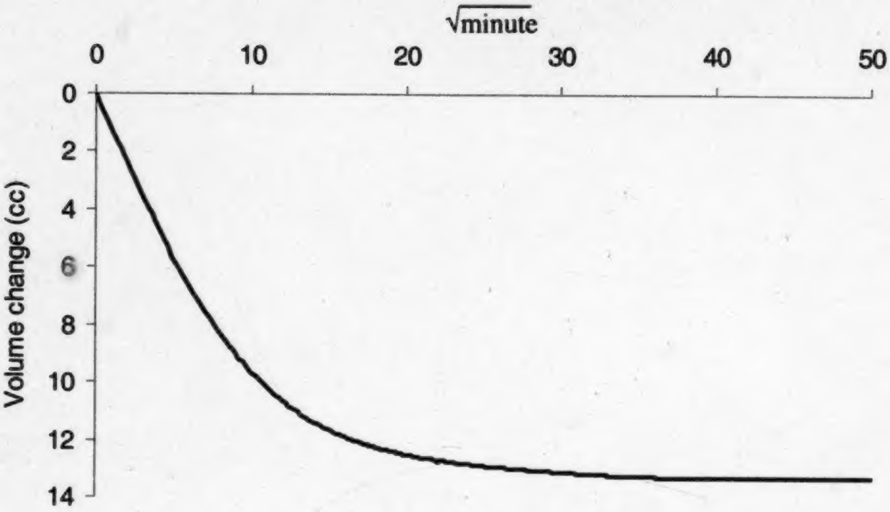

Figure 7.3 Consolidation curve: volume change versus square root time for Athabasca clay

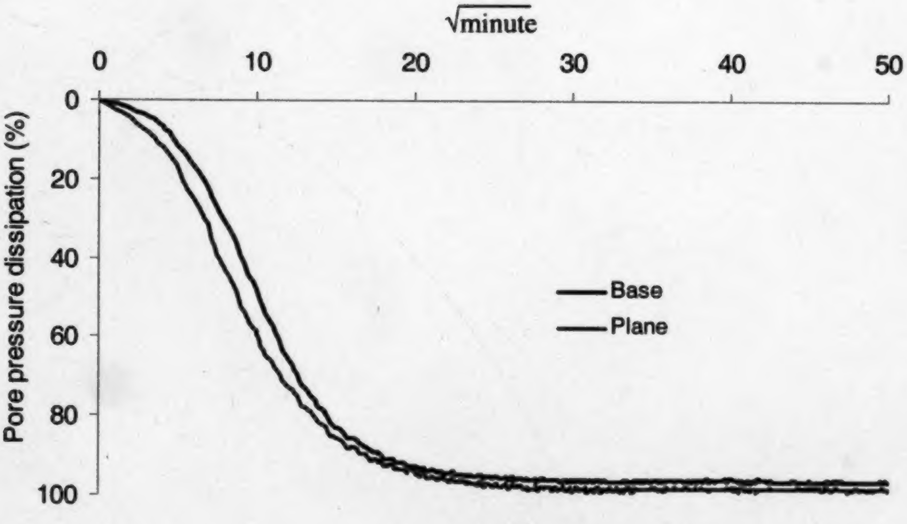

Figure 7.4 Pore-pressure-dissipation curve for Athabasca clay

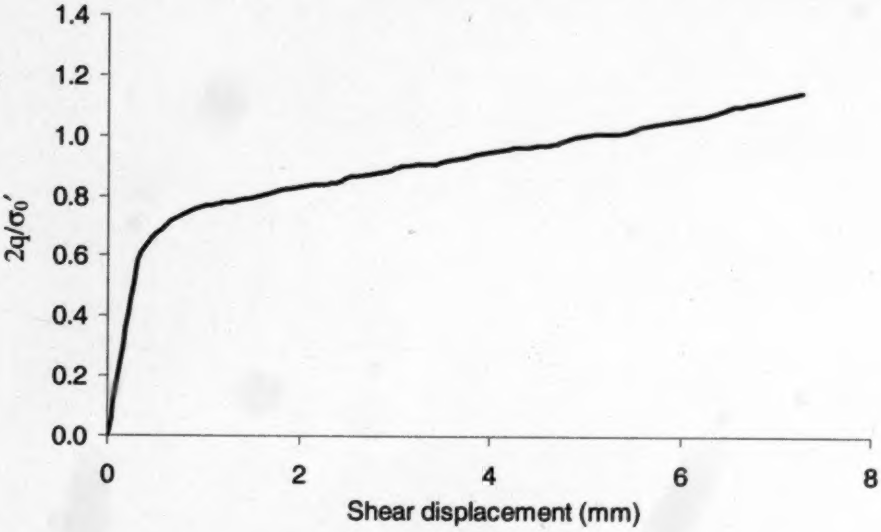

Figure 7.5 Relationship between normalized deviator stress and shear displacement for Athabasca clay at the axial displacement rate of 2 mm/minute

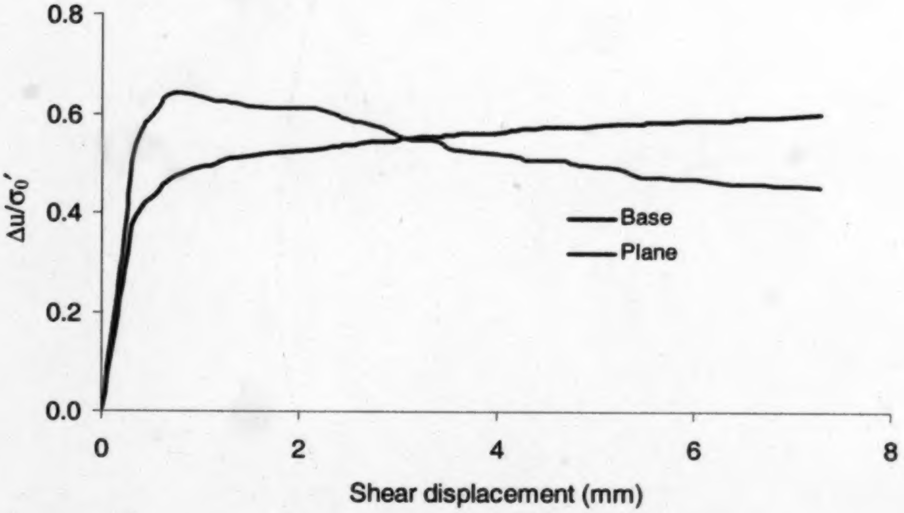

Figure 7.6 Relationship between normalized pore-water pressure and shear displacement for Athabasca clay at the axial displacement rate of 2 mm/minute

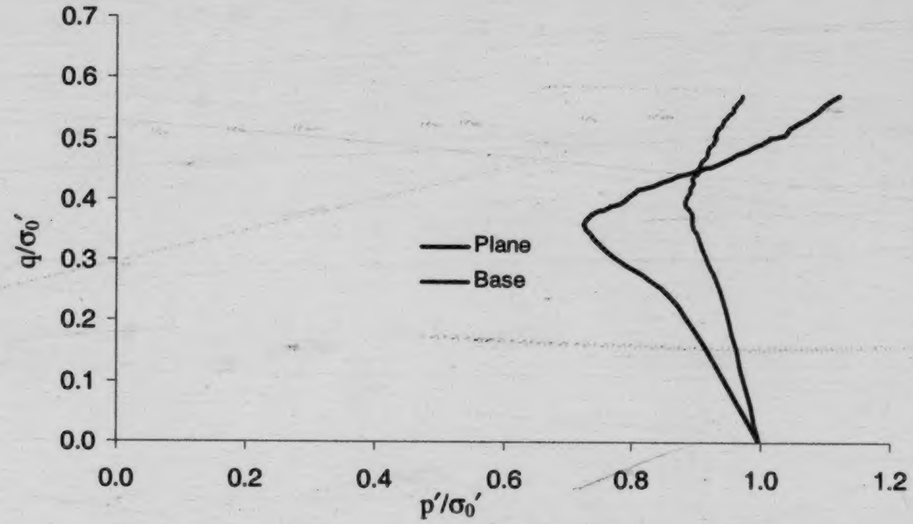

Figure 7.7 Normalized effective stress paths for Athabasca clay at the axial displacement rate of 2 mm/minute

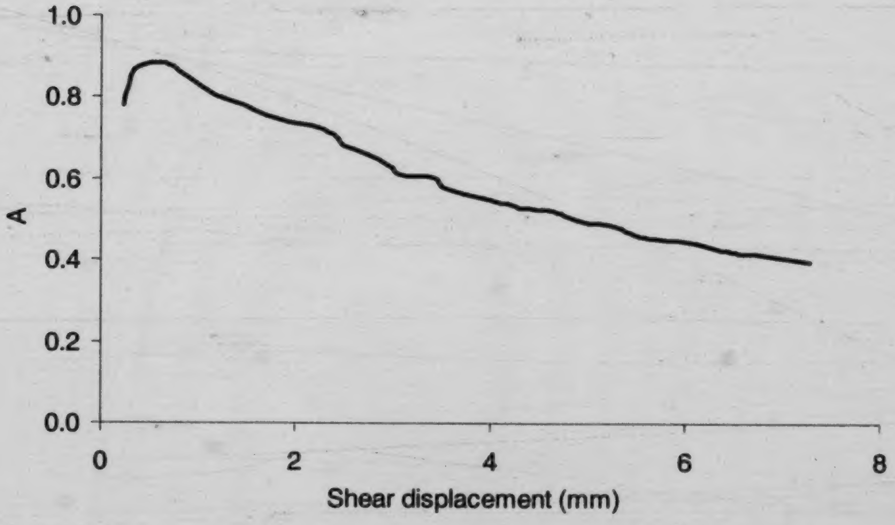

Figure 7.8 Relationship between the pore-pressure parameter A and the shear displacement for Athabasca clay at the axial displacement rate of 2 mm/minute

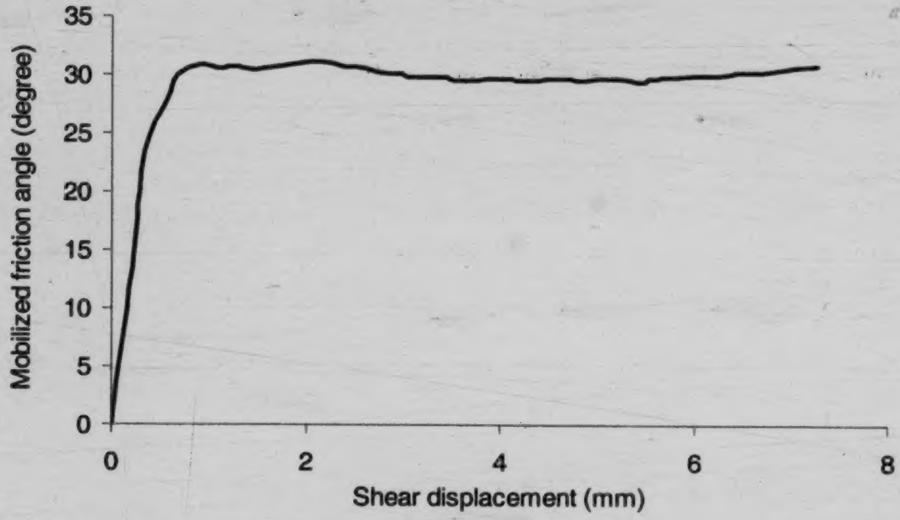

Figure 7.9 Relationship between mobilized friction angle and shear displacement for Athabasca clay at the axial displacement of 2 mm/minute

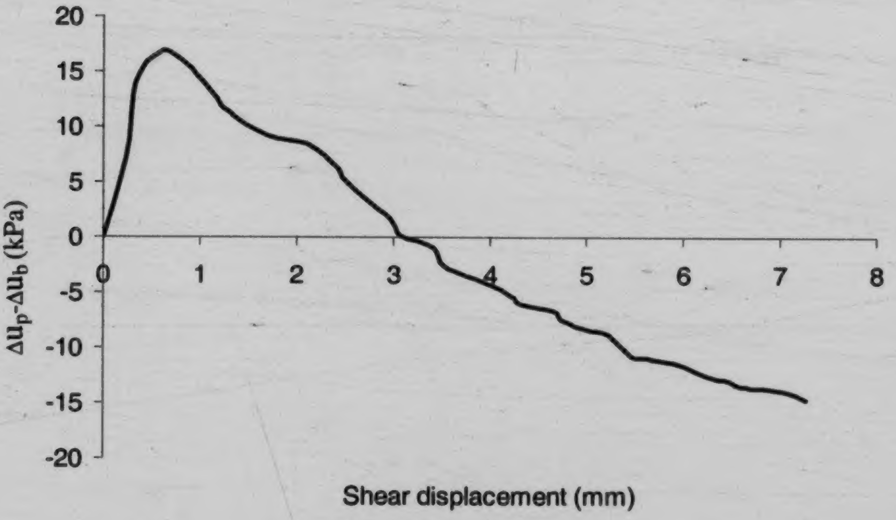

Figure 7.10 Difference between the pore-pressure-change on the plane and on the base of an Athabasca clay specimen at the axial displacement rate of 2 mm/minute

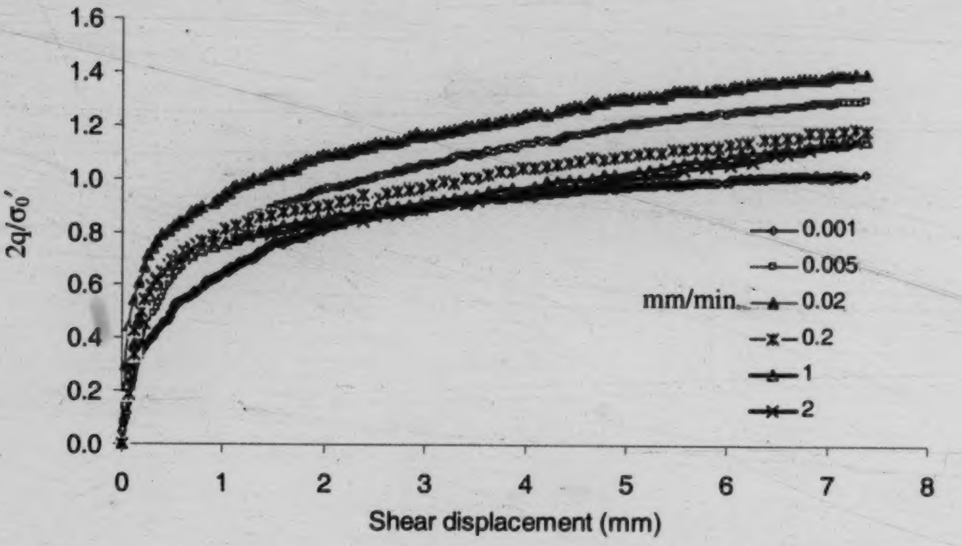

Figure 7.11 Normalized deviator stresses at the different axial displacement rates for Athabasca clay

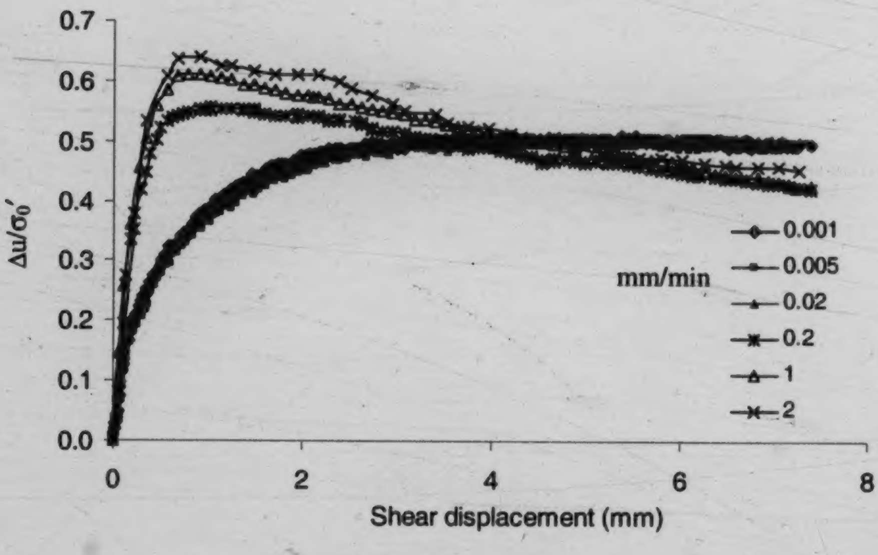

Figure 7.12 Normalized pore-water pressures on the plane at the different axial displacement rates for Athabasca clay

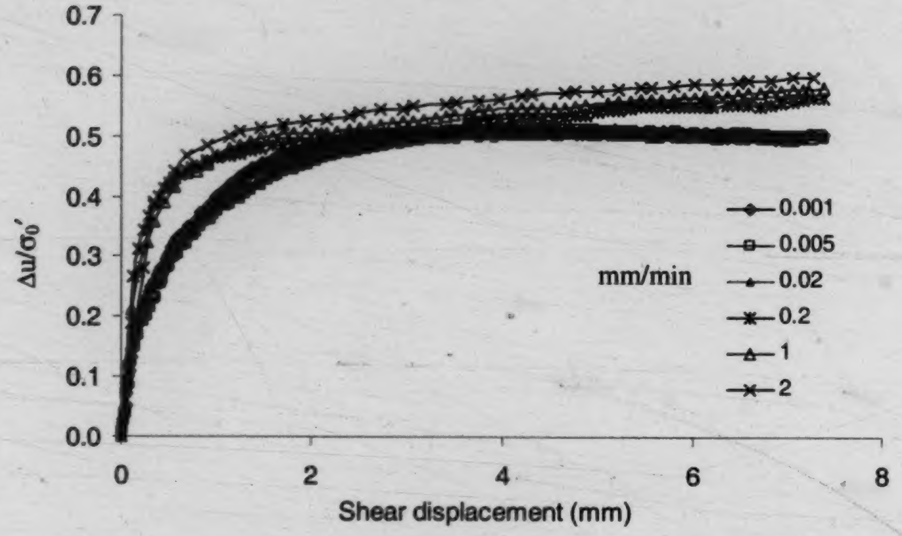

Figure 7.13 Normalized pore-water pressures on the base at the different axial displacement rates for Athabasca clay

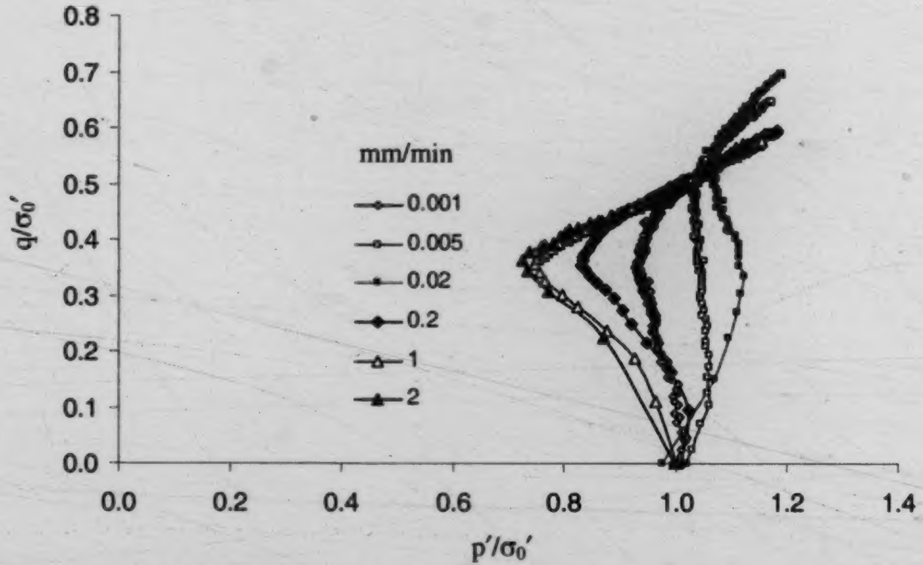

Figure 7.14 Normalized effective stress paths on the shear plane at the different axial displacement rates for Athabasca clay

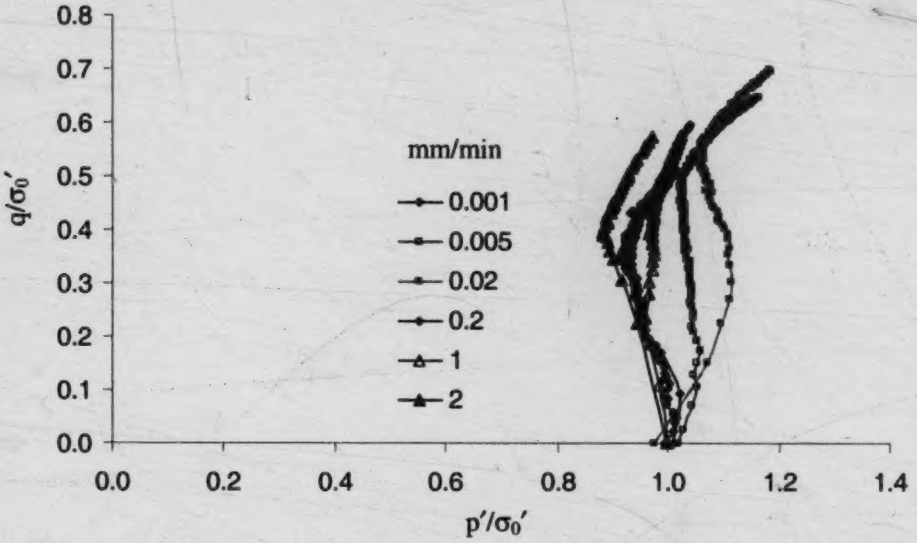

Figure 7.15 Normalized effective stress paths on the base at the different axial displacement rates for Athabasca clay

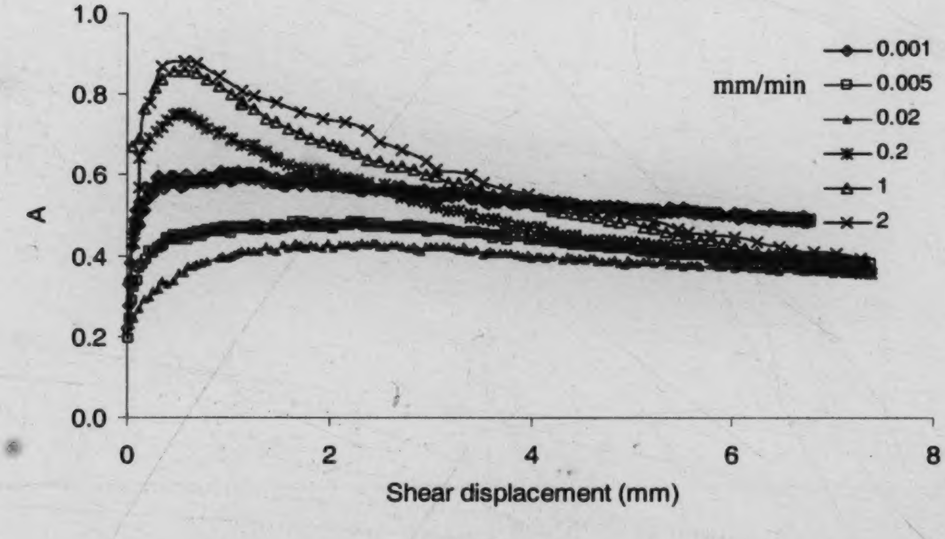

Figure 7.16 Relationship between the pore-pressure parameter A (on the shear plane) and the shear displacement at the different axial displacement rates for Athabasca clay

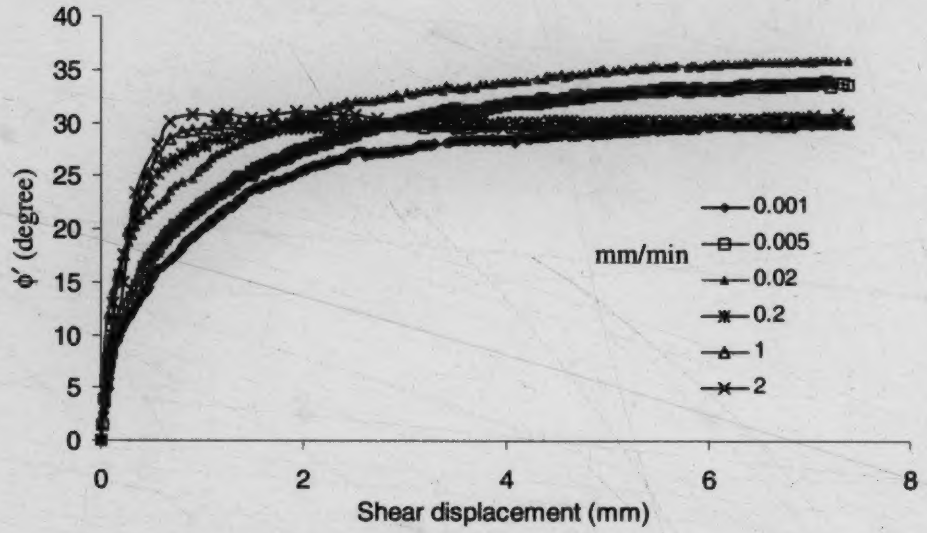

Figure 7.17 Mobilized friction angles with the shear displacement at the different axial displacement rates for Athabasca clay

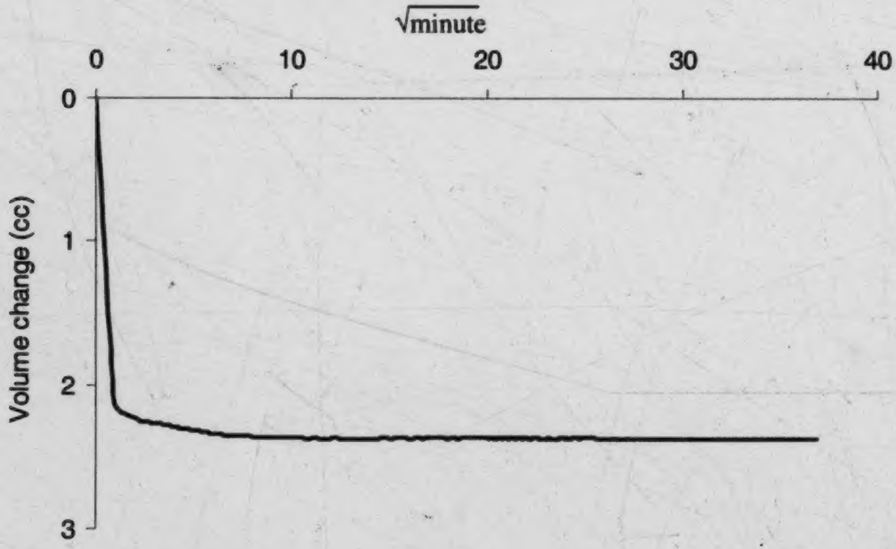

Figure 7.18 Consolidation curve: volume change versus square root time for Highvale mudstone

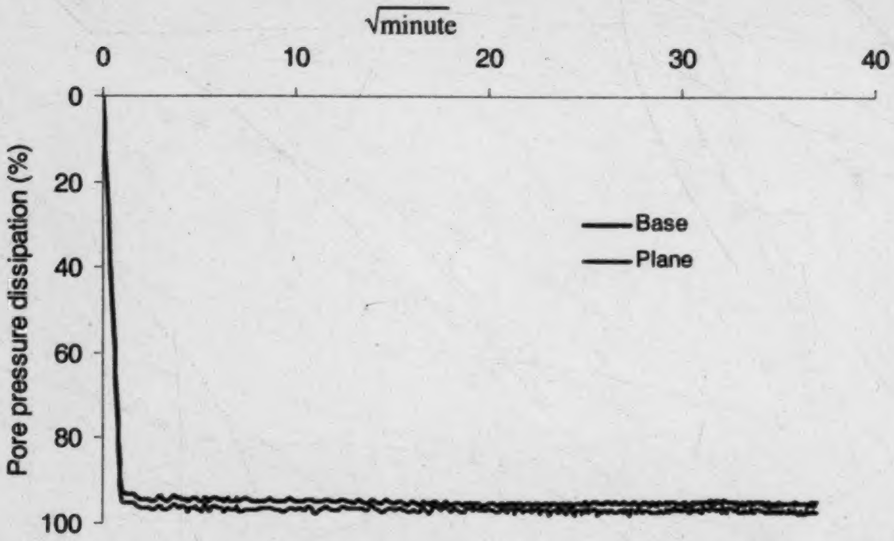

Figure 7.19 Pore-pressure-dissipation curve for Highvale mudstone

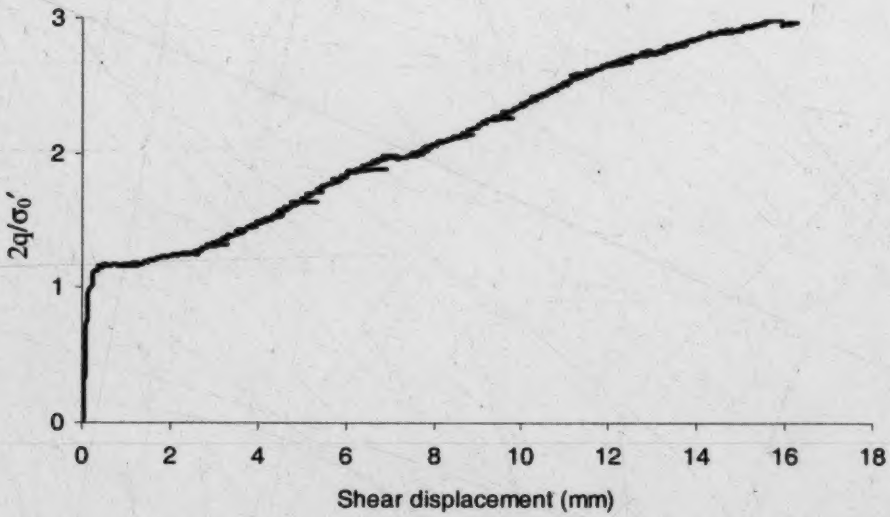

Figure 7.20 Relationship between normalized deviator stress and shear displacement for Highvale mudstone at the axial displacement rate of 0.01 mm/minute

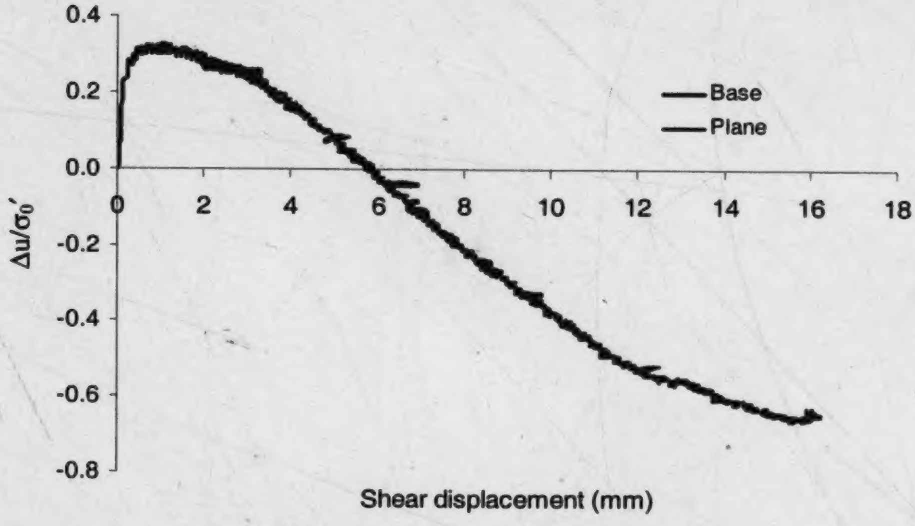

Figure 7.21 Relationship between normalized pore-water pressure and shear displacement for Highvale mudstone at the axial displacement rate of 0.01 mm/minute

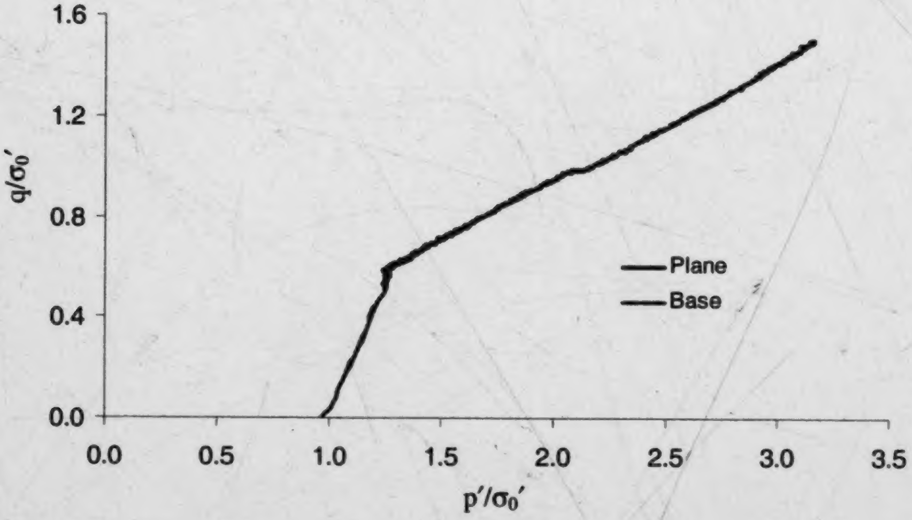

Figure 7.22 Normalized stress paths for Highvale mudstone at the axial displacement rate of 0.01 mm/minute

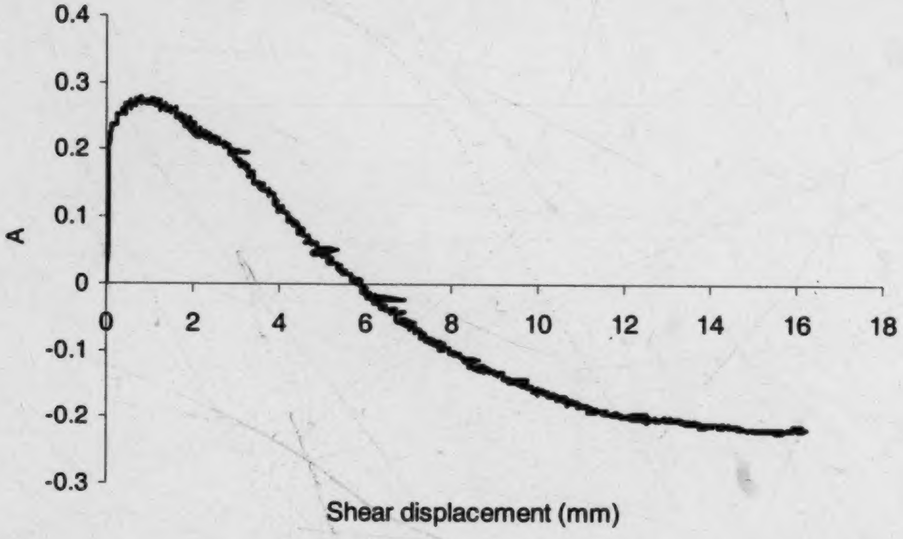

Figure 7.23 Relationship between the pore-pressure parameter A and the shear displacement for Highvale mudstone at axial displacement rate of 0.01 mm/minute

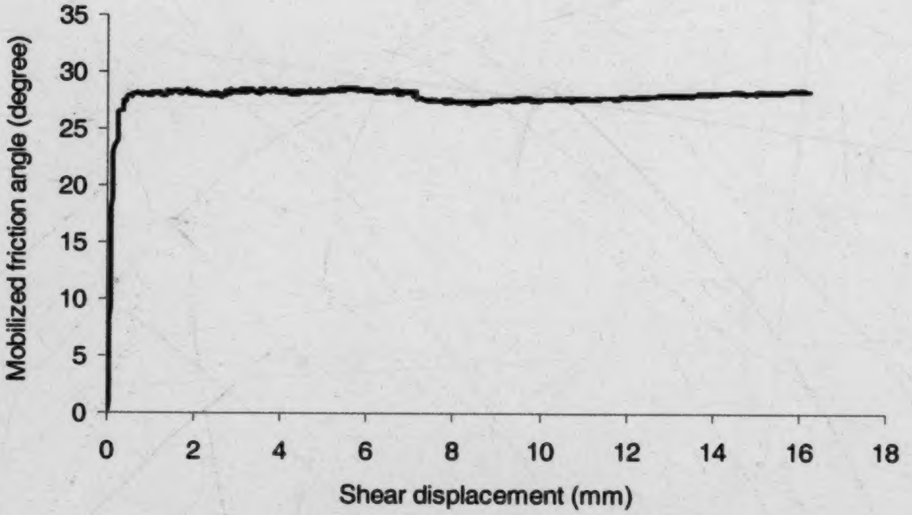

Figure 7.24 Relationship between mobilized friction angle and shear displacement for Highvale mudstone at the axial displacement of 0.01 mm/minute

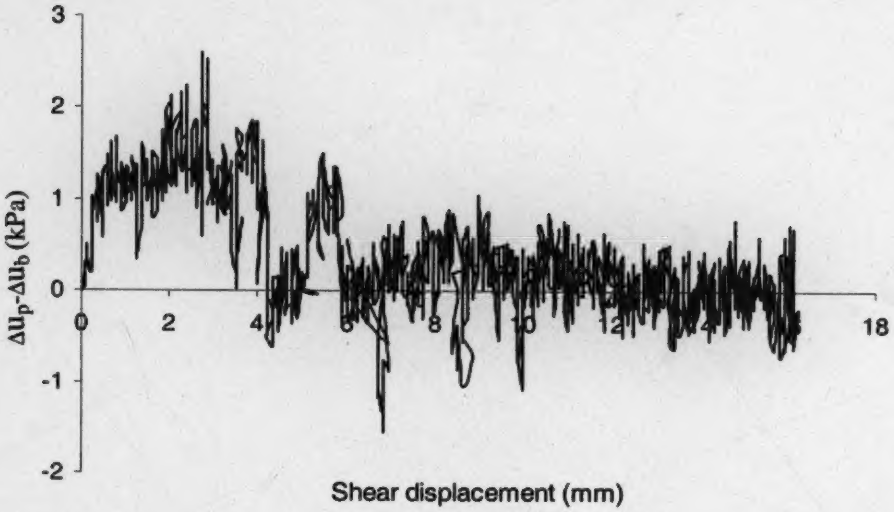

Figure 7.25 Difference between the pore-pressure-changes on the plane and on the base of a Highvale mudstone specimen at the axial displacement rate of 0.01 mm/minute

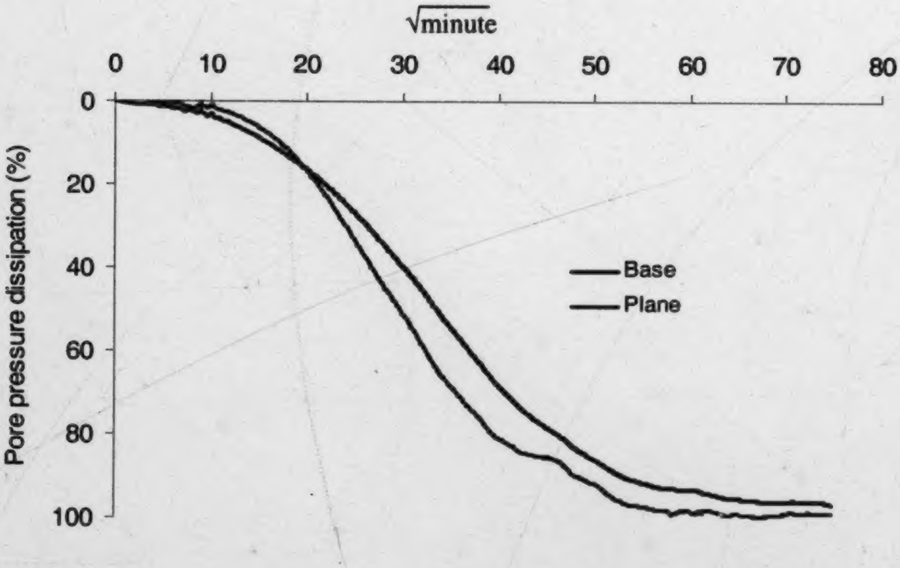

Figure 7.26 Pore-pressure-dissipation curve for Suncor weathered limestone

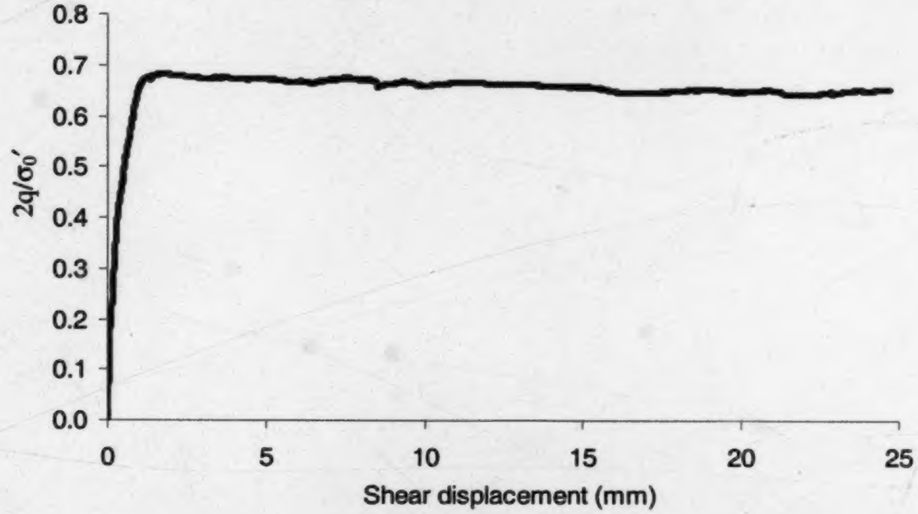

Figure 7.27 Relationship between normalized deviator stress and shear displacement for Suncor weathered limestone at the axial displacement rate of 0.002 mm/minute

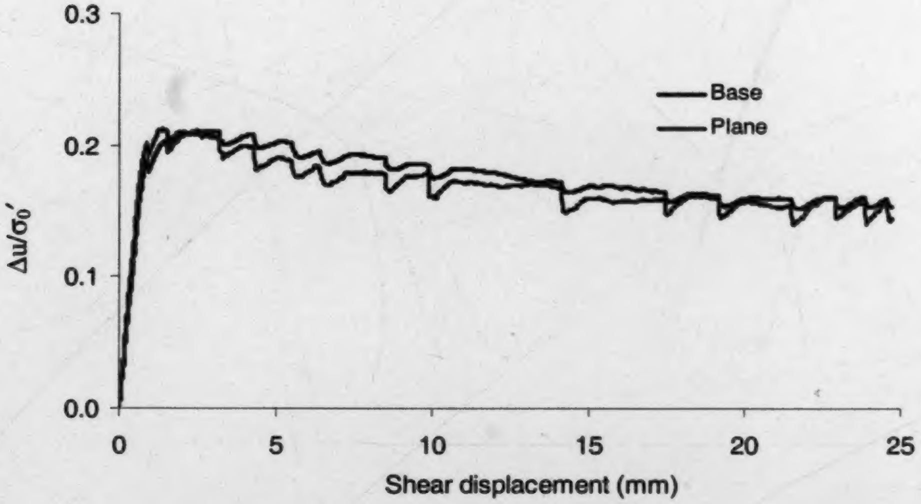

Figure 7.28 Relationship between normalized pore-water pressure and shear displacement for Suncor weathered limestone at the axial displacement rate of 0.002 mm/minute

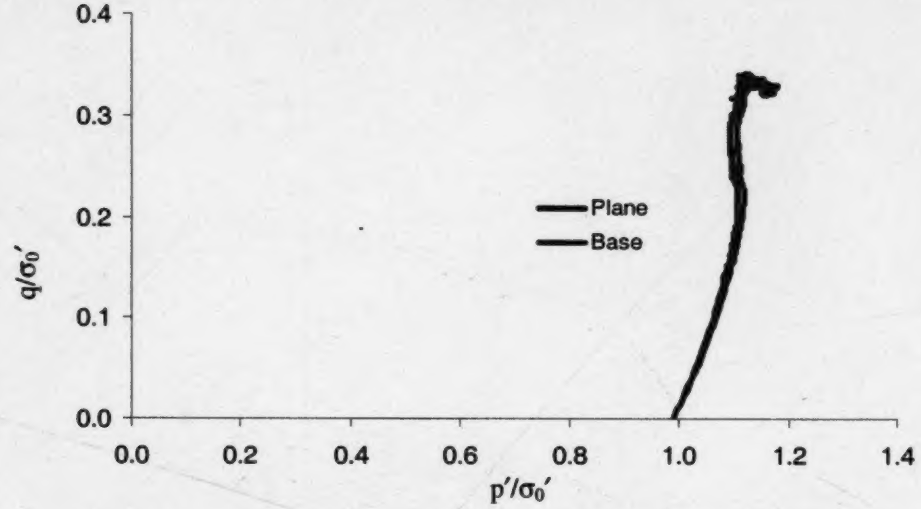

Figure 7.29 Normalized effective stress paths for Suncor weathered limestone at the axial displacement rate of 0.002 mm/minute

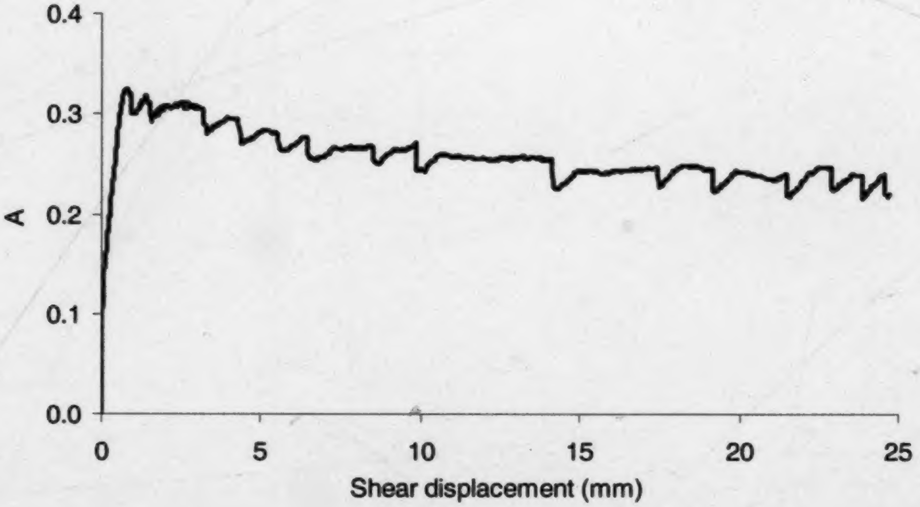

Figure 7.30 Relationship between the pore-pressure parameter A and the shear displacement for Suncor weathered limestone at the axial displacement rate of 0.002 mm/minute

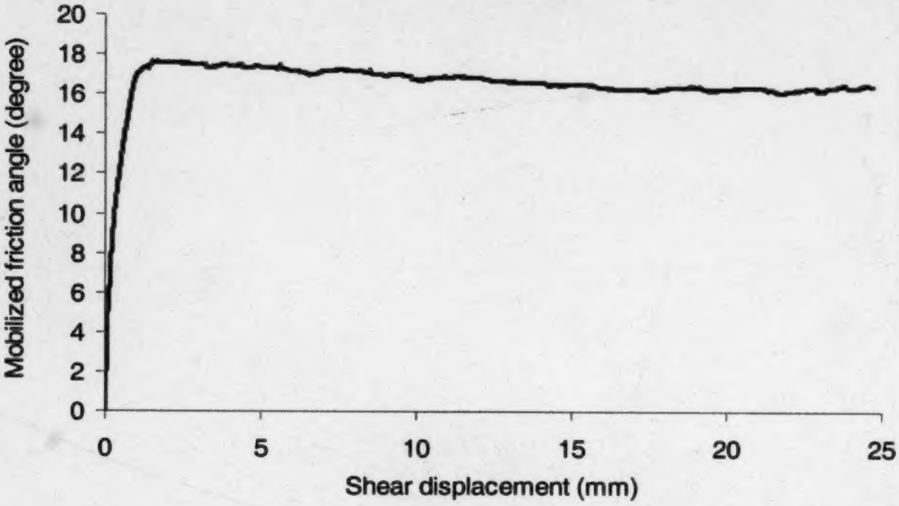

Figure 7.31 Relationship between mobilized friction angle and shear displacement for Suncor weathered limestone at the axial displacement rate of 0.002 mm/minute

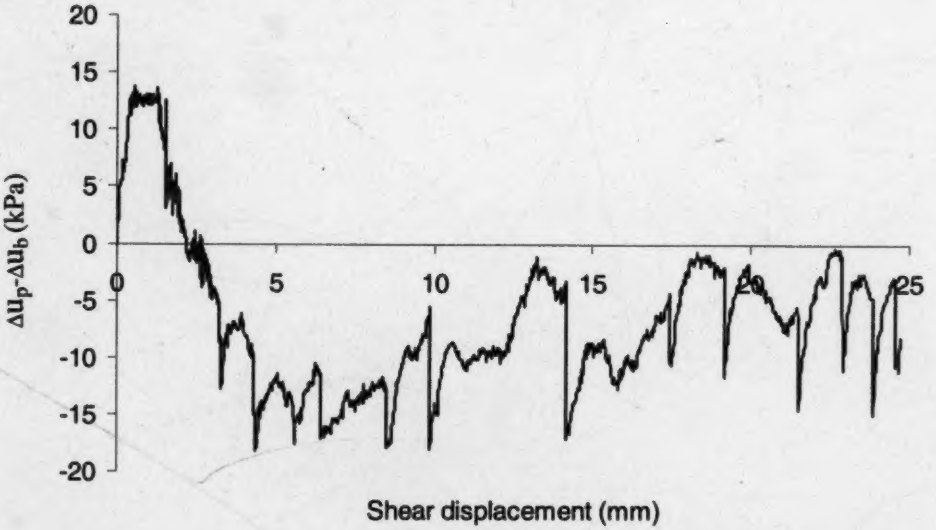

Figure 7.32 Difference between the pore-pressure-changes on the plane and on the base of a Suncor weathered limestone specimen at the axial displacement rate of 0.002 mm/minute

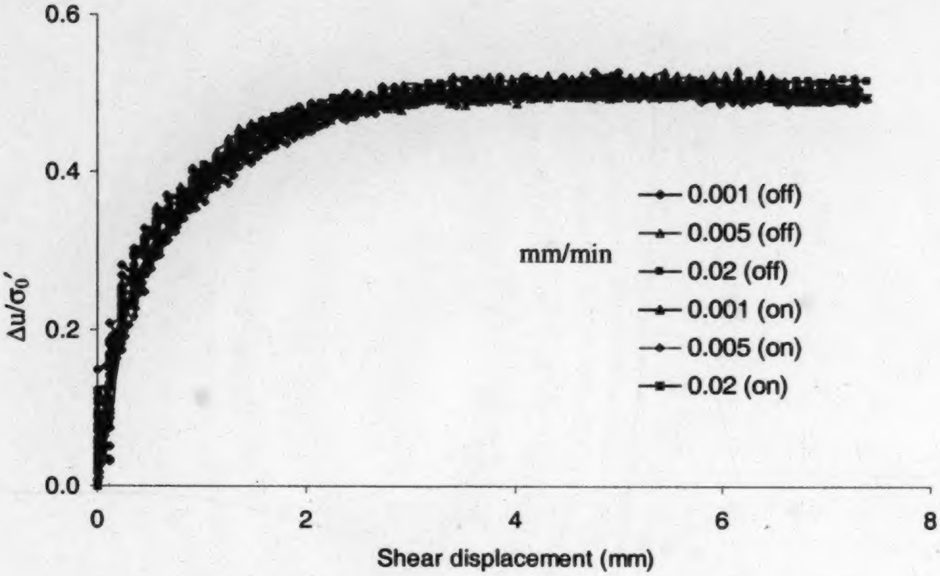

Figure 7.33 Comparison of the normalized pore-pressure-changes for Athabasca clay measured on and off the shear plane at axial displacement rates of 0.001, 0.005, and 0.02 mm/minute

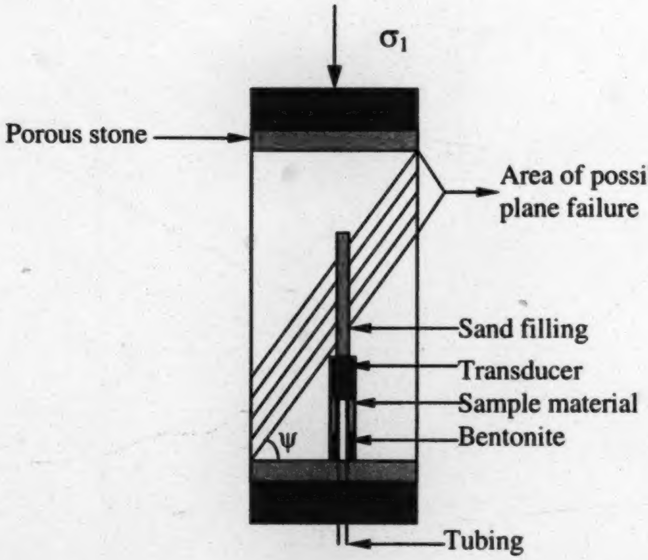
σ1
Porous stone
Area of possible plane failure
Sand filling
Transducer
Sample material
Bentonite
ψ
Tubing

Figure 7.34 Sketch of installation of the pore-pressure transducer in a Paleosol specimen

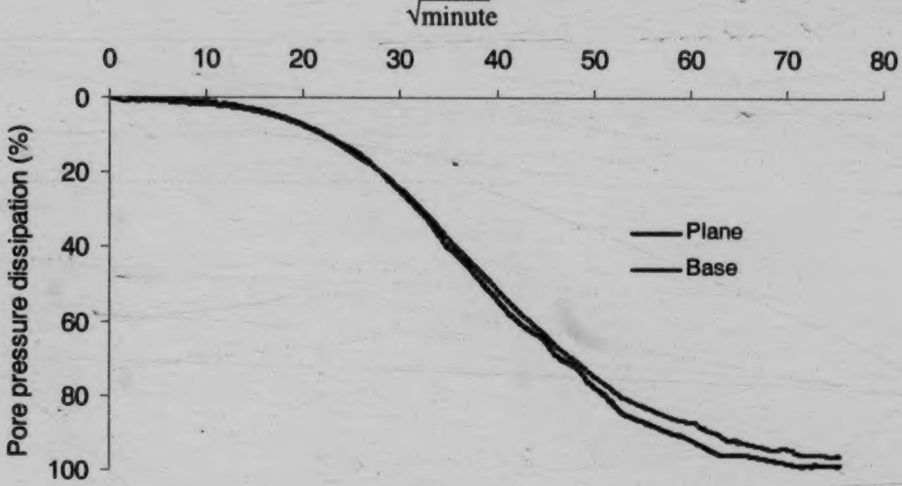

Figure 7.35 Pore-pressure-dissipation curve for Paleosol

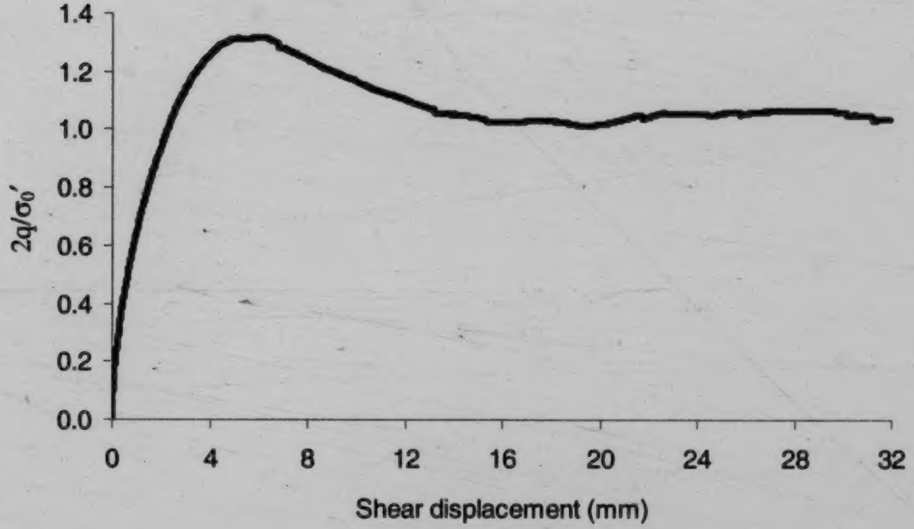

Figure 7.36 Relationship between normalized deviator stress and shear displacement for Paleosol at the axial displacement rate of 0.01 mm/minute

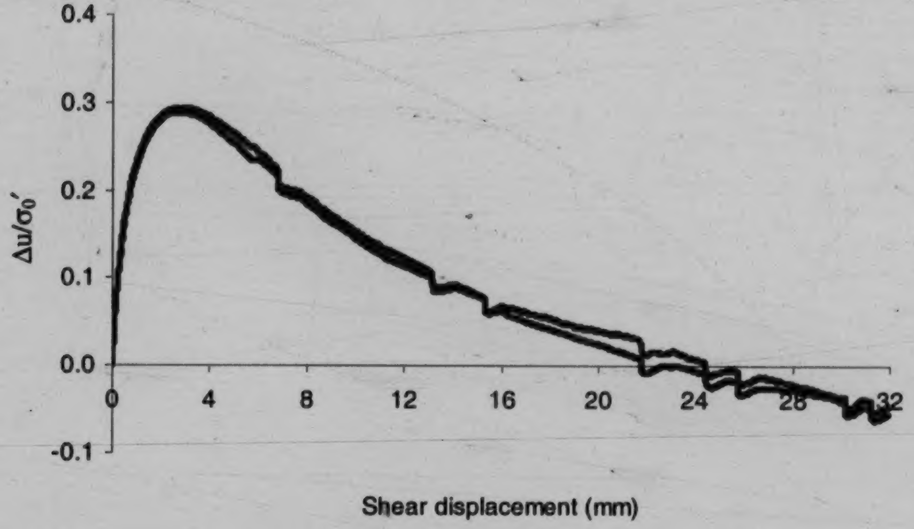

Figure 7.37 Relationship between normalized pore-water pressure and shear displacement for Paleosol at the axial displacement rate of 0.01 mm/minute

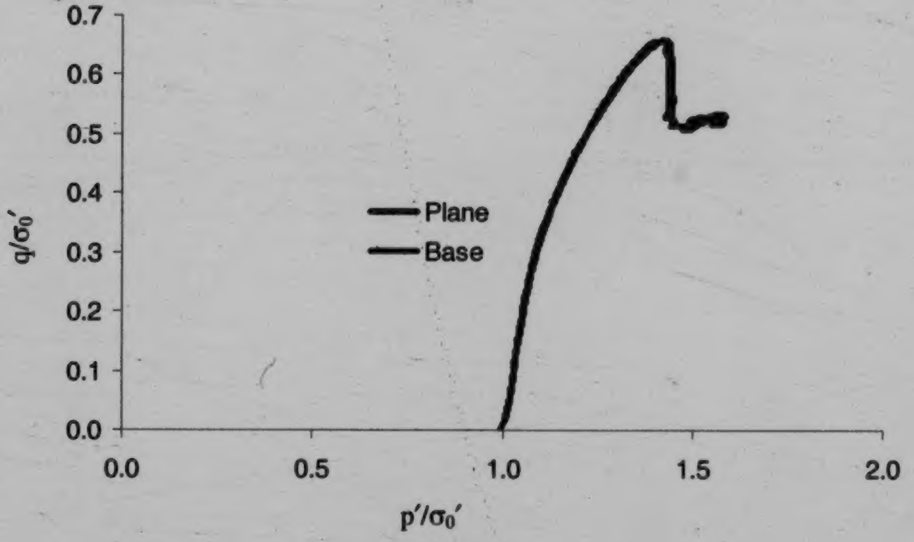

Figure 7.38 Normalized effective stress paths for Paleosol at the axial displacement rate of 0.01 mm/minute

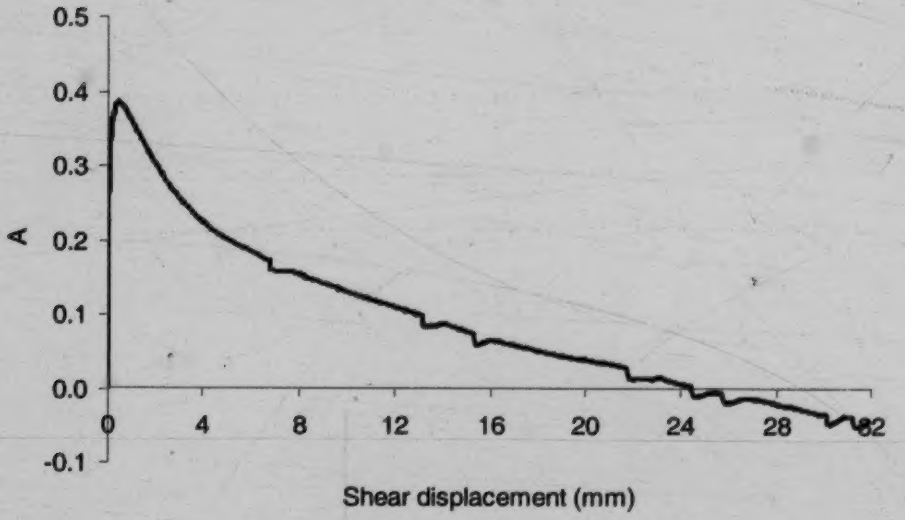

Figure 7.39 Relationship between the pore-pressure parameter A and the shear displacement for Paleosol at the axial displacement rate of 0.01 mm/minute

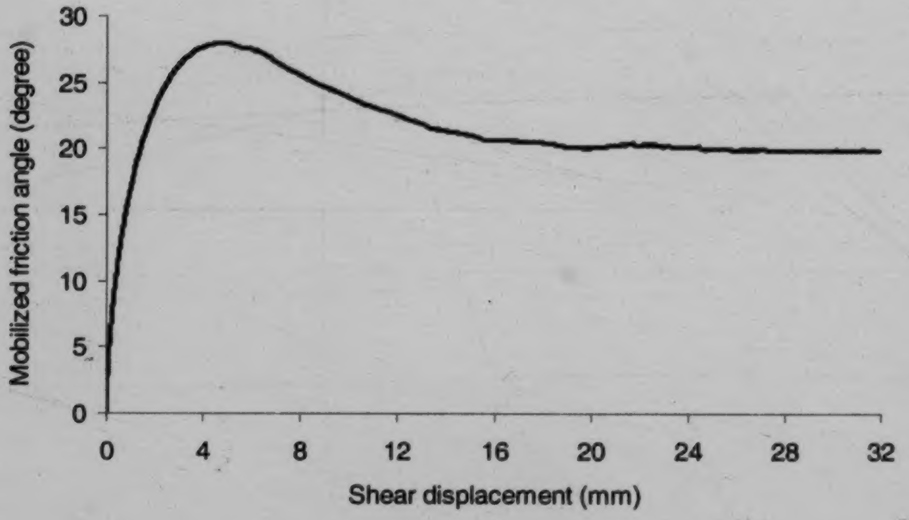

Figure 7.40 Relationship between mobilized friction angle and shear displacement for Paleosol under the assumption of no cohesion

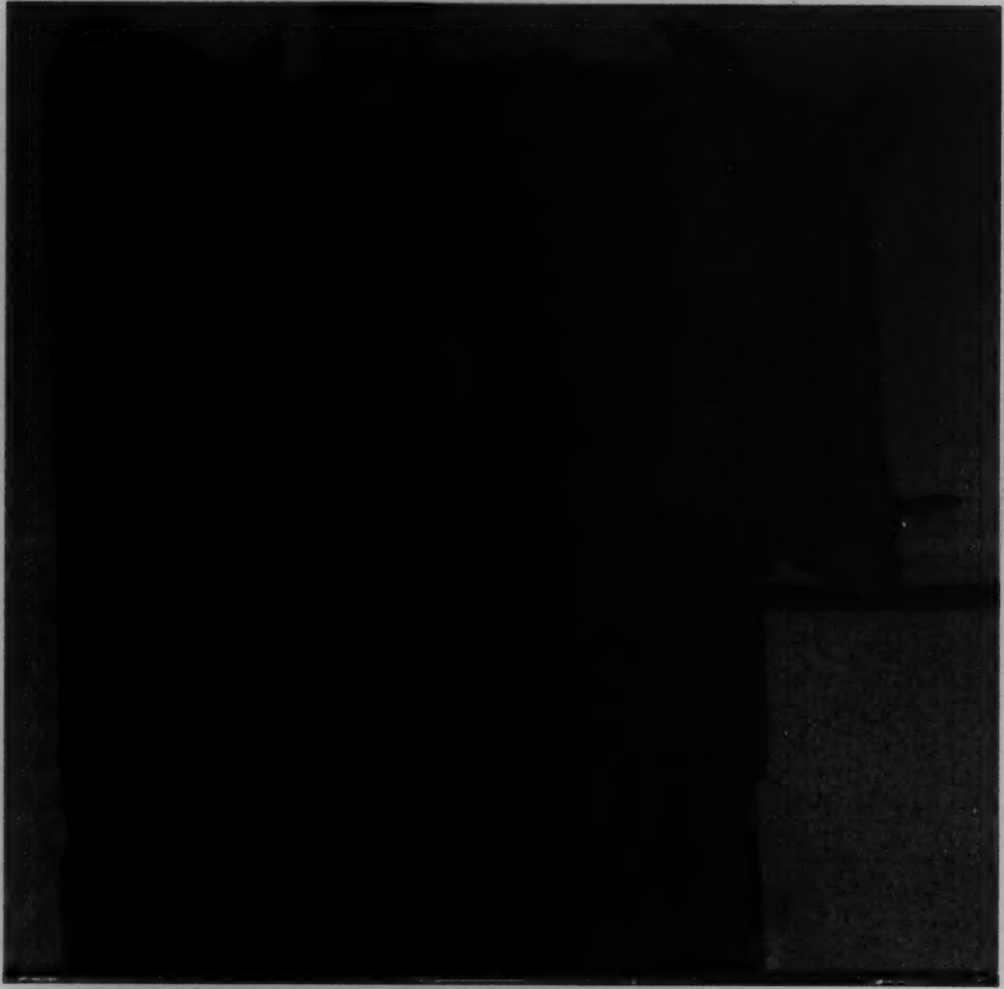

Figure 7.41 Photograph showing the upper sheared part against the right-angle steel strip

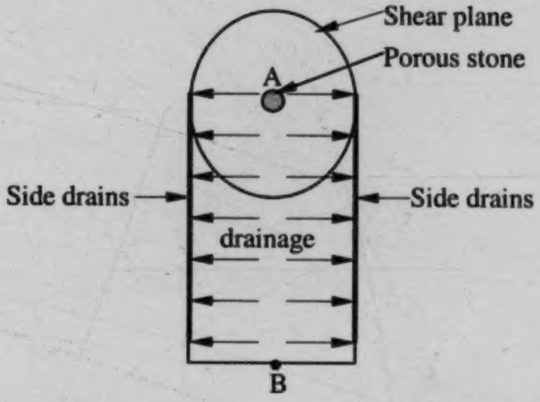
Shear plane
Porous stone
A
Side drains
Side drains
drainage
B

Figure 7.42 Lower half sample drainage from the radial boundary

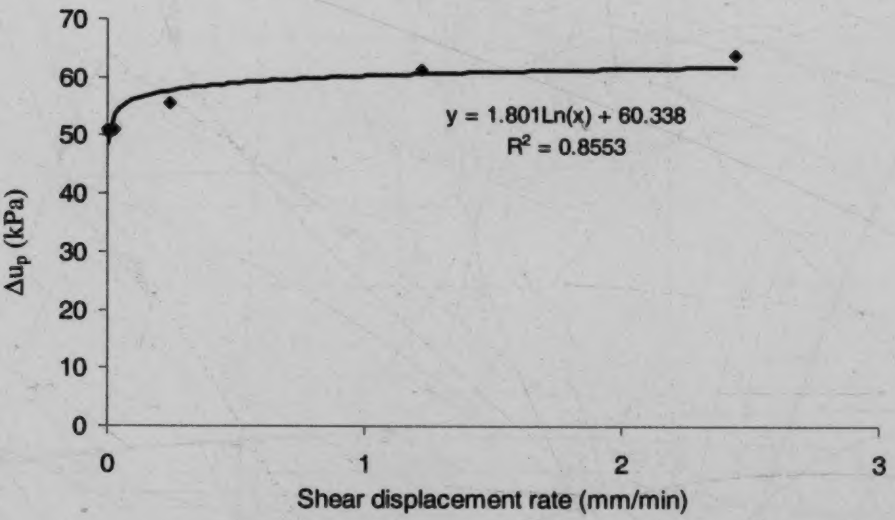

Figure 7.43 Relationship between the peak pore-pressure-changes and the shear displacement rates for Athabasca clay

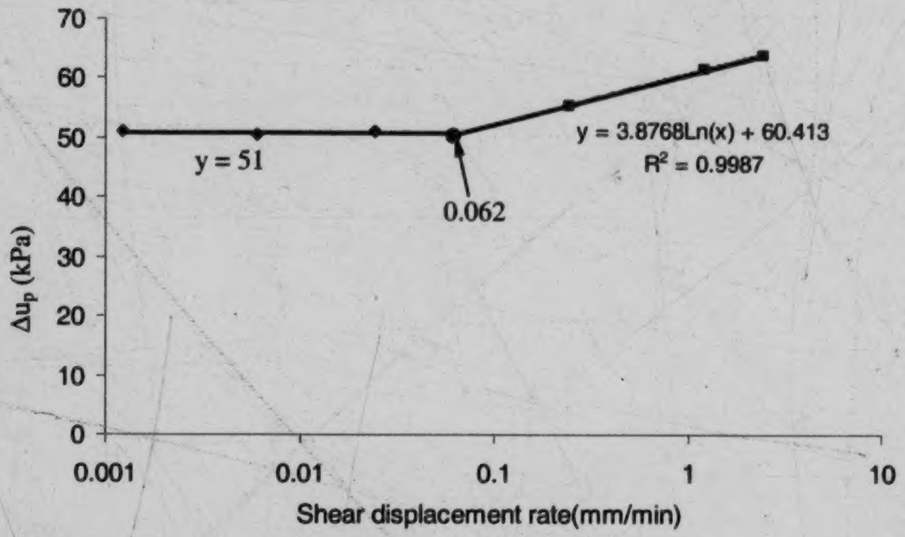

Figure 7.44 Relationship between the peak pore-pressure-changes and the shear displacement rates for Athabasca clay

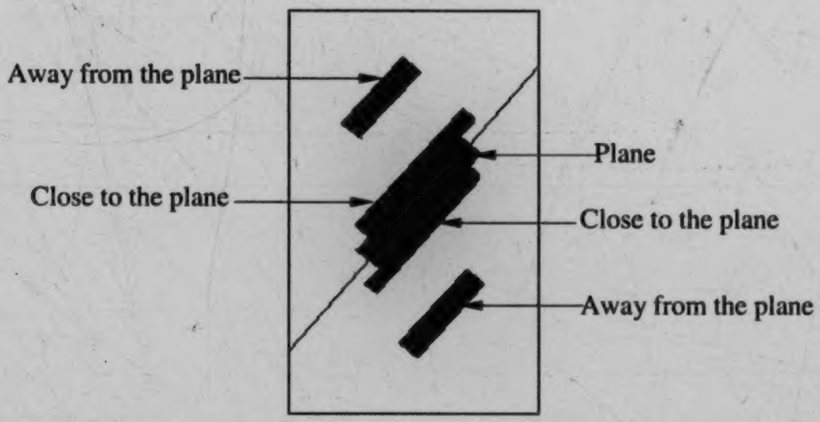
Away from the plane
Close to the plane
Plane
Close to the plane
Away from the plane

Figure 7.45 Positions for water content measurements in a Athabasca clay sample after testing

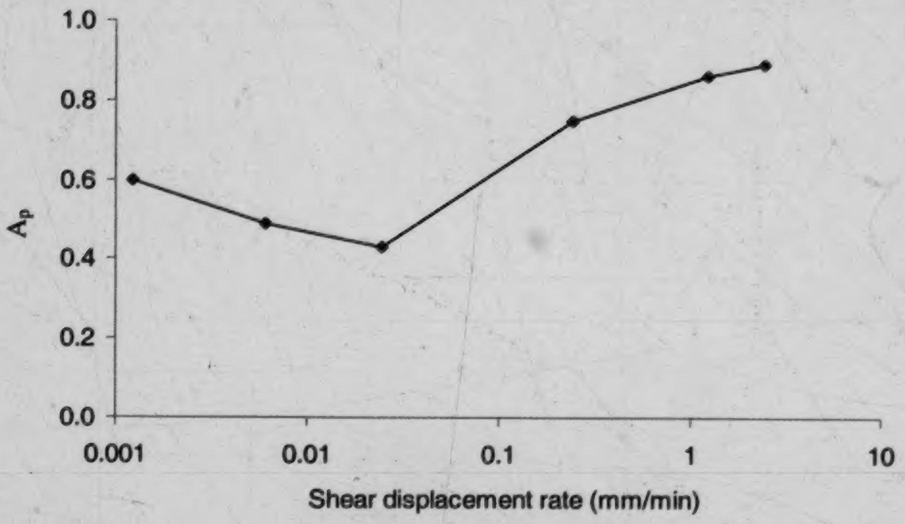

Figure 7.46 Relationship between the peak pore-pressure parameter A_p and the shear displacement rates for Athabasca clay

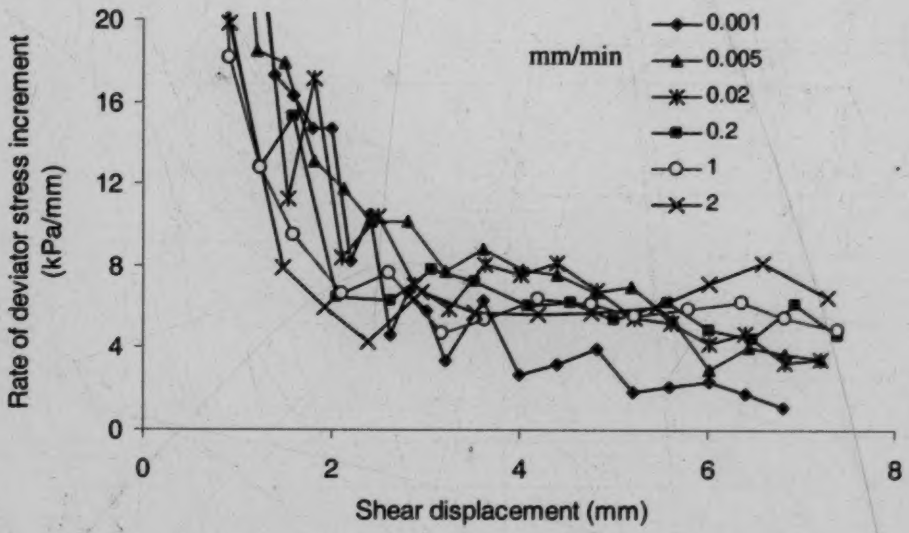

Figure 7.47 Relationship between the rate of deviator-stress-increment and the shear displacement for Athabasca clay at the different axial displacement rates

Figure 7.48 Sub-planar and moderately rough shear plane in one Paleosol sample (diameter of Canadian one-dollar is 26mm)

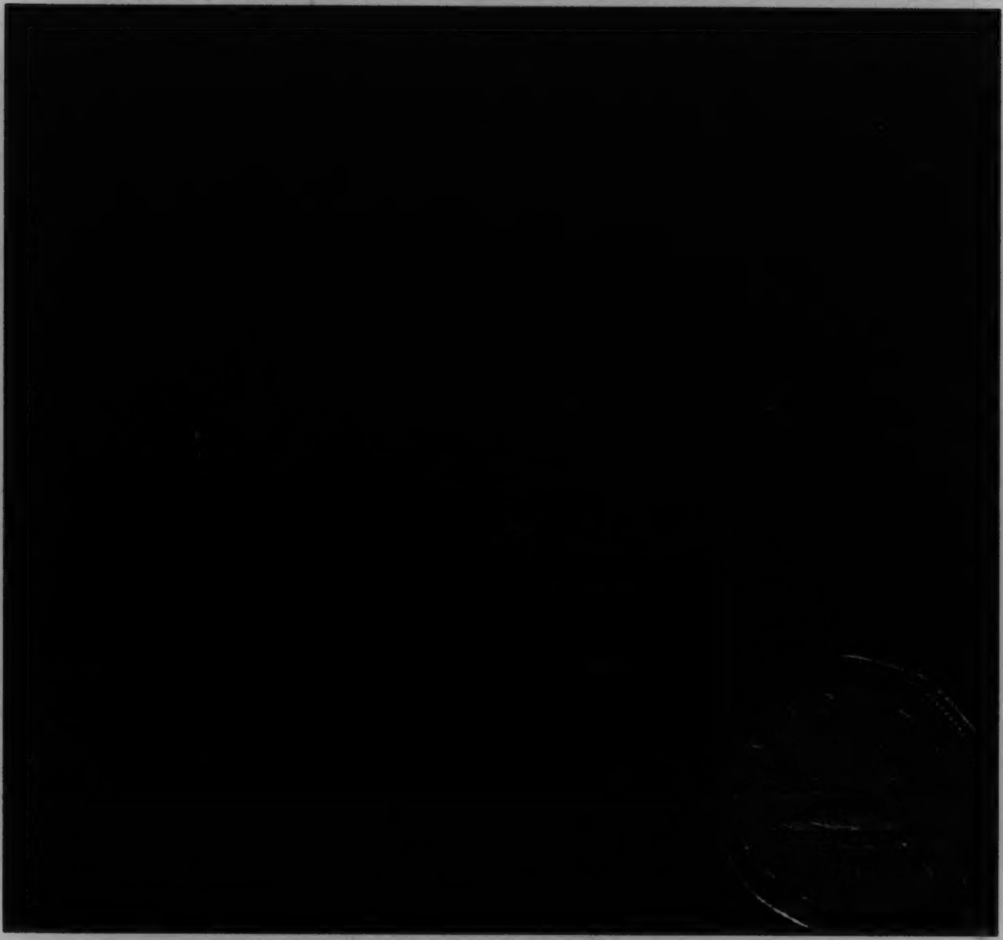

Figure 7.49 Photo showing a sub-planar and moderately rough shear plane in another Paleosol sample (diameter of Canadian one-dollar is 26mm)

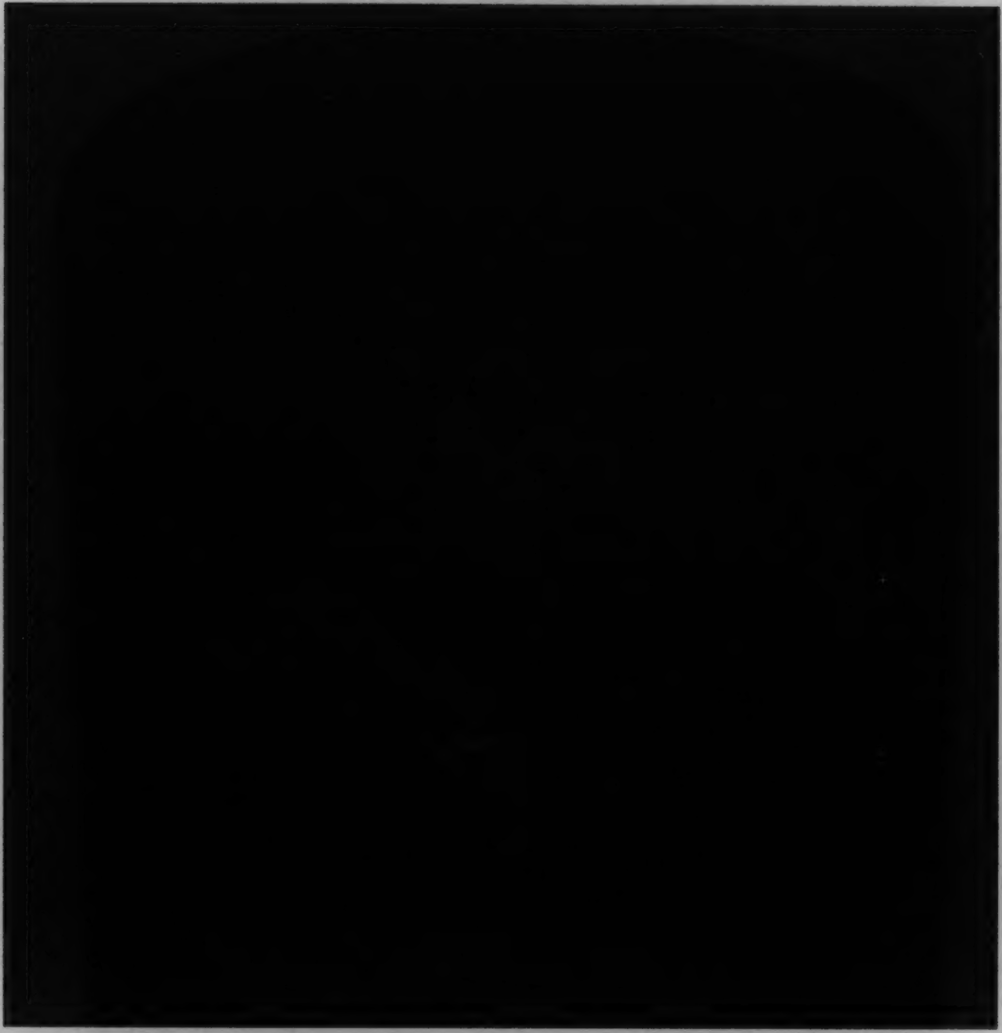

Figure 7.50 Photo showing many calcium carbonate nodules in Paleosol (diameter of the specimen is 100mm)

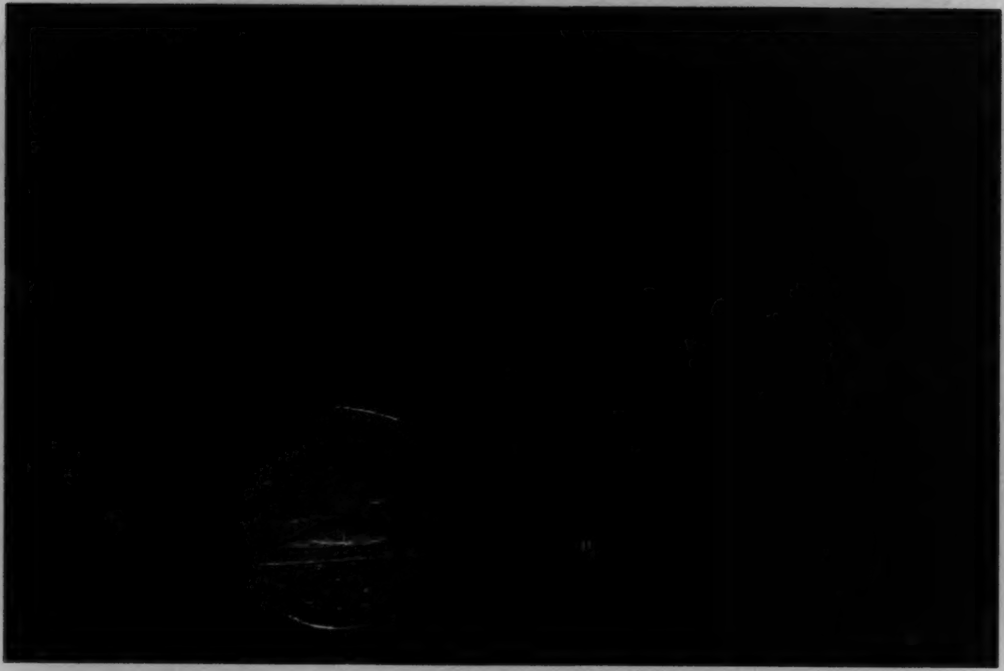

Figure 7.51 Photo showing a rough and striated shear plane in the third Paleosol sample (diameter of Canadian one-dollar is 26mm)

CHAPTER 8 SUMMARY, CONCLUSIONS, AND RECOMMENDATIONS

8.1 SUMMARY AND CONCLUSIONS

Shear zones, containing internal fractures and resulting from strain localization, are common in soils and rocks. A shear zone has lower strength than adjacent materials. Therefore, whenever pre-existing shear zones occur, their complex internal fractures and geometries, and weak mechanical behavior may exert a controlling influence on engineering design and construction. In the Athabasca Oil Sands area near Fort McMurray, shear zones developed by glaciation, valley rebound, erosion, and other natural geological events pose a major challenge for oil sands geotechnics. Some slope failures and large dam movements have been caused by such shear zones. Therefore, understanding the behavior of these shear zones is important for facilities founded on such weak shear zones.

Shear zone geotechnics involves the shear behavior and the pore-pressure response of a shear zone, which demands a thorough understanding of the material's behavior and of the detailed geometry of fractures within the zone itself. Detailed geological field mapping of two excavations for shear keys for the construction of tailing dykes at Suncor Energy Ltd.'s Oil Sands mine near Fort McMurray was carried out to establish the shear zone geometry. Observations and descriptions are given of several shear zones. A series of laboratory index tests were performed to identify the basic physical and engineering properties of the materials associated with these shear zones. Based on the shear zone geometry, shear strength and pore-pressure parametric-sensitivity analyses were conducted to reveal the influence of a minor change in the residual friction angle and pore pressure on the stability and displacement of a soil structure founded on a shear zone. Furthermore, an innovative large triaxial testing system and related transducers, especially an internal pore pressure transducer and local displacement transducer, were developed. Sampling methods, laboratory techniques, and testing procedures were established to measure the pore pressure in a shear zone and its different response from that of the adjacent material under normally practical displacement rates. Large samples were used for shear-behavior testing to reduce size effects. Three materials were tested: compacted Athabasca clay, over-consolidated Highvale mudstone, and Fort McMurray weak rocks, and the test results were presented and analyzed.

This study had four phases. Phase One involved background investigation and parametric sensitivity analysis. Phase Two consisted of field investigation and laboratory index tests to establish the shear zones' geometry and their basic physical and engineering properties. Phase Three included equipment development and establishing a testing methodology. The final phase involved conducting laboratory tests to explore the pore-pressure response and the shear behavior of shear zones in different materials. The following sections concluded the main findings of this research.

8.1.1 Field Investigation of Shear Zones and Laboratory Index Tests

Detailed field mapping of several shear zones was carried out by using the baseline and network method to establish their geometries. Observations and descriptions were given of four shear zones. A series of laboratory tests was conducted to identify the basic physical properties of shear zones and the adjacent materials. The main conclusions drawn from this phase of the study are:

1. Shear zones are common in the Athabasca Oil Sands area. They often develop in clay beds with high clay content such as clay shale, basal clay, Paleosol, pond mud, and the highly weathered limestone. These shear zones make the weak clay beds much weaker than the rest of the materials.
2. Shear zones have a complex fracture pattern that is strongly related to the amount of deformation that has occurred in the past. The one or more principal D shears and minor shears are typical in a shear zone. The D shears are the weakest place in the shear zone.

3. The shear zone's water content is markedly higher than that of the adjacent unsheared over-consolidated weak rocks.
4. The grain size of the material within a shear zone is much smaller than that of the adjacent unsheared material since the material experiences intense comminution and destruction under high stresses during the shear zone's formation, causing grain-size reduction and clay may accumulate in the shear zone.
5. The Atterberg limits of the material within a shear zone are significantly larger than those of the adjacent unsheared material.

8.1.2 Testing Equipment and Procedures

An innovative large triaxial testing system and related transducers were developed by the author. Their design and installation techniques were described in detail. The laboratory techniques and procedures were established for this experimental study. The following conclusions can be drawn from this phase of the study:

1. The newly developed large dimensional triaxial apparatus or a modified conventional triaxial apparatus can be used to conduct triaxial compression tests on different materials with pore pressure measurements on a pre-existing shear plane.
2. The apparatus can be used with various pressure-control systems. A compressed air-water system and a syringe pump were used for the confining pressure system. The axial load was applied using a syringe pump for the large cell. Data Dolphin software and Agilent Benchlink Data Logger II software were used for the data-logging.
3. The internal pore-pressure transducer made with a Kyowa Model PS-10KB pressure sensor has an inclined end face and is a good tool to measure the pore pressure on the shear plane.
4. The local displacement along a shear plane can be measured by using either a "tilt" transducer made with two electronic Levels or a submersible LVDT.
5. The sampling technique and laboratory procedures for this specific experiment have been established as practical and operational. This methodology and the

special transducers can be considered to be two of this study's main contributions to the measurement of pore pressure on a shear plane.

8.1.3 Laboratory Testing

Laboratory tests on three materials (Athabasca clay, Highvale mudstone, and Fort McMurray weak rocks) were carried out to measure the pore pressure on a shear plane, to investigate the pore pressure response of different materials, and to explore their shear behavior by using either a modified triaxial cell or a newly developed large cell. The results were presented and analyzed. The following conclusions are drawn from these laboratory tests:

1. Pore pressures measured on the shear plane and on the base are identical provided that the displacement rate used is in the slow range (mm/day) no matter whether the material is normally-consolidated or over-consolidated.
2. The pore pressure measured in the shear zone or on the shear plane is the same as the pore pressure measured nearby (same material and centimeters in distance) for any material, provided the soil structure founded on such a shear zone moves slowly (mm/day). Therefore, under slow movement, the pore pressure obtained from the in situ instrumentation by using piezometers, whose tips can be located in the shear zone's adjacent material, can be viewed as an accurate representation of the shear zone's pore pressure.
3. The measurement of the pore pressure on a shear plane can speed up laboratory tests and reduce testing times because a fast loading rate can be used.
4. The pore-pressure responses differ for materials with different stress histories (over-consolidation ratios).
5. If the shear displacement rate is less than 0.062 mm/minute, the pore pressure on the shear plane of Athabasca clay has no rate effect; i.e., the pore pressure remains identical at any shear displacement rate less than this critical value. If the shear displacement rate is higher than 0.062 mm/minute, the peak pore pressure on the shear plane increases with increase in shear displacement rate. At a specific rate >0.062 mm/minute, the pore pressure increases first to reach its peak,

followed by a gradually decrease with further shear displacement to a value even lower than the pore pressure obtained at a low displacement rate. The pore pressure response for a shear zone/plane in Athabasca clay can be expressed as either Equation 7.7 or Equation 7.8.

6. For Athabasca clay, the deviator stress increases with increase in shear displacement rate if such a rate is less than 0.0244 mm/minute. This behavior may be attributed to the increase in inter-particle friction and the subsequent increase in the mobilized friction angle. At a relatively small shear displacement, the deviator stress decreases with the further increase in the shear displacement rate and is less than those obtained at the small displacement rates. When the shear displacement becomes large, the deviator stress obtained at a high displacement rate may increase to a value even higher than those obtained at a low displacement rate. The change in the deviator stress at a high displacement rate results from the pore-pressure-change; i.e., a higher pore pressure results in a lower deviator stress, and *vice versa*.
7. The effective stress paths on the shear plane and on the base differ for Athabasca clay at the high shear displacement rates. The effective stress paths on the shear plane tend to an identical obliquity and then result in an identical friction angle.
8. The pore pressure on the shear plane dissipates quicker than that on the base, resulting from the larger permeability on the shear plane. This larger permeability is contributed by the sample installation procedures, i.e. a sample is separated along the shear plane into two parts and then put back together. However, in practice the permeability of a shear zone in a normally-consolidated material is slightly smaller than that of the material itself. Besides, the drainage path is an important factor influencing the pore pressure dissipation of a shear zone. A long drainage path contributes to a slow dissipation and *vice versa.*
9. Even shear zones developed in the same material might not have identical shear behaviors (stress-displacement curve, post-peak characteristics, and strength parameters) due to the different internal shear zone structure resulting from the displacements that have occurred. The stress-displacement curve of a polished shiny planar shear surface in highly weathered limestone with a relatively large

prior displacement shows no peak, and at small displacement, reaches the residual strength. Conversely, the stress-displacement curve of a rough shear surface with small prior displacement has a significant peak followed by a decrease towards the residual. A large displacement is needed to reach the residual strength.

10. Paleosol contains many minor shears. The internal structure of the shear zone, i.e., the minor shears combination, controls its shear behavior. When the shearing is along different minor shear combinations, Paleosol has different stress-displacement curves, post-peak characteristics, and shear-strength parameters.

8.2 RECOMMENDATIONS FOR FUTURE RESEARCH

The following recommendations are suggested for future research on the pore-pressure response and shear behavior of shear zones in weak rocks:

1. Field tests, based on more observations of shear-zone characteristics, to explore shear zones pore-pressure responses and shear behavior would be helpful to increase our understanding of natural shear zones' performance in soil structures. Both the pore-pressure response and the shear behavior of shear zones are influenced by the slip-surface features that are size-dependent. Field tests could use large specimens to obtain more accurate results than have been obtained previously.
2. Laboratory tests on shear zones with different OCRs under both triaxial compression and extension shearing should increase our knowledge and understanding of both the pore-pressure response and the shear behavior of shear zones.
3. Research on the displacement rate effects of natural shear zones in weak rocks would increase our understanding of the performance of such shear zones during earthquake or other rapid loading events.
4. Further improvements of testing equipment would help to increase the accuracy of test results. The use of a load cell within the triaxial cell could provide a more accurate stress-displacement curve for the shear plane in an indurated weak rock

than has been provided previously. By improving the pressure-supply system, researchers could use a large cell to study the rate effects under a large displacement rate. The continuous development of the internal pore-pressure transducers will reduce the difficulty of their installation and their relatively high failure rate.

5. The numerical modeling of the pore-pressure response of shear zones is another possibility for future research.

REFERENCES

Agar, J.G. 1984. Behavior of oil sands at elevated temperatures. Ph.D thesis, Department of Civil Engineering, University of Alberta, Edmonton, Canada.

AGRA Earth and Enviromental 1999. Geotechnical data report – Suncor Millenium external pond (8A), Fort McMurray, AB. File No. EG08440.

Alberro, J. and Santoyo, E. 1973. Long term behavior of Mexica City clay. In Proceedings of the 8th International Conference on Soil Mechanics and Foundation Engineering, Moscow, Vol. 1, pp. 1-9.

Archambault, G., Daigneault, R., Rouleau, A., and Tavchandjian, O. 1990. Mechanics of shear zones and faults belts development by anastomosing patterns of fractures at all scales. Mechanics of Jointed and Faulted Rocks, Balkema, Rotterdam, pp. 197-204.

Asaro, R.J., and Rice, J.R. 1977. Strain localization in ductile single crystals. Journal of the Mechanics and Physics of Solids, **25**: 309-338.

Asaro, R.J. 1978. Geomechanical effects in the inhomogeneous deformation of ductile single crystals. Acta Metallurgica, **27**: 445-453.

Asaro, R.J. 1983. Micromechanics of Crystals and Polycrystals. Advances in Applied Mechanics, **23**: 1-115.

Aydan, O., Ito, T., and Ichikawa, Y. 1993. Failure phenomena and strain localization in rock mechanics and rock engineering: A phenomenological description. *In* Assessment and Prevention of Failure Phenomena in Rock Engineering, edited by Pasamehmetoglu, A.G., Kawamoto, T., Whittaker, B.N. and Aydan, O., A.A. Balkama, Rotterdam, pp.119-128.

Babcock, E.A. 1973. Regional jointing in southern Alberta. Can. J. Earth Sci., **10**: 1769-1781.

Beardow, A.P. and Horne, E.J. 1987. Facies delineation on Suncor's mining lease 86. CIM third district five meeting, Fort McMurray, Alberta. pp. 31.

Benes, V., and Davy, P. 1996. Modes of continental lithospheric extention: experimental verification of strain localization processes. Tectonophysics, **254**(1-2): 69-87.

Bishop, A.W. 1966. Soils and soft rocks as engineering materials. Inaugural lecture, Imperial College of Science and technology, **6**: 289-313.

Bishop, A.W., and Morgenstern, N.R. 1960. Stability coefficients for earth slopes. Geotechnique, **10**: 129-150.

Bishop, A.W., Alpan, I., Blight, G.E., and Donald, B. 1960. Factors controlling the strength of partly saturated cohesive soils. Proceedings, American Society of Civil Engineers, Research Conference on Shear Strength of Cohesive Soils, Boulder, Colorado, pp. 503-532.

Bishop, A.W. and Henkel, D.J. 1962. The measurement of soil properties in the triaxial test. Edward Arnold Ltd.

Bjerrum, L. 1967. Progressive failure in slopes of overconsolidated plastic clay and clay shale. ASCE Journal of Soil Mechanics and Foundation division, **93**: 1-49.

Black, D.K. and Lee, K.L. 1973. Saturating laboratory samples by back pressure. ASCE JSMFD SM1, **99**: 75-93.

Blight, G.E. 1963. The effect of nonuniform pore pressures on laboratory measurements of the shear strength of soils. American Society for Testing and Materials, Special Technical Publication 361, pp. 173-191.

Blight, G.E. 1963. Discussion on pore pressures within soil specimens in triaxial compression. American Society for Testing and Materials, Special Technical Publication 361, pp. 199-211.

Burland, J.B., Longworth, T.I., and Moore, J.F.A. 1977. A study of ground movement and progressive failure caused by a deep excavation in Oxford Clay. Geotechnique, **27**(4): 557 – 591.

Burland, J.B. and Symes, M. 1982. Simple axial displacement gauge for use in the triaxial apparatus. Geotechnique, **32**(1): 62-65.

Burland, J.B. 1990. On the compressibility and shear strength of natural clays. *Geotechnique*, **40**(3): 329-378.

Carrigy, M.A. 1966. Lithology of the Athabasca Oil Sands. Research Council of Alberta. Bulletin 18, 48pp.

Casagrande, A. and Wilson, S.D. 1951. Effect of rate of loading on the strength on clays and shales at constant water content. Geotechnique, **2**(3): 251-263.

Casey, J.F. 1985. Strain localization within oceanic lithosphere at mid-ocean ridges; implications for the depths of sea water penetration. Eos, Transactions, American Geophysical Union, **68**(44): 1509.

Chandler, R.J., Wllis, M.R., Hamilto, P.S., and Andreou, I. 1998. Tectonic shear zones in the London Clay Formation. Geotechnique, **48**(2): 257-270.

Cloos, H. 1928. Experimental zur inneren Tektonik. *Centralbl. Mineral.* Geol. u. Pal., **1928 B**: 609-621.

Corkum, A.G., and Martin, C.D. 2002. Discrete element analysis of the effect of a toe berm on a large rockslide. Ground and Water: Theory and Practice, Proceedings of 55th Canadian Geotechnical and 3rd Joint IAH-CNC and CGS Groundwater Specialty Conferences, Niagara Falls, Canada, On CD.

Craig, R.F. 1987. Soil Mechanics, Fourth edition, Chapman & Hall

Crawford, C.B. 1959. The influence of rate of strain on effective stresses in a sensitive clay. American Society for Testing and Materials, Special Technical Publication 254, pp. 36-61.

Crawford, C.B. 1963. Pore pressures within soil specimens in triaxial compression. American Society for Testing and Materials, Special Technical Publication 361, pp. 192-199.

Deere, D.U. 1963. Technical description of rock cores for engineering purposes. Felsmechanik und Ingenieurgeologie, **1**: 16-22.

D'Elia, B., Federico, G., Grisolia, M., Rossi Doria, M., and Tancredi, G. 1977. Mechanical behaviour of a highly tectonic Miocene "mudstone". *In* Proceedings of the International Symposium on the Geotechnics of Structurally Complex Formations, Capri, AGI, Vol. 2, pp. 215-221.

Dewar, D.L. 1996. The MacKay River Terrain Analysis and Landslide Inventory. MSc Thesis, University of Alberta, Edmonton, Canada.

Dewhurst, D.N., Brown, K.M., Clennell, M.B., and Westbrook, G.K. 1996a. A comparison of the fabric and permeability anisotropy of consolidated and sheared silty clay. Engineering Geology; **42**: 253-267.

Dewhurst, D.N., Clennell, M.B., Brown, K.M., and Westbrook, G.K. 1996b. Fabric and hydraulic conductivity of sheared clays. Geotechnical, **46**: 761-768.

Dounias, G.T., Potts, D.M., and Vaughan, P.R. 1988. The shear strength of soils containing undulating shear zone-a numerical study. Can. Geot. J., **25**: 550-558.

Dounias, G.T., and Potts, D.M. 1993. Numerical analysis of drained direct and simple shear tests. Journal of Geotechnical Engineering, ASCE, **119**(12): 1870-1891.

El-Ramly, H. 2001. Risk assessment in earth slopes and landslides. PhD Thesis, University of Alberta, Edmonton, Canada.

Fair, A.E., and Handford, G.T. 1986. Overview of the tailings dyke instrumentation program at Syncrude Canada Ltd. *In* Geotechnical Stability in Surface Mining. Edited by R.K. Singhal. A.A. Blakema, Rotterdam, pp. 245-254.

Faure, R.M., Seve, G., Farhat, H., Virollet, M., and Delmas, P. 1991. A new methodology for evaluation of landslides displacements. Landslide, Bell(ed.), Balkema, Rotterdam, pp. 391- 396.

Fookes, P.G. 1965. Orientation of fissures in stiff overconsolidated clay of the Siwalik system. Geotechnique. **15**: 195-206.

Fookes, P.G., and Wilson, D.D. 1966. The geometry of discontinuities and slope failure in Siwalik clay. Geotechnique, **16**: 305-320.

Fookes, P.G. 1969. Geotechnical mapping of soils and sedimentary rock for engineering purposes with examples of practice from the Mangla dam project. Geotechnique, **19**(1): 52-74.

Fourie, A.B. and Dong, X.B. 1991. Advantages of midheight pore pressure measurements in undrained triaxial testing. Geotechnical testing journal, ASCE, **14**(2): 138-145.

Fredlund, D.G. 1976. Density and compressibility characteristics of air-water mixtures. Canadian Getechnical Journal, **13**: 386-396.

Geological Society Engineering Group, 1970. Working Party Report on " The logging of rock cores for engineering purposes". Q. J. Engng Geol., **3**: 1-24.

Ghisetti, F., and Vezzani, L. 1996. Strain localization in the central Apennines thrust belt (Italy); implication for deformation mechanisms and kinematic reconstructions. International Geological Congress, Abstracts, Vol. 2, pp. 295.

Gibbs, H.J., Hilf, J.W., Holtz, W.G., and Walker, F.C. 1960. Shear strength of cohesive soils. Proceedings, American Society of Civil Engineers. Research Conference on Shear Strength of Cohesive Soils, Boulder, Colorado, pp. 33-162.

Gilbert, L.E., Scholz, C.H., and Beavan, J. 1994. Strain localization along the San Andreas Fault; consequences for loading mechanisms. Journal of geophysical research, **99**(B12): 23975-23984.

Guerriero, G., Picarelli, L., and Urciuoli, G. 1993. Some considerations on the ultimate condition of hard clays in triaxial tests. [illegible]c. Int. Symp. Geotechnical Engineering of Hard Soils – Soft Rocks, Athens, Vol. 1, pp. 1909-1911.

Hardy, R.M., and Hemstock, R.A. 1963. Shearing strength characteristics of Athabasca oil sands. K.A. Clark Volume. Research Council of Alberta, Information Series 45, pp. 109-122.

Hawkins, A.B. 1996. Observation and analysis of the ground conditions in the Jurassic landslip terrain of southern Britain. Landslides. Balkman, Rotterdam.

Head, K.H. 1986. Manual of soil laboratory testing. Vol. 3, Pentech press, London.

Henkel, D.J. 1956. Discussion of Watson. Proc. Inst. Civil Engnrs 5, Part II, pp. 320-323.

Henkel, D.J., and Skempton, A.W. 1955. A landslide at Jackfield, Shropshire, in heavily overconsolidated clay. Geotechnique **5**: 131-137.

Hicher, P.Y., Wahyudi, H., and Tessier, D. 1994. Microstructural analysis of strain localization in clay. Computers and Geotechnics, **16**: 205-222.

Hodgson, R.A. 1961. Regional study of jointing in the Comb Ridge-Navajo Mountain area, Arizona and Utah. Bull. Am. Ass. Petrol. Geol., **45**: 1-38.

Hudson, J. and Harrison, J. 1997. Engineering Rock Mechanics - An Introduction to the Principles. Pergamon.

International Society for Rock Mechanics Commission on Standardization of Laboratory and Field Tests, 1978. Suggested methods for the quantitative description of discontinuities in rock masses. Int.J. Rock Mech. Min. Sci. & Geomech. Abstr. **15**: 319-368.

Iverson, R.M. 1991. Sensitivity of stability analyses to groundwater data. Landslide, Bell(ed.), Balkema, Rotterdam, pp. 451-457.

Iverson, R.M. and LaHusen, R.G. 1989. Dynamic pore-pressure fluctuations in rapidly shearing granular materials. Science, **246**: 796-799.

Iverson, R.M., Reid, M.E., and LaHusen, R.G. 1997. Debris-flow mobilization from landslides. Annual Review of Earth Planetary Science, **25**: 85-138.

Jardine, R.J., Symes, M., and Burland, J.B. 1984. The measurement of soil stiffness in the triaxial tests on saturated soils. Geotechnique, **34**(3): 323

Jaroslow, G.E., Hirth, G., and Dick, H.J.B. 1996. Abyssal peridotite mylonites; implications for grain-size sensitive flow and strain localization in the oceanic lithosphere. Tectonophysics, **256**(1-4): 17-34.

Kawabe, H. 1991. On the influence of pore pressure on land deformation of a landslide. Landslide, Bell(ed.), Balkema, Rotterdam, pp. 459-464.

Kenney, T.C. 1967. The influence of mineral composition on the residual strength of natural soils. Proc. Geotech. Conf. on Shear Strength Prop. Natural Soils and Rocks, Oslo, Vol.1, pp. 123-129.

Kimura, T. and Saitoh, K. 1983. The influence of strain rate on pore pressures in consolidated undrained triaxial tests on cohesive soils. Soils and Foundations, **23**(1): 80-91.

Kosar, K.M. 1992. Geotechnical properties of oil sands and related strata. PhD Thesis, University of Alberta, Edmonton, Canada.

La Gatta, D.P. 1970. Residual strength of clays and clay shales by rotation shear tests. Harvard Soil Mechanics Series No. 86, Harvard University, Cambridge, Massachusetts.

La Rochelle, P. 1967. Membrane, drain and area correction in triaxial test on soil samples failure along a single shear plane. Proc. 3rd Pan-Am. Conf. on Soil Mechanics and Foundation Engineering, Caracas, Venezuela, Vol. 1, pp. 273-292.

Lefebvre, G. 1981. Strength and slope stability in Canadian soft clay deposits. Canadaian Geotechnical Journal. **18**: 420-442.

Lefebvre, G. and LeBoeuf, D. 1987. Rate effects and cyclic loading of sensitive clays. Journal of Geotechnical Engineering, ASCE, **113**(5): 476-489.

Leroueil, S. 2001. Natural slopes and cuts: movement and failure mechanisms. Geotechnique, **51**(3): 197-243.

Lowe, J. and Johnson, T.C. 1960. Use of back pressure to increase degree of saturation of triaxial test specimens. ASCE Research Conference on Shear Strength of Cohesive Soils, Boulder, Colorado, USA, pp. 819-836.

Lupini, J.F., Skinner, A.E., and Vaughan, P.R. 1981. The drained residual strength of cohesive soils. Geotechnique **31**(2): 181-213.

Majorana, C.E., Salomoni, V., and Schrefler, B.A. 1996. Some observations about strain localization and shear band formation in concrete samples. Journal of Materials Proceeing Technology, **78**(1-3): 128-137

McRobert, E. 2001. Oil sand geotechnique. The Norbert R. Morgenstern Symposium celebrating 40 years of teaching and research excellence, On CD.

Morgenstern, N.R., and Tchalenko, J.S. 1967a. Microstructural observations on shear zones from slips in natural clays. Proc. Geotechnical Conf Oslo, Vol. 1, pp.147-152.

Morgenstern, N.R., and Tchalenko, J.S. 1967b. Microscopic structures in kaolin subjected to direct shear. Geotechnique, **17**: 309-328.

Morgenstern, N.R. 1987. Geological Control of Stability on Large Projects. Proc. 8th Pan American Conference on Soil Mechanics and Foundation Engineering. Cartagena, Colombia, Vol. 1, pp. 293-316.

Morgenstern, N.R., and Scott, J.D. 1997. Oil Sand Geotechnique. Geotechnical News, Special Commemorative Edition, **15**(109): 102-109.

Morgenstern, N.R. 1999. Geotechnics and Mine Waste Management (Keynote Lecture). International Symposium on Seismic and Environmental Aspects of Dam Design. Santiago, Vol. 2, pp. 5-27.

Nakase, A. and Kamei, T. 1986. Influence of strain rate on undrained shear characteristics of K_0-consolidated cohesive soils. Soils and Foundations, **26**(1): 85-95.

Nickelsen R. P., and Hough, V. N. D. 1967. Jointing in the Appalachian Plateau of Pennsylvania. Bull. Geol. Soc. Am., **78**: 609-630.

Nicolell, D.P., Lankford, J. Jepsen, K.J., and Davy, D.J. 1997. Correlation of physical damage development with microstructure and strain localization in bone. American Society of Mechanical Engineers, -Bioengineering Division (Publication), **35:** 311-312.

Oldakowski, K. 1994. Stress induced permeability changes in Athabasca oil sands. M.Sc thesis, Department of Civil Engineering, University of Alberta, Edmonton, Canada.

Picarelli, L., Leroueil, S., Delisle, M.C., Urciuoli, G., and Guerriero, G. 1998. Occurrence and features of shear zones in clay. *In* Localization and Bifurcation Theory for Soils and Rocks, edited by Adachi, Oka and Yashima, Balkema, Rotterdam, pp. 259-268.

Priest, S.D. 1993. Discontinuity analysis for rock engineering. Chapman & Hall, New York.

Rangers, N. 1967. Terresrtial photogrammetry: a valuable tool for engineering geological purposes. Rock Mech. Engng Geol., **5**: 150-154.

Richardson, A.M. and Whitman, R.V. 1963. Effect of strain rate upon undrained shear resistance of a saturated remounded fat clay. Geotechnique, **13**: 310-324.

Riedel, W. 1929. Zur Mechanik geologischer Brucherscheinungen. Centralbl. F. Mineral. Geol. u. Pal., **1929 B**: 354-368.

Rojas, E. 1988. Stress strain time constitutive model. *In* Proceedings of the International Conference of Rheology and Soil Mechanics, U.K., pp. 108-122.

Roscoe, K.H. 1970. Influence of strains in soil mechanics. Geotechnique, **20**(2): 129-170.

Ross-Brown, D.M., Wickens, E.H. and Markland, J.T. 1973. Terrestial photogrammetry in open pits: 2--- an aid to geological mapping. Trans. Inst. Min. Metall., **82**: A115-A130.

Savage, J.F. 1965. Terrestial photogrammetry for geological purposes. International Training Center for Aerial Survey, Publication series **B**(33): 41-53.

Scruggs, V.J., and Tullis, T.E. 1998. Correlation between velocity dependence of friction and strain localization in large displacement experiments on feldspar, muscovite and biotite gouge. Tectonophysics. **295**(1-2): 15-40.

Sheahan, T.C., Ladd, C.C., and Germaine, J.T. 1996. Rate-dependent undrained shear behavior of saturated clay. Journal of Geotechnical Engineering, ASCE, **122**(2): 99-108.

Shuri, F.S., Driscoll, D.D., and Garner, S.J. 1985. Controlled displacement-rate in situ shear tests with pore pressure measurements. Can. Geotech. J., **22**: 136-142.

Sinclair, S.R., and Brooker, E.W. 1967. The shear strength of Edmonton shale. Proc. Geotechnical Conf., Oslo, Vol. 1, pp. 295-299.

Skempton, A.W. 1954. The pore pressure coefficients A and B. Geotechnique, **4**(4): 143-147

Skempton, A.W. 1964. Long-term stability of clay slopes. Geotechnique **14**(2): 75-101.

Skempton, A.W. 1966. Some observations on tectonic shear zones. Proc. 1st Cogr. Int. Soc. Rock Mech., Lisbon, Vol. 1, pp. 329-335.

Skempton, A.W., and Petley, D.J. 1967. The strength along structural discontinuities of stiff clays. Proceedings of the Geotechnical Conference, Oslo, Vol. 2, 29-46.

Skempton, A.W., Schuster, R.L., and Petley, D.J. 1969. Joints and Fissures in the London clay at Wraysbury and Edgware. Geotechnique, **19**(2): 205-217.

Skempton, A.W. 1985. Residual strength of clays in landslides, folded strata and the laboratory. Geotechnique, **35**(1): 3-18.

Small, C. A. 1989. Failure in mine highwall in soft sedimentary rock. MS Thesis, University of Alberta, Edmonton, Canada.

Snow, D.T. 1968. Rock fracture spacing, opening, and porosities. Journal of the Soil Mechanics and Foundations Division, ASCE, **94**(SM1): 73-91.

South African Core Logging Committee, 1976. A guide to core logging for rock engineering. Proc. Of Symp. on Exploration for Rock Engineering, Johannesburg, Vol. 1, pp. 71-86.

Su, X.Q., Martin, C.D., and Tannant, D.D. 2002. Shear zone mapping in weak mudstones near Fort McMurray. 55th Canadian Geotechnical Conference, on CD.

Su, X.Q., Martin, C.D., and Tannant, D.D. 2003. Shear strength mobilization of Ottawa sand with HDPE interference. 56th Canadian Geotechnical Conference, on CD.

Tchalenko, J.S. 1968. The evolution of kink-bands and development of compression textures in sheared clays. Tectonophysics, **6**(2): 159-174.

Tchalenko, J.S. 1970. Similarities between shear zones of different magnitudes. Geological Society of America Bulletin, **81**: 1625-1640.

Thomson, S., and Tweedie, R.W. 1978. The Edgerton Landslide. Can. Geotech. J., **15**: 510-521.

Tika, T. M., Vaughan, P. R., and Lemos, L. J. L. 1996. Fast shearing of pre-existing shear zones in soils. Géotechnique, **46**(2): 197-233.

Tika, T.M. and Hutchinson, J.N. 1999. Ring shear tests on soil from the Vaiont landslide slip surface. Geotechnique, **49**(1): 59-74.

Tommasi, A, Vauchez, A., and Daudre, B. 1995. Strain localization in a heterogeneous continental lithosphere; insights from a natural shear zone system and numerical modeling. International Union of Geodesy and Geophysics, general assembly. **21**(Week B): 333.

Tsui, P.C., Cruden, D.M., and Thomson, S. 1988. Mesofabric, microfabric and submicrofabric of ice-thrust bedrock, Highvalve mine, Wabamun lake area, Alberta. Can. J. Earth Sci., **25**: 1420-1431.

Tweedie, R.W. 1976. An Investigation of the Edgerton Landslide, Wainwright, Alberta. MS Thesis, University of Alberta, Edmonton, Canada.

Vallejo, L.E. 1982. Development of a shear zone structure in stiff clays. Proceedings of the Fourth International Conference on Numerical Methods in Geomechanics, (editor Eisenstein), Vol. 1, pp. 255-262.

Walters, J.V., and Thomas, J.N. 1982. Shear zone development in granular materials. Proceedings of the Fourth International Conference on Numerical Methods in Geomechanics, (editor Eisenstein), Vol. 1, pp. 263-274.

Wang, G.H., Sassa, K., and Fukuoka, H. 2003. Role of grain size and fine-particle content on the pore-pressure generation and movement of rainfall-induced landslides: an experimental study. International Workshop on Occurrence and Mechanisms of Flows in Natural Slopes and Earthfills. *At* www.unina2.it/fsm2002.

Wedage, A.M.P., Morgenstern, N.R., and Chan, D.H. 1998a. Simulation of time-dependent movements in Syncrude tailings dyke foundation. Canadian Geotechnical Journal. **35**(2): 284-298.

Wedage, A.M.P., Morgenstern, N.R., and Chan, D.H. 1998b. A strain rate dependent constitutive model for clays at residual strength. Canadian Geotechnical Journal. **35**(2): 364-373.

Whitman, R.V. 1960. Some considerations and data regarding the shear strength of clays. Proceedings, American Society of Civil Engineers. Research Conference on Shear Strength of Cohesive Soils, Boulder, Colorado, pp. 581-614.

Wickens, E.H., and Barton, N.R. 1971. The application of photogrammetry to the stability of excavated rock slopes. Photogram. Rec., **7**(37): 46-54.

Wissa, A.E.Z. 1969. Pore pressure measurement in saturated stiff soils. ASCE JSMFD **SM4**: 1063-1073.

Zhu, J.G., Yin, J.H., and Luk, S.T. 1999. Time dependent stress-strain behavior of soft Hong Kong marine deposits. Geotechnical Testing Journal, **22**(2): 118-126.

Zhu, J.G. and Yin, J.H. 2000. Strain-rate-dependent stress-strain behavior of overconsolidated Hong Kong marine clay. Canadian Geotechnical Journal, **37**: 1272-1282.

APPENDIX A INDEX PROPERTY TEST RESULTS

Table A1 Water content of the shear zone II (pit 18) and the shear zone III (pit 26)

No. of samples	Water (g)	Dry soil (g)	Water content (%)
T18-1-1	6.9	93.36	7.4
T18-1-2	9.92	98.79	10.0
T18-1-3	14.68	110.46	13.3
T18-1-4	14.02	111.15	12.6
T18-1-5	15.37	131.31	11.7
T18-1-6	7.85	113.78	6.9
T18-1-7	6.7	93.8	7.1
T18-1-8	5.57	82.34	6.8
T18-1-9	7.93	104.36	7.6
T18-2-1	9.19	125.85	7.3
T18-2-2	7.71	112.62	6.8
T18-2-3	10.76	137.79	7.8
T18-2-4	12.43	105.8	11.7
T18-2-5	14.24	105.88	13.4
T18-2-6	8.93	70.49	12.7
T18-2-7	14.71	106.72	13.8
T18-2-8	19.89	252.57	7.9
T18-2-9	7.34	97.3	7.5
T18-2-10	7.3	100.7	7.2
T26-1-1	16.07	126.75	12.7
T26-1-2	24.86	161.89	15.4
T26-1-3	19.41	133.93	14.5
T26-1-4	17.55	118.08	14.9
T26-1-5	14.08	108.32	13.0
T26-1-6	12.95	105.25	12.3

Table A2 Hydrometer test on MSF in the shear zone I

Inside the shear zone		Outside the shear zone	
Diameter (mm)	Percentage finer (%)	Diameter (mm)	Percentage finer (%)
0.0478	94.6	0.0534	75.2
0.034	93.6	0.0388	69.2
0.0242	92.6	0.0284	61.2
0.0171	92.6	0.0208	52.2
0.0122	91.5	0.0153	42.2
0.0087	91.4	0.0122	33.2
0.0064	91.3	0.0083	30.1
0.0046	89.1	0.0059	29
0.0033	87.8	0.0043	26.8
0.0024	87.6	0.0031	24.6
0.0019	84.4	0.0021	21.4
0.001	79.2	0.0013	19.2
0.0009	76.3	0.0011	18.3
0.0007	76.4	0.0009	17.4
0.0007	75.4	0.0008	17.4
0.0006	74.4	0.0008	17.4
0.0006	73.4	0.0007	16.4
0.0006	73.4	0.0008	16.4

Table A3 Hydrometer test on the material in the shear zone II

Inside the shear zone		Outside the shear zone	
Diameter (mm)	Percentage finer (%)	Diameter (mm)	Percentage finer (%)
0.0496	92	0.0548	71.1
0.0355	90	0.0404	61.1
0.0256	86	0.0295	53.1
0.0187	80	0.0212	49.1
0.0138	71	0.0153	43.1
0.0101	62	0.0111	37
0.0076	56.9	0.0083	33
0.0055	50.8	0.006	29.9
0.004	46.7	0.0043	28.7
0.0029	44.5	0.0031	26.5
0.0022	42.4	0.0024	24.4
0.0013	36.2	0.0013	21.2
0.001	34.3	0.0011	19.3
0.0009	33.4	0.0009	19.4
0.0008	32.4	0.0008	18.4
0.0007	32.4	0.0008	18.4
0.0007	31.4	0.0007	18.4
0.0007	31.4	0.0008	18.4

Table A4 Atterberg Limit test on MSF in the shear zone I

	Inside the shear zone						Outside the shear zone					
	Liquid Limit			Plastic Limit			Liquid Limit			Plastic Limit		
Trial No.	1	2	3	1	2	3	1	2	3	1	2	3
No. of blows	18	31	36				11	23	45			
Water content (%)	106.5	97.0	95.2	47.5	47.5	47.7	38.0	35.1	32.4	24.9	25.2	24.9
Atterberg Limit	**$W_l = 101$, $W_p = 47.6$, $I_p = 53.5$**						**$W_l = 34.8$, $W_p = 25.0$, $I_p = 9.8$**					

Table A5 Atterberg Limit test on material inside the shear zone II

Sample No.	1						2					
	Liquid Limit			Plastic Limit			Liquid Limit			Plastic Limit		
Trial No.	1	2	3	1	2	3	1	2	3	1	2	3
No. of blows	16	24	36				14	22	24			
Water content (%)	43.9	41.3	38.4	19.9	19.9	20.0	45.0	39.8	39.6	19.2	19.0	19.4
Atterberg Limit	**$W_l = 41.0$, $W_p = 19.9$, $I_p = 21.1$**						**$W_l = 38.7$, $W_p = 19.2$, $I_p = 19.5$**					

Table A6 Atterberg Limit test on material outside the shear zone II

Sample No.	1						2					
	Liquid Limit			Plastic Limit			Liquid Limit			Plastic Limit		
Trial No.	1	2	3	1	2	3	1	2	3	1	2	3
No. of blows	16	19	38				15	24	50			
Water content (%)	26.1	25.7	24.0	14.8	14.8	14.8	26.1	24.5	22.3	14.5	14.5	14.5
Atterberg Limit	**$W_l = 25.0$, $W_p = 14.8$, $I_p = 10.2$**						**$W_l = 24.3$, $W_p = 14.5$, $I_p = 9.8$**					

Table A7 Hydrometer test on Athabasca clay, Paleosol, and weathered limestone

Athabasca clay		Paleosol		Weathered limestone	
Diameter (mm)	Percentage finer (%)	Diameter (mm)	Percentage finer (%)	Diameter (mm)	Percentage finer (%)
0.051	89.2	0.0485	105.8	0.049	100.3
0.0363	88.2	0.0346	104.6	0.0349	98.7
0.0258	87.2	0.0248	102.2	0.0251	95.8
0.0183	86.2	0.0179	99.2	0.018	93.7
0.013	85.2	0.0129	95.7	0.0133	85.7
0.0093	78.2	0.01	85	0.01	78.9
0.0066	72.2	0.0074	75.7	0.0074	70.5
0.0052	66.8	0.0056	60.2	0.0054	61.9
0.0037	57.6	0.0041	50.7	0.0041	55.9
0.0031	53.2	0.003	45.7	0.0029	48.7
0.0024	47.6	0.0021	39.3	0.0021	44.4
0.0012	37.3	0.0017	36.7	0.0017	41.3
0.0011	35.3	0.0013	35.3	0.0013	36.8
		0.0009	30.4	0.001	33.3
		0.0007	26.2	0.0009	32
		0.0006	24.7	0.0007	29.9
		0.0006	23	0.0007	29.2
		0.0005	22.5		
		0.0006	22		

Table A8 Atterberg Limit test on Athabasca clay

	Liquid Limit			Plastic limit		
Trial No.	1	2	3	1	2	3
No. of Blows	42	15	12			
Moisture content (%)	38.0	44.0	46.8	22.4	23.2	23.1
Atterberg Limit	$W_l = 41$, $W_p = 22.9$, $I_p = 18.1$					

Table A9 Atterberg Limit test on Paleosol

	Liquid Limit			Plastic limit		
Trial No.	1	2	3	1	2	3
No. of Blows	45	30	10			
Moisture content (%)	31.01	31.81	34.14	20.52	21.21	21.06
Atterberg Limit	$W_l = 32.2$, $W_p = 20.9$, $I_p = 11.3$					

Table A10 Atterberg Limit test on highly weathered limestone

	Liquid Limit			Plastic limit		
Trial No.	1	2	3	1	2	3
No. of Blows	42	26	12			
Moisture content (%)	37.83	40.67	44.95	21.12	21.27	21.89
Atterberg Limit	$W_l = 40.8$, $W_p = 21.4$, $I_p = 19.4$					

APPENDIX B FLAC PROGRAMS FOR PARAMETER SENSITIVE ANALYSIS

B1 FLAC Program for Calculating the Slope Displacement at the Different Friction Angles

```
grid 170,20
model mohr
gen 0,236 0,270 33,267.5 33,236 i=1,12 j=1,11
gen 0,270 0,302 33,302 33,267.5 i=1,12 j=11,21
gen 33,236 33,267.5 116,261.5 116,236 i=12,54 j=1,11
gen 33,267.5 33,302 116,278 116,261.5 i=12,54 j=11,21
gen 116,236 116,261.5 150,259 150,236 i=54,71 j=1,11
gen 116,261.5 116,278 150,278 150,259 i=54,71 j=11,21
gen 150,236 150,259 426,239 426,236 i=71,171 j=1,11 rat .98 1
gen 150,259 150,278 426,243 426,239 i=71,171 j=11,21 rat .98 1
plot hold grid
; material properties (high strength)
prop density=1850.0 bulk=0.167E9 shear=0.56E8 cohesion=1e10 &
friction=30 dilation=0.0 tension=1e10 j=11,21
prop density=2200.0 bulk=0.83E8 shear=0.18E8 cohesion=1e10 &
friction=15 dilation=0.0 tension=1e10 j=1,11
; define water table
table 1 0 277 33 277 116 270 150 267 426 242
water table 1 den 1000.0
def wet_den
  loop i (1,izones)
    loop j (11,jzones)
     if model (i,j)>1 then
       xa=(x(i,j)+x(i+1,j)+x(i+1,j+1)+x(i,j+1))
```

```
        xc=0.25*xa
        ya=(y(i,j)+y(i+1,j)+y(i+1,j+1)+y(i,j+1))
        yc=0.25*ya
        if yc < table(1,xc)then
          density (i,j) = 1950
        endif
      endif
    endloop
  endloop
end
wet_den
; boundary and initial conditions
fix x i=1
fix x i=171
fix x y j=1
set gravity=9.81
; histories
hist unbal
hist ydisp i 36 j 11
hist xdisp i 36 j 11
; equilibration
solve
print xdis i=36 j=1,11
save edsl_el.sav
; material properties (actual strength)
prop coh=0.0 tension=0.0 j=9,21
prop coh=0.2e5 tension=0.2e5 j=1,9
solve
save edsl_0.sav
hist reset
hist unbal
hist xdisp i 36 j 11
ini xdis 0 ydis 0
prop  fric 23 j 11 21
prop  fric 14 j 9 11
solve
plot hist 1
plot hist 2
print xdis i=36 j=11
save edsl_1.sav
hist unbal
hist xdisp i 36 j 11
prop  fric 23 j 11 21
prop  fric 13 j 9 11
solve
plot hist 1
plot hist 2
print xdis i=36 j=11
save edsl_2.sav
hist unbal
hist xdisp i 36 j 11
prop  fric 23 j 11 21
prop  fric 12 j 9 11
solve
plot hist 1
plot hist 2
print xdis i=36 j=11
save edsl_3.sav
hist unbal
hist xdisp i 36 j 11
prop  fric 23 j 11 21
prop  fric 11 j 9 11
```

```
solve
plot hist 1
plot hist 2
print xdis i=36 j=11
save edsl_4.sav
hist unbal
hist xdisp i 36 j 11
prop  fric 23 j 11 21
prop  fric 10 j 9 11
solve
plot hist 1
plot hist 2
print xdis i=36 j=11
save edsl_5.sav
hist unbal
hist xdisp i 36 j 11
prop  fric 23 j 11 21
prop  fric 9 j 9 11
set force 4.0e3
solve
plot hist 1
plot hist 2
print xdis i=36 j=11
save edsl_6.sav
hist unbal
hist xdisp i 36 j 11
prop  fric 23 j 11 21
prop  fric 8 j 9 11
set force 4.0e3
solve
plot hist 1
plot hist 2
print xdis i=36 j=11
save edsl_7.sav
hist unbal
hist xdisp i 36 j 11
prop  fric 23 j 11 21
prop  fric 7 j 9 11
set force 4.0e3
solve
plot hold hist 1
plot hold hist 2
print xdis i=36 j=11
save edsl_8.sav
ret
```

B2 FLAC Program for Calculating the Slope Displacement at *in Situ* Water Level

```
grid 170,20
model mohr
gen 0,236 0,270 33,267.5 33,236 i=1,12 j=1,11
gen 0,270 0,302 33,302 33,267.5 i=1,12 j=11,21
gen 33,236 33,267.5 116,261.5 116,236 i=12,54 j=1,11
gen 33,267.5 33,302 116,278 116,261.5 i=12,54 j=11,21
gen 116,236 116,261.5 150,259 150,236 i=54,71 j=1,11
gen 116,261.5 116,278 150,278 150,259 i=54,71 j=11,21
gen 150,236 150,259 426,239 426,236 i=71,171 j=1,11 rat .98 1
gen 150,259 150,278 426,243 426,239 i=71,171 j=11,21 rat .98 1
plot hold grid
; material properties (high strength)
prop density=1850.0 bulk=0.167E9 shear=0.56E8 cohesion=1e10 &
friction=30 dilation=0.0 tension=1e10 j=11,21
prop density=2200.0 bulk=0.83E8 shear=0.18E8 cohesion=1e10 &
friction=15 dilation=0.0 tension=1e10 j=1,11
; define water table
table 1 0 277 33 277 116 270 150 267 426 242
water table 1 den 1000.0
def wet_den
  loop i (1,izones)
    loop j (11,jzones)
      if model (i,j)>1 then
        xa=(x(i,j)+x(i+1,j)+x(i+1,j+1)+x(i,j+1))
        xc=0.25*xa
        ya=(y(i,j)+y(i+1,j)+y(i+1,j+1)+y(i,j+1))
        yc=0.25*ya
        if yc < table(1,xc)then
```

```
            density (i,j) = 1950
          endif
        endif
      endloop
   endloop
end
wet_den
; boundary and initial conditions
fix x i=1
fix x i=171
fix x y j=1
set gravity=9.81
; histories
hist unbal
hist ydisp i 36 j 11
hist xdisp i 36 j 11
; equilibration
solve
print xdis i=36 j=1,11
plot hold hist 1
; material properties (actual strength)
prop coh=0.0 tension=0.0 j=9,21
prop coh=0.2e5 tension=0.2e5 j=1,9
solve
hist reset
hist unbal
hist xdisp i 36 j 11
ini xdis 0 ydis 0
prop  fric 24 j 11 21
prop  fric 8 j 9 11
set force 2.5e3
```

```
solve
print xdis i=36 j=1,11
plot hold hist 1
plot hold hist 2
ret
```

APPENDIX C INSTRUMENT CALIBRATION

Table C1 Summary of the instruments calibration

Name of the instrument	Calibration Coefficient	Cell used
2 klb load cell	735.71 N/mv	Small cell
15 psi pressure transducer (cell and back pressure)	28.39 kPa/mv	Small cell
15 psi pressure transducer (base pore pressure)	22.27 kPa/mv	Small cell
Volume change LVDT	16.45 cc/v	Small cell
External LVDT	20.078 mm/v	Small cell
Electronic level A	17°/v	Small cell
Electronic level B	18°/v	Small cell
1 MPa internal pore pressure transducer	10.391 kPa/mv	Small cell
1 MPa internal pore pressure transducer	1.783 kPa/mv	Small cell
1 MPa internal pore pressure transducer	9.9376 kPa/mv	Small cell
2 MPa internal pore pressure transducer	3.3038 kPa/mv	Small cell
50 klb load cell	9.0544 kN/mv	Large cell
500 psi pressure transducer (cell pressure)	280.247 kPa/mv	Large cell
500 psi pressure transducer (back pressure)	278.579 kPa/mv	Large cell
500 psi pressure transducer (base pore pressure)	141.596 kPa/mv	Large cell
2 MPa internal pore pressure transducer	1169.1 kPa/mv	Large cell
3 MPa internal pore pressure transducer	1159.8 kPa/mv	Large cell
3 MPa internal pore pressure transducer	1142.4 kPa/mv	Large cell
3 MPa internal pore pressure transducer	5214.8 kPa/mv	Large cell
Internal submersible LVDT (41337)	1.3402 mm/v	Large cell
Internal submersible LVDT (41338)	1.3392 mm/v	Large cell
External LVDT	3.4829 mm/v	Large cell
Ram friction	0.045kN/kN	Large cell

APPENDIX D TRIAXIAL TEST RESULTS

Table D1 Specimen information

	Specimen No.	C1	C2	C3	C4	C5	C6
Athabasca Clay	Diameter (mm)	65.88	66.93	67.45	65.94	66.47	65.95
	Height (mm)	141.89	142.22	141.70	139.78	142.26	141.73
	Moisture content (%)	22.8	23.1	22.0	22.4	23.2	22.2
	Bulk density (kN/m^3)	20.0	19.7	20.2	20.2	19.8	20.3
Highvale mudstone	Specimen No.	M1	M2	M3			
	Diameter (mm)	65.6	65.7	65.8			
	Height (mm)	135.4	135.8	135.6			
	Bulk density (kN/m^3)	22.7	22.5	22.4			
Weathered limestone	Specimen No.	L1	L2	L3			
	Diameter (mm)	100.03	100.01	99.85			
	Height (mm)	199.86	199.65	195			
	Moisture content (%)	14.8	13.5	13.3			
	Bulk density (kN/m^3)	21.7	21.9	21.5			
Paleosol	Specimen No.	P1	P2	P3			
	Diameter (mm)	100.03	99.96	100.05			
	Height (mm)	199.93	202.3	199.96			
	Moisture content (%)	15.9	14.6	14			
	Bulk density (kN/m^3)	21.3	21.5	21.4			

D1 TESTS ON ATHABASCA CLAY

Sample 1 0.001 mm/minute of the axial displacement rate

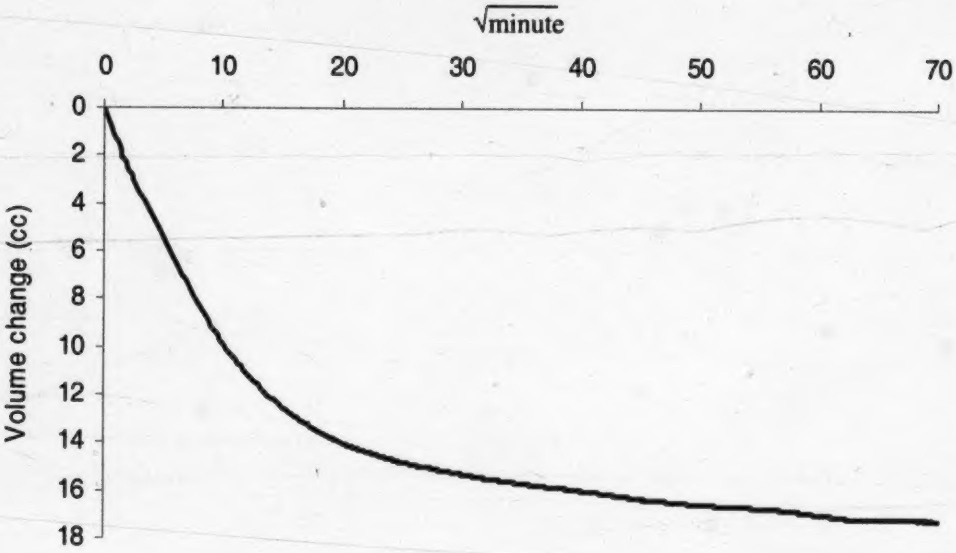

Figure D1 Consolidation curve: volume change versus square root time for specimen C1

7

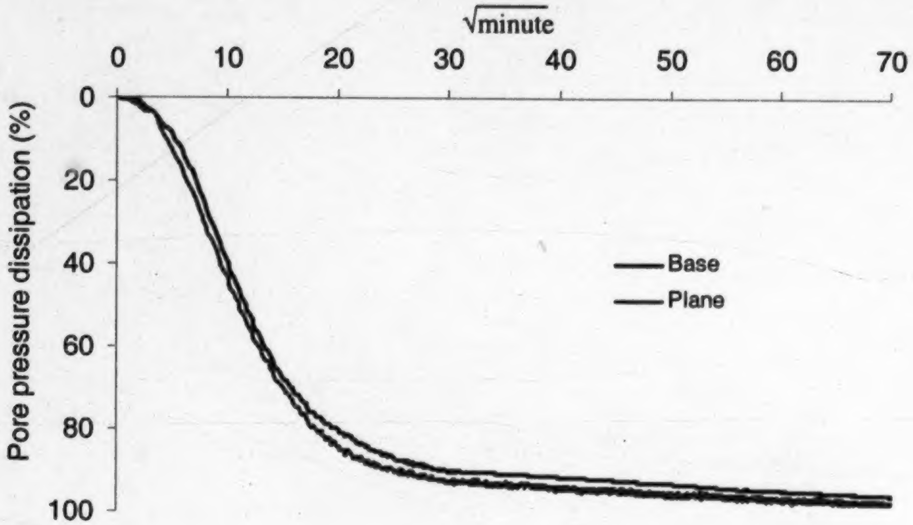

Figure D2 Pore-pressure-dissipation curve for specimen C1

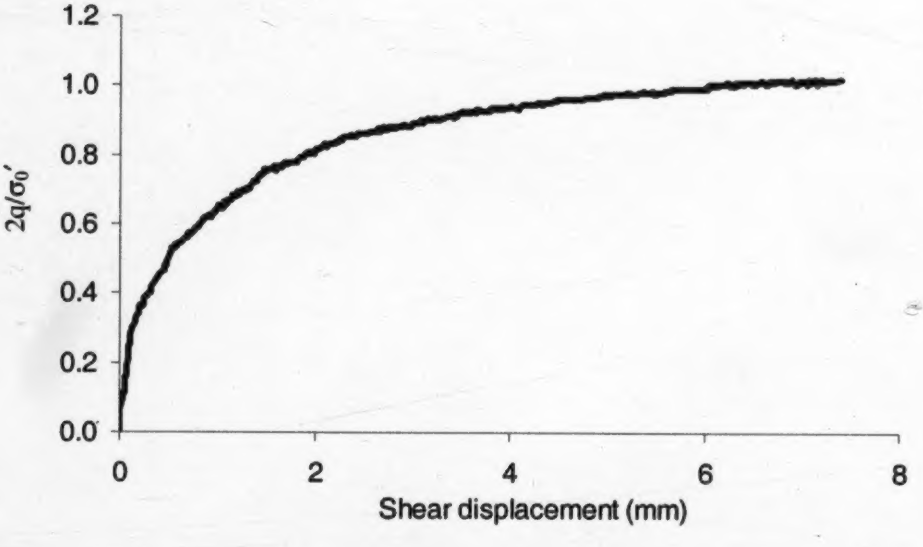

Figure D3 Relationship between the normalized deviator stress and the shear displacement for specimen C1

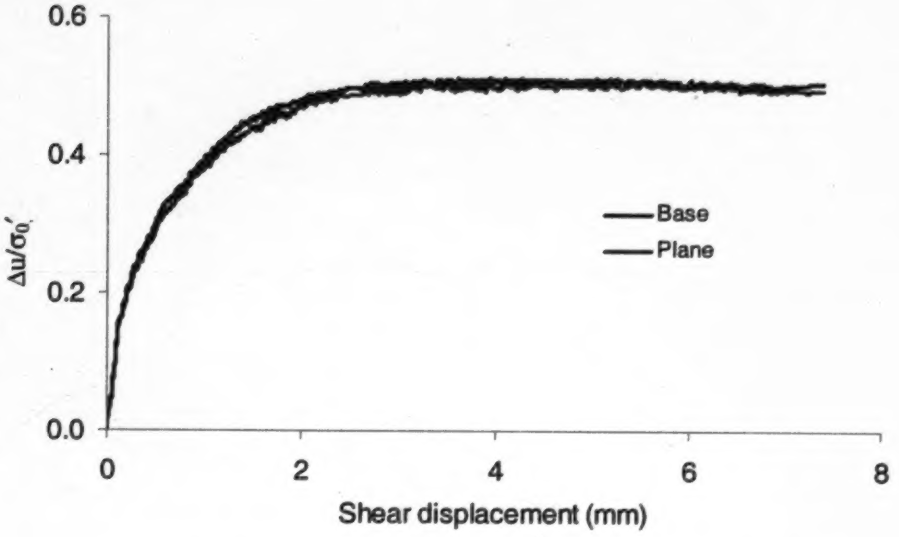

Figure D4 Relationship between the normalized pore-water pressure and the shear displacement for specimen C1

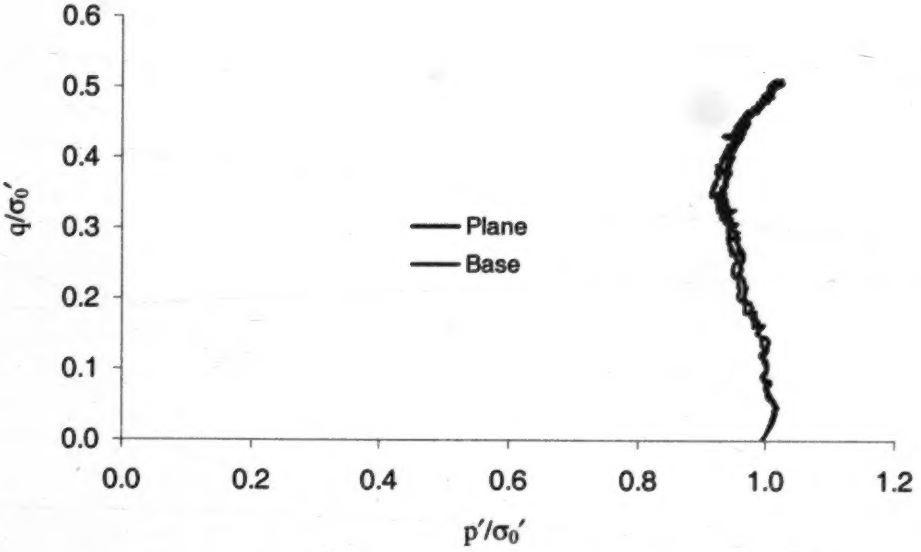

Figure D5 Normalized effective stress paths for specimen C1

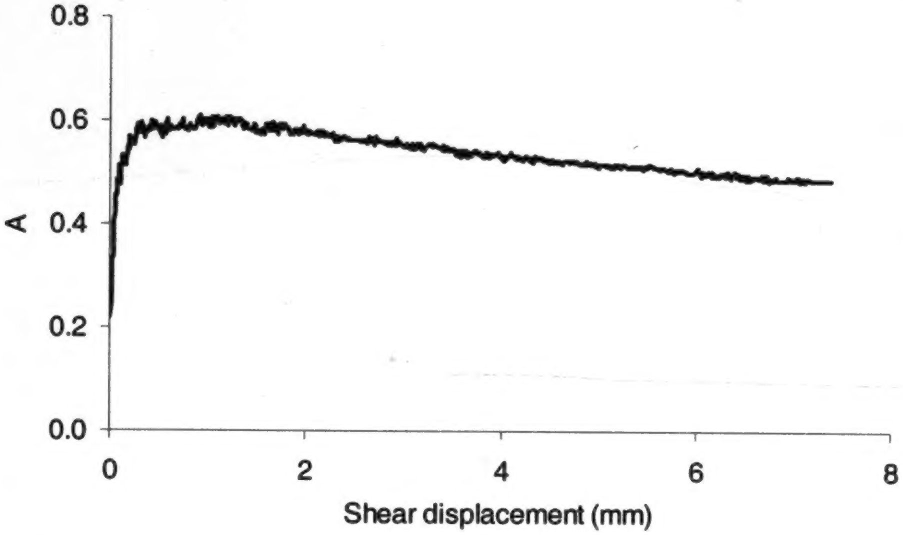

Figure D6 Relationship between the pore-pressure parameter A and the shear displacement for specimen C1

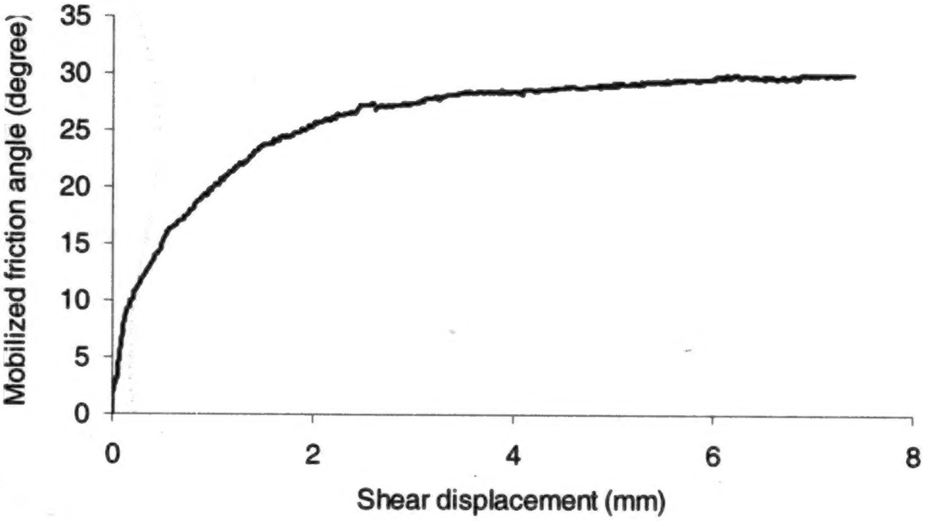

Figure D7 Relationship between the mobilized friction angle and the shear displacement for specimen C1

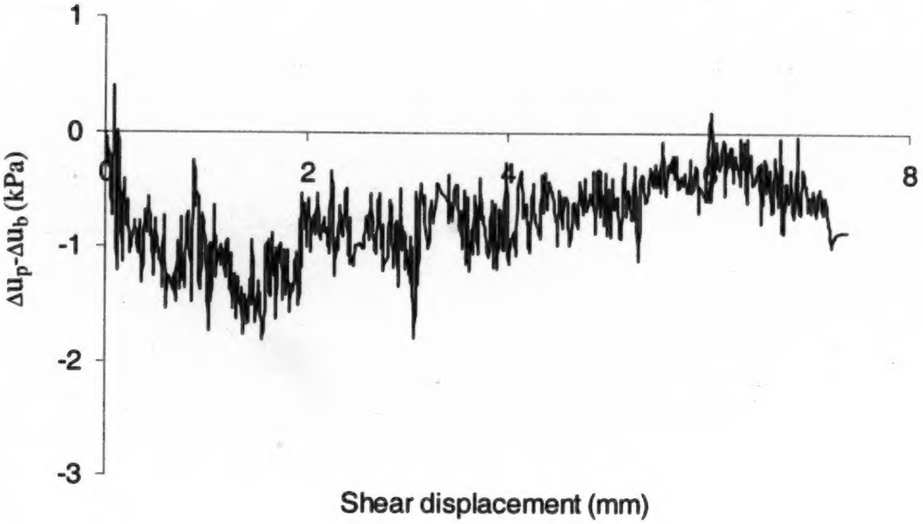

Figure D8 Difference between the pore-pressure-changes on the plane and on the base of specimen C1

Sample 2 0.005 mm/minute of the axial displacement rate

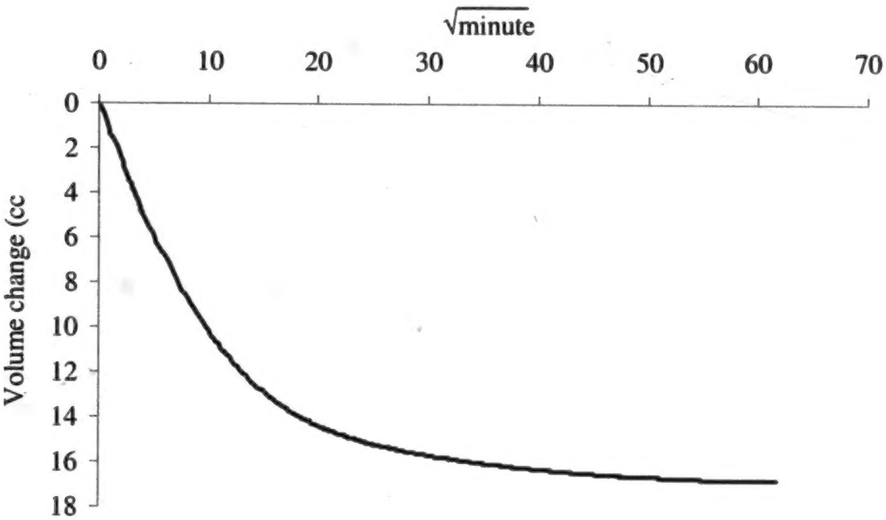

Figure D9 Consolidation curve: volume change versus square root time for specimen C2

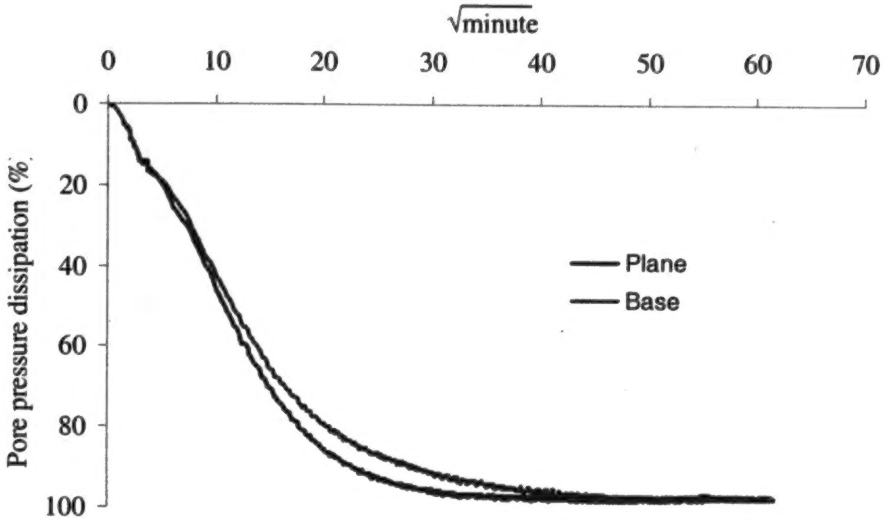

Figure D10 Pore-pressure-dissipation curve for specimen C2

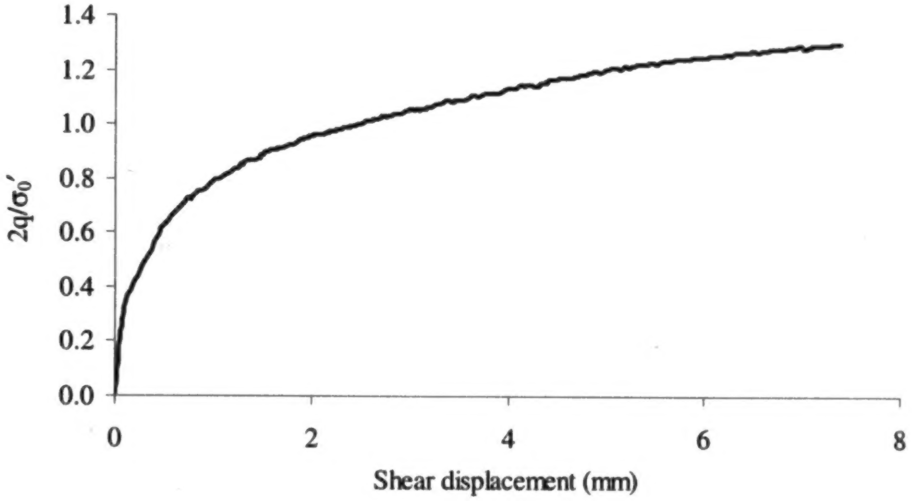

Figure D11 Relationship between the normalized deviator stress and the shear displacement for specimen C2

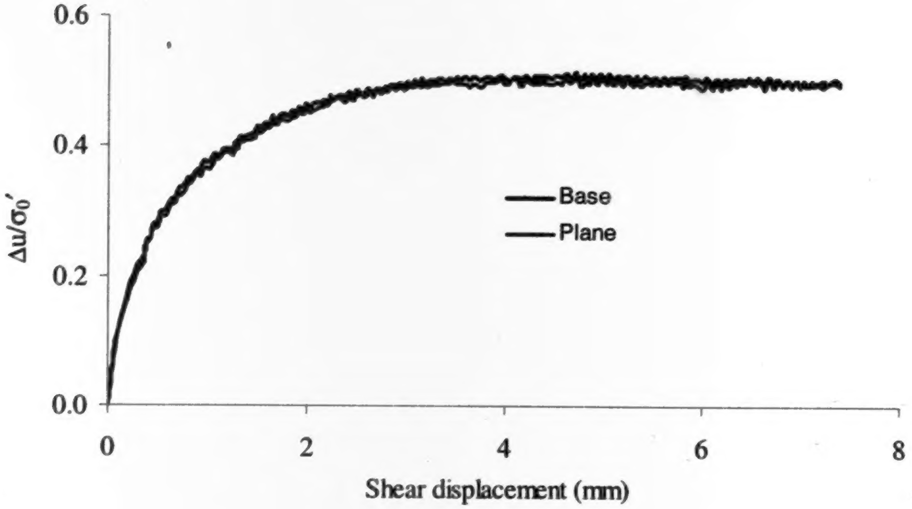

Figure D12 Relationship between the normalized pore-water pressure and the shear displacement for specimen C2

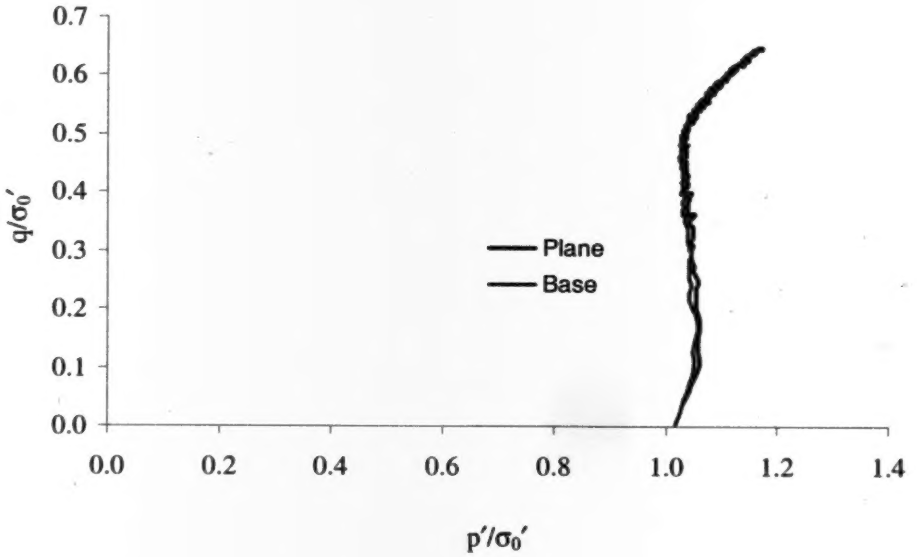

Figure D13 Normalized effective stress paths for specimen C2

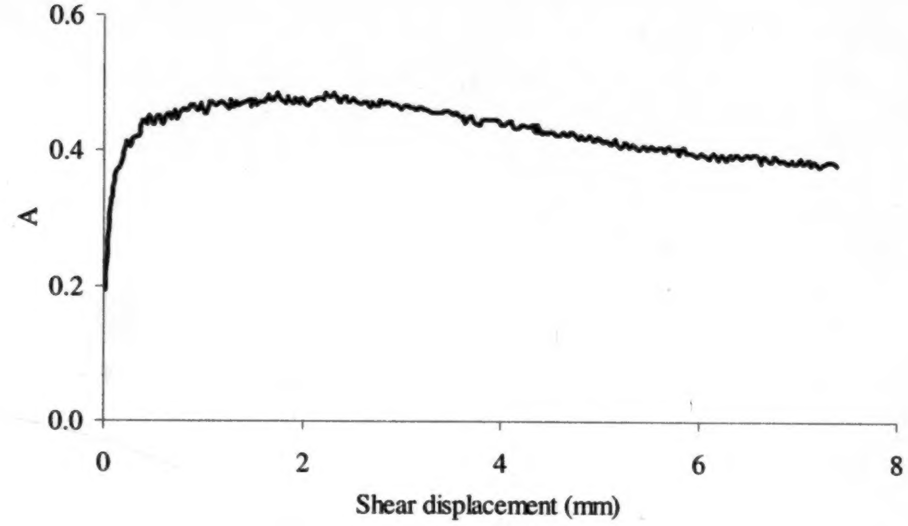

Figure D14 Relationship between the pore-pressure parameter A and the shear displacement for specimen C2

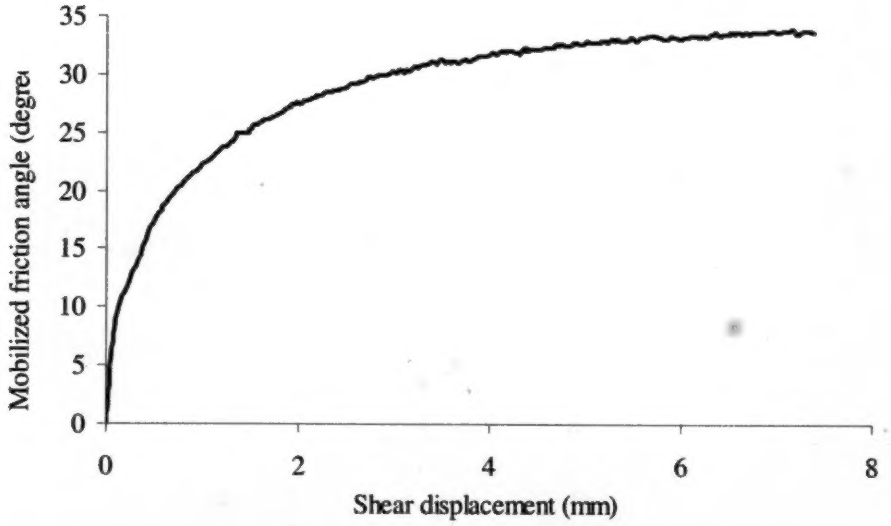

Figure D15 Relationship between the mobilized friction angle and the shear displacement for specimen C2

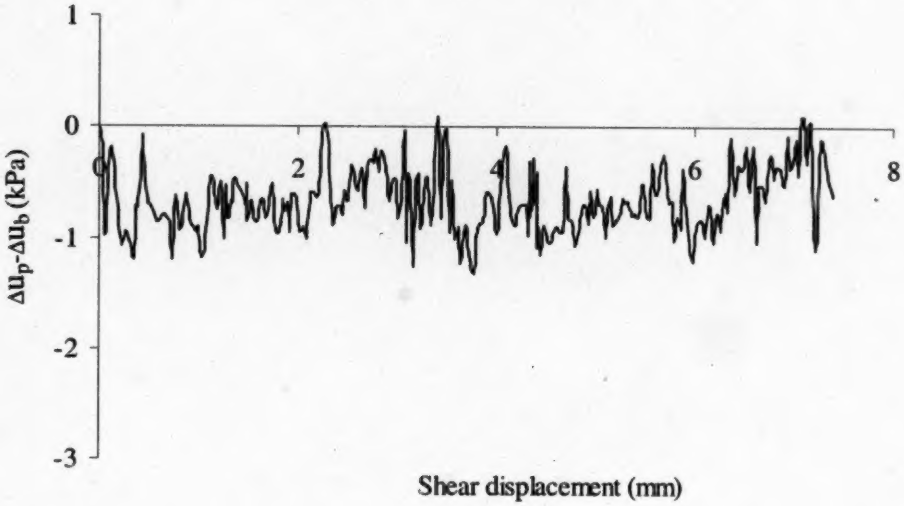

Figure D16 Difference between the pore-pressure-changes on the plane and on the base of specimen C2

Sample 3 0.02 mm/minute of the axial displacement rate

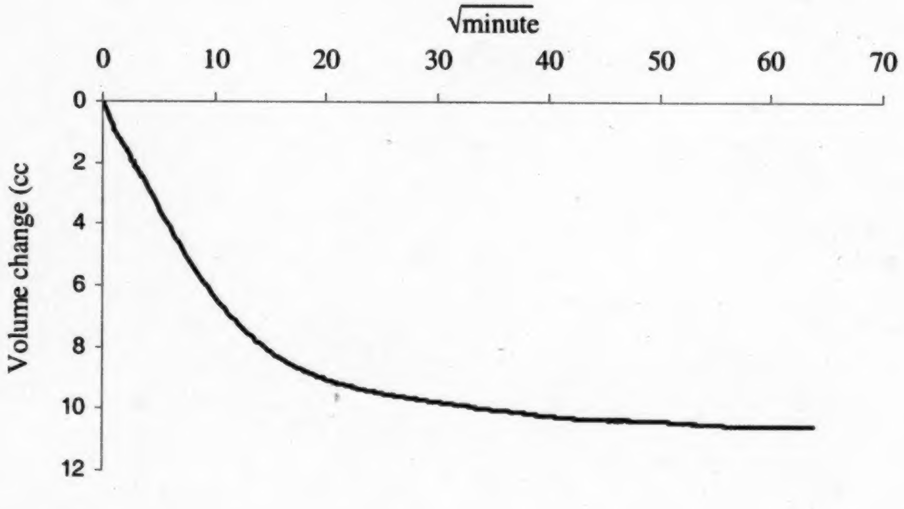

Figure D17 Consolidation curve: volume change versus square root time for specimen C3

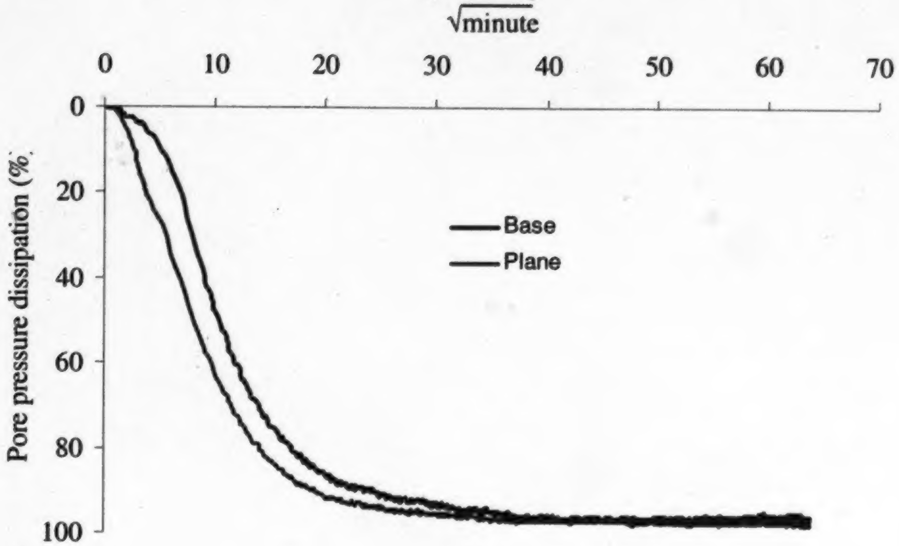

Figure D18 Pore-pressure-dissipation curve for specimen C3

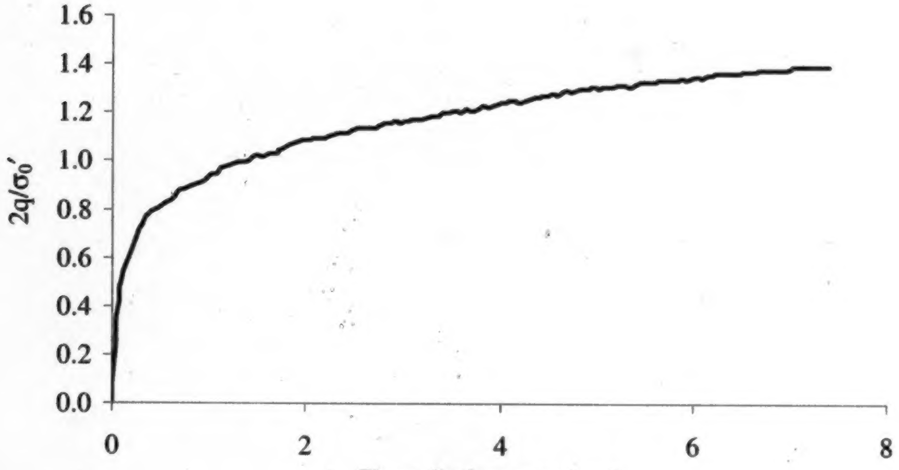

Figure D19 Relationship between the normalized deviator stress and the shear displacement for specimen C3

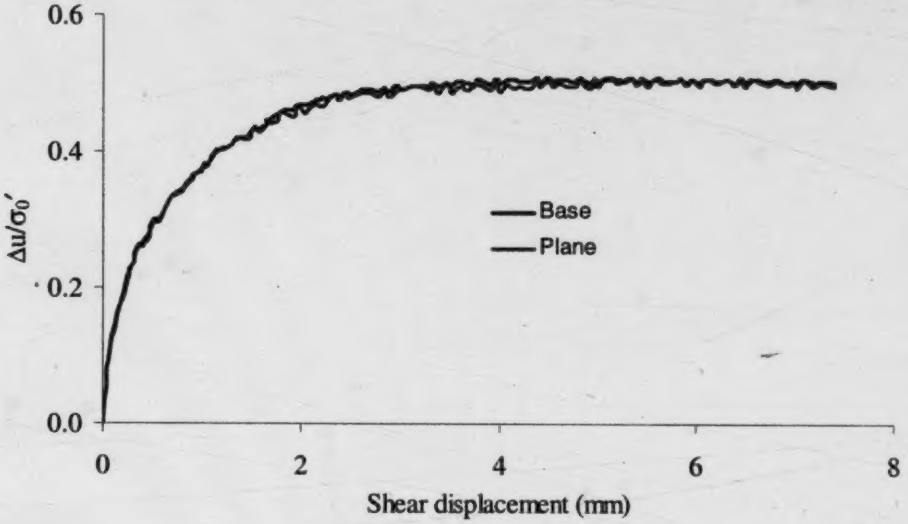

Figure D20 Relationship between the normalized pore-water pressure and the shear displacement for specimen C3

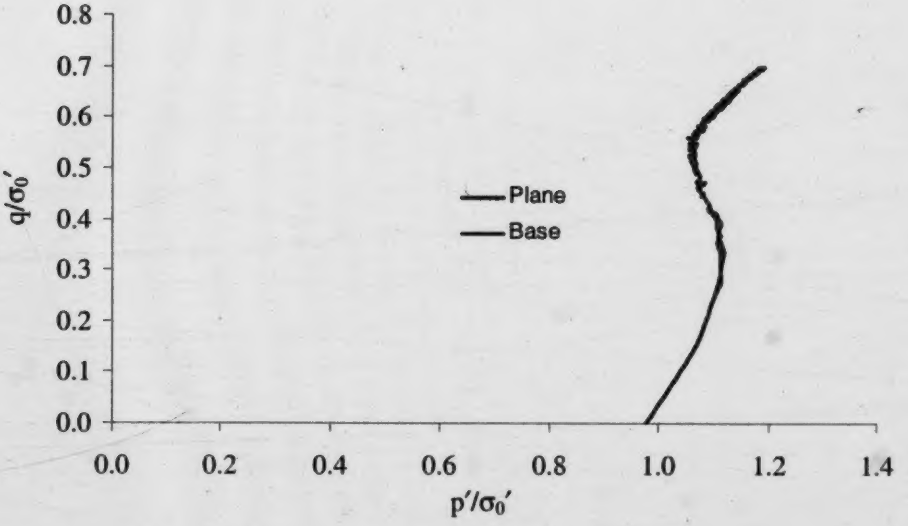

Figure D21 Normalized effective stress paths for specimen C3

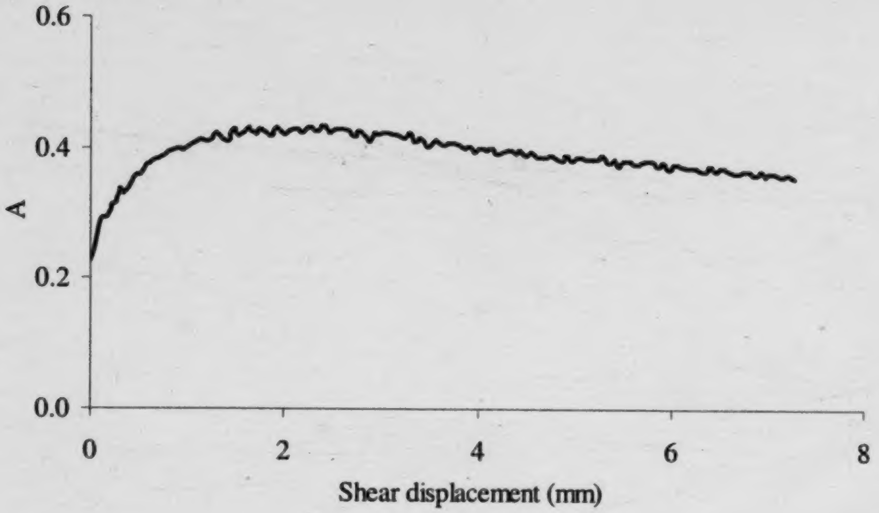

Figure D22 Relationship between the pore-pressure parameter A and the shear displacement for specimen C3

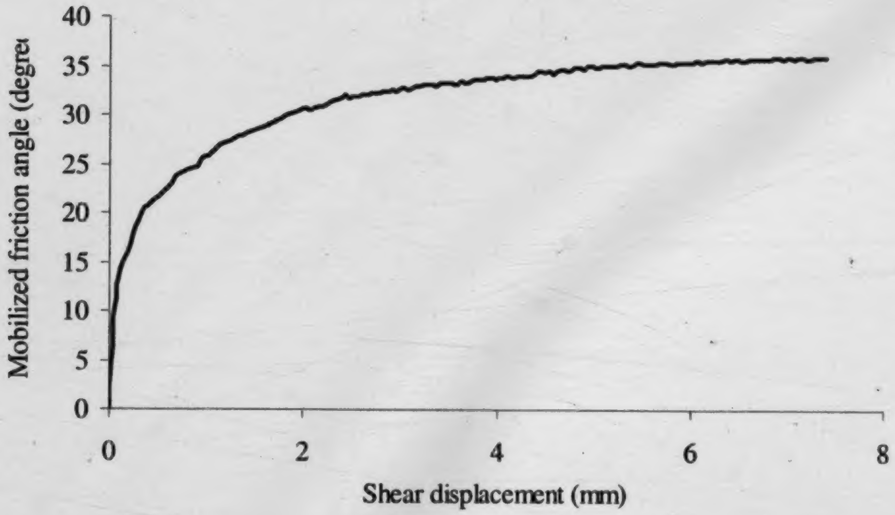

Figure D23 Relationship between the mobilized friction angle and the shear displacement for specimen C3

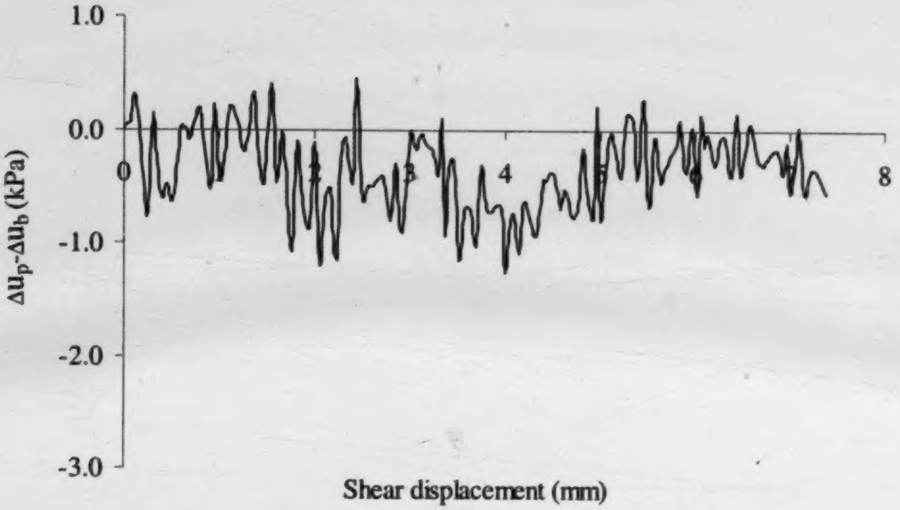

Figure D24 Difference between the pore-pressure-changes on the plane and on the base of specimen C3

Sample 4 0.2 mm/minute of the axial displacement rate

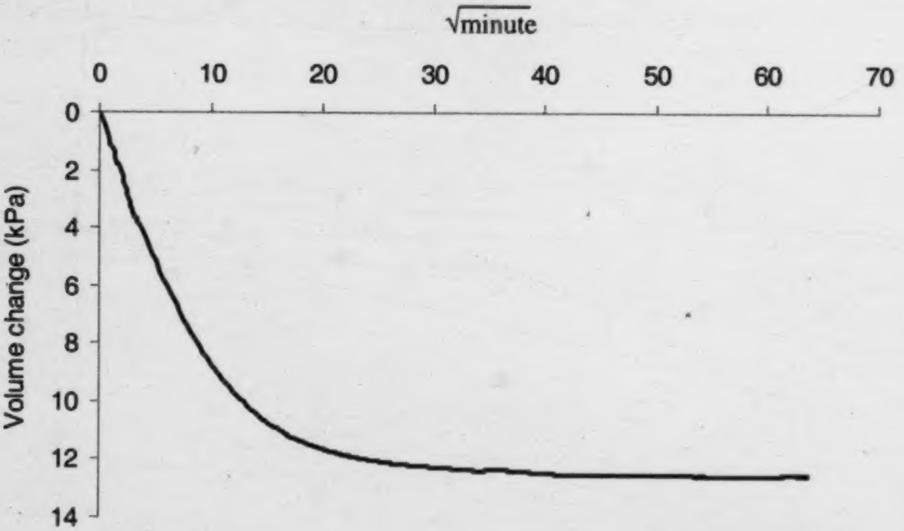

Figure D25 Consolidation curve: volume change versus square root time for specimen C4

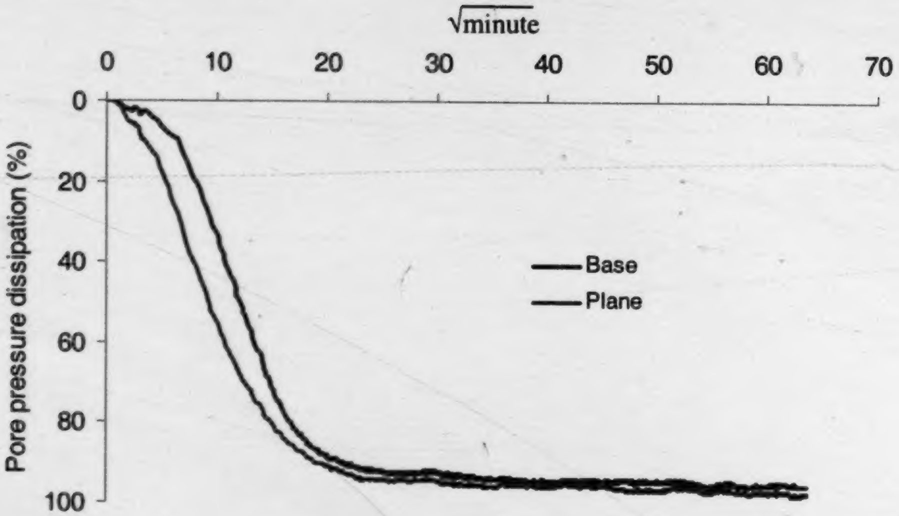

Figure D26 Pore-pressure-dissipation curve for specimen C4

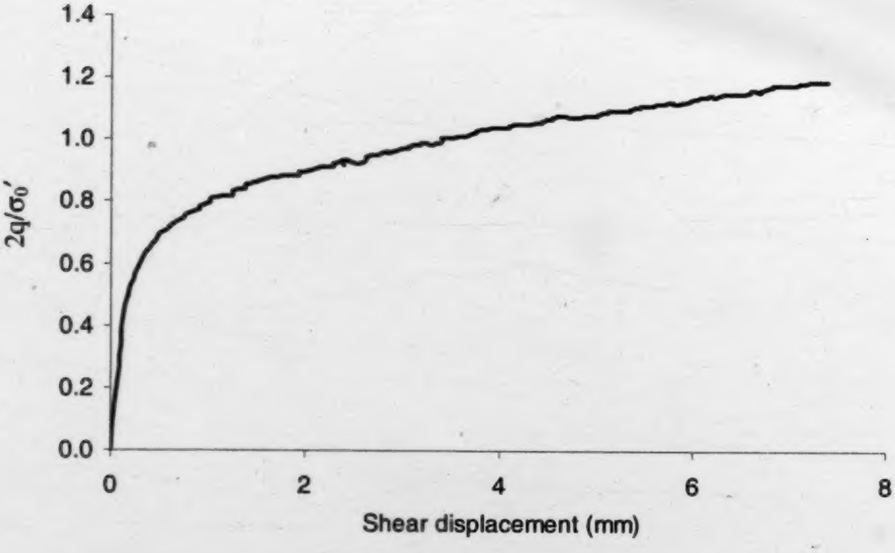

Figure D27 Relationship between the normalized deviator stress and the shear displacement for specimen C4

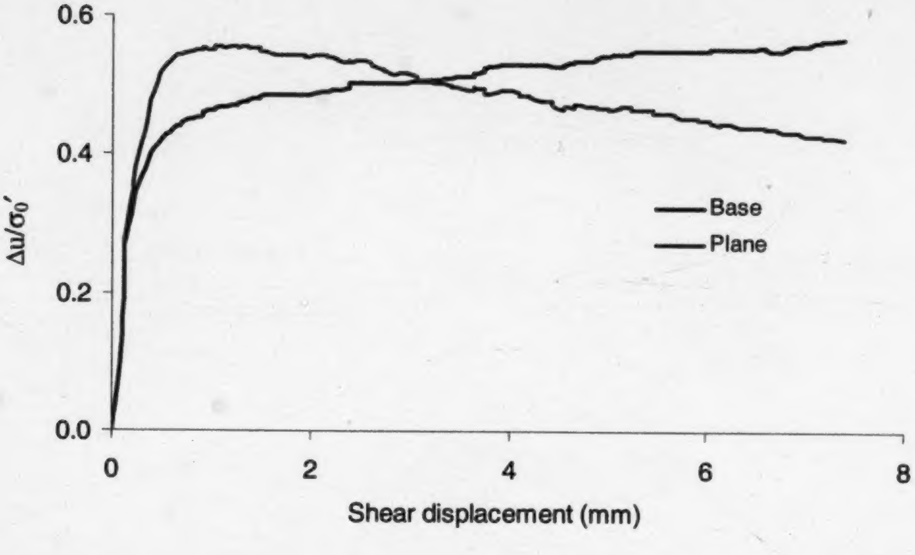

Figure D28 Relationship between the normalized pore-water pressure and the shear displacement for specimen C4

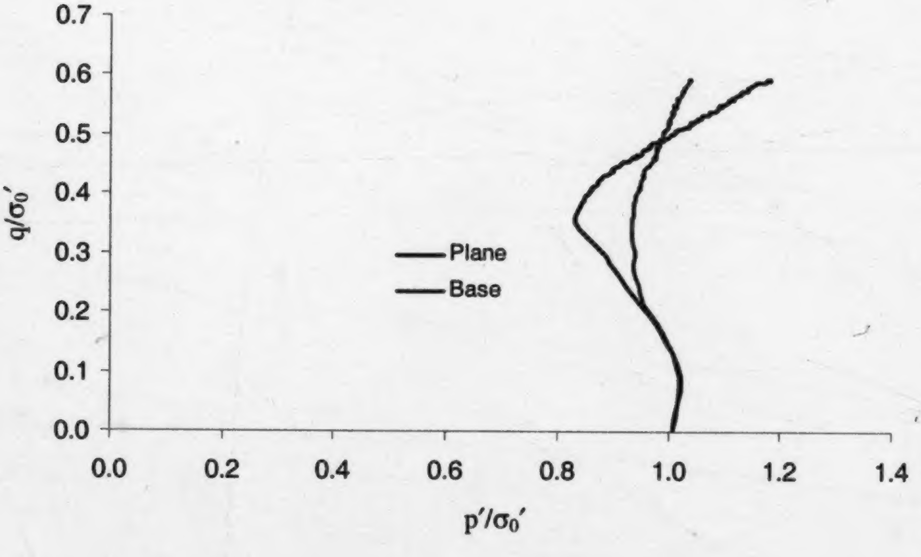

Figure D29 Normalized effective stress paths for specimen C4

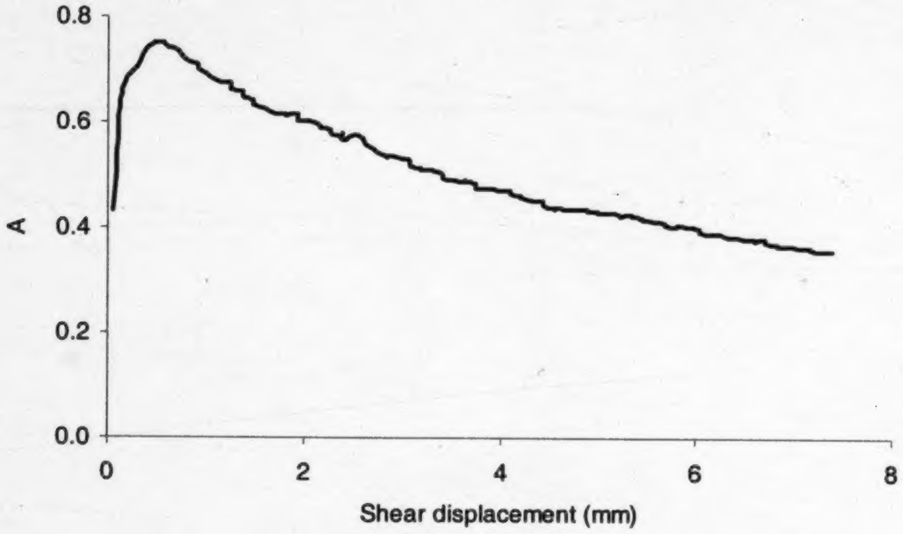

Figure D30 Relationship between the pore-pressure parameter A and the shear displacement for specimen C4

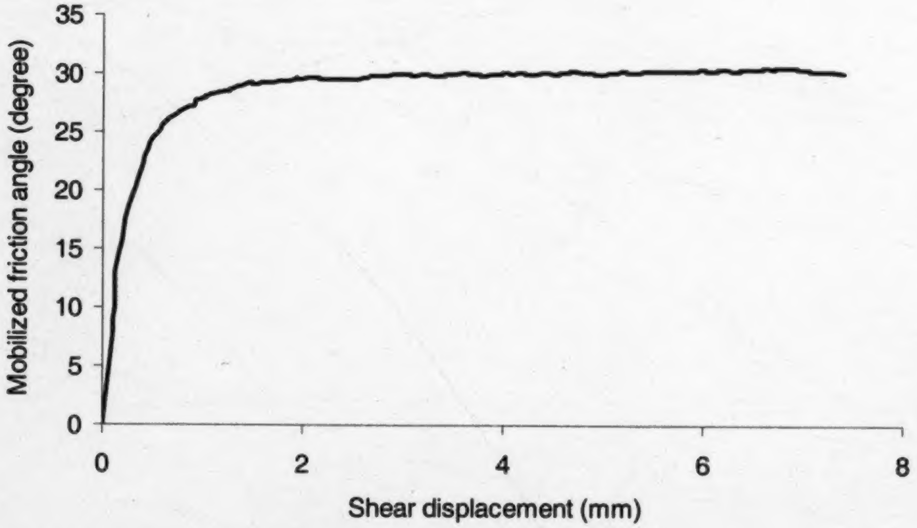

Figure D31 Relationship between the mobilized friction angle and the shear displacement for specimen C4

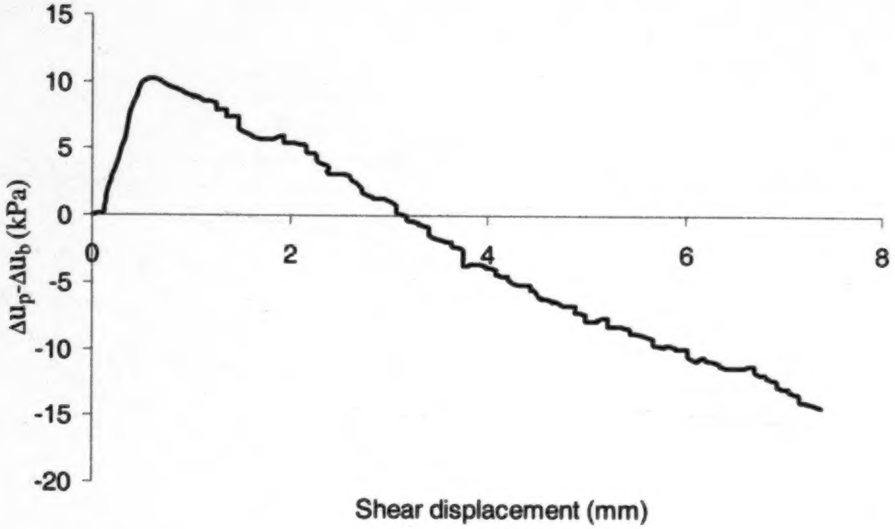

Figure D32 Difference between the pore-pressure-changes on the plane and on the base of specimen C4

Sample 5 1 mm/minute of the axial displacement rate

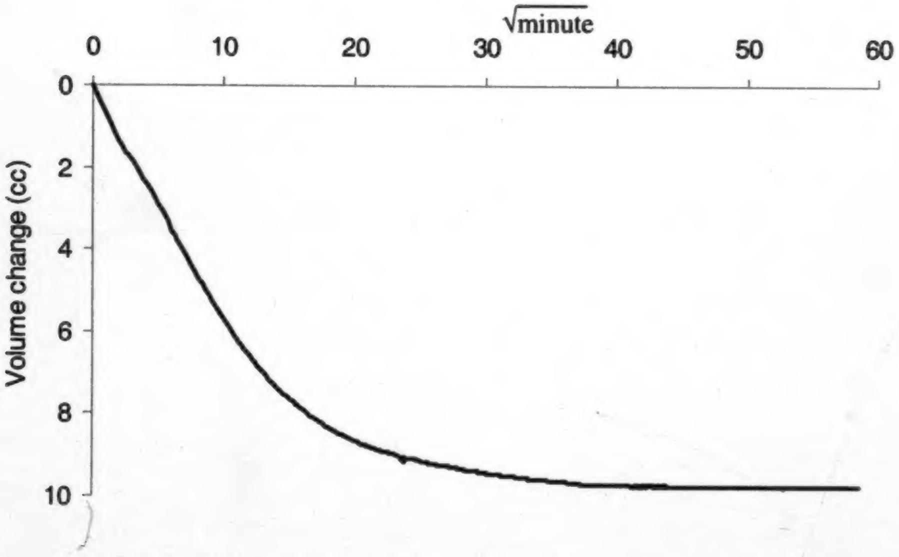

Figure D33 Consolidation curve: volume change versus square root time for specimen C5

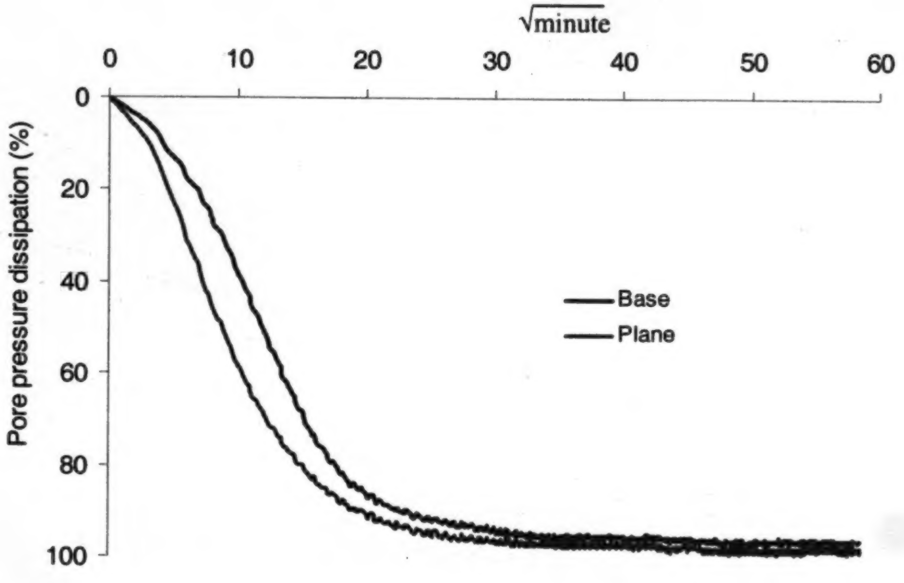

Figure D34 Pore-pressure-dissipation curve for specimen C5

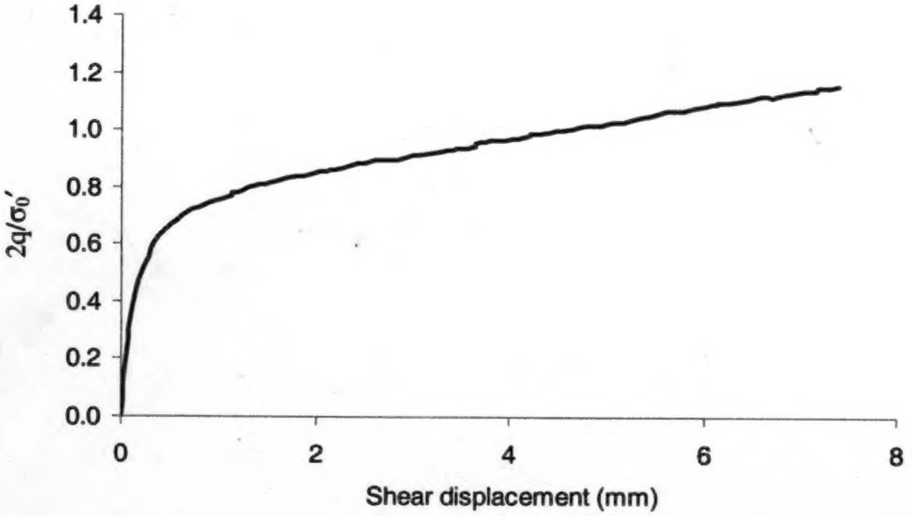

Figure D35 Relationship between the normalized deviator stress and the shear displacement for specimen C5

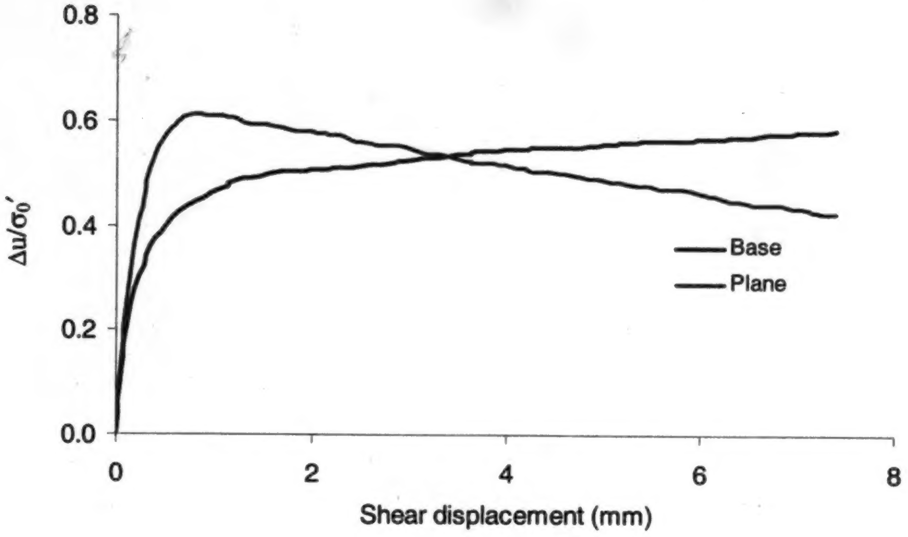

Figure D36 Relationship between the normalized pore-water pressure and the shear displacement for specimen C5

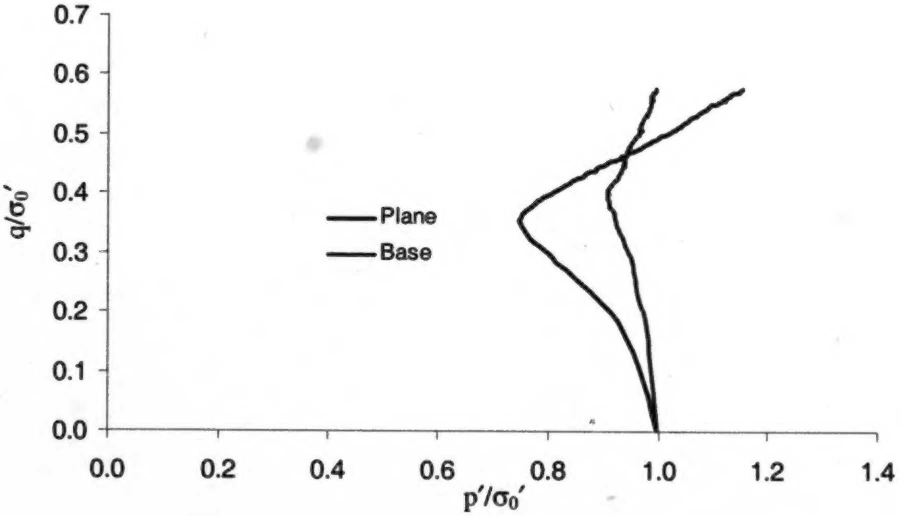

Figure D37 Normalized effective stress paths for specimen C5

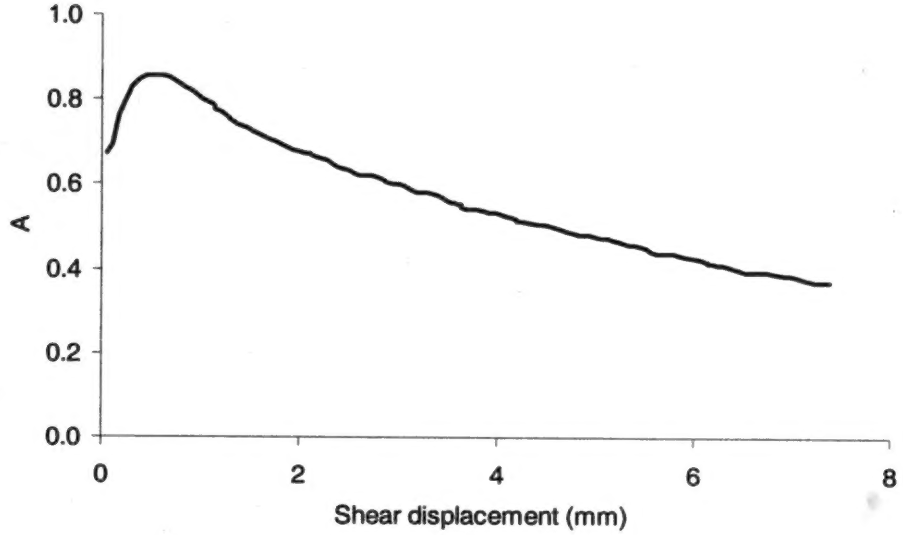

Figure D38 Relationship between the pore-pressure parameter A and the shear displacement for specimen C5

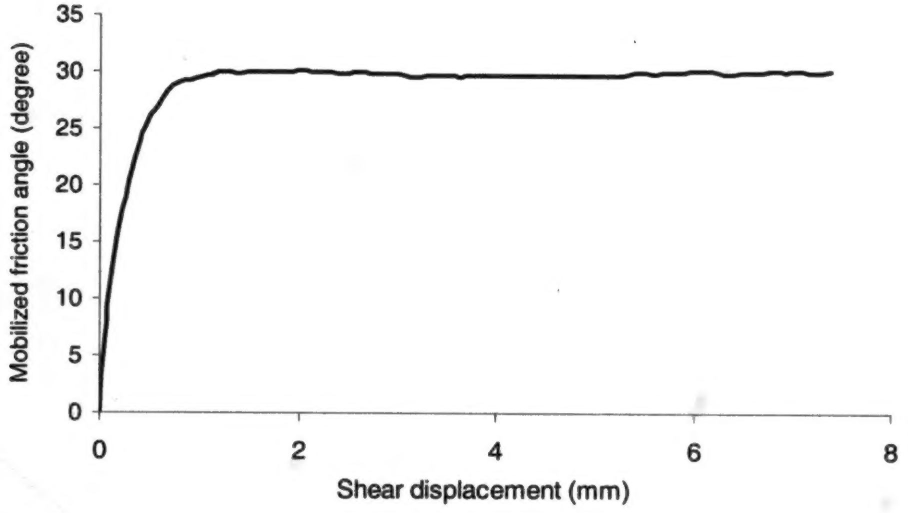

Figure D39 Relationship between the mobilized friction angle and the shear displacement for specimen C5

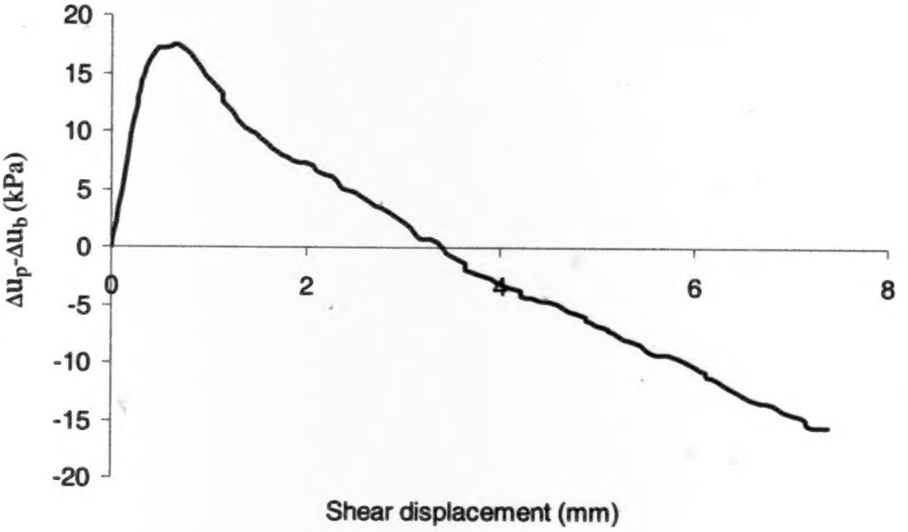

Figure D40 Difference between the pore-pressure-changes on the plane and on the base of specimen C5

D2 TESTS ON THE HIGHVALE MUDSTONE

Sample 1 0.001 mm/minute of the axial displacement rate

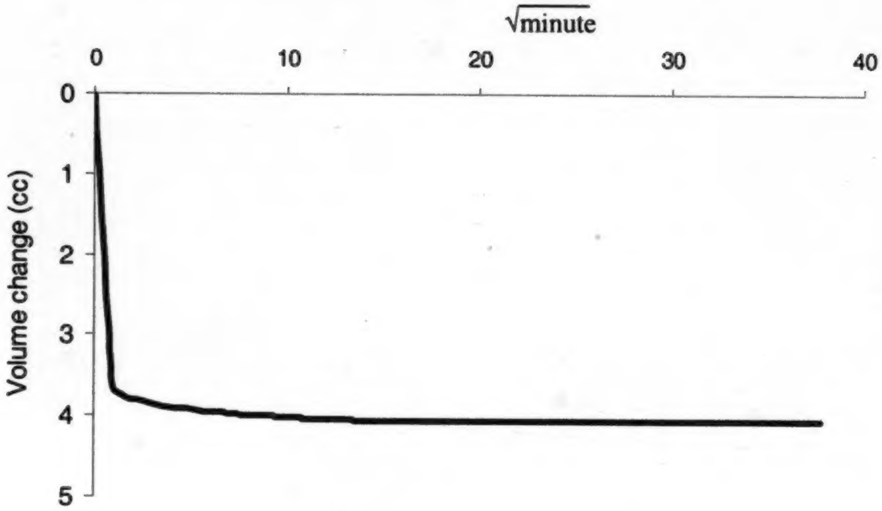

Figure D41 Consolidation curve: volume change versus square root time for specimen M1

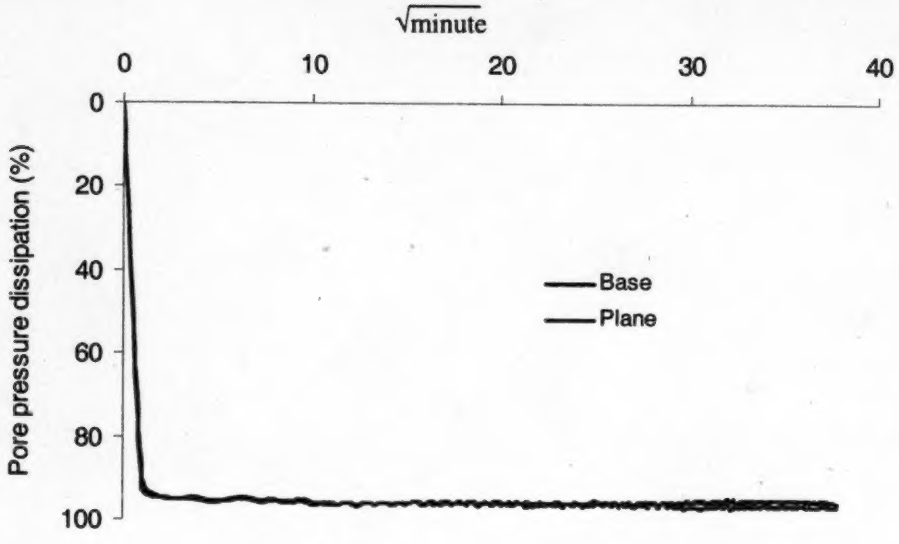

Figure D42 Pore-pressure-dissipation curve for specimen M1

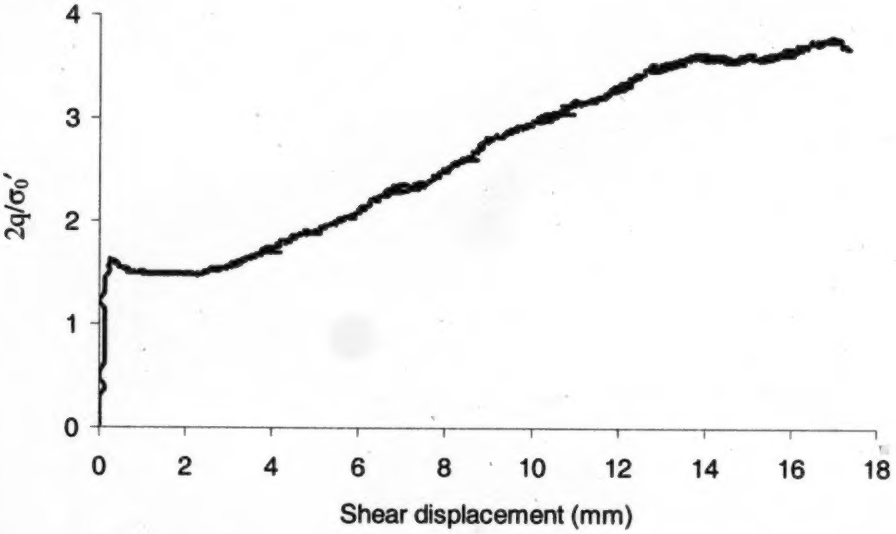

Figure D43 Relationship between the normalized deviator stress and the shear displacement for specimen M1

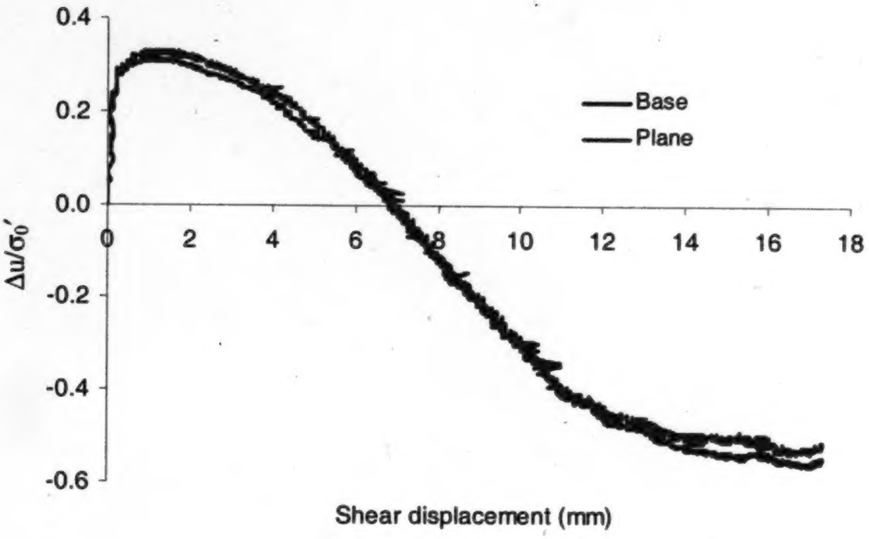

Figure D44 Relationship between the normalized pore-water pressure and the shear displacement for specimen M1

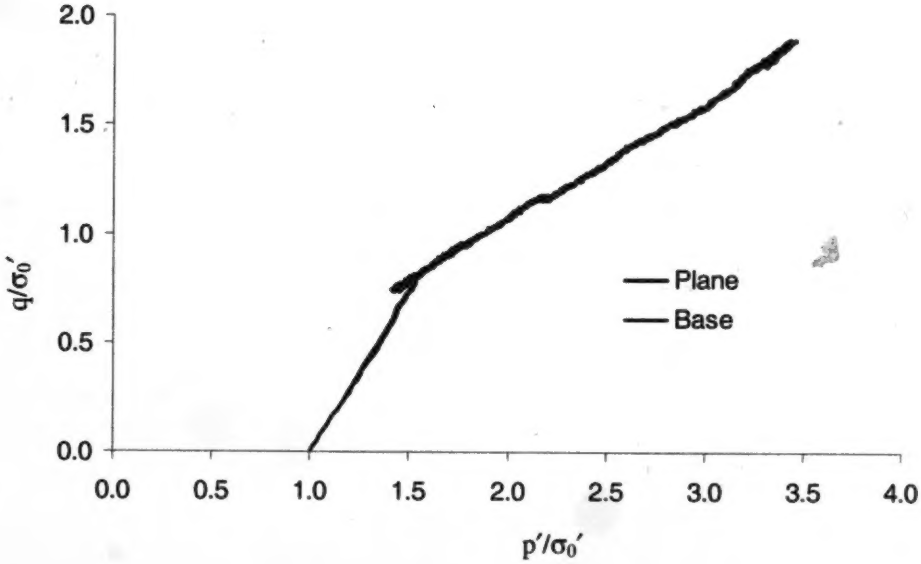

Figure D45 Normalized effective stress paths for specimen M1

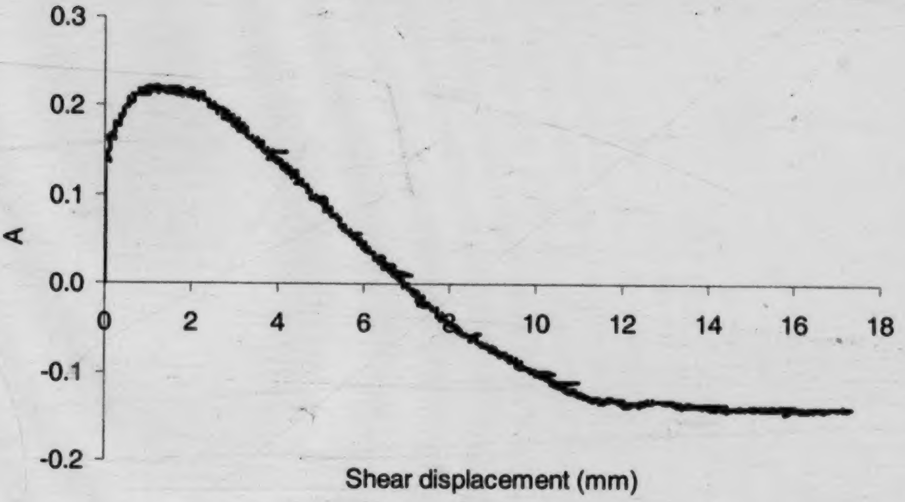

Figure D46 Relationship between the pore-pressure parameter A and the shear displacement for specimen M1

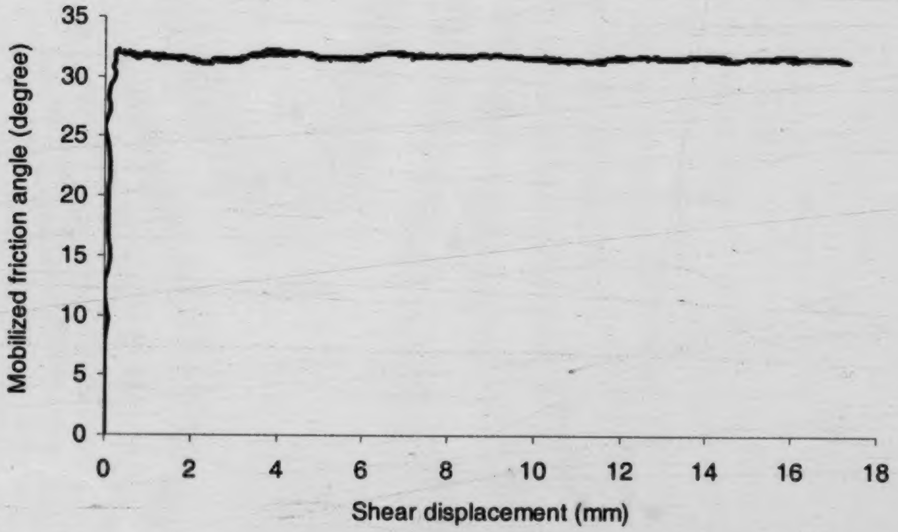

Figure D47 Relationship between the mobilized friction angle and the shear displacement for specimen M1

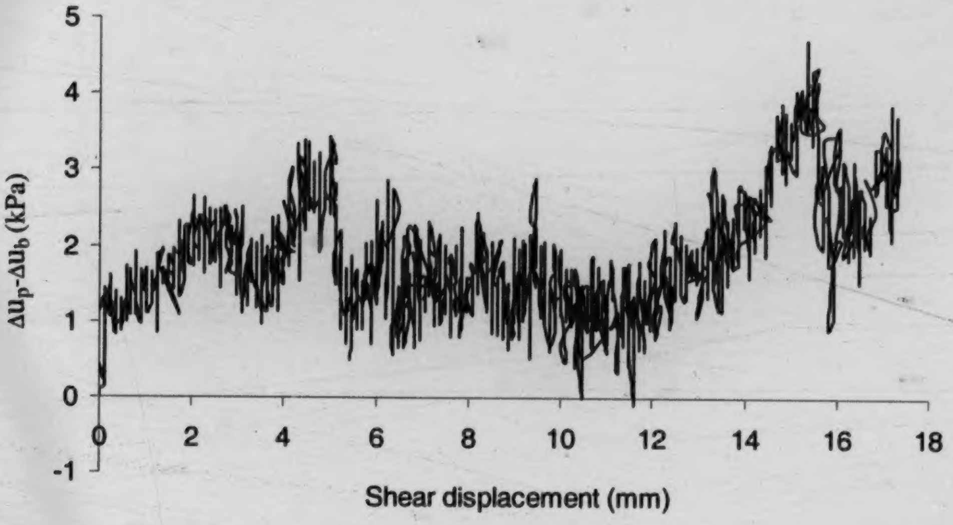

Figure D48 Difference between the pore-pressure-changes on the plane and on the base of specimen M1

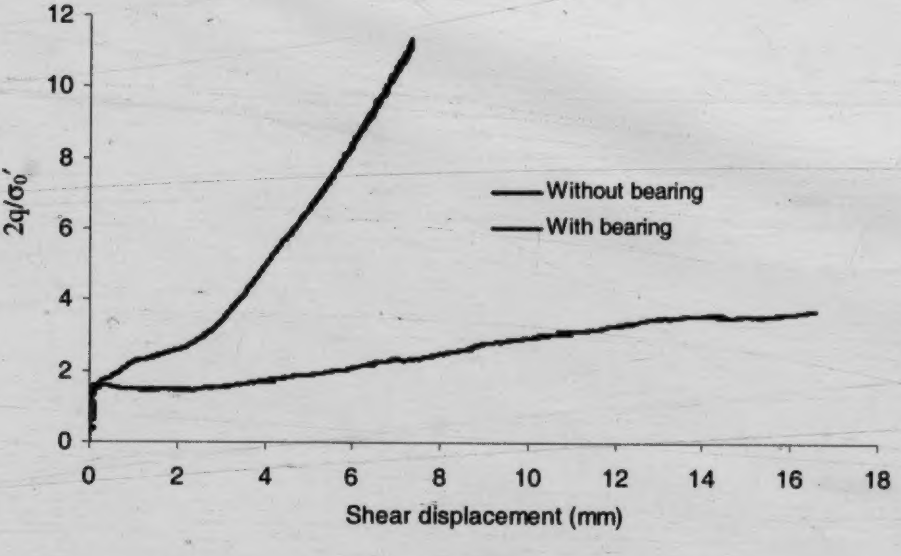

Figure D49 Normalized deviator stresses measured by using a ring bearing and not using a ring bearing for Highvale mudstone at the axial displacement rate of 0.001 mm/minute

Sample 2 0.005 mm/minute of the axial displacement rate

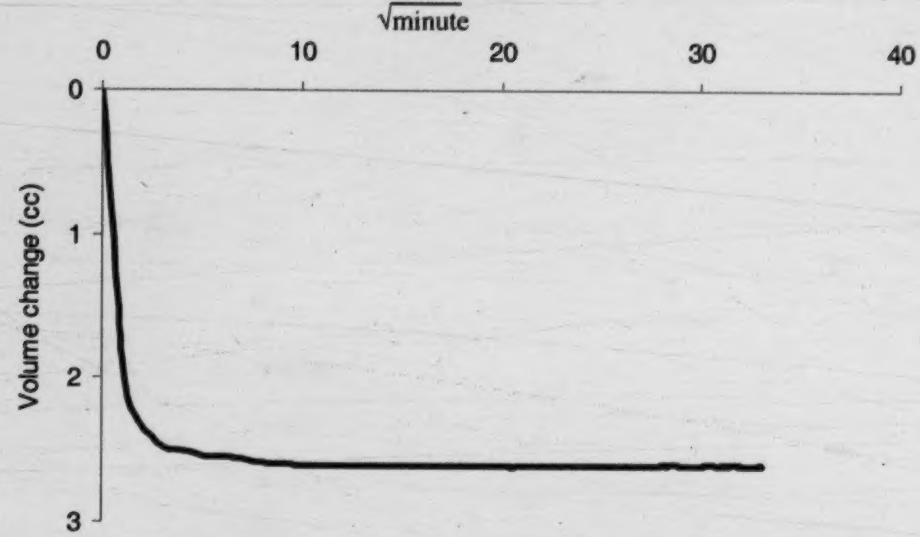

Figure D50 Consolidation curve: volume change versus square root time for specimen M2

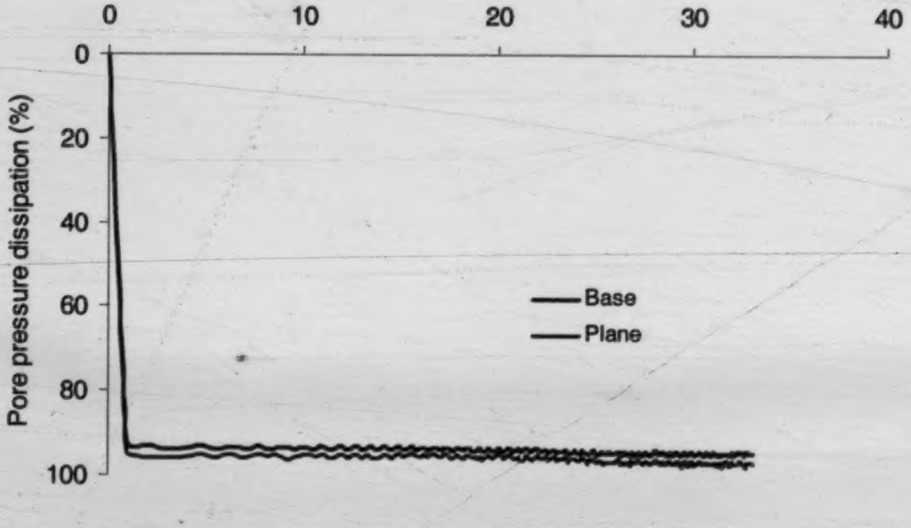

Figure D51 Pore-pressure-dissipation curve for specimen M2

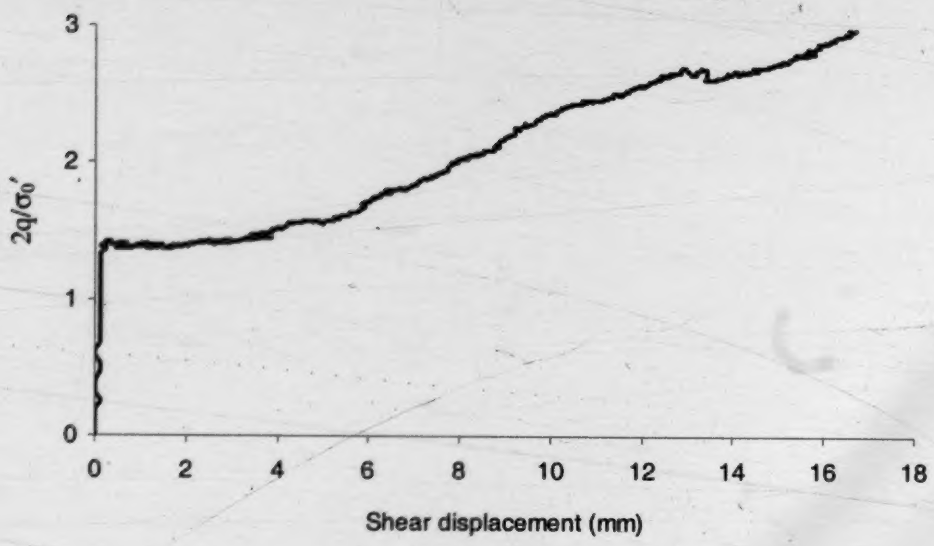

Figure D52 Relationship between the normalized deviator stress and the shear displacement for specimen M2

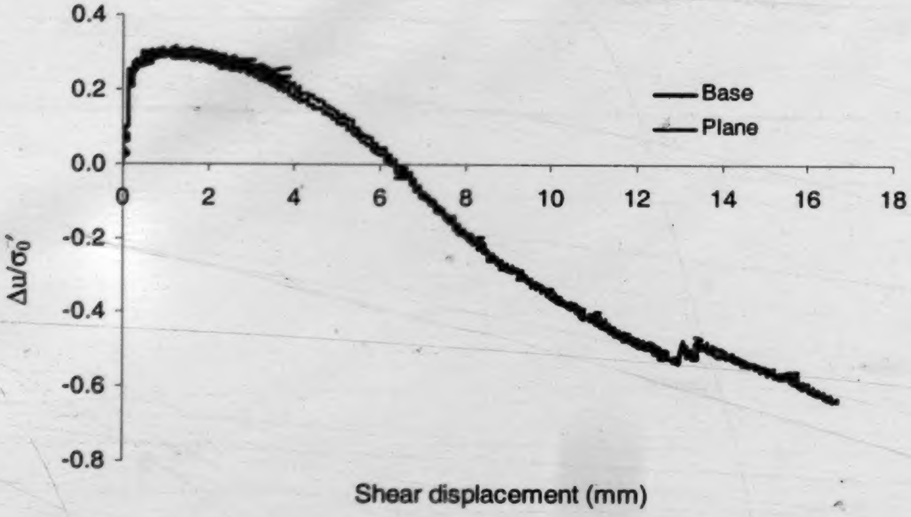

Figure D53 Relationship between the normalized pore-water pressure and the shear displacement for specimen M2

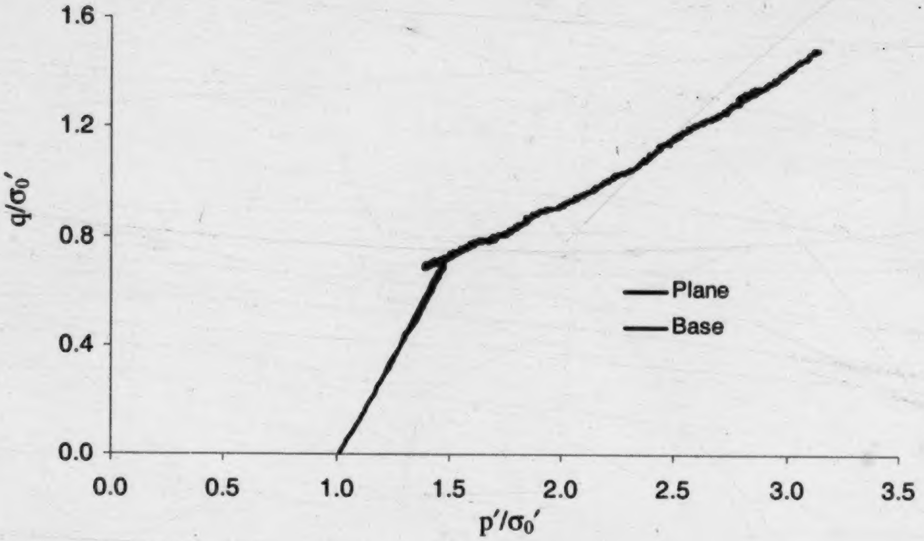

Figure D54 Normalized effective stress paths for specimen M2

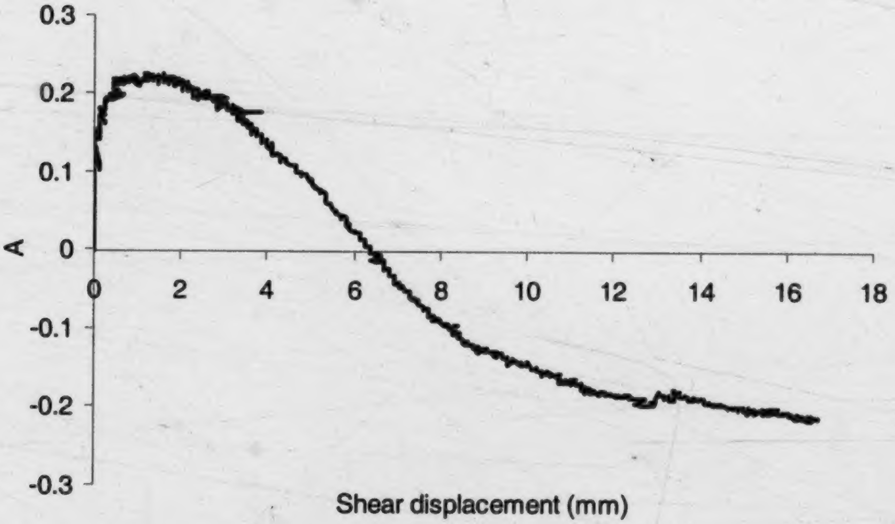

Figure D55 Relationship between the pore-pressure parameter A and the shear displacement for specimen M2

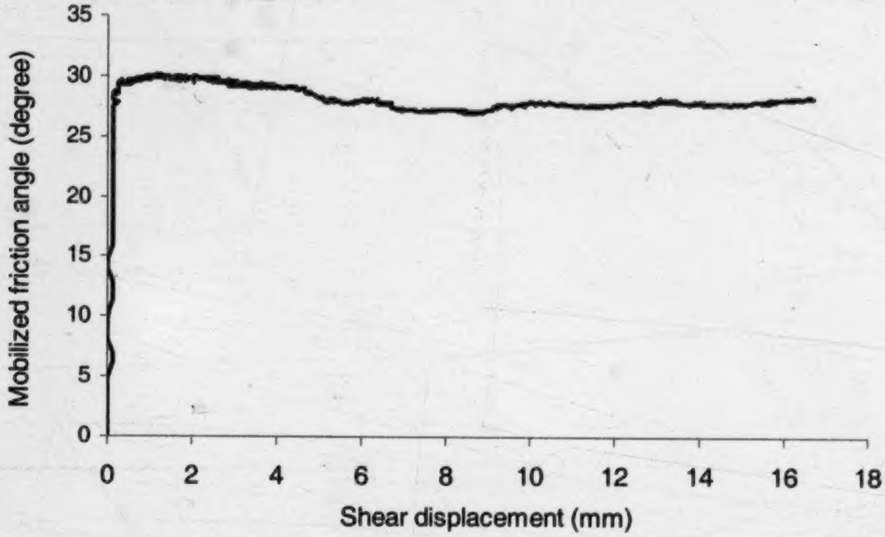

Figure D56 Relationship between the mobilized friction angle and the shear displacement for specimen M2

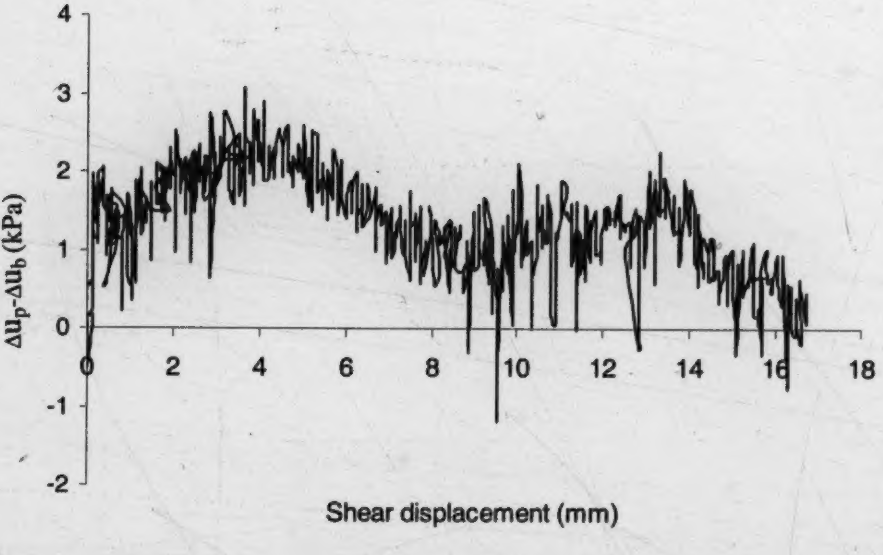

Figure D57 Difference between the pore-pressure-changes on the plane and on the base of specimen M2

D3 TESTS ON THE HIGHLY WEATHERED LIMESTONE

Sample 1 0.005 mm/minute of the axial displacement rate

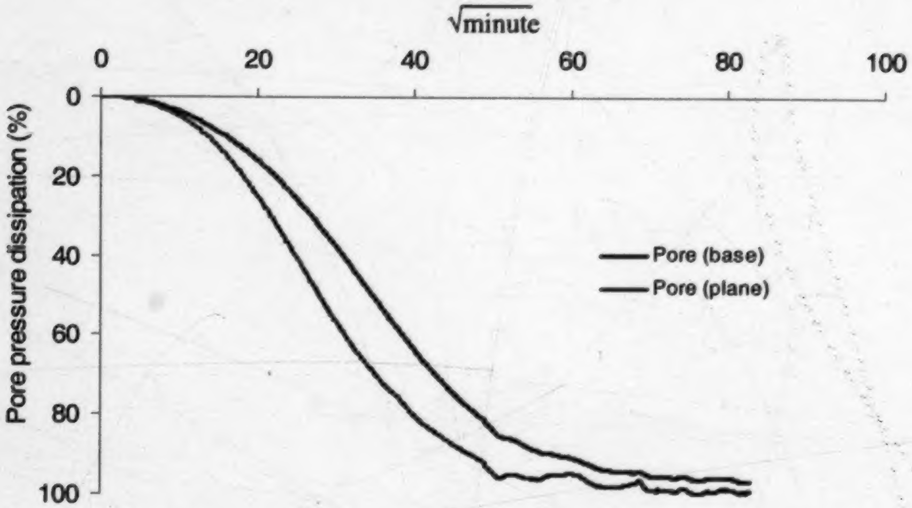

Figure D58 Pore-pressure-dissipation curve for specimen L2

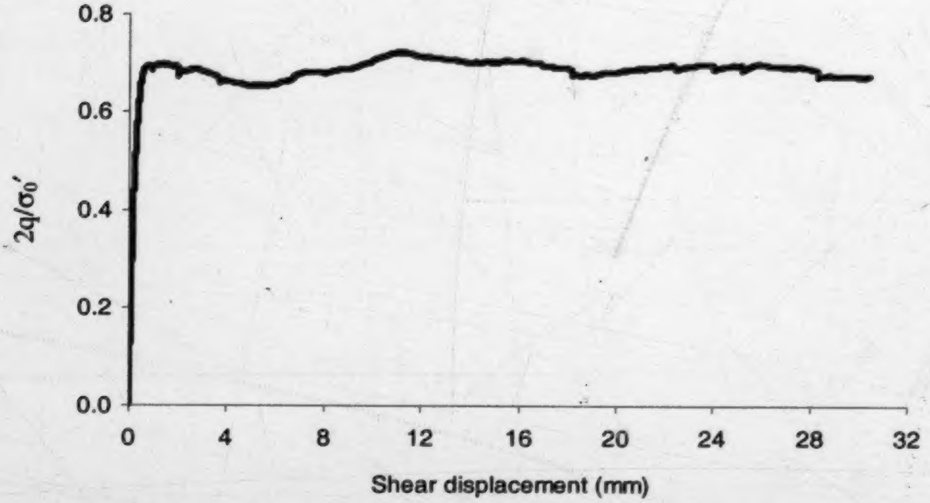

Figure D59 Relationship between the normalized deviator stress and the shear displacement for specimen L2

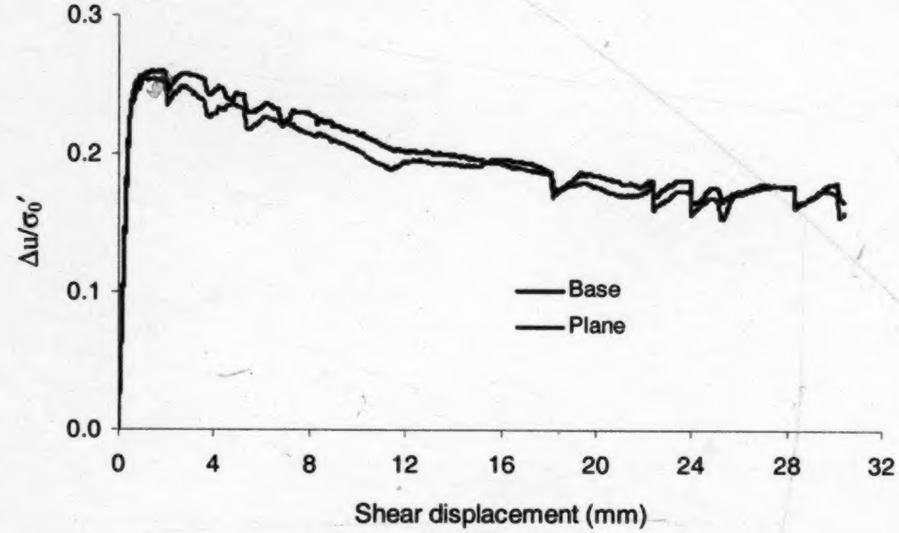

Figure D60 Relationship between the normalized pore-water pressure and the shear displacement for specimen L2

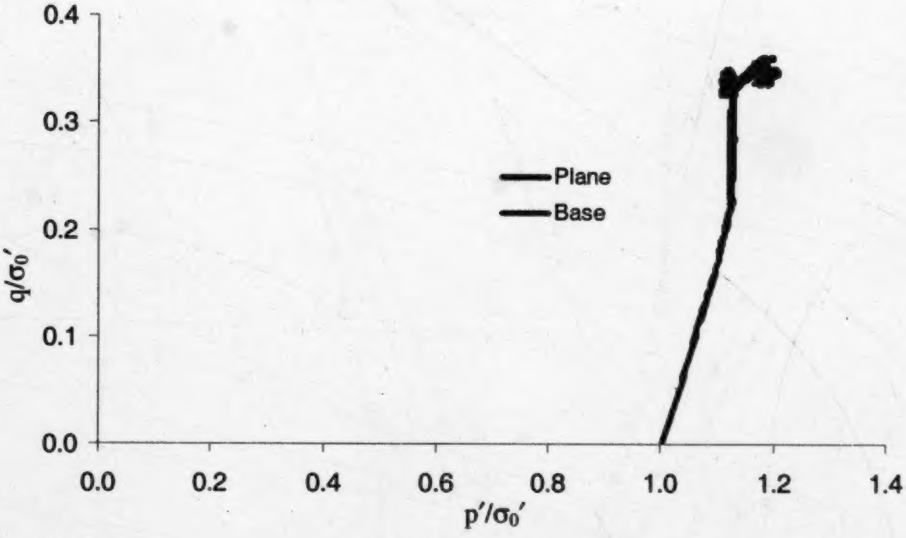

Figure D61 Normalized effective stress paths for specimen L2

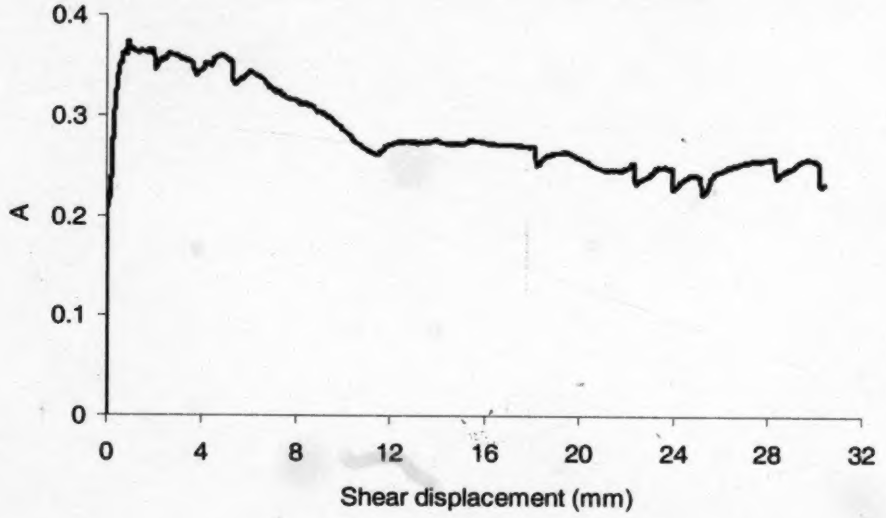

Figure D62 Relationship between the pore pressure parameter A and the shear displacement for specimen L2

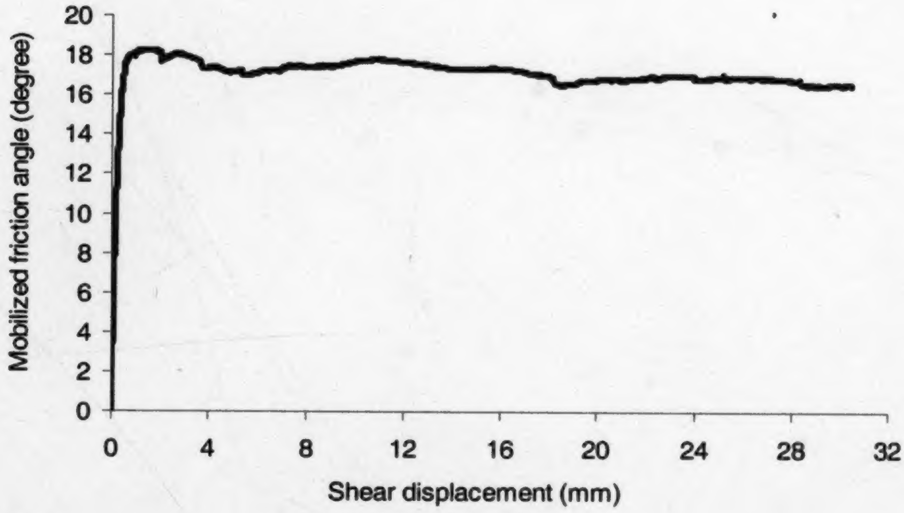

Figure D63 Relationship between the mobilized friction angle and the shear displacement for specimen L2

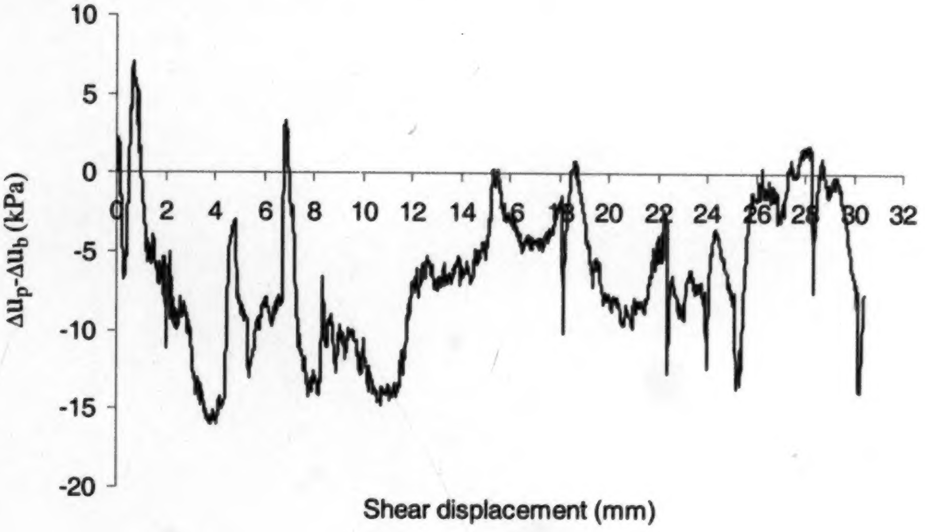

Figure D64 Difference between the pore-pressure-changes on the plane and on the base of specimen L2

Sample 2 0.01 mm/minute of the axial displacement rate

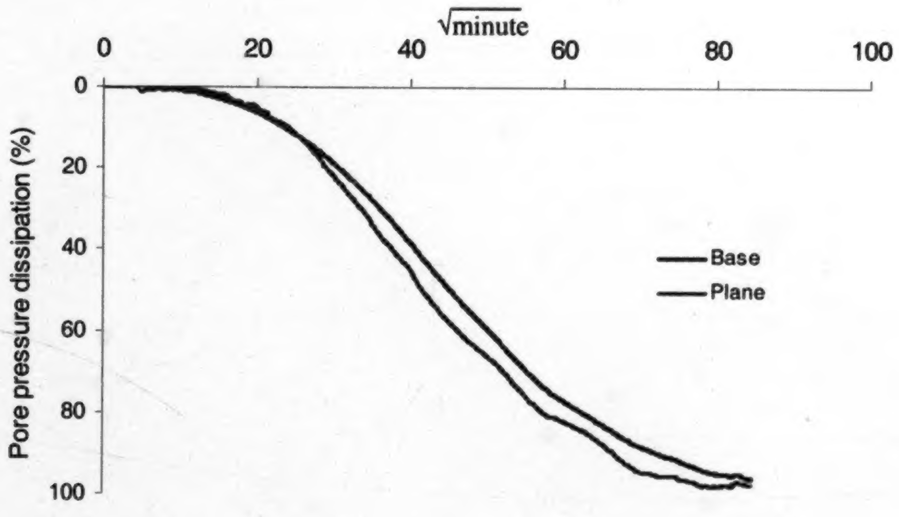

Figure D65 Pore-pressure-dissipation curve for specimen L3

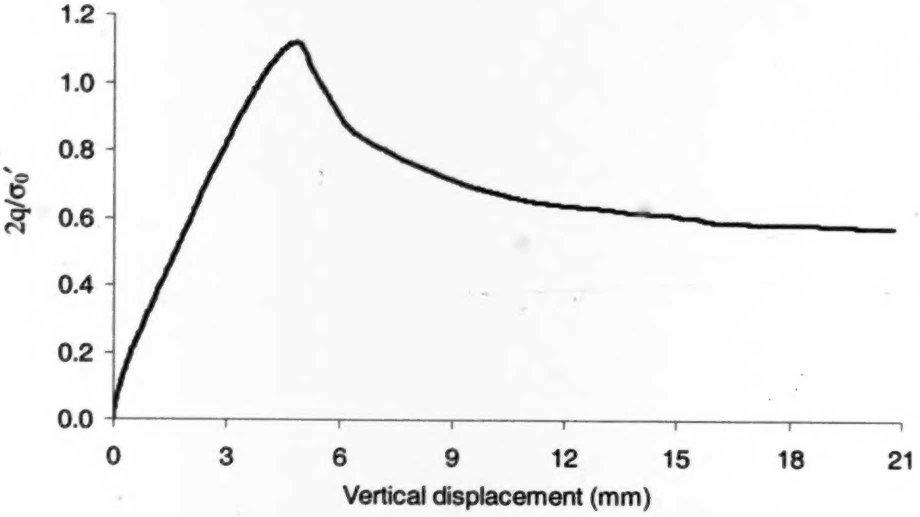

Figure D66 Relationship between the normalized deviator stress and the shear displacement for specimen L3

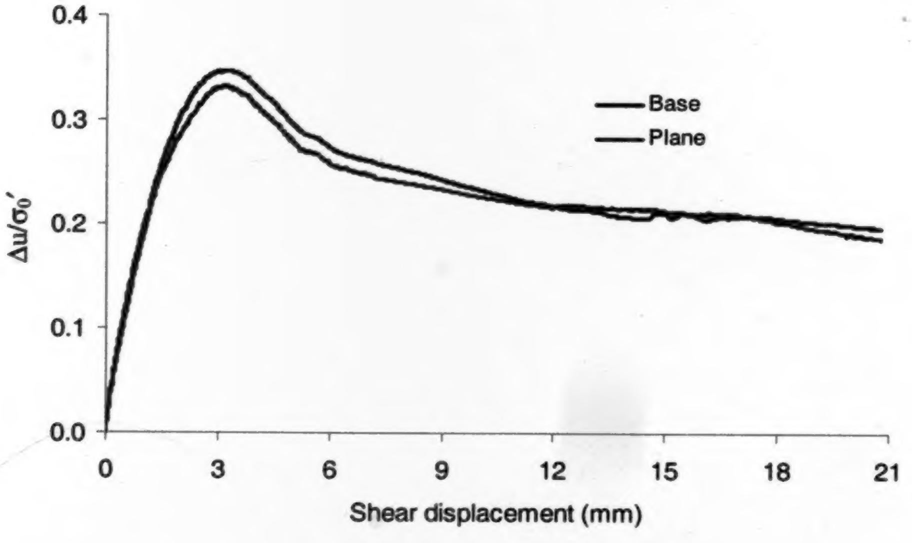

Figure D67 Relationship between the normalized pore-water pressure and the shear displacement for specimen L3

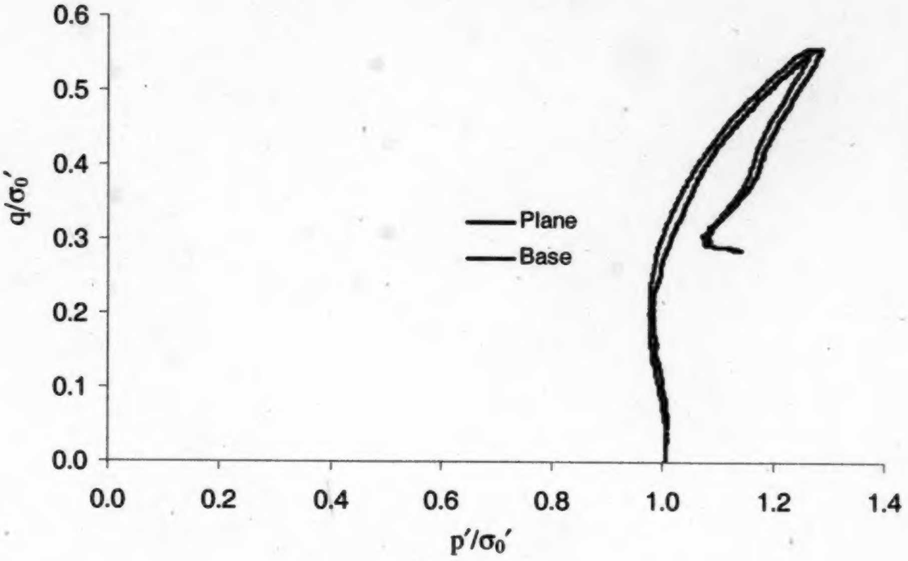

Figure D68 Normalized effective stress paths for specimen L3

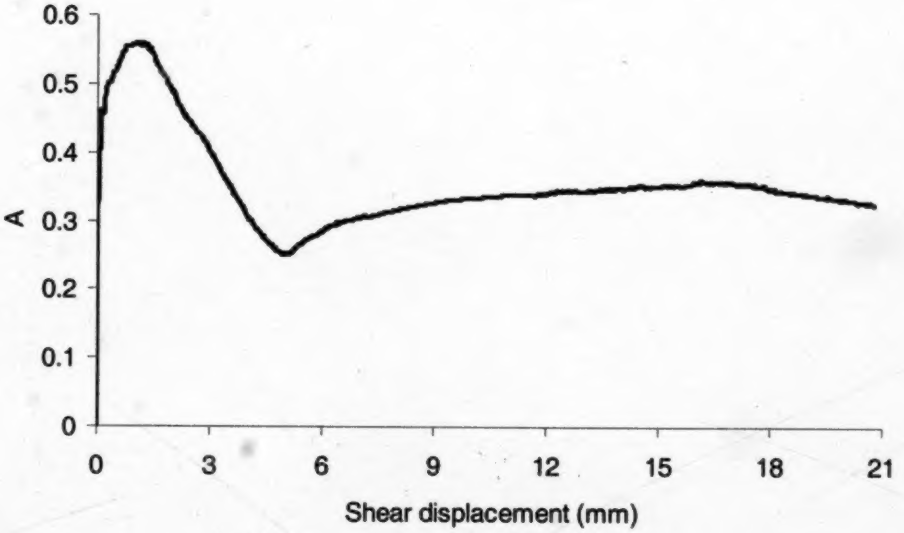

Figure D69 Relationship between the pore-pressure parameter A and the shear displacement for specimen L3

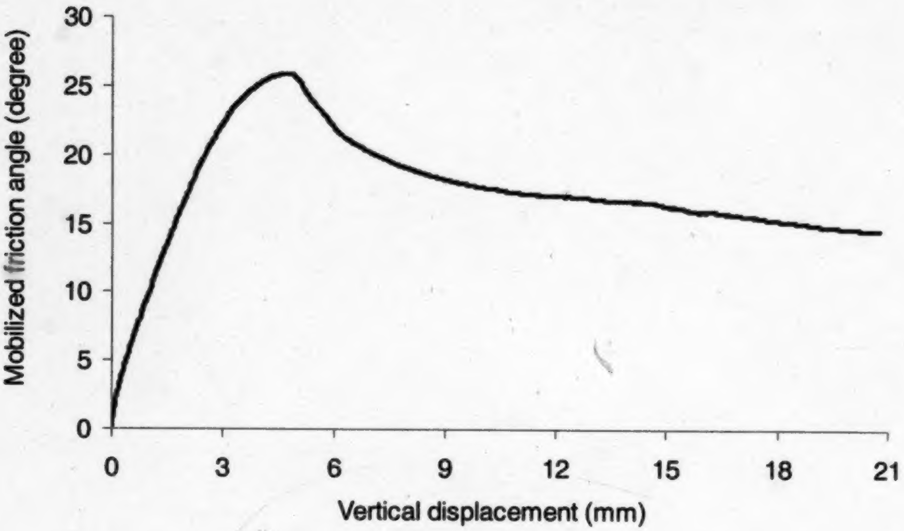

Figure D70 Relationship between the mobilized friction angle and the shear displacement for specimen L3

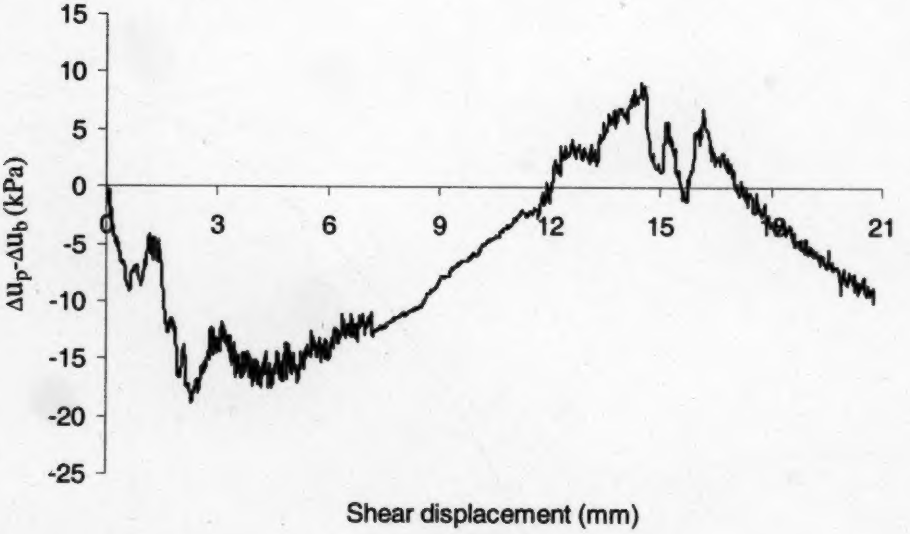

Figure D71 Difference between the pore-pressure-changes on the plane and on the base of specimen L3

D4 TESTS ON PALEOSOL

Sample 1 0.01 mm/minute of the axial displacement rate

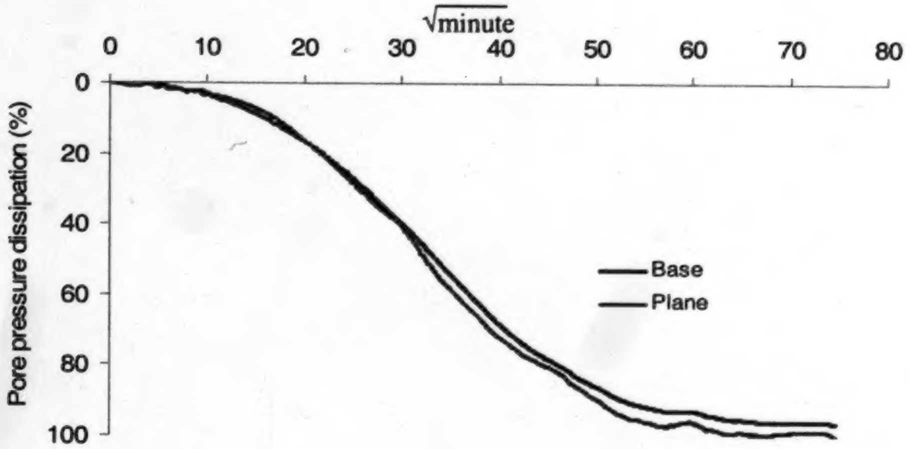

Figure D72 Pore-pressure-dissipation curve for specimen P2

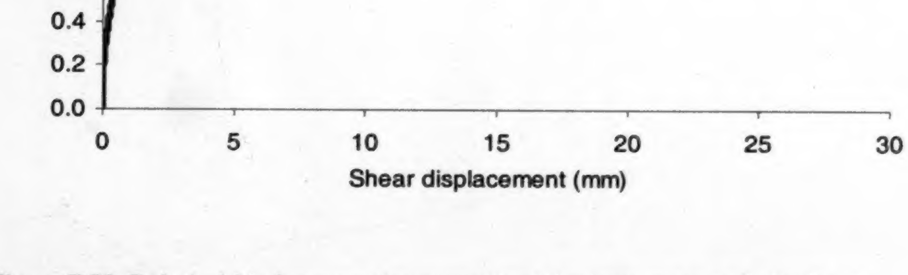

Figure D73 Relationship between the normalized deviator stress and the shear displacement for specimen P2

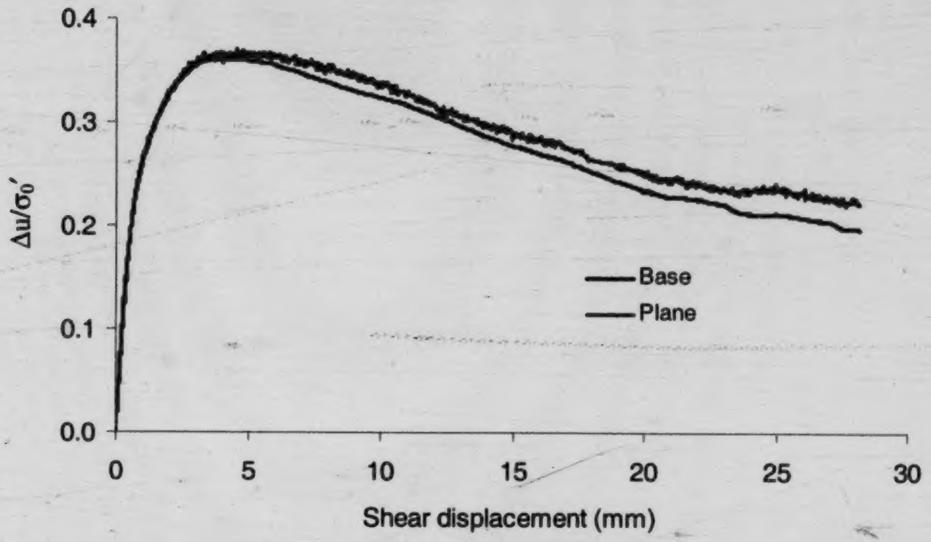

Figure D74 Relationship between the normalized pore-water pressure and the shear displacement for specimen P2

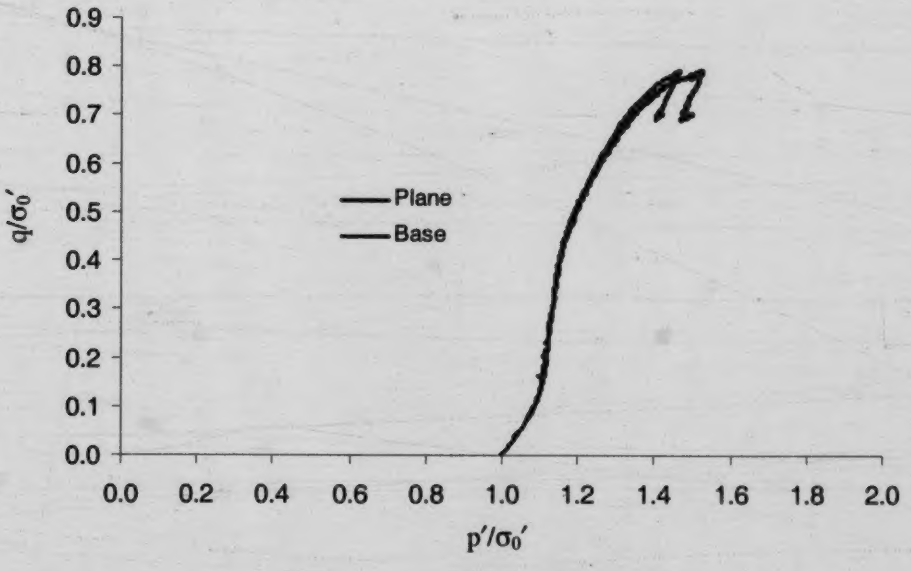

Figure D75 Normalized effective stress paths for specimen P2

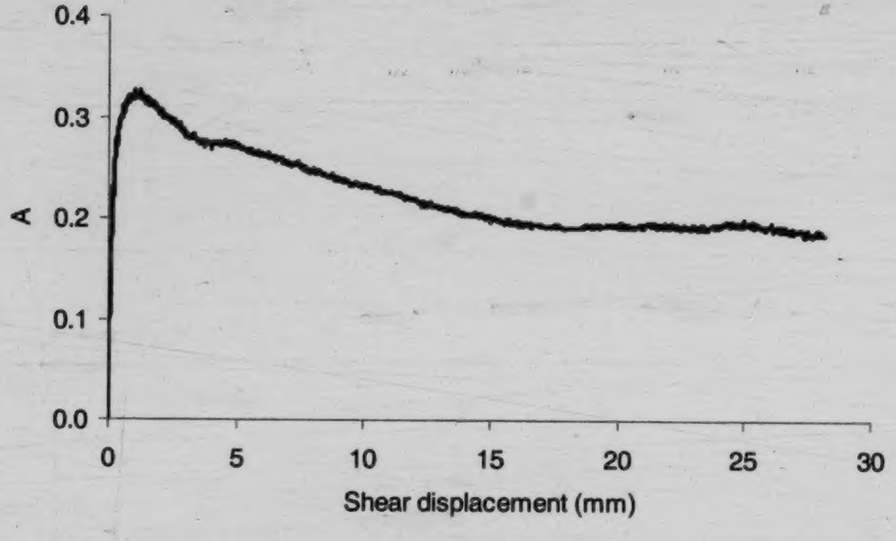

Figure D76 Relationship between the pore-pressure parameter A and the shear displacement for specimen P2

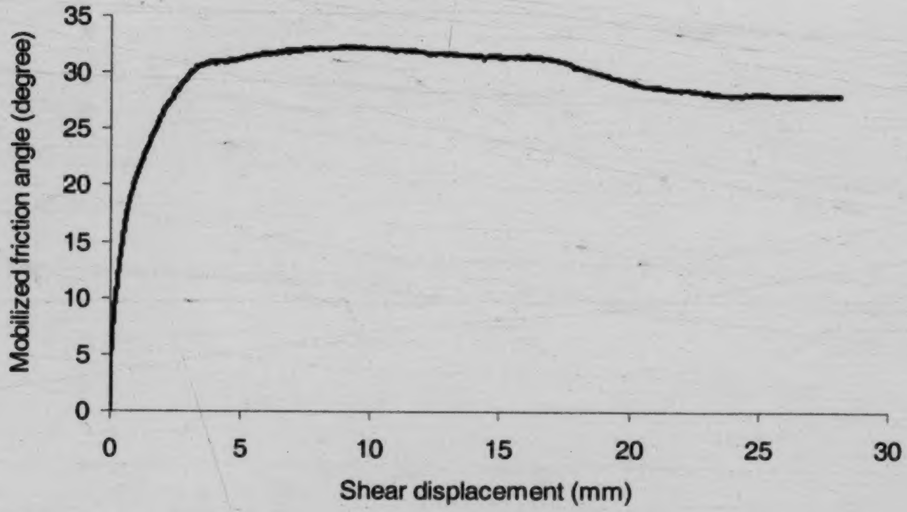

Figure D77 Relationship between the mobilized friction angle and the shear displacement for specimen P2 under the assumption of no cohesion

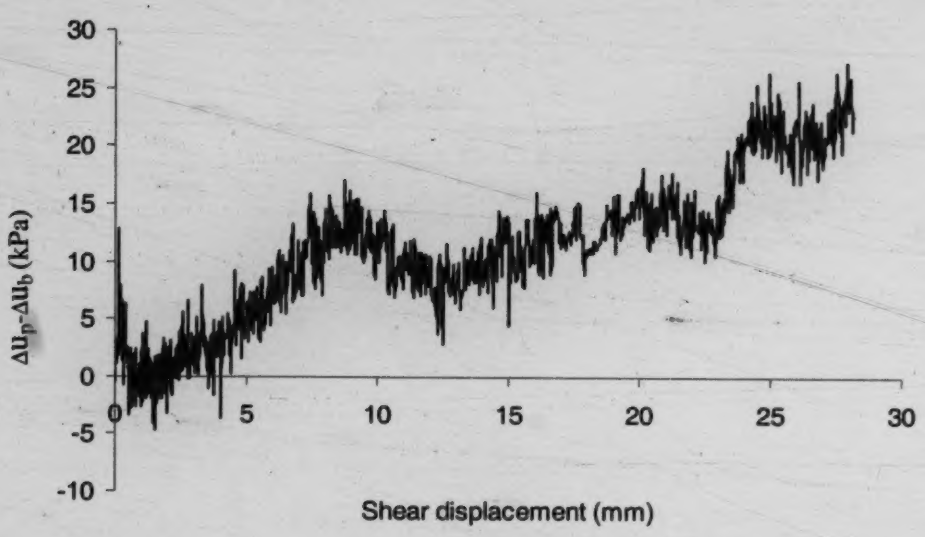

Figure D78 Difference between the pore-pressure-changes on the plane and on the base of specimen P2

Sample 2 0.01 mm/minute of the axial displacement rate

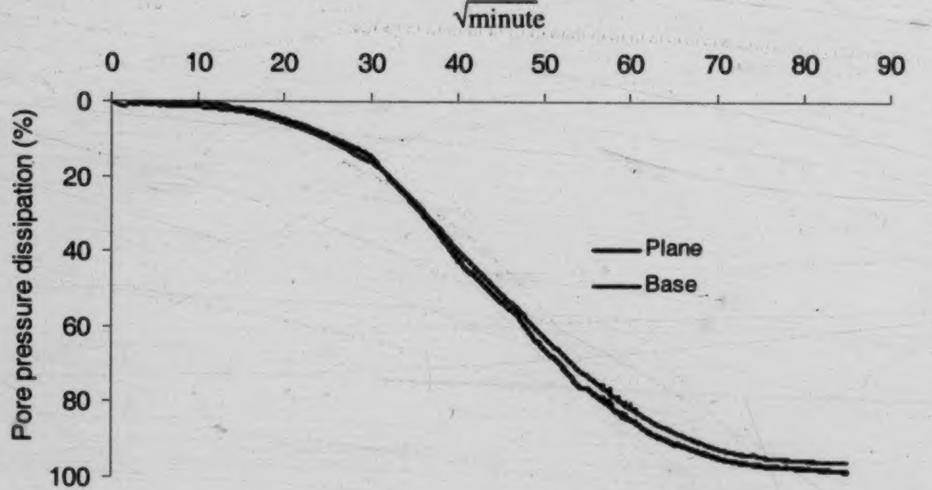

Figure D79 Pore-pressure-dissipation curve for specimen P3

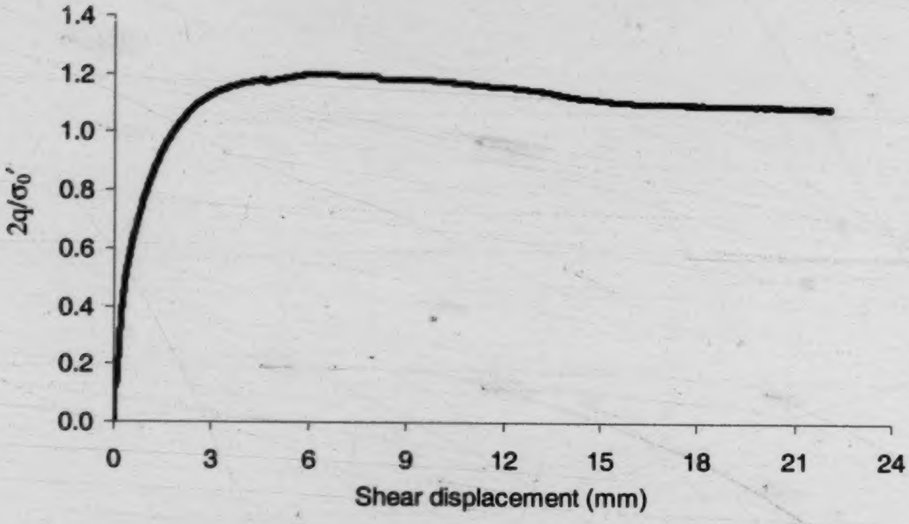

Figure D80 Relationship between the normalized deviator stress and the shear displacement for specimen P3

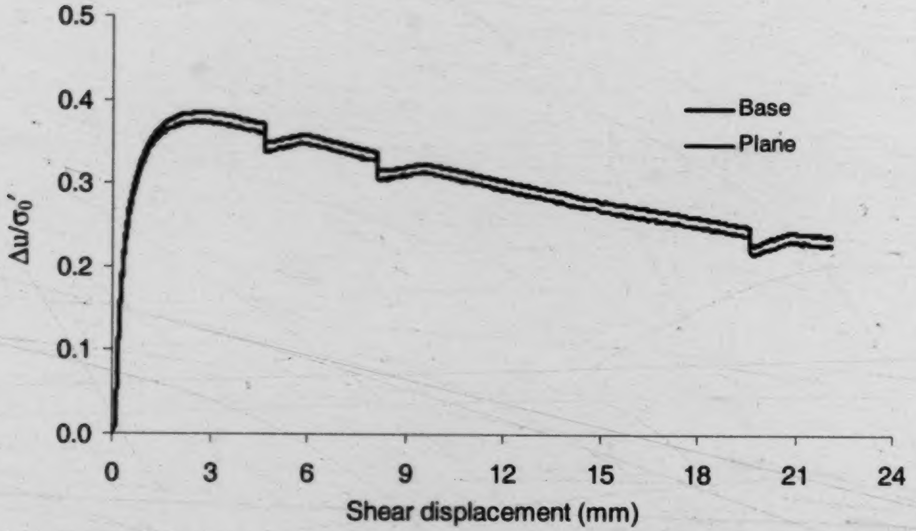

Figure D81 Relationship between the normalized pore-water pressure and the shear displacement for specimen P3

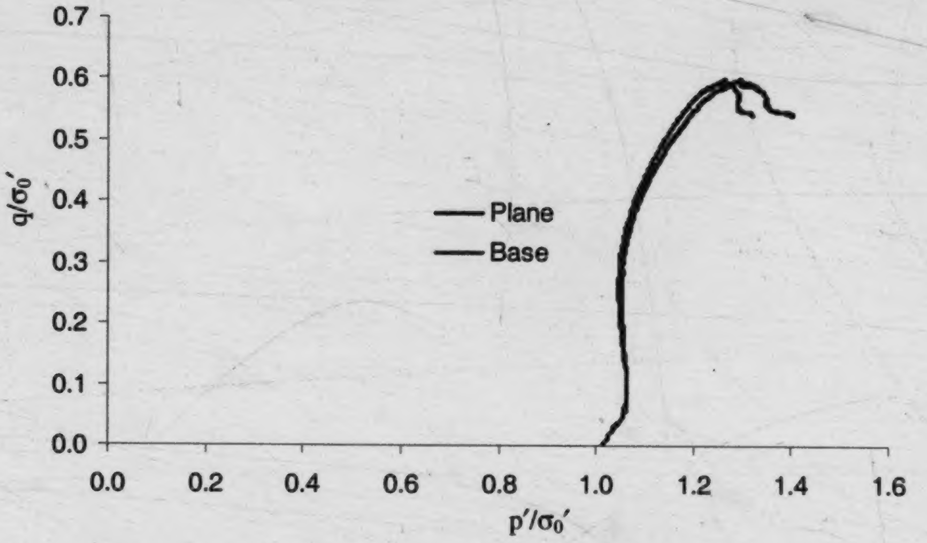

Figure D82 Normalized effective stress paths for specimen P3

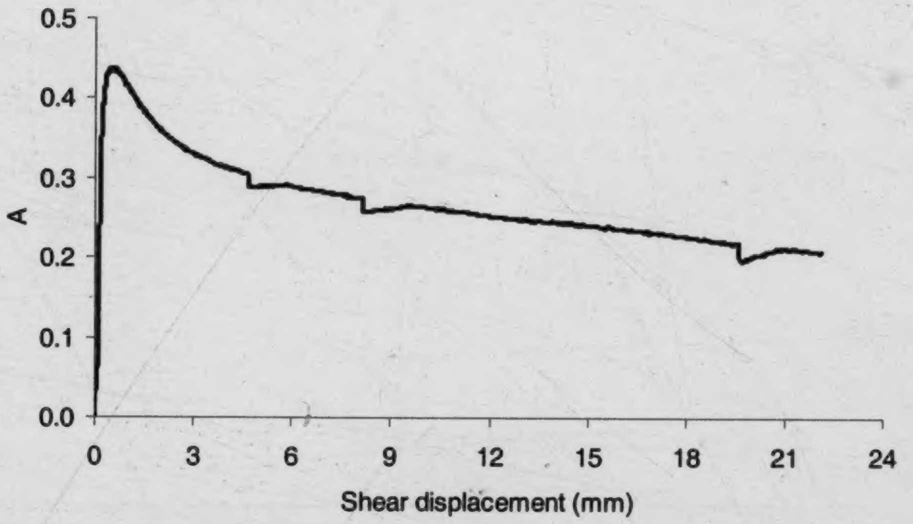

Figure D83 Relationship between the pore-pressure parameter A and the shear displacement for specimen P3

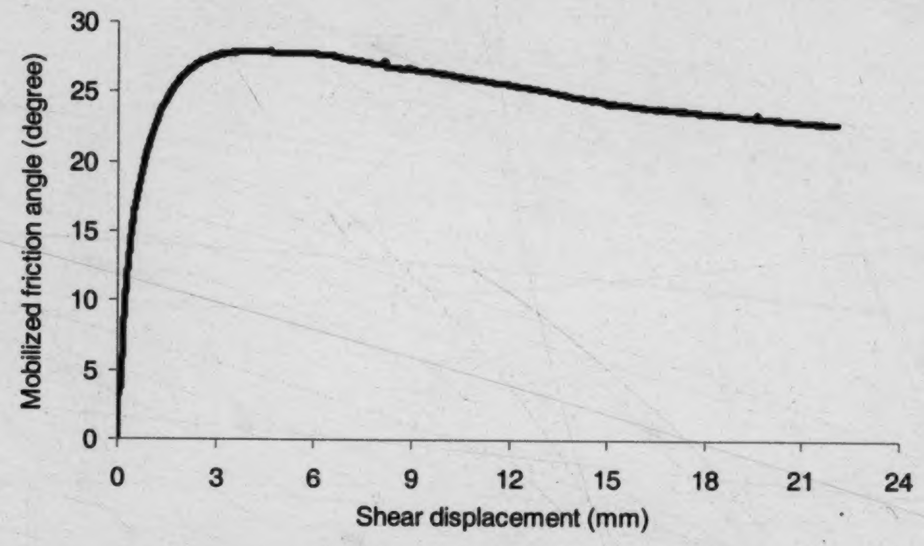

Figure D84 Relationship between the mobilized friction angle and the shear displacement for specimen P3 under the assumption of no cohesion

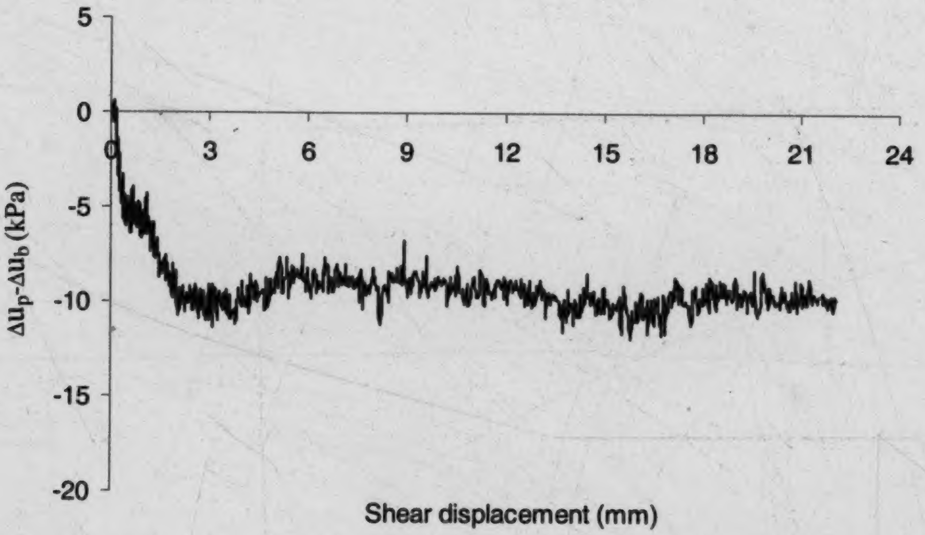

Figure D85 Difference between the pore-pressure-changes on the plane and on the base of specimen P3